# INFORMATION TO USERS

This manuscript has been reproduced from the microfilm master. UMI films the text directly from the original or copy submitted. Thus, some thesis and dissertation copies are in typewriter face, while others may be from any type of computer printer.

**The quality of this reproduction is dependent upon the quality of the copy submitted.** Broken or indistinct print, colored or poor quality illustrations and photographs, print bleedthrough, substandard margins, and improper alignment can adversely affect reproduction.

In the unlikely event that the author did not send UMI a complete manuscript and there are missing pages, these will be noted. Also, if unauthorized copyright material had to be removed, a note will indicate the deletion.

Oversize materials (e.g., maps, drawings, charts) are reproduced by sectioning the original, beginning at the upper left-hand corner and continuing from left to right in equal sections with small overlaps.

ProQuest Information and Learning
300 North Zeeb Road, Ann Arbor, MI 48106-1346 USA
800-521-0600

# Insights from Across the Periodic Table into NMR Chemical Shift, Electric Field Gradient, and Spin-Spin Coupling Tensors: New Information from Solid-State NMR and Computational Chemistry

by

David L. Bryce

Submitted in partial fulfillment of the requirements
for the degree of Doctor of Philosophy

at

Dalhousie University
Halifax, Nova Scotia
September, 2002

DALHOUSIE UNIVERSITY

FACULTY OF GRADUATE STUDIES

The undersigned hereby certify that they have read and recommend to the Faculty of Graduate Studies for acceptance a thesis entitled "Insights from Across the Periodic Table into NMR Chemical Shift, Electric Field Gradient, and Spin-Spin Coupling Tensors: New Information from Solid-State NMR and Computational Chemistry" by David L. Bryce in partial fulfilment for the degree of Doctor of Philosophy.

Dated: September 5, 2002

External Examiner:

Research Supervisor:

Examining Committee:

DALHOUSIE UNIVERSITY

DATE: September 5, 2002

AUTHOR: David L. Bryce

TITLE: Insights from Across the Periodic Table into NMR Chemical Shift, Electric Field Gradient, and Spin-Spin Coupling Tensors: New Information from Solid-State NMR and Computational Chemistry

DEPARTMENT OR SCHOOL: Department of Chemistry

DEGREE: Ph.D. CONVOCATION: October YEAR: 2002

Permission is herewith granted to Dalhousie University to circulate and to have copied for non-commercial purposes, at its discretion, the above title upon the request of individuals or institutions.

Signature of Author

*Having been some days in preparation,*
*a splendid time is guaranteed for all.*

- John Lennon and Paul McCartney
from the Beatles'
"Being for the Benefit of Mr. Kite!"

**List of Illustrations**

**List of Tables**

**Abstract**

To properly interpret the information available from nuclear magnetic resonance (NMR) parameters, it is advantageous to study the complete second-rank interaction tensors, *i.e.*, chemical shift (CS), indirect nuclear spin-spin coupling (**J**), and electric field gradient (EFG) tensors. Two distinct courses of research based on a combined experimental and theoretical approach have been followed.

Modern solid-state NMR techniques have been applied to several quadrupolar nuclei to characterize the magnitude and orientations of their EFG and CS tensors. Results have been obtained for $^{11}B$, $^{35/37}Cl$, $^{53}Cr$, and $^{95}Mo$ at magnetic fields of 4.7 to 18.8 T. The first measurement of a boron CS tensor is reported and interpreted in terms of a simple MO picture. Chlorine NMR of organic hydrochlorides reveals a correlation between the chlorine EFG tensor and the local hydrogen bonding environment. The first $^{53}Cr$ NMR spectra of diamagnetic solids are presented and analyzed. Mo-95 NMR results provide an example of the relationship between the local molecular and electronic structure and the molybdenum CS and EFG tensors. *Ab initio* and density-functional theory (DFT) calculations have been employed to complement the experimental data.

The second aspect of the research involves the application of recent advances in the calculation of **J** *via* multiconfigurational SCF and relativistic DFT methods. Calculations on several diatomics for which highly precise experimental data exist from high-resolution molecular beam spectroscopy have helped to elucidate the connection between **J** and rotational hyperfine parameters. This connection has been exploited to establish the accuracy of the computational methods and to develop a more complete understanding of periodic trends in **J** coupling. This work illustrates the importance of various mechanisms which contribute to **J**. New insight into the phenomenon of **J** coupling between heavy nuclei across hydrogen bonds has been gained. The first experimental attempts to measure the antisymmetric part of **J** are reported.

**List of Abbreviations and Symbols Used**

| | |
|---|---|
| $\mathbf{1}$ | unit tensor |
| $\nabla$ | gradient operator |
| $\xi$ | reduced displacement from equilibrium |
| $\mathbf{A}$ | general second-rank interaction tensor |
| $A$ | antisymmetric indirect nuclear spin-spin coupling constant |
| ACQ | acquire or acquisition |
| ADF | Amsterdam Density Functional |
| AO | atomic orbital |
| $\alpha, \beta, \gamma$ | Euler angles |
| $B_e$ | equilibrium rotational constant |
| $B_0$ | applied external magnetic field (magnetic induction) |
| B3LYP | Becke-3 / Lee-Yang-Parr hybrid functional |
| $c_1, c_2$ | nuclear spin-rotation constants |
| $c_3$ | tensor part of the spin-spin coupling interaction (mol. beam notation) |
| $c_3$(direct) | direct dipolar part of $c_3$ |
| $c_3$(indirect) | indirect part of $c_3$ |
| $c_4$ | isotropic spin-spin coupling constant (mol. beam notation) |
| $C$ | mixing term |
| CAS | complete active space |
| $C_Q$ | nuclear quadrupolar coupling constant |

| | |
|---|---|
| CP | cross-polarization |
| Cp* | pentamethylcyclopentadienide |
| CS | chemical shift |
| CSA | chemical shift anisotropy |
| $\delta_{11}, \delta_{22}, \delta_{33}$ | principal components of the chemical shift tensor |
| $\boldsymbol{\delta}$ | chemical shift tensor |
| $\delta_{iso}, \delta$ | isotropic chemical shift |
| **D** | direct dipolar coupling tensor |
| DFT | density functional theory |
| DSO | diamagnetic spin-orbit |
| $e$ | fundamental charge |
| $eQ$ | nuclear quadrupole moment |
| EFG | electric field gradient |
| EMSL | Environmental Molecular Sciences Laboratory |
| FC | Fermi-contact |
| FID | free-induction decay |
| FT | Fourier transform |
| $\gamma_N$ | magnetogyric ratio for nucleus N |
| GIAO | gauge-including atomic orbitals |
| GGA | generalized gradient approximation |
| $\mathcal{H}$ | Hamiltonian operator |
| $h$ | Planck's constant |

| | |
|---|---|
| $\hbar$ | $h/2\pi$ |
| HOMO | highest occupied molecular orbital |
| $\eta_J$ | asymmetry in the indirect spin-spin coupling tensor |
| $\eta_Q$ | asymmetry in the EFG tensor |
| **I, S** | nuclear spin operators |
| $I, S$ | nuclear spin angular momentum quantum numbers |
| $I_x, I_y, I_z$ | Cartesian components of the nuclear spin operator |
| $I_+, I_-$ | Raising and lowering nuclear spin operators |
| IGLO | individual gauge for localized orbitals |
| INDO | intermediate neglect of differential overlap |
| **J** | indirect nuclear spin-spin coupling tensor |
| $J_{11}, J_{22}, J_{33}$ | principal components of the **J** tensor |
| $\mathbf{J}^{sym}$ | symmetric part of **J** |
| $\mathbf{J}^{antisym}$ | antisymmetric part of **J** |
| $J_{iso}$ | isotropic portion of the indirect spin-spin coupling tensor |
| $\Delta J$ | anisotropy in the indirect spin-spin coupling tensor |
| **K** | reduced indirect nuclear spin-spin coupling tensor |
| $K_{iso}$ | isotropic portion of the reduced indirect spin-spin coupling tensor |
| $\Delta K$ | anisotropy in the reduced indirect spin-spin coupling tensor |
| $\kappa$ | skew of the chemical shift or nuclear magnetic shielding tensor |
| LCAO | linear combination of atomic orbitals |
| LUMO | lowest unoccupied molecular orbital |

| | |
|---|---|
| $\mu_0$ | permeability of free space |
| $\mu_B$ | Bohr magneton |
| $m$ | z-component nuclear spin angular momentum quantum number |
| MAS | magic angle spinning |
| MCSCF | multiconfigurational self-consistent field |
| MO | molecular orbital |
| MQMAS | multiple quantum magic-angle spinning |
| NA | natural abundance |
| NMR | nuclear magnetic resonance |
| $\nu_L$ | Larmor frequency |
| $\nu_r$, $\nu_{rot}$ | magic angle spinning frequency |
| $\nu_i$ | resonance frequency of nucleus i |
| PAS | principal axis system |
| PSO | paramagnetic spin-orbit |
| $\theta$, $\phi$ | polar angles relating the principal axis system of a tensor to the applied external magnetic field |
| $\theta_R$ | angle between the internuclear vector and the applied magnetic field |
| QCPMG | quadrupolar Carr-Purcell-Meiboom-Gill |
| $r_{12}$ | distance between nuclei 1 and 2 |
| RAS | restricted active space |
| $R_{DD}$ | direct dipolar coupling constant |

| | |
|---|---|
| $R_{eff}$ | effective dipolar coupling constant |
| REX | relativistically parametrized extended Hückel |
| rf | radiofrequency |
| $\sigma_{11}$, $\sigma_{22}$, $\sigma_{33}$ | principal components of the nuclear magnetic shielding tensor |
| $\boldsymbol{\sigma}^t$ | transpose of the nuclear magnetic shielding tensor |
| $\boldsymbol{\sigma}$ | nuclear magnetic shielding tensor |
| $\boldsymbol{\sigma}^d$ | diamagnetic part of the nuclear magnetic shielding tensor |
| $\boldsymbol{\sigma}^p$ | paramagnetic part of the nuclear magnetic shielding tensor |
| $\boldsymbol{\sigma}^{sym}$ | symmetric portion of the nuclear magnetic shielding tensor |
| $\boldsymbol{\sigma}^{antisym}$ | antisymmetric portion of the nuclear magnetic shielding tensor |
| $\sigma_{iso}$ | isotropic nuclear magnetic shielding constant |
| SD | spin-dipolar |
| so | spin-orbit |
| STMAS | satellite transition magic angle spinning |
| $T_1$ | nuclear spin-lattice relaxation time constant |
| *Tr* | trace |
| $t$ | time |
| $\tau_c$ | rotational correlation time |
| $\tau_p$ | pulse duration |
| TPPM | two-pulse phase-modulated |
| TMS | tetramethylsilane |

| | |
|---|---|
| VACP | variable-amplitude cross-polarization |
| $\mathbf{V}$ | electric field gradient (EFG) tensor |
| $V_{XX}$, $V_{YY}$, $V_{ZZ}$ | principal components of the EFG tensor |
| VWN | Vosko-Wilk-Nusair |
| $\Omega$ | span of the chemical shift or nuclear magnetic shielding tensor |
| $\omega_r$ | angular rotation frequency, $2\pi\nu_r$ |
| $\omega_1$ | angular frequency of a radiofrequency pulse |
| $\mathbf{Z}$ | Zeeman interaction tensor |
| $Z^{(N)}$ | atomic number of nucleus N |
| ZORA | zeroth-order regular approximation |

**Acknowledgments**

First and foremost, I thank Professor Rod Wasylishen for supervision, guidance, and friendship during the course of my Ph.D. studies. I find it difficult to imagine a superior supervisor. I have been extremely fortunate to be able to carry out my studies in Rod's lab.

I have benefited from interacting with many people during the course of my Ph.D. research. The original group of grad students at Dalhousie when I joined consisted of Scott Kroeker, Rob Schurko, Myrlene Gee, and Guy Bernard. I thank all of them for everything they have taught me. I also thank Scott for the Saturday morning coffee and jazz, and Rob for the guitar jams. I thank Myrlene for her essential contributions to the chlorine and boron projects, and Guy for much assistance with both experimental and computational aspects of various projects. Mike Lumsden is thanked for all of his help on the spectrometers, and for the squash game. The efforts of summer students Chris McDonald and Richard Warren are very much appreciated as well.

I thank the current group at the University of Alberta: Shelley Forgeron, Kirk Feindel, Kris Ooms, Kris Harris, Guy Bernard, Takahiro Ueda, Renée Siegel, and Se-Woung Oh. Kris Harris is thanked for all of his efforts in the synthesis of compounds for various projects. I thank Shelley for collaborations on borazine and chromium projects. Kirk is thanked for helpful discussions concerning the computational aspects of various projects. I thank Kris Ooms for helpful discussions about quadrupolar nuclei. I thank Kirk, Shelley, Kris and Kris for many memorable times both inside and outside the lab. I

am also grateful to our honorary group member, Tom Nakashima, for many useful discussions. The efforts of summer students Andy Hammerlindl, Karen Wei, and Joelle Repka are much appreciated.

I thank Klaus Eichele, Wasylishen group member-at-large, who has been a great help over the past 4 years. Klaus' exceptional work and attention to detail are inspiring. I thank Professor Gang Wu, who introduced me to solid-state NMR at Queen's University, for suggesting Rod as a supervisor and for helpful discussions. I also thank Jim Frye who first got me started on the CMX Infinity spectrometer.

I thank Professors Russell Boyd, Neil Burford, John Coxon, and Bruce Grindley for very useful and informative courses at Dal, helpful discussions, and/or for serving on my advisory committee.

The high-field part of the research in this thesis was performed in the Environmental Molecular Sciences Laboratory (a national scientific user facility sponsored by the U.S. DOE Office of Biological and Environmental Research) located at Pacific Northwest National Laboratory, operated by Battelle for the DOE. I thank Nancy Isern, Andrew Lipton, Jesse Sears, and David Hoyt for their assistance with the 17.6 and 18.8 T NMR systems.

I thank Professor Kenneth Ruud for his invaluable assistance in learning how to use the Dalton Quantum Chemistry program for the calculation of spin-spin coupling tensors. Dr. Jochen Autschbach is also thanked for his extensive help with the ADF program and the CPL module for calculating spin-spin coupling tensors. I thank Professor James Cederberg for helpful discussions and data in advance of publication.

Financial support over the past four years from Dalhousie University, NSERC, the Izaak Walton Killam Trust, and the Walter C. Sumner Foundation is gratefully acknowledged.

I thank my family for their love and support during my ongoing studies.

Finally, I thank Melanie for everything.

## Chapter 1: Introduction and Objectives

### 1.1 Introduction

To say that the discovery of the nuclear magnetic resonance (NMR) phenomenon in the gas phase in 1938 (*1*, *2*) and subsequently in solids (*3*) and liquids (*4*) in 1946 has revolutionized the science of chemistry and has had an enormous impact on related areas of study such as physics, biochemistry, medicine, and materials science would not be an overstatement. Despite the fact that NMR in solids and liquids was discovered essentially simultaneously, the popularity of studying liquids and solutions quickly surpassed that for solids. The observation of subtle chemical shift (*5*) and *J*-coupling (*6*) interactions soon led chemists to realize the vast potential of solution-state NMR in characterizing a variety of chemical systems. In the solid state, however, strong anisotropic chemical shift, dipolar, and possibly quadrupolar interactions were found to generally result in broad, featureless lines which were of little use to chemists. Thus, while solution-state NMR became a routine spectroscopic characterization technique for chemists in the subsequent decades, NMR of solids remained largely confined to the realm of physicists for several years.

Several important developments in the NMR spectroscopy of solids during the 1950s, 60s, and 70s led to the establishment of solid-state NMR as something more than a curiosity for chemists. The first key discovery was made in the 1950s by Andrew, Bradbury, and Eades (*7*, *8*) and by Lowe (*9*), who showed that rapid rotation of a solid powder sample at an angle of 54.74° (the "magic" angle) resulted in a marked narrowing

of the solid-state NMR lineshape due to averaging of many of the anisotropic interactions. While this method provided narrow spectral lines more reminiscent of solution-state NMR spectra, there were still two crucial problems which needed to be overcome. The first was potentially prohibitively long nuclear spin relaxation time constants, and the second was a problem of sensitivity. For a dilute spin-½ nucleus such as $^{13}C$, which is of great interest to synthetic organic chemists, these two problems essentially precluded routine and rapid application of solid-state NMR spectroscopy.

Ernst's implementation of pulsed Fourier transform NMR in the 1960s, for which he was awarded the Nobel Prize in Chemistry in 1991 (*10*), improved sensitivity for both solution- and solid-state NMR, but this was not enough to make solid-state NMR of dilute spin-½ nuclei routine. In 1962, Hartmann and Hahn (*11*) showed how magnetically dilute spins could benefit from the presence of abundant spins, typically protons. Their method both improved the sensitivity in the NMR spectrum of the dilute spins, and allowed the experiment to be repeated on the shorter timescale of the proton nuclear spin relaxation time constant. Pines, Gibby, and Waugh (*12*) developed and applied the Hartmann-Hahn method, which was re-termed "Proton Enhanced Nuclear Induction Spectroscopy" and subsequently "Cross-Polarization" (CP), and demonstrated its effectiveness in acquiring solid-state NMR spectra of dilute spin-½ nuclei in stationary powder samples.

In 1976, Schaefer and Stejskal (*13*) took the critical, if not somewhat obvious in hindsight, step of combining the magic-angle spinning (MAS) method of Andrew and Lowe with the CP technique of Pines, Gibby, and Waugh. The result was a high-

resolution solution-like spectrum which could be acquired with good signal-to-noise in a short period of time. The importance of Schaefer and Stejskal's work towards establishing solid-state NMR of dilute spin-½ nuclei such as $^{13}C$, $^{15}N$, $^{31}P$, and $^{29}Si$ is paramount. The new-found status of solid-state NMR as a useful technique for chemists was nicely emphasized in the 1983 text by Fyfe, "Solid-State NMR for Chemists" (*14*).

Most of the spin-active nuclei in the periodic table are quadrupolar, that is they have a nuclear spin of greater than ½, e.g., $^{11}B$, $^{17}O$, $^{23}Na$, $^{27}Al$. Solution-state NMR of quadrupolar nuclei is in general not feasible due to extremely rapid nuclear spin relaxation. Solid-state NMR of quadrupolar nuclei is complicated by the quadrupolar interaction. Briefly, this interaction is not completely averaged by the MAS technique and the spectroscopist is confronted with broad, anisotropic lineshapes which are anything but "high-resolution". For many years, the potential of high-resolution solid-state NMR of quadrupolar nuclei was grossly hampered by these residual broadenings. The situation changed in 1995 with the introduction of the multiple-quantum MAS experiment by Frydman and co-workers (*15*). This two-dimensional experiment finally allowed, under favourable circumstances, for high-resolution NMR spectra consisting of isotropic resonances to be acquired for half-integer spin quadrupolar nuclei. Needless to say, this discovery has had a tremendous impact on solid-state NMR in the last seven years.

While the above-mentioned developments have extended the appeal of solid-state NMR, the complicated broad anisotropic lineshapes which are observed in the absence of MAS contain a wealth of information. Under these circumstances, the true three-

dimensional orientation-dependent nature of NMR interactions becomes most apparent. Whereas solution-state NMR spectra and CP/MAS solid-state NMR spectra give rise to isotropic observables, e.g., chemical shifts and *J*-couplings, in fact these interactions are properly represented by second-rank tensors which may contain up to *nine* independent elements. Solid-state NMR of stationary samples therefore holds enormous potential for characterizing and interpreting NMR interaction *tensors*, which in principle contain much more information that may be related to the molecular and electronic structure of the chemical system of interest. Essentially one may argue: if useful information on molecular structure and dynamics can be gleaned through the observation of a single isotropic quantity (as has been successfully done for the past 50 years), then surely much more can be learned when up to *nine* observables are measured for a given nucleus instead of just one.

## 1.2 Objectives

The overriding objective of the work presented in this thesis is to provide a combined experimental and theoretical basis for an improved interpretation of nuclear magnetic resonance properties, especially chemical shifts and indirect nuclear spin-spin (**J**) couplings, in their full orientation-dependent second-rank tensor forms, in the context of more familiar chemical concepts such as molecular geometries, electronic structures, and where possible, the periodic table.

This objective is met on two separate, but interrelated fronts. The first is concerned with experimental measurements of chemical shift and electric field gradient

tensors for non-integer quadrupolar nuclei in the solid state, with an emphasis on low-frequency nuclei which have received little if any attention in the history of NMR. The reasons for this lack of attention are not associated with a lack of interest, but with technical problems. Ongoing technical advances, in particular ever-increasing applied magnetic field strengths, have opened up much of the periodic table for study via solid-state NMR spectroscopy. The goal of this aspect of the thesis is to establish the viability of high-field solid-state NMR spectroscopy for several nuclei whose potential has yet to be exploited, to provide benchmark measurements of NMR interaction tensors for these nuclei, as well as to provide interpretations of the experimental data with the aid of computational chemistry and simple molecular orbital pictures.

The second major goal of the thesis is to provide new theoretical and experimental insights into the orientation-dependent nature of the indirect nuclear spin-spin coupling (**J**) interaction. Central to this goal is establishing a link between hyperfine parameters measured from molecular beam spectroscopy and **J** tensors measured by NMR spectroscopy. **J** coupling constants have been of ubiquitous experimental importance since they were first observed 5 decades ago; however, accurate theoretical calculations of this important NMR property have lagged significantly behind experiment and have only begun to become feasible during the past few years. One key objective is therefore to establish the reliability of various computational methods for calculating **J** tensors, in part through explicit comparisons with highly precise experimental data available from molecular beam experiments. The feasibility of modeling **J** coupling in selected biologically important systems is also investigated. Periodic trends in **J** coupling

tensors are also sought. The final aim of this part of the thesis is to provide the first experimental evidence for the existence of the antisymmetric portion of the **J** tensor. This is a particularly challenging task because this property does not influence solution NMR spectra at all, and does not influence solid-state NMR spectra to first order.

## Chapter 2: Principles, Theory, and Techniques

### 2.1 NMR Interactions

The relevant internal NMR Hamiltonian may be summarized as (*16*, *17*):

$$\mathcal{H} = \mathcal{H}_Z + \mathcal{H}_{CS} + \mathcal{H}_Q + \mathcal{H}_{DD} + \mathcal{H}_J + \mathcal{H}_{SR} \qquad [2.1]$$

where the contributing Hamiltonians represent the Zeeman, nuclear magnetic shielding (or chemical shielding), quadrupolar, direct dipolar, indirect nuclear spin-spin, and spin-rotation interactions, respectively. The Zeeman, magnetic shielding, quadrupolar, and spin-rotation interactions have single-spin Hamiltonians. The direct dipolar and indirect nuclear spin-spin Hamiltonians are bilinear in the spin operators, implying that in principle every spin is coupled to every other spin.

Each of the NMR Hamiltonians may be written in either a Cartesian or spherical tensor form (*17*, *18*). In general, the Cartesian representations have the advantage of being more closely and easily tied to a physical picture of the interaction. The spherical tensor representations are advantageous in certain situations, e.g., when one needs to carry out rotations. Below, the Cartesian representations of each of the NMR interactions will be presented in detail, and their spherical counterparts will be discussed where their forms turn out to be useful.

All of the NMR spin interactions may be written in the Cartesian form:

$$\mathcal{H} = c\mathbf{I}\cdot\mathbf{A}\cdot\mathbf{S} = \begin{bmatrix} I_x, I_y, I_z \end{bmatrix} \begin{bmatrix} A_{xx} & A_{xy} & A_{xz} \\ A_{yx} & A_{yy} & A_{yz} \\ A_{zx} & A_{zy} & A_{zz} \end{bmatrix} \begin{bmatrix} S_x \\ S_y \\ S_z \end{bmatrix} \qquad [2.2]$$

where **I** is a nuclear spin operator, **A** is a second-rank tensor, and **S** is a column vector which may be a second spin operator, or an applied magnetic field, for example. The constant $c$ may or may not be equal to unity, depending on the interaction being described.

In the spherical basis, the general form for the NMR Hamiltonians is given as:

$$\mathcal{H} = \sum_{k=0}^{2} \sum_{q=-k}^{+k} (-1)^q A_{kq} T_{k-q} \qquad [2.3]$$

Expansion of this sum gives the following equation:

$$\begin{aligned} \mathcal{H} = {} & A_{00}T_{00} + A_{10}T_{10} - (A_{11}T_{1-1} + A_{1-1}T_{11}) + A_{20}T_{20} \\ & - (A_{21}T_{2-1} + A_{2-1}T_{21}) + A_{22}T_{2-2} + A_{2-2}T_{22} \end{aligned} \qquad [2.4]$$

The relationship between the Cartesian components of **A** given in equation 2.2 and the spherical components given in equation 2.4 is:

$$\begin{aligned} A_{00} &= -\frac{1}{\sqrt{3}}\left(A_{xx} + A_{yy} + A_{zz}\right) = -\frac{1}{\sqrt{3}} Tr(\mathbf{A}) \\ A_{10} &= -\frac{i}{\sqrt{2}}\left(A_{xy} - A_{yx}\right) \\ A_{1\pm1} &= -\frac{1}{2}\left[A_{zx} - A_{xz} \pm i\left(A_{zy} - A_{yz}\right)\right] \\ A_{20} &= \frac{1}{\sqrt{6}}\left[3A_{zz} - \left(A_{xx} + A_{yy} + A_{zz}\right)\right] \\ A_{2\pm1} &= \mp\frac{1}{2}\left[A_{xz} + A_{zx} \pm i\left(A_{yz} + A_{zy}\right)\right] \\ A_{2\pm2} &= \frac{1}{2}\left[A_{xx} - A_{yy} \pm i\left(A_{xy} + A_{yx}\right)\right] \end{aligned} \qquad [2.5]$$

The **T** tensor is the spherical equivalent to the **I** and **S** column vectors in equation 2.2. The $k$ subscript on $A_{kq}$ and $T_{kq}$ refers to the rank of the tensor, where $k = 0$ represents a scalar, $k = 1$ represents a vector, and $k = 2$ represents a matrix (*18*).

*2.1.1 The Zeeman Interaction*

The Zeeman interaction is the fundamental NMR interaction; it is what gives rise to an observable signal. The Zeeman Hamiltonian describes the interaction of the nuclear spin, **I**, with an external applied magnetic field, $\boldsymbol{B}_0$:

$$\mathcal{H}_Z = \mathbf{I} \cdot \mathbf{Z} \cdot \boldsymbol{B}_0 \qquad [2.6]$$

where $\boldsymbol{B}_0$ is the column vector ($B_x$, $B_y$, $B_z$) and **Z** is a tensor which represents the magnetogyric ratio of spin **I**, equal to $-\gamma_I \mathbf{1}$, where **1** is the unit tensor. Typically one is only concerned with the largest component of the $\boldsymbol{B}_0$ vector, which is chosen to be along the z-direction. Thus the Zeeman Hamiltonian reduces to

$$\hbar^{-1}\mathcal{H}_Z = -\gamma_I B_z I_z \qquad [2.7]$$

Usually, the z-component of the $\boldsymbol{B}_0$ field is referred to as $B_0$. For a spin ½ nucleus, the above equation yields two possible states, the energies of which are different. The frequency corresponding to this energy difference is given by the fundamental Larmor equation,

$$\nu_L = \frac{\gamma B_0}{2\pi} \qquad [2.8]$$

where $\nu_L$ is known as the Larmor frequency.

*2.1.2 The Nuclear Magnetic Shielding Interaction*

2.1.2.1 The Nuclear Magnetic Shielding Tensor and Ramsey's Theory

The nuclear magnetic shielding interaction (alternatively the "chemical shielding" interaction) modifies the effective magnetic field at the nucleus as a result of the motions of the surrounding electrons. It is represented by the following Hamiltonian:

$$\mathcal{H}_{CS} = \gamma_I \mathbf{I} \cdot \boldsymbol{\sigma} \cdot \boldsymbol{B}_0 \qquad [2.9]$$

Here, $\gamma_I$ is the magnetogyric ratio of nucleus **I**, and $\boldsymbol{\sigma}$ is the nuclear magnetic shielding tensor:

$$\boldsymbol{\sigma} = \begin{bmatrix} \sigma_{xx} & \sigma_{xy} & \sigma_{xz} \\ \sigma_{yx} & \sigma_{yy} & \sigma_{yz} \\ \sigma_{zx} & \sigma_{zy} & \sigma_{zz} \end{bmatrix} \qquad [2.10]$$

The magnetic shielding tensor (and any 2nd rank tensor in general) can be broken down into three portions: isotropic, symmetric, and antisymmetric:

$$\sigma_{iso} = \frac{1}{3} Tr(\sigma) = \frac{1}{3} Tr(\sigma^{sym}) = \frac{\sigma_{xx} + \sigma_{yy} + \sigma_{zz}}{3} \qquad [2.11]$$

$$\sigma^{sym} = \frac{1}{2}(\sigma + \sigma^t) = \begin{bmatrix} \sigma_{xx} & 0 & 0 \\ 0 & \sigma_{yy} & 0 \\ 0 & 0 & \sigma_{zz} \end{bmatrix} \qquad [2.12]$$

$$\sigma^{antisym} = \frac{1}{2}(\sigma - \sigma^t) = \frac{1}{2} \begin{bmatrix} 0 & \sigma_{xy} - \sigma_{yx} & \sigma_{xz} - \sigma_{zx} \\ \sigma_{yx} - \sigma_{xy} & 0 & \sigma_{yz} - \sigma_{zy} \\ \sigma_{zx} - \sigma_{xz} & \sigma_{zy} - \sigma_{yz} & 0 \end{bmatrix} \qquad [2.13]$$

where $\sigma^t$ is the transpose of $\sigma$. These tensors are given in their principal axis system (PAS), which ensures that the symmetric tensor will be a diagonal tensor with all off-diagonal components equal to zero. In the PAS, the three components of the symmetric portion of the tensor are referred to as the "principal components" and are designated $\sigma_{11}$, $\sigma_{22}$, and $\sigma_{33}$. By convention, $\sigma_{11} \leq \sigma_{22} \leq \sigma_{33}$. The antisymmetric part does not influence NMR spectra to first order. In the zeroth approximation, *i.e.*, where the antisymmetric components are ignored, equation 2.8 may be modified to include the shielding interaction, and its orientation dependence with respect to $B_0$:

$$\nu(\theta,\phi) = \frac{\gamma_I B_0}{2\pi}\left[1 - \left(\sigma_{11}\sin^2\theta\cos^2\phi + \sigma_{22}\sin^2\theta\sin^2\phi + \sigma_{33}\cos^2\theta\right)\right] \qquad [2.14]$$

Here, the angles $\theta$ and $\phi$ define the PAS of the CS tensor with respect to $B_0$ (see Figure 2.1).

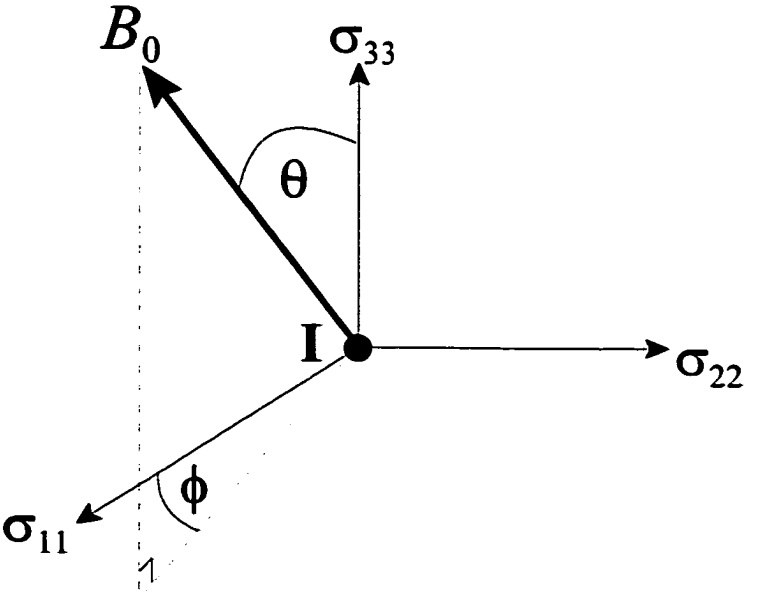


Figure 2.1: Polar angles relating the nuclear magnetic shielding tensor to the direction of the applied magnetic field, $\boldsymbol{B}_0$.

Ding and Ye have provided the analogue to equation 2.14 which incorporates effects on the resonance frequency due to the antisymmetric part of the nuclear magnetic shielding tensor (*19*):

$$\nu(\theta,\phi) = \frac{\gamma_I B_0}{2\pi}\left(\frac{1}{2}\right)\left\{\begin{array}{l}\left(\sigma_{11}\sin 2\theta\cos^2\phi + \sigma_{22}\sin 2\theta\sin^2\phi - \sigma_{33}\sin 2\theta - 2(\sigma_{xz}-\sigma_{zx})\cos\phi + 2(\sigma_{yz}-\sigma_{zy})\sin\theta\right)^2 \\ + \left[(\sigma_{11}-\sigma_{22})\sin\theta\sin 2\phi + 2(\sigma_{xy}-\sigma_{yx})\sin\theta - 2(\sigma_{xz}-\sigma_{zx})\cos\theta\sin\phi - 2(\sigma_{yz}-\sigma_{zy})\cos\theta\cos\phi\right]^2 \\ + 4\left(1-\sigma_{11}\sin^2\theta\cos^2\phi - \sigma_{22}\sin^2\theta\sin^2\phi - \sigma_{33}\cos^2\theta\right)^2\end{array}\right\}^{1/2} \qquad [2.15]$$

From this equation, the zeroth-order equation involving only the principal components of the nuclear magnetic shielding tensor may be identified as the final term in curly brackets. A very few reports of the influence of the antisymmetric part of $\sigma$ on nuclear spin relaxation have been published (*20*, *21*). Haeberlen has discussed the requirements to observe the effects of the antisymmetric components (*16*). Recently, Wi and Frydman have presented the first direct detection of antisymmetric components of the cobalt chemical shift tensor (*vide infra*) in cobalt (III) tris(acetylacetonate): $\delta_{zx} = 1000 \pm 500$ ppm, $\delta_{zy} = -1000 \pm 500$ ppm, $\delta_{xy} = 1000 \pm 1000$ ppm (*22*).

In providing a theoretical basis for nuclear magnetic shielding, Ramsey (*23*) decomposed the shielding into *diamagnetic*, $\sigma^d$, and *paramagnetic*, $\sigma^p$, terms:

$$\sigma = \sigma^d + \sigma^p \qquad [2.16]$$

The diamagnetic contribution depends only on the ground electronic state of the molecule, while the paramagnetic contribution depends on a sum over excited states and hence, the latter is the more difficult term to calculate. The expressions for $\sigma^d$ and $\sigma^p$ are:

$$\sigma_{\alpha\beta}^{d} = \left(\frac{\mu_0}{4\pi}\right)\left(\frac{e^2}{2m}\right)\langle 0|\sum_{k}\frac{(r^2\delta_{\alpha\beta} - r_{k\alpha}r_{k\beta})}{r_k^3}|0\rangle \qquad [2.17]$$

$$\sigma_{\alpha\beta}^{p} = -\left(\frac{\mu_0}{4\pi}\right)\left(\frac{e^2}{2m^2}\right)\sum_{n\neq 0}\left[\frac{\langle 0|\sum_{k} r_k^{-3}\,\ell_{k\alpha}|n\rangle\langle n|\sum_{k}\ell_{k\beta}|0\rangle + \langle 0|\sum_{k}\ell_{k\beta}|n\rangle\langle n|\sum_{k} r_k^{-3}\,\ell_{k\alpha}|0\rangle}{^{1}\varepsilon_n - \varepsilon_0}\right] \qquad [2.18]$$

Here, $e$ is the charge of an electron, $m$ is the mass of an electron, k indicates a sum over all electrons, n indicates a sum over excited singlet states, $r_k$ is the position vector for electron k, and $\ell$ is the angular momentum operator with respect to the gauge origin. Equations 2.17 and 2.18 may be used to obtain any of the shielding tensor components by appropriate permutation of $\alpha$ and $\beta$ over x, y, and z; $\delta_{\gamma\upsilon}$ is the Kronecker delta.

The utility of the magnetic shielding tensor (and chemical shift tensor, *vide infra*) is summarized in Ramsey's equations. The geometry and electronic structure of the molecule about the nucleus under consideration manifests itself in the nuclear magnetic shielding tensor. Hence, measurement of chemical shift tensors has the potential to offer insight into the electronic structure about nuclei (*24*, *25*, *26*).

### 2.1.2.2 The Chemical Shift Tensor

The magnetic shielding tensor is directly related to the experimentally observable property, *chemical shift*. The chemical shift, $\delta$, is related to the magnetic shielding by the following equation:

$$\delta = \frac{\sigma_{ref} - \sigma}{1 - \sigma_{ref}} \qquad [2.19]$$

where $\sigma_{ref}$ is the shielding for a chosen reference compound. Both $\sigma$ and $\delta$ are measured in ppm. The above discussion of the symmetry properties (isotropic, symmetric, and antisymmetric components) of the nuclear magnetic shielding tensor apply identically to the chemical shift tensor by virtue of the definition given here. For most nuclei, and in particular light nuclei, the denominator in equation 2.19 is approximated by unity such that one writes

$$\delta \cong \sigma_{ref} - \sigma \qquad [2.20]$$

In practice, one measures the resonance frequency of the compound of interest with respect to that of a primary reference:

$$\delta = \frac{\upsilon - \upsilon_{ref}}{\upsilon_{ref}} \times 10^6 \qquad [2.21]$$

Equation 2.21 is the working definition of the chemical shift. The principal components of the chemical shift (CS) tensor, $\delta$, correspond to those of the shielding tensor, *i.e.*, $\delta_{11}$ corresponds to $\sigma_{11}$ etc. It is convenient to define two related quantities, the span ($\Omega$) and the skew ($\kappa$) which help in describing the shape of the powder pattern resulting from a particular CS tensor (see Figure 2.2) (*27*):

$$\Omega = \sigma_{33} - \sigma_{11} \approx \delta_{11} - \delta_{33} \qquad [2.22]$$

$$\kappa = \frac{3\left(\sigma_{iso} - \sigma_{22}\right)}{\Omega} \approx \frac{3\left(\delta_{22} - \delta_{iso}\right)}{\Omega} \qquad [2.23]$$

The approximate equality arises due to the approximation made upon writing equation 2.20 from equation 2.19. The span has units of ppm. The skew is unitless and can take on values between -1 and +1. A CS tensor is said to be axially symmetric if two of the principal components are identical, e.g., $\sigma_{11} = \sigma_{22} \neq \sigma_{33}$.

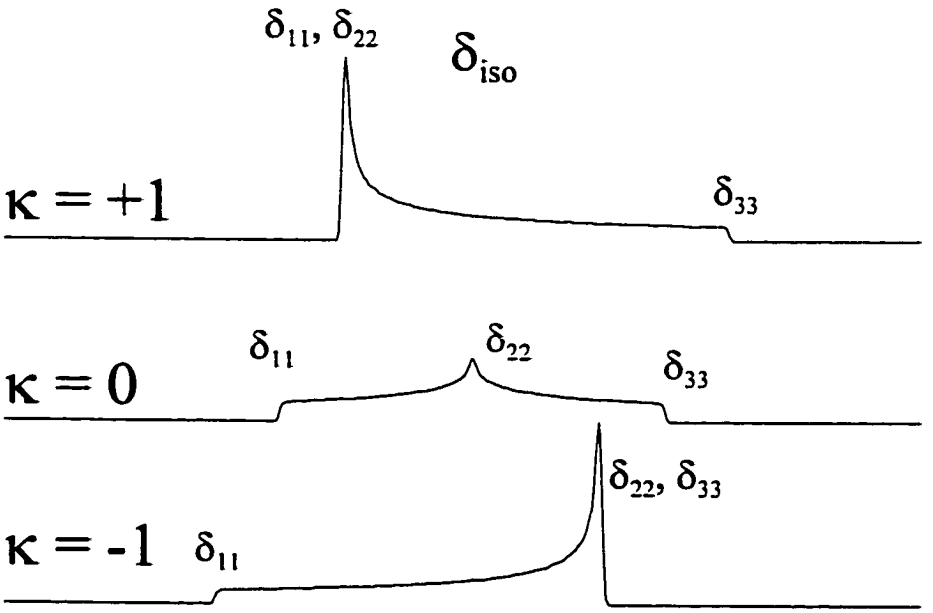


Figure 2.2: Simulated spectra of an isolated spin-½ nucleus exhibiting anisotropic magnetic shielding.

*2.1.3 The Nuclear Electric Quadrupolar Interaction*

The majority of elements in the periodic table have an isotope with a quadrupolar nucleus. Nuclei with spin $I > ½$ possess a nuclear quadrupole moment, $eQ$, because the nuclear charge distribution is non-spherical (*28*). If the shape of the charge distribution is that of a prolate spheroid, $eQ$ is positive; if it is oblate, $eQ$ is negative (Figure 2.3).

The nuclear quadrupole moment interacts with the electric field gradient (EFG) at the nucleus. The EFG tensor differs from the nuclear magnetic shielding tensor in that the former is described by a symmetric, traceless second-rank tensor, **V**, with five independent components, $V_{\tau\upsilon}$. These components are also denoted $eq_{\tau\upsilon}$. There is no

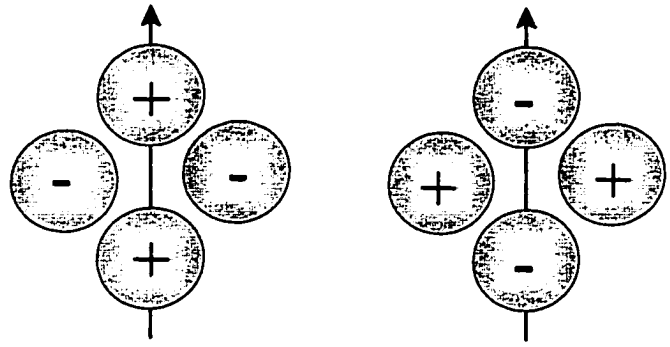


prolate, $eQ > 0$ oblate, $eQ < 0$

Figure 2.3: General form of the distribution of nuclear charge with respect to the nuclear spin axis for quadrupolar nuclei.

zero-rank (isotropic) or first-rank (antisymmetric) contribution to the EFG, only a second-rank (symmetric) contribution. Laplace's equation for the electrostatic potential demands that $V_{XX} + V_{YY} + V_{ZZ} = 0$. The Hamiltonian describing the interaction of the nuclear quadrupole moment with the EFG at a nucleus is:

$$\mathcal{H}_Q = \frac{eQ}{6I(2I-1)h}\mathbf{I}\cdot\mathbf{V}\cdot\mathbf{I} \qquad [2.24]$$

In its principal axis system, the EFG tensor is diagonal and can be characterized by two independent parameters: the largest principal component, $V_{ZZ} = eq_{ZZ} = \partial^2 V/\partial z^2$, and the asymmetry parameter, $\eta_Q = (V_{XX} - V_{YY})/V_{ZZ}$, with the convention that $|V_{ZZ}| \geq |V_{YY}| \geq |V_{XX}|$. The product of the nuclear quadrupole moment and the largest component of the EFG tensor is known as the nuclear quadrupolar coupling constant,

$$C_Q = eQV_{ZZ}/h = e^2q_{ZZ}Q/h \qquad [2.25]$$

Some authors use the symbol $\chi$ to denote the quadrupolar coupling constant.

In the absence of an external applied magnetic field, the axis of quantization for the quadrupolar nucleus depends upon the orientation of the EFG tensor at the nucleus. That is, the quadrupolar interaction ties the spin to the molecular framework since the EFG depends on the local environment of a nucleus. In the presence of an external applied magnetic field, $B_0$, the Zeeman and quadrupolar interactions compete to determine the axis of quantization of the nuclear spin angular momentum. Pound first described quadrupolar effects on NMR spectra in crystals (*29*, *30*). If the Zeeman interaction is much larger than the quadrupolar interaction (the high-field approximation), a number of simplifications result in treating quantum mechanical problems involving quadrupolar nuclei.

The first- and second-order corrections to the pure Zeeman energies due to the quadrupolar interaction may be obtained from perturbation theory. The energy corrections are (*31*):

$$E_{\mathrm{m}}^{(1)} = \frac{hC_{\mathrm{Q}}}{4I(2I-1)}(I(I+1)-3m^2)\left[\frac{1}{2}\left(3\cos^2\theta-1\right)-\eta_{\mathrm{Q}}\cos 2\phi\left(\cos^2\theta-1\right)\right] \qquad [2.26]$$

$$E_m^{(2)} = -\left(\frac{hC_{\mathrm{Q}}}{4I(2I-1)}\right)^2\left(\frac{m}{\omega_0}\right)\left\{\begin{array}{l} -\frac{1}{5}(I(I+1)-3m^2)(3+\eta_Q^2) \\ +\frac{1}{28}(8I(I+1)-12m^2-3)\left[(\eta_Q^2-3)(3\cos^2\theta-1)+6\eta_Q\sin^2\theta\cos 2\phi\right] \\ +\frac{1}{8}(18I(I+1)-34m^2-5)\left[\begin{array}{l}\frac{1}{140}(18+\eta_Q^2)(35\cos^4\theta-30\cos^2\theta+3) \\ +\frac{3}{7}\eta_Q\sin^2\theta(7\cos^2\theta-1)\cos 2\phi+\frac{1}{4}\eta_Q^2\sin^4\theta\cos 4\phi\end{array}\right]\end{array}\right\}$$

[2.27]

The angles define the orientation of the EFG tensor with respect to the external applied magnetic field, $B_0$. The first-order term vanishes in the limit of very rapid (in principle infinite) MAS. Although the second order term is cumbersome, it is worth including here and merits further comment. It is in fact this second-order quadrupolar interaction which

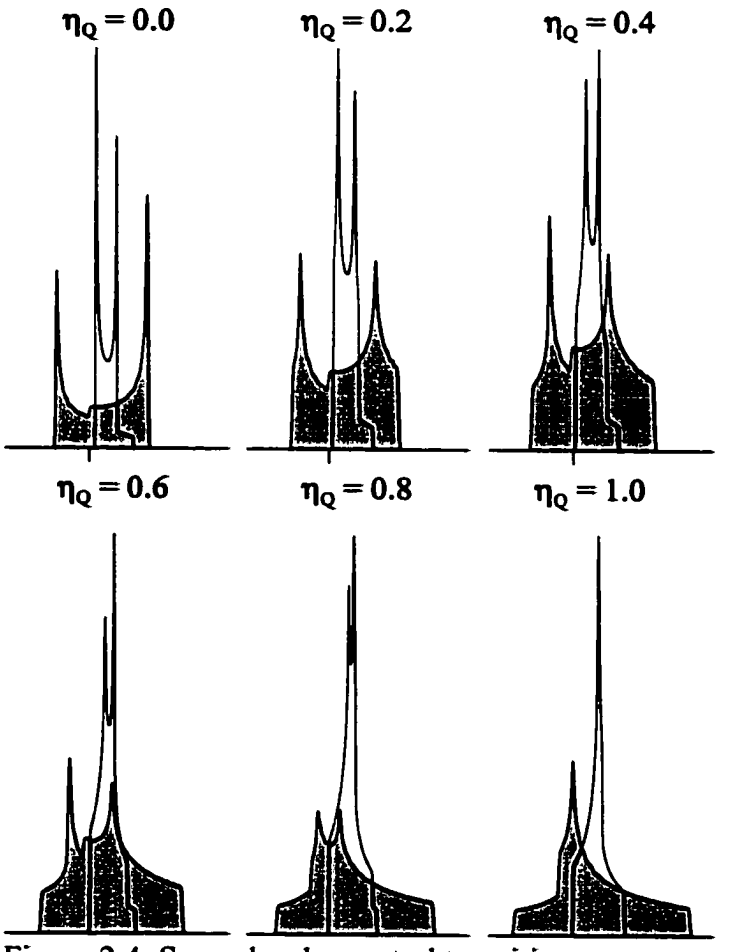


Figure 2.4: Second-order central transition quadrupolar powder patterns for a spin-n/2 quadrupolar nucleus for an arbitrary value of $C_Q$ and various values of $\eta_Q$. The filled spectra are for stationary samples and the empty spectra are under conditions of magic-angle spinning.

gives rise to useful lineshapes in MAS NMR spectroscopy of half-integer spin quadrupolar nuclei (see Figure 2.4). The first term in the large brackets has no orientation dependence. This means that the apparent centre-of-gravity of the NMR spectrum of the central or satellite transitions of a quadrupolar nucleus will in fact be a sum of contributions from the isotropic portion of the second-order quadrupolar interaction and the isotropic chemical shift. Samoson has shown that the so-called second-order quadrupolar shift relative to the isotropic chemical shift in a powdered sample is given by (*32*):

$$\Delta \nu_{m,m-1} = -\frac{3}{40}\left(\frac{C_Q^2}{\nu_L}\right)\left\{\frac{I(I+1)-9m(m-1)-3}{I^2(2I-1)^2}\right\}\left(1+\frac{\eta_Q^2}{3}\right) \qquad [2.28]$$

where $m$ is the magnetic quantum number of the spin state in question. Thus, the equation may be used to determine not only the position of the central ½ ↔-½ transition relative to the isotropic chemical shift, but also the satellite transitions. As an example, the second-order shifts for a spin-5/2 nucleus such as $^{95}$Mo are:

$$\begin{aligned}
\Delta \nu_{\pm\frac{5}{2},\pm\frac{3}{2}} &= \frac{84}{4000}\left(\frac{C_Q^2}{\nu_L}\right)\left(1+\frac{\eta_Q^2}{3}\right) \\
\Delta \nu_{\pm\frac{3}{2},\pm\frac{1}{2}} &= \frac{3}{4000}\left(\frac{C_Q^2}{\nu_L}\right)\left(1+\frac{\eta_Q^2}{3}\right) \\
\Delta \nu_{+\frac{1}{2},-\frac{1}{2}} &= \frac{-24}{4000}\left(\frac{C_Q^2}{\nu_L}\right)\left(1+\frac{\eta_Q^2}{3}\right)
\end{aligned} \qquad [2.29]$$

Further details concerning the theory of NMR spectroscopy of quadrupolar nuclei may be found in informative articles by Duer and Farnan (*31*), Man (*33*), and Vega (*34*).

*2.1.4 Direct Dipolar Coupling*

The direct dipolar coupling between two nuclei is analogous to the classical magnetic interaction between two bar magnets. The direct dipolar Hamiltonian is written as:

$$\mathcal{H}_{DD} = \mathbf{I} \cdot \mathbf{D} \cdot \mathbf{S} \qquad [2.30]$$

Here, **I** and **S** are the nuclear spin operators of the two nuclei involved. These may be either homonuclear or heteronuclear. In its PAS, the direct dipolar coupling tensor, **D**, is given in Cartesian coordinates as follows (*35*):

$$\mathbf{D} = R_{DD} \begin{bmatrix} 1 & 0 & 0 \\ 0 & 1 & 0 \\ 0 & 0 & -2 \end{bmatrix} \qquad [2.31]$$

In the absence of motion, this tensor is axially symmetric about the internuclear vector which joins the dipolar-coupled nuclei. The direct dipolar coupling constant, $R_{DD}$, depends directly on the distance separating the two spins involved:

$$R_{DD} = \frac{\mu_0}{4\pi} \frac{\gamma_1 \gamma_2 \hbar}{2\pi} \left\langle r_{12}^{-3} \right\rangle \qquad [2.32]$$

Here, $\langle r_{12}^{-3} \rangle$ is the motionally-averaged inverse cube of the internuclear distance. Motional averaging will inevitably result in a reduction in $R_{DD}$ and a corresponding apparent increase in $r_{12}$ (*36*). Bond lengths obtained from NMR experiments are known to be typically 1 to 4 % larger than those obtained from X-ray or neutron diffraction experiments (*36, 37, 38, 39*). While molecular "stretching" vibrations contribute in part to a partial averaging of the direct dipolar interaction, bending and torsional librations are primarily responsible. Incorporation of librational effects increases the accuracy but

reduces the precision of internuclear distances derived from NMR. A further complication in converting measured dipolar coupling constants to internuclear distances involves the anisotropic portion of the indirect nuclear spin-spin coupling tensor (see Sections 2.1.5 and 2.1.6 below).

### *2.1.5 Indirect Nuclear Spin-Spin Coupling*

In addition to the direct dipolar coupling of nuclei described above, nuclear spins are also coupled indirectly *via* the intervening electrons. This indirect nuclear spin-spin coupling, or **J**, interaction is represented by the following Hamiltonian:

$$\mathcal{H}_J = \mathbf{I} \cdot \mathbf{J} \cdot \mathbf{S} \qquad [2.33]$$

Like the nuclear magnetic shielding tensor, the **J** coupling tensor has in principle up to nine independent elements.

$$\mathbf{J} = \begin{bmatrix} J_{xx} & J_{xy} & J_{xz} \\ J_{yx} & J_{yy} & J_{yz} \\ J_{zx} & J_{zy} & J_{zz} \end{bmatrix} \qquad [2.34]$$

Thus **J** contains contributions in principle from isotropic, symmetric, and antisymmetric components, given here in the principal axis system of the symmetric tensor:

$$J_{iso} = \frac{1}{3} Tr(\mathbf{J}) = \frac{J_{xx} + J_{yy} + J_{zz}}{3} \qquad [2.35]$$

$$\mathbf{J}^{sym} = \frac{1}{2}\left(\mathbf{J} + \mathbf{J}^{t}\right) = \begin{bmatrix} J_{xx} & 0 & 0 \\ 0 & J_{yy} & 0 \\ 0 & 0 & J_{zz} \end{bmatrix} \qquad [2.36]$$

$$\mathbf{J}^{\text{antisym}} = \frac{1}{2}\left(\mathbf{J} - \mathbf{J}^{t}\right) = \frac{1}{2}\begin{bmatrix} 0 & J_{xy} - J_{yx} & J_{xz} - J_{zx} \\ J_{yx} - J_{xy} & 0 & J_{yz} - J_{zy} \\ J_{zx} - J_{xz} & J_{zy} - J_{yz} & 0 \end{bmatrix} \quad [2.37]$$

The symmetric part of the **J** tensor may be described by its principal components, defined and ordered as $|J_{33} - J_{iso}| \geq |J_{11} - J_{iso}| \geq |J_{22} - J_{iso}|$, or by the derived anisotropy ($\Delta J$) and asymmetry ($\eta_J$) parameters:

$$\Delta J = J_{33} - \frac{\left(J_{11} + J_{22}\right)}{2} \quad [2.38]$$

$$\eta_J = \left(J_{22} - J_{11}\right)/\left(J_{33} - J_{iso}\right) \quad [2.39]$$

The theory of indirect spin-spin coupling was originally described by Ramsey (*40*, *41a,b*, *42*). Qualitatively, the indirect nuclear spin-spin coupling may be pictured as a two-step process, in which one nucleus polarizes neighbouring electrons and this polarization is transferred *via* the electronic network to a second nucleus. In Ramsey's non-relativistic theory, there are three basic mechanisms by which the nucleus may interact with neighbouring electrons. In the first of these, electronic currents are established by action of the magnetic field of one nuclear magnetic dipole on the orbital angular momentum of the electrons. The induced currents then produce magnetic fields at the site of the second nucleus. This effect, termed the spin-orbit (SO) mechanism, is usually further subdivided into a diamagnetic (DSO) and paramagnetic (PSO) part. Secondly, the dipolar interaction between the magnetic moment of one nucleus and the electron spins produces an electron spin polarization so that there are non-vanishing magnetic fields which act on other nuclei; this is known as the spin-dipolar (SD)

mechanism. Finally, there is the Fermi-contact (FC) interaction between a nuclear magnetic moment and electrons which have finite probability of being at the nucleus. Again, electron spins are coupled by spin-polarization which in turn induces a field at the second nucleus. The different allowed spin states of the nuclei involved in the coupling lead to the spectral *J*-splittings commonly observed in NMR spectra of solutions and solids.

Treatment of the **J** coupling interaction between two nuclei N and N' by first-order perturbation theory leads to the DSO contribution (*43*, *44*):

$$\mathbf{J}^{\mathrm{DSO}} = \left(\frac{4}{h}\right) e\hbar\mu_{\mathrm{B}}\left(\frac{\mu_0}{4\pi}\right)^2 \gamma_{\mathrm{N}}\gamma_{\mathrm{N'}}\left\langle 0\left|\sum_k \left(\mathbf{r}_{k\mathrm{N}}\cdot\mathbf{r}_{k\mathrm{N'}}\right)r_{k\mathrm{N}}^{-3}r_{k\mathrm{N'}}^{-3}\right|0\right\rangle \qquad [2.40]$$

The remaining terms (eqs. 2.41 - 2.44) arise as a result of second-order perturbation theory. It is important to note that the second-order terms are by no means smaller in magnitude than the first-order DSO term; in fact the DSO term is often negligible.

$$\mathbf{J}^{\mathrm{PSO}} = \left(\frac{-2}{h}\right)\left(2\mu_{\mathrm{B}}\hbar\right)^2\left(\frac{\mu_0}{4\pi}\right)^2 \gamma_{\mathrm{N}}\gamma_{\mathrm{N'}} \times$$
$$\sum_n \left({}^1E_n - E_0\right)^{-1}\left\langle 0\left|\sum_k r_{k\mathrm{N}}^{-3}\left(\mathbf{r}_{k\mathrm{N}}\times\nabla_k\right)\right|n\right\rangle\left\langle n\left|\sum_j r_{j\mathrm{N'}}^{-3}\left(\mathbf{r}_{j\mathrm{N'}}\times\nabla_j\right)\right|0\right\rangle \qquad [2.41]$$

$$\mathbf{J}^{\mathrm{SD}} = \left(\frac{-2}{h}\right)\left(2\mu_{\mathrm{B}}\hbar\right)^2\left(\frac{\mu_0}{4\pi}\right)^2 \gamma_{\mathrm{N}}\gamma_{\mathrm{N'}} \times$$
$$\sum_n \left({}^3E_n - E_0\right)^{-1}\left\langle 0\left|\sum_k 3r_{k\mathrm{N}}^{-3}\left(\mathbf{S}_k\cdot\mathbf{r}_{k\mathrm{N}}\right)\mathbf{r}_{k\mathrm{N}} - r_{k\mathrm{N}}^{-3}\mathbf{S}_k\right|n\right\rangle\left\langle n\left|\sum_j 3r_{j\mathrm{N'}}^{-3}\left(\mathbf{S}_j\cdot\mathbf{r}_{j\mathrm{N'}}\right)\mathbf{r}_{j\mathrm{N}} - r_{j\mathrm{N'}}^{-3}\mathbf{S}_j\right|0\right\rangle$$

[2.42]

$$\mathbf{J}^{FC} = \left(\frac{-2}{h}\right)\left(16\pi\mu_B\hbar/3\right)^2\left(\frac{\mu_0}{4\pi}\right)^2\gamma_N\gamma_{N'} \times \sum_n \left({}^3E_n - E_0\right)^{-1}\left\langle 0\left|\sum_k \delta(r_{kN})\mathbf{S}_k\right|n\right\rangle\left\langle n\left|\sum_j \delta(r_{jN'})\mathbf{S}_j\right|0\right\rangle \quad [2.43]$$

$$\mathbf{J}^{FC\times SD} = \left(\frac{-4}{h}\right)\left(2\mu_B\hbar\right)\left(16\pi\mu_B\hbar/3\right)\left(\frac{\mu_0}{4\pi}\right)^2\gamma_N\gamma_{N'} \times \sum_n \left({}^3E_n - E_0\right)^{-1}\left\langle 0\left|\sum_k \delta(r_{kN})\mathbf{S}_k\right|n\right\rangle\left\langle n\left|\sum_j r_{jN'}^{-3}\left(\mathbf{S}_j \cdot \mathbf{r}_{jN'}\right)\mathbf{r}_{jN} - r_{jN'}^{-3}\mathbf{S}_j\right|0\right\rangle \quad [2.44]$$

Here, $e$ is the fundamental charge; $\mu_B$ is the Bohr magneton; $n$ labels excited states of appropriate symmetry, either singlet (for PSO) or triplet (for FC, SD, and FCxSD); $\mathbf{r}_{kN}$ is the vector between electron $k$ and nucleus N; $\nabla$ is the gradient operator; $\mathbf{S}$ is the electron spin angular momentum vector, and $\delta(r_{kN})$ is the Dirac delta function which is zero unless electron $k$ coincides with nucleus N. Some qualitative insight may be gained by an examination of the form of these equations. First, the DSO term is simply an expectation value and is the most easily calculated contribution. The PSO term depends on a sum over excited singlet states while the FC, SD, and FC x SD terms depend on sums over excited triplet states. The equations 2.40 - 2.44 remain exact at the non-relativistic level for a point nucleus (*45*). The theory describing relativistic treatments of **J** coupling will not be described in detail here; an overview of the progress made in this area will be given in Chapter 4.

It is beneficial to define a reduced coupling tensor $\mathbf{K}_{N,N'}$ which is related to $\mathbf{J}_{N,N'}$ by the following equation:

$$\mathbf{J}_{N,N'} = \gamma_N \gamma_{N'} h \mathbf{K}_{N,N'} / 4\pi^2 \qquad [2.45]$$

The reduced coupling tensor is independent of the magnitude of the nuclear magnetic moments; therefore, it is useful in comparing indirect spin-spin coupling tensors involving different spin pairs. Note that $\mathbf{J}_{N,N'}$ has units of Hz ($s^{-1}$) and $\mathbf{K}_{N,N'}$ has units of $N\ A^{-2}\ m^{-3}$ or equivalently, $T^2\ J^{-1}$ (*46*).

The relationships between the various coupling mechanisms and the three parts of the **J** tensor are summarized in Table 2.1.

**Table 2.1**: Relationships between the mechanisms which contribute to **J** and the symmetry properties of **J**.

| Mechanism | Isotropic | Symmetric | Antisymmetric |
|---|---|---|---|
| DSO | ✓ | ✓ | ✓ |
| PSO | ✓ | ✓ | ✓ |
| FC | ✓ | ✗ | ✗ |
| SD | ✓ | ✓ | ✓ |
| FC x SD | ✗ | ✓ | ✗ |

*2.1.6 The Total Symmetric Spin-Spin Coupling Tensor*

It is instructive to consider the total spin-spin coupling tensor (direct dipolar and indirect) for the case of a diatomic molecule, where symmetry dictates the orientation of the tensors and forces the antisymmetric components of **J** to be zero (*47*). The sum spin-spin coupling Hamiltonian in this simple case may be written as

$$\mathcal{H}_{DD} + \mathcal{H}_J = \mathbf{I}\cdot(\mathbf{D}+\mathbf{J})\cdot\mathbf{S} \qquad [2.46]$$

Separating the isotropic and symmetric portions of the tensors gives:

$$\mathcal{H}_{DD} + \mathcal{H}_J = J_{iso}\mathbf{I}\cdot\mathbf{S} + \mathbf{I}\cdot(\mathbf{D}+\mathbf{J}^{sym})\cdot\mathbf{S} \qquad [2.47]$$

In the PAS of the diatomic, the symmetric tensor part of the above equation may be written in Cartesian form as:

$$\mathbf{D}+\mathbf{J}^{sym} = R_{DD}\begin{bmatrix}1&0&0\\0&1&0\\0&0&-2\end{bmatrix} - \frac{\Delta J}{3}\begin{bmatrix}1&0&0\\0&1&0\\0&0&-2\end{bmatrix} \qquad [2.48]$$

where $\Delta J$ is equal to $J_{\parallel} - J_{\perp}$ in the case of a diatomic molecule. Equation 2.48 may be condensed to give the simpler form (eq. 2.49):

$$\mathbf{D}+\mathbf{J}^{sym} = R_{eff}\begin{bmatrix}1&0&0\\0&1&0\\0&0&-2\end{bmatrix} \qquad [2.49]$$

where

$$R_{eff} = R_{DD} - \frac{\Delta J}{3} \qquad [2.50]$$

The key result of this description of the total symmetric spin-spin coupling tensor is that the direct dipolar coupling constant and the anisotropic part of the **J** tensor, $\Delta J$, are inseparable in a real system. That is to say, it is possible to consider their Hamiltonians

separately as has been done in this chapter, but due to the form of these Hamiltonians, only an effective dipolar coupling constant $R_{eff}$ may be directly measured in any experiment. This fact is exemplified in the manner in which the total internal Hamiltonian is written from the perspective of molecular beam spectroscopists. For example, for the diatomic ClF, the hyperfine molecular beam Hamiltonian is given by (*41*, *48*, *49*):

$$h^{-1}\mathcal{H}_{hf} = \mathbf{V}_{Cl} \cdot \mathbf{Q}_{Cl} + c_{Cl}\mathbf{I}_{Cl} \cdot \mathbf{J} + c_F\mathbf{I}_F \cdot \mathbf{J} + c_3\mathbf{I}_{Cl} \cdot \mathbf{d}_T \cdot \mathbf{I}_F + c_4\mathbf{I}_{Cl} \cdot \mathbf{I}_F \qquad [2.51]$$

where the terms describe the $^{35}$Cl quadrupolar, $^{35}$Cl spin-rotation, $^{19}$F spin-rotation, tensor spin-spin, and scalar spin-spin interactions, respectively. Note that here **J** refers to the angular momentum of the molecule. Rather than separating the direct dipolar and indirect nuclear spin-spin coupling Hamiltonians, the molecular beam Hamiltonian separates the total spin-spin coupling interaction based on their tensor properties. The scalar terms (zero for direct dipolar coupling and $J_{iso}$ for indirect coupling) are represented as $c_4\mathbf{I}_{Cl} \cdot \mathbf{I}_F$, while the symmetric tensor terms are represented in the $c_3\mathbf{I}_{Cl} \cdot \mathbf{d}_T \cdot \mathbf{I}_F$ term. These expressions correspond exactly to the NMR-based equations described above, such that:

$$c_4\mathbf{I} \cdot \mathbf{S} = J_{iso}\mathbf{I} \cdot \mathbf{S} \qquad [2.52]$$

and

$$c_3\mathbf{I} \cdot \mathbf{d}_T \cdot \mathbf{S} = R_{eff}\mathbf{I} \cdot \left(\mathbf{D} + \mathbf{J}^{sym}\right) \cdot \mathbf{S} \qquad [2.53]$$

and therefore $c_4 = J_{iso}$ and $c_3 = R_{eff}$. While these relationships have been alluded to, they certainly have not been exploited to gain useful information on the anisotropic portion of **J**, and they are not widely appreciated in the NMR community.

*2.1.7 The Manifestation of Antisymmetric Components of the J tensor*

The theory for predicting the NMR spectrum for a pair of spin-1/2 nuclei in solution or in the solid state, based on isotropic chemical shifts and an isotropic *J* coupling constant is well-established. VanderHart and Gutowsky (*50*) as well as Zilm and Grant (*51*) have presented the theory describing the solid-state NMR lineshapes for two spin-1/2 nuclei taking into account anisotropic symmetric chemical shift, **D**, and **J** tensors, but neglecting the rank-1 antisymmetric parts. In 1968, Andrew and Farnell examined the situation for a pair of spin-1/2 nuclei in the solid-state, taking into account the full second-rank tensor nature of the chemical shift tensor, the direct dipolar coupling tensor, and the indirect nuclear spin-spin coupling tensor (*52*). Under rapid MAS conditions, the chemical shift tensors are averaged to their isotropic values for each of the two nuclei involved; the direct dipolar coupling tensor is averaged to its isotropic value (zero); the isotropic *J* coupling constant manifests itself in a fashion analogous to the situation observed in solution, and the anisotropic rank-2 part of the **J** tensor is averaged to zero. The most interesting aspect of their analysis, however, is with regards to the antisymmetric rank-1 part of **J**, which is averaged to zero in solution, but *not under MAS conditions*. The key equations describing how the antisymmetric part of **J** is predicted to manifest itself in solid-state NMR spectra of a pair of spin-1/2 nuclei are presented here.

Andrew and Farnell showed that although there are up to three independent antisymmetric components of **J**, only a single averaged antisymmetric coupling constant will be observed under conditions of MAS. The average interaction due to $\mathbf{J}^{antisym}$ under MAS conditions is given by:

$$\frac{1}{4} i J^{\text{antisym}}_{N,N',\alpha,\beta} \left( I_{N,+} I_{N',-} - I_{N,-} I_{N',+} \right) \sin\alpha_1 \sin\alpha_2 \sin\xi_{N,N',a} \times \sin\xi_{N,N',b} \left\{ \cos\left( \varepsilon_{N,N',1,a} - \varepsilon_{N,N',2,b} \right) - \cos\left( \varepsilon_{N,N',1,b} - \varepsilon_{N,N',2,a} \right) \right\} \quad [2.54]$$

where $\xi_{N,N',a}$ is the angle between the sample rotation axis and the molecular axis *a*, and $\varepsilon_{N,N',T,a}$ is the azimuth angle at $t = 0$ of the molecular axis *a* relative to the plane containing the axis of rotation and the laboratory axis α. Clearly the derivation and implications of this equation are not intuitively or easily obvious. However, a few important pieces of information may be obtained upon careful examination. First, and most importantly, the expression is not zero under conditions of MAS. Second, it may be surmised that the time-averaged interaction represents an averaging over the three components of the antisymmetric coupling tensor.

For convenience, the averaged antisymmetric contribution may be written simply as a function of the spin operators:

$$A_{N,N'} \left( I_{N,x} I_{N',y} - I_{N,y} I_{N',x} \right) = \frac{1}{2} i A_{N,N'} \left( I_{N,+} I_{N',-} - I_{N,-} I_{N',+} \right) \quad [2.55]$$

where the coupling constant $A_{N,N'}$ incorporates the remaining terms in equation 2.54.

The form of the NMR Hamiltonian under conditions of MAS incorporating isotropic nuclear magnetic shielding and the complete **J** tensor, including the antisymmetric **J** coupling constant, is:

$$\begin{aligned} \mathcal{H} = & -\nu_L \left[ \left( 1 - \sigma_N \right) I_{N,Z} + \left( 1 - \sigma_{N'} \right) I_{N',Z} \right] \\ & + J_{iso} I_{N,Z} I_{N',Z} + \frac{1}{2} J_{iso} \left( I_{N,+} I_{N',-} + I_{N,-} I_{N',+} \right) \\ & + \frac{i}{2} A \left( I_{N,+} I_{N',-} - I_{N,-} I_{N',+} \right) \end{aligned} \quad [2.56]$$

To predict the NMR spectrum resulting from this Hamiltonian, one must find the allowed transition energies. The Zeeman states are taken as basis functions:

$$\begin{aligned} &|\alpha\alpha\rangle \\ &|\alpha\beta\rangle \\ &|\beta\alpha\rangle \\ &|\beta\beta\rangle \end{aligned} \qquad [2.57]$$

And the matrix elements of the Hamiltonian are found:

$$\mathcal{H} = \begin{bmatrix} \langle\alpha\alpha|\mathcal{H}|\alpha\alpha\rangle & \langle\alpha\alpha|\mathcal{H}|\alpha\beta\rangle & \langle\alpha\alpha|\mathcal{H}|\beta\alpha\rangle & \langle\alpha\alpha|\mathcal{H}|\beta\beta\rangle \\ \langle\alpha\beta|\mathcal{H}|\alpha\alpha\rangle & \langle\alpha\beta|\mathcal{H}|\alpha\beta\rangle & \langle\alpha\beta|\mathcal{H}|\beta\alpha\rangle & \langle\alpha\beta|\mathcal{H}|\beta\beta\rangle \\ \langle\beta\alpha|\mathcal{H}|\alpha\alpha\rangle & \langle\beta\alpha|\mathcal{H}|\alpha\beta\rangle & \langle\beta\alpha|\mathcal{H}|\beta\alpha\rangle & \langle\beta\alpha|\mathcal{H}|\beta\beta\rangle \\ \langle\beta\beta|\mathcal{H}|\alpha\alpha\rangle & \langle\beta\beta|\mathcal{H}|\alpha\beta\rangle & \langle\beta\beta|\mathcal{H}|\beta\alpha\rangle & \langle\beta\beta|\mathcal{H}|\beta\beta\rangle \end{bmatrix} \qquad [2.58]$$

The only non-zero elements are the diagonal ones which lead to terms containing isotropic magnetic shielding and $J$ coupling terms,

$$\begin{aligned} \langle\alpha\alpha|\mathcal{H}|\alpha\alpha\rangle &= -\nu_L\left[\frac{1-\sigma_A}{2}+\frac{1-\sigma_B}{2}\right]+\frac{J_{iso}}{4} \\ \langle\alpha\beta|\mathcal{H}|\alpha\beta\rangle &= -\nu_L\left[\frac{1-\sigma_A}{2}-\frac{1-\sigma_B}{2}\right]-\frac{J_{iso}}{4} \\ \langle\beta\alpha|\mathcal{H}|\beta\alpha\rangle &= -\nu_L\left[\frac{1-\sigma_B}{2}-\frac{1-\sigma_A}{2}\right]-\frac{J_{iso}}{4} \\ \langle\beta\beta|\mathcal{H}|\beta\beta\rangle &= -\nu_L\left[-\frac{1-\sigma_A}{2}-\frac{1-\sigma_B}{2}\right]+\frac{J_{iso}}{4} \end{aligned} \qquad [2.59]$$

and two off-diagonal ones which contain the contributions from $A$:

$$\begin{aligned} \langle\beta\alpha|\mathcal{H}|\alpha\beta\rangle &= \frac{J_{iso}}{2}-i\frac{A}{2} \\ \langle\alpha\beta|\mathcal{H}|\beta\alpha\rangle &= \frac{J_{iso}}{2}+i\frac{A}{2} \end{aligned} \qquad [2.60]$$

The outermost energy levels are given by the $<\alpha\alpha|\mathcal{H}|\alpha\alpha>$ and $<\beta\beta|\mathcal{H}|\beta\beta>$ elements, while the inner two energy levels are obtained by diagonalizing the 2x2 submatrix containing the remaining four non-zero matrix elements:

$$\begin{aligned} E_1 &= \nu_L\left(1-\frac{\sigma_A+\sigma_B}{2}\right)+\frac{J_{iso}}{4} \\ E_2 &= -\frac{J_{iso}}{4}+C \\ E_3 &= -\frac{J_{iso}}{4}-C \\ E_4 &= -\nu_L\left(1-\frac{\sigma_A+\sigma_B}{2}\right)+\frac{J_{iso}}{4} \end{aligned} \qquad [2.61]$$

where

$$C^2=\frac{1}{4}\left(J_{iso}^2+A^2+\nu_L^2(\sigma_B-\sigma_A)^2\right) \qquad [2.62]$$

The frequencies of the allowed transitions are found by identifying all transitions where the total magnetic quantum number $m$ changes by $\pm 1$:

$$\begin{aligned} \nu_{2,1} &= -\frac{J_{iso}}{2}-C+\nu_L\left(1-\frac{\sigma_A+\sigma_B}{2}\right) \\ \nu_{3,1} &= -\frac{J_{iso}}{2}+C+\nu_L\left(1-\frac{\sigma_A+\sigma_B}{2}\right) \\ \nu_{4,2} &= +\frac{J_{iso}}{2}+C+\nu_L\left(1-\frac{\sigma_A+\sigma_B}{2}\right) \\ \nu_{4,3} &= +\frac{J_{iso}}{2}-C+\nu_L\left(1-\frac{\sigma_A+\sigma_B}{2}\right) \end{aligned} \qquad [2.63]$$

Thus, the NMR spectrum will consist of four lines centred around the average chemical shift. The eigenfunctions and relative intensities of the lines may also be derived but these will not differ substantially from the case where $A$ is ignored and will not be presented in this thesis. The general appearance of the NMR spectrum under conditions of fast MAS is given in Figure 2.5.

Following the description of Andrew, the spectral positions of the four lines may be alternatively described if one of three assumptions may be made about the relative magnitudes of the isotropic chemical shift difference between the nuclei in the spin pair, the value of $J_{iso}$, and the value of $A$. Shown in Figure 2.6(a) is the expected NMR

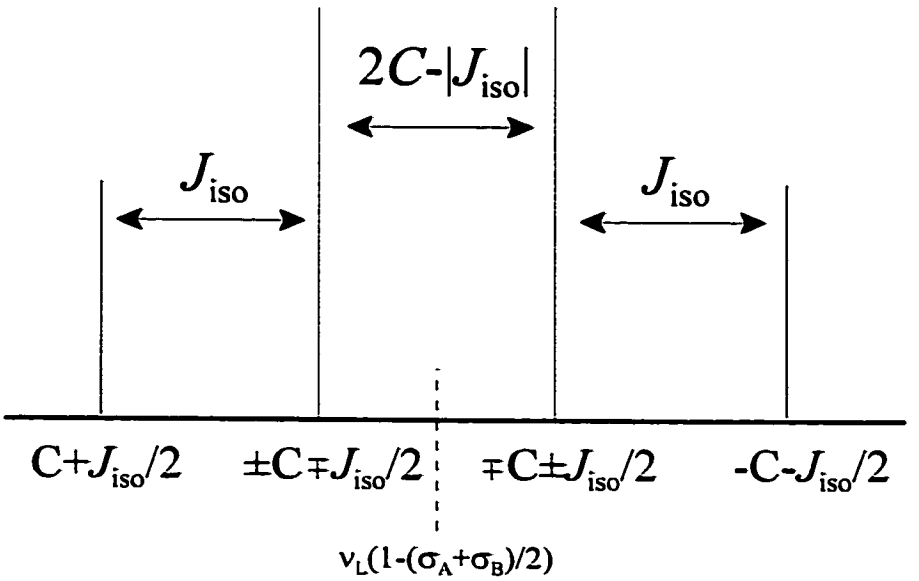


Figure 2.5: General appearance of a solid-state MAS NMR spectrum of a pair of spin-1/2 nuclei, taking into account isotropic magnetic shielding and the full **J** tensor.

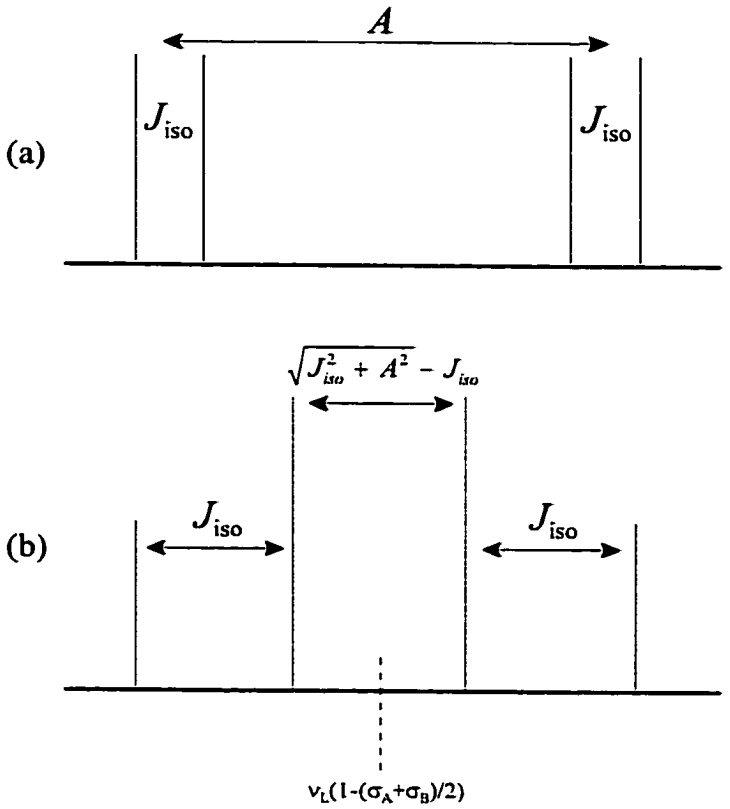


Figure 2.6: (a) Solid-state NMR spectrum expected for an isolated pair of spin-1/2 nuclei, under the assumption that the antisymmetric coupling constant, $A$, is large compared to the chemical shift difference between the two sites. (b) Same as part (a) except the assumption is made that both $A$ and $J_{iso}$ are large compared to the chemical shift difference.

spectrum if the coupling constant $A$ is large compared to the chemical shift difference. In Figure 2.6(b), the expected NMR spectrum if the coupling constants $J_{iso}$ and $A$ are both large compared to the chemical shift difference is given. There is a third generalization which may be made if both $J_{iso}$ and $A$ are small compared to the chemical shift difference; in this case one approaches an "AX" spin pair and the effects of $A$ on the spectrum are negligible.

Finally, it is noted that in principle the antisymmetric part of **J** contributes to

nuclear spin relaxation although its effect has never been observed experimentally (*256*).

### *2.1.8 Euler Angles*

Euler angles are commonly used in solid-state NMR to describe the relationship between two axis systems, or frames of reference. In the present work, Euler angles are primarily used to describe the relative orientations of CS and EFG tensors for a given nucleus. Shown in Figure 2.7 are the definitions of the Euler angles for relating two coordinate systems. As an example, the angles $\alpha$, $\beta$, $\gamma$ may be used to describe the

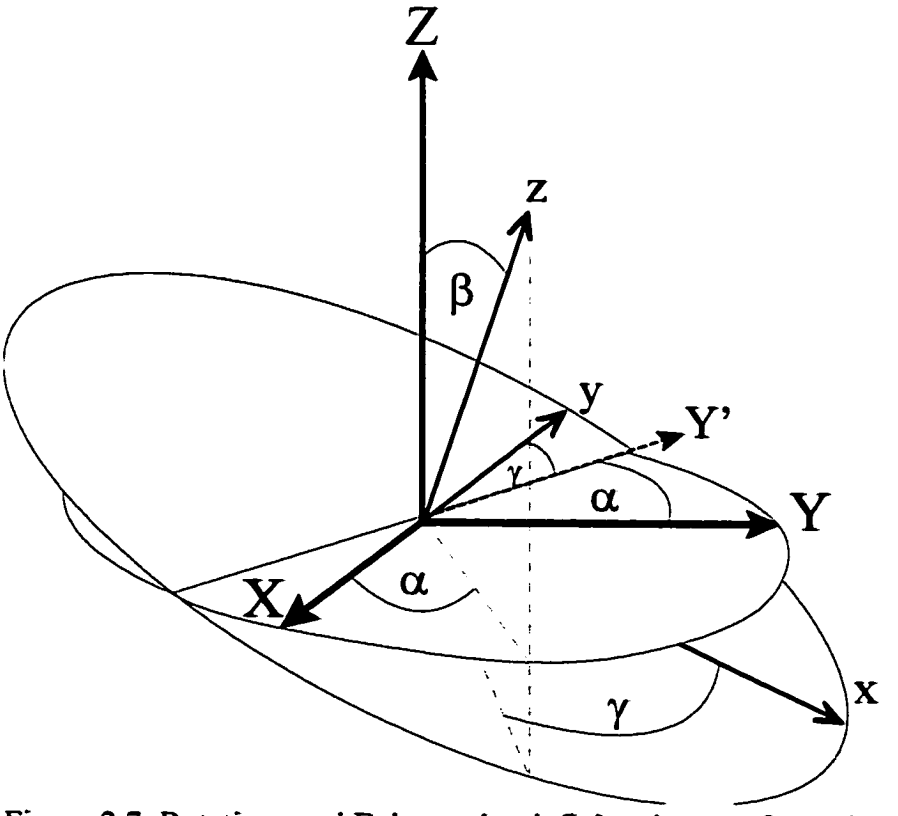


Figure 2.7: Rotations and Euler angles defining the transformation from one coordinate system (X, Y, Z) to another (x,y,z).

rotations required to bring the EFG PAS into coincidence with the CS PAS. Referring to Figure 2.7, the (X,Y,Z) axes are taken as the principal axes of the EFG tensor and the (x,y,z) axes are those of the CS tensor. In order to describe the relative orientations of the EFG and CS tensors, the EFG PAS is rotated about its Z axis by an angle $\alpha$. This is followed by a rotation about the new EFG Y' axis by an angle $\beta$. Finally, the new EFG axis system is rotated about the new z axis about an angle $\gamma$. All rotations are positive, *i.e.* counterclockwise.

## 2.2 Experimental Techniques and Methods in Solid-State NMR

Detailed reviews and descriptions of the theoretical and practical aspects of routine solid-state NMR experiments are available (*53*, *54*, *55*, *56*). In this section, the techniques relevant to this thesis will be presented in brief.

### *2.2.1 Magic-Angle Spinning, Cross-Polarization, and Decoupling*

NMR of solids exhibits several similarities, but also several important differences, in comparison with NMR of solutions. The rapid molecular tumbling which occurs in liquids results in an averaging of the NMR interactions to their isotropic values, thus generally providing spectra composed of very narrow lines which are influenced by chemical shift and isotropic *J* coupling interactions. In the solid state, motion is comparatively highly restricted, although there are inevitable molecular vibrations and librations which may in certain cases play an important role in the interpretation of solid-state NMR data. The restricted motion in solids means that much of the information

contained in the complete second-rank interaction tensors becomes available to the experimentalist, in contrast to the situation in solution. At the same time, the anisotropic NMR interactions, e.g., the chemical shift and direct dipolar coupling interactions, can give rise to extremely broad and sometimes featureless NMR spectra.

Thus, one of the goals of solid-state NMR spectroscopists is to obtain "solution-like" spectra for solid samples, while at the same time accessing the orientation-dependent second-rank tensor information which is available. As mentioned in Chapter 1, to obtain high-resolution NMR spectra of dilute spin-½ nuclei in solid samples, usually three techniques are combined (*13*, *57*, *58*): (*i*) cross-polarization (CP) from abundant spins (typically but not necessarily $^{1}H$ or $^{19}F$) (*11*, *12*, *17*, *59*, *60*, *61*, *62*, *63*, *64*, *65*), (*ii*) magic-angle spinning (*7*, *8*, *9*, *17*, *66*, *67*, *68*), and (*iii*) high-power heteronuclear decoupling (*55*, *69*, *70*, *71*, *72*).

Many of the NMR interactions discussed in the previous sections take on an angular dependence of the form

$$\left(3\cos^2\theta - 1\right) \qquad [2.64]$$

when the Hamiltonians are expanded and converted to polar coordinates. In the case of the dipolar interaction, for example, $\theta$ corresponds to the angle between the internuclear vector and the external applied magnetic field. After some lengthy trigonometry, it is possible to show that the time average of expression 2.64 for mechanical spinning of the sample about any particular axis is given by (*57*, *73*):

$$\left\langle 3\cos^2\theta - 1\right\rangle = \frac{1}{2}\left(3\cos^2\beta - 1\right)\left\langle 3\cos^2\chi - 1\right\rangle \qquad [2.65]$$

where the angle β corresponds to the angle between $B_0$ and the sample rotation axis, and χ is the (time dependent) angle between the internuclear vector and the sample rotation axis (Figure 2.8). Under conditions of rapid sample rotation, the angle χ takes on a range of values which are beyond the control of the experimentalist. The angle β, however, is under the control of the experimentalist. When this angle is set to 54.7356°, the first term on the right side of equation 2.65 vanishes, and therefore the time average of equation 2.64 is also zero. The interaction of interest (e.g., dipolar, chemical shift, 1st-order quadrupolar) will be averaged to its isotropic value when the rate of sample rotation is significantly greater than the magnitude of the interaction.

CP allows the dilute spins to gain magnetization from the abundant spins. In principle, CP results in a signal enhancement given by $\gamma_I/\gamma_S$, where $\gamma_I$ is the magnetogyric

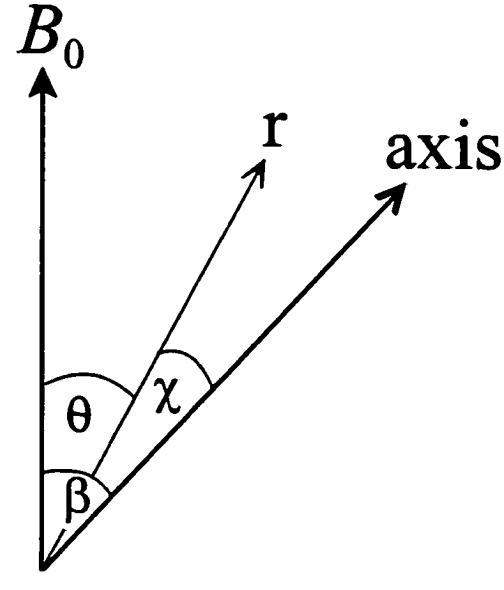


Figure 2.8: Angles describing the relative orientations of the external applied magnetic field, internuclear vector, and sample rotation axis.

ratio of the abundant spin and $\gamma_S$ is that of the dilute or rare spin. Equally important is the reduction in the recycle time between radiofrequency pulses. CP allows one to use recycle delays on the order of the $I$ spin $T_1$ instead of the $S$ spin $T_1$. Since typically the $S$ spin $T_1$ values are long, this reduction can often be many orders of magnitude, and allows for the acquisition of a spectrum with an improved signal-to-noise ratio for a given amount of experiment time. The most common form of CP is known as Hartmann-Hahn CP (*11*) or "single-contact matched CP". When setting up a CP experiment, one must ensure that the well-known Hartmann-Hahn match condition is satisfied:

$$\gamma_I B_{1I} = \gamma_S B_{1S} \qquad [2.66]$$

The rf fields which are associated with the $B_1$ magnetic fields are turned on for a period known as the contact time, or mixing time, which is on the order of milliseconds. It is during this time that magnetization is transferred from the $I$ spins to the $S$ spins. The degree to which the $S$ spins have been magnetized depends on the contact time. The rate of CP is initially governed by $T_{IS}$, a time constant which is proportional to the second moment (*74, 73, 75*) of the dipolar coupling between the $I$ and $S$ spins (*57*). At longer contact times, however, spin-lattice relaxation of the $I$ spins in the rotating frame ($T_{1\rho}$) dominates.

Cross-polarization to quadrupolar nuclei has been the subject of several recent discussions; however its application is not routine in the sense that CP is for spin-1/2 nuclei. For half-integer quadrupolar nuclei, the Hartmann-Hahn equation must be modified as follows, to cross-polarize to a quadrupolar nucleus Q from protons:

$$\alpha_Q \gamma_Q B_{1Q} = \alpha_H \gamma_H B_{1H} \qquad [2.67]$$

where $\alpha = [S(S+1) - m(m-1)]^{1/2}$ for a transition between the $m$ and $m$ - 1 levels (*76*).

For solids, decoupling of abundant spins such as protons requires much more power than is generally required for solution samples. In the solid state, decoupling fields on the order of at least 60-100 kHz are required for $^1$H decoupling. Typically, higher decoupling fields provide better signal-to-noise. Standard high-power proton decoupling in the solid state involves continuous wave (CW) decoupling. A technique which provides improvements in both the resolution and sensitivity of the dilute-spin spectrum is known as two-pulse phase-modulated (TPPM) decoupling (*69*). Briefly, this scheme involves a series of pulses of alternating phase, applied to the abundant-spin channel. The result is comparable to using a higher CW decoupling field.

### *2.2.2 Solid-state NMR of Quadrupolar Nuclei*

In many cases, the central ½ ↔ - ½ transition is of primary interest in the NMR of half-integer quadrupoles since the first-order quadrupolar interaction is zero for this transition; the satellite transitions extend over a wider spectral range, making them more difficult to observe. Single-pulse experiments on quadrupolar nuclei are referred to as broad line experiments (*77*, *126*). As outlined by Abragam (*78*), radiofrequency pulses on these nuclei may be classified as *selective* and *non-selective*. These terms refer to whether one or all of the allowed NMR transitions are excited. When the magnitude of the quadrupolar interaction is much less than the rf field strength, the equation $\tau_p = \pi/2\omega_1$ is valid for maximizing the intensity for *non-selective* excitation of a quadrupolar nucleus. This corresponds to applying a "hard" pulse. In most non-cubic compounds it is

not possible to satisfy the conditions for applying a strictly non-selective pulse (*126*). When the quadrupolar interaction is much larger than the applied rf field, the optimum pulse widths for *selective* NMR excitation of any single-quantum transition for quadrupolar nuclei in the solid state are given by (*79*)

$$t_p = \frac{\pi}{2\omega_{rf}\sqrt{I(I+1) - m(m+1)}} \qquad [2.68]$$

For selective excitation of the central transition, equation 2.68 simplifies to dividing the solution $\pi/2$ pulse length by $(I + \frac{1}{2})$. For a powder sample, it is important to note that this does *not* mean that *only* the central transition is excited since, for certain orientations, the satellite transitions will be in the same spectral range as the central transition. Thus, for powder samples it is preferable to speak of "partly selective" pulses. In single crystals it may also be difficult, if not impossible, to apply perfectly "selective" or "non-selective" pulses (*80*, *81*).

The nutation behaviour for a non-selective pulse may be described by the following equation (*34*):

$$S(\tau_p) = S_0 \sin(\omega_1 \tau_p) \qquad [2.69]$$

where the signal intensity for a given pulse of length $\tau_p$ and angular frequency $\omega_1$ is related in a sinusoidal fashion to the initial intensity prior to the pulse, $S_0$. The signal following a selective pulse is similarly described as:

$$S(\tau_p) = \frac{S_0}{I + \frac{1}{2}} \sin((I + \frac{1}{2})\omega_1 \tau_p) \qquad [2.70]$$

The signal behaviour for various situations as a function of flip angle is shown in Figure

2.9. As is clearly demonstrated in this figure, the optimal flip angle for selective excitation of the central transition of e.g., a spin 3/2 or 5/2 quadrupolar nucleus is not $\pi/2$.

In practice, to establish an appropriate pulse width, one may calibrate the $\pi/2$

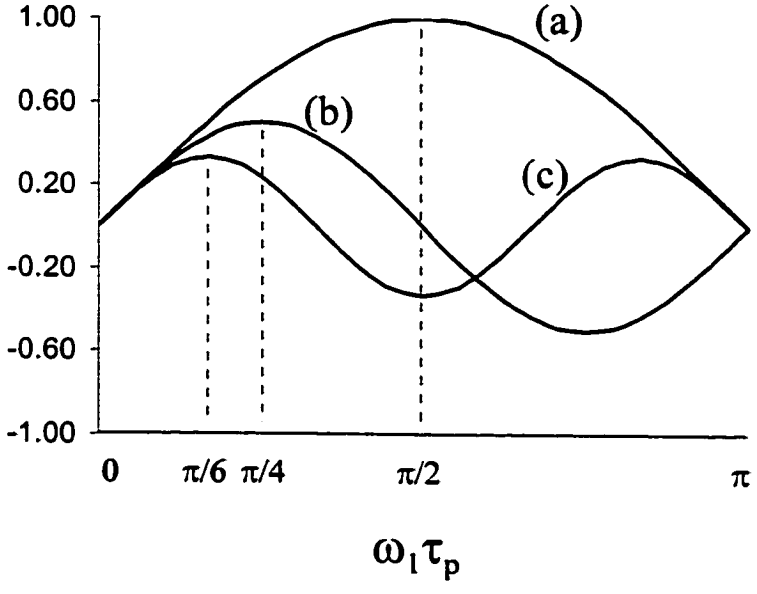


Figure 2.9: Plots of signal intensity as a function of flip angle for (a) non-selective excitation, (b) selective excitation of the central transition for a spin-3/2 nucleus, and (c) selective excitation of the central transition of a spin-5/2 nucleus. Optimal flip angles are indicated by the dotted lines.

pulse on a solution containing the nucleus of interest, e.g., NaCl(aq) for $^{23}$Na. Equation 2.68 may then be applied to determine the appropriate selective pulse width.

Many of the nuclei studied by solid-state NMR methods in this thesis are low-frequency quadrupolar nuclei, for which the dominant interaction is generally the quadrupolar interaction. The experimental methods employed for acquisition of NMR spectra of such nuclei involve simple one-pulse experiments as well as two types of spin-

echoes (*82*, *83*), which are discussed below.

The general form of a spin-echo pulse sequence is:

$$p_1 - t_1 - p_2 - t_2 - acquire \qquad [2.71]$$

where $p_1$ and $p_2$ are radiofrequency pulses and $t_1$ and $t_2$ are time delays. In the case of low-frequency quadrupolar nuclei, the purpose of using an echo pulse sequence is two-fold. For a given probe quality factor, $Q$, lower resonance frequencies lead to longer dead times which can corrupt the beginning of the FID. For particularly broad powder patterns this becomes especially important since most of the spectral information defining the line shape will be contained in the initial part of the FID. Probe ringing can also be a significant problem for low-$\gamma$ nuclei (*54*, *84*). These problems may be overcome by the use of quadrupolar spin echoes (*83*, *85*).

A very useful recent paper by Bodart *et al.* provides a theoretical analysis and experimental investigation of quadrupolar echoes for half-integer spins in stationary samples (*86*). They provide some general instructions for acquiring relatively distortion-free central-transition spectra. The optimum rf field is determined to be $\Delta / (I + \frac{1}{2})$, where $\Delta$ denotes the static line width (in Hz) and $I$ is the spin of the relevant nucleus, and irradiation must be performed at the centre-of-gravity of the line. The usual $\pi/2 - \tau - \pi - \tau$ - ACQ sequence will give the maximum signal but does not minimize spectral distortions. To minimize the distortions, modifications must be made to pulse lengths and the optimum rf field strength must be reduced. The authors conclude that a $\pi/2 - \tau - \pi/2 - \tau$ - ACQ sequence is a valid compromise.

The quadrupolar Carr-Purcell-Meiboom-Gill (*87*) (QCPMG) echo experiment ("spikelet echo") has received considerable attention in the past few years (*88*, *89*, *90*, *91*, *92*, *93*) as a useful one-dimensional NMR probe of quadrupolar nuclei in stationary and MAS samples. This technique involves sampling the quadrupolar echo during a CPMG pulse sequence and can yield spectra with high signal-to-noise ratios when compared to a standard one-pulse or spin-echo experiment. The technique is therefore particularly useful for low-$\gamma$ nuclei; some of the nuclei which have been studied using this technique include $^{87}$Rb, $^{59}$Co, $^{39}$K, $^{25}$Mg, $^{67}$Zn, and $^{87}$Sr (*89*, *92*, *93*). The form of the pulse sequence is shown in Figure 2.10.

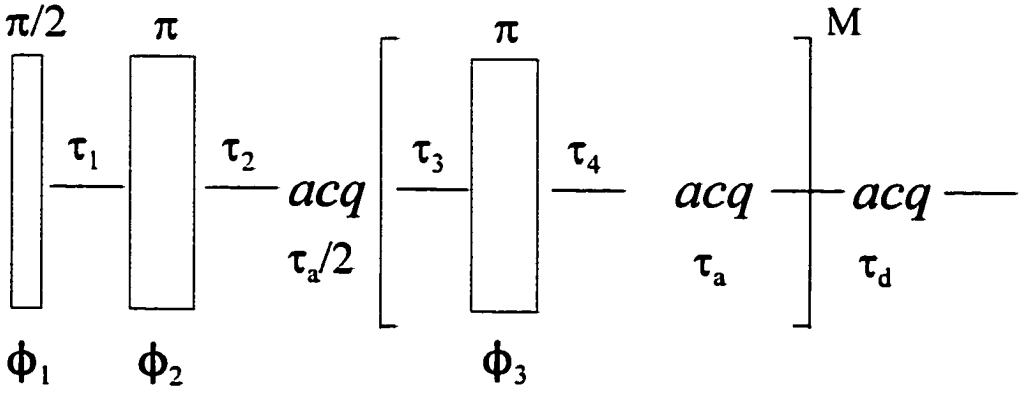


Figure 2.10: Quadrupolar Carr-Purcell-Meiboom-Gill echo sequence. An initial spin-echo sequence with time delays $\tau_1$ and $\tau_2$ is followed by a series of M echoes which are formed by repeating a $\pi$ pulse buffered by appropriate delays $\tau_3$ and $\tau_4$.

## 2.3 Quantum Chemical Methods for the Calculation of NMR Parameters

*Ab initio* restricted Hartree-Fock (RHF) calculations, multiconfigurational self-consistent field (MCSCF), and density-functional theory (DFT) calculations are discussed in this thesis. A detailed description of these methods, and the technical details concerning the various implementations used in the calculation of NMR parameters are beyond the scope of this thesis. The concepts which are essential to applying, understanding, and critically evaluating *ab initio* and DFT calculations of NMR parameters are discussed below.

*Ab initio* methods for the calculation of shielding tensors and indirect nuclear spin-spin coupling tensors have been discussed thoroughly in the review by Helgaker *et al.* (*94*). In computational chemistry programs such as Gaussian (*95*), Dalton (*96*), and ACES II (*97*), for example, the shielding tensor is not calculated using Ramsey's equations, but equivalently by taking a second derivative of the energy with respect to the magnetic moment of the nucleus, $\mu$, and with respect to the external applied magnetic field, $B$ (*94*, *98*, *99*, *100*):

$$\sigma_{\alpha\beta} = \left[\frac{\partial^2 E}{\partial \mu_\alpha \partial B_\beta}\right]_{\mu,B=0} \qquad \alpha,\beta = \mathrm{x,y,z} \qquad [2.72]$$

Depending on where the origin of the vector potential of the external applied magnetic field is chosen (called the "gauge origin"), the calculated nuclear magnetic shieldings will differ (in the absence of a complete basis set). This is known as the gauge origin problem (*99*, *101*, *102*). In the limit of a complete basis set, the choice of gauge origin is unimportant because shielding is a molecular property; it cannot depend on the

choice of origin in a calculation. Since complete basis sets are not generally practical, methods have been proposed to circumvent the problem of gauge variance, including "gauge-including atomic orbitals" or "gauge-independent atomic orbitals" (GIAOs) (or equivalently London orbitals) (*103*, *104*), "individual gauge origins for different localized molecular orbitals" (IGLO) (*98*, *105*, *106*), "localized orbital/local origin" (LORG) (*107*), and "individual gauges for atoms in molecules" (IGAIM) (*108*). The GIAO method uses a "gauge factor" in the atomic orbitals used in a calculation (*99*, *104*); this method is employed in this thesis. One of the main advantages of the GIAO method is its more rapid convergence behaviour with respect to basis set size (*100*).

For relatively light nuclei, a Hartree-Fock calculation of shielding tensors using the GIAO method generally provides reliable results. For heavier nuclei where relativistic effects are expected to become more important, the HF method is no longer practical or accurate. Relativistic effects may be divided into "scalar" effects and "spin-orbit" effects (*109*). A common consequence of the former is the contraction of *s*-orbitals; this can have significant effects on, for example, the diamagnetic portion of $\sigma$, and on the Fermi-contact contribution to **J**. Spin-orbit relativistic effects are those which arise due to the coupling of spin and orbital angular momenta.

Malkin and co-workers formulated a DFT/IGLO method for the calculation of shielding tensors which incorporates spin-orbit relativistic corrections (*110*). Ziegler and co-workers have developed DFT/GIAO methods which employ either a relativistic Pauli Hamiltonian (*111*, *112*, *113*) or a zeroth-order regular approximation (ZORA) Hamiltonian (*114*) to calculate shielding tensors for heavy nuclei. A ZORA Hamiltonian

(*115*, *116*, *117*) has also been used for relativistic calculations of EFG tensors (*118*).

The same as for the calculation of nuclear magnetic shielding tensors, the **J** tensor is not calculated using Ramsey's equations, rather it is calculated by taking the appropriate second derivative of the energy with respect to the nuclear magnetic moments:

$$J_{\alpha\beta} = \gamma_N \gamma_{N'} \left[ \frac{\partial^2 E}{\partial \mu_{N,\alpha} \partial \mu_{N',\beta}} \right]_{\mu_N, \mu_{N'}=0} \qquad \alpha, \beta = x, y, z \qquad [2.73]$$

The origins and utility of the reduced spin-spin coupling tensor, **K** (*vide supra*), may be easily seen from this equation. **J** tensors are the most difficult NMR property to calculate *ab initio* or from DFT methods; calculations of **J** are far less routine than are calculations of nuclear magnetic shielding and EFG tensors. This is in part due to the fact that the electronic structure in the region around the nuclei (and exactly at the nuclei) must be very-well described in order to obtain accurate results. The reasons for this are exemplified in the expression for the Fermi-contact coupling interaction (eq. 2.43) where a delta function is used to describe the spin-spin coupling *at* the nuclei. The nuclear magnetic shielding and EFG tensors, for example, do not have such stringent requirements. Gaussian-type orbitals, which are typically used in computational chemistry, have many advantages but one significant drawback in the context of **J** tensors is their poor ability to accurately describe the region close to the nuclei. The problem may be addressed by using very large basis sets to model the core region (*119*); or alternatively Slater-type orbitals may be used.

While standard restricted Hartree-Fock calculations in many cases provide

reasonable results for the calculation of nuclear magnetic shielding tensors, these types of calculations generally fail completely in the calculation of **J** tensors, even for small molecules. This is due to the so-called triplet instability problem; the uncorrelated HF method simply does not describe excited triplet states sufficiently well to provide reliable **J** tensors. Accurate description of excited singlet and triplet states is crucial to producing reliable **J** values; this is exemplified in the energy difference terms shown in equations 2.41-2.44.

The two computational methods used in this thesis to calculate **J** tensors are the post-HF MCSCF method and the ZORA-DFT method. The ZORA-DFT method, including both scalar and spin-orbit relativistic effects, for calculating **J** tensors has been developed and implemented by Autschbach and Ziegler (*120*, *121*).

In the MCSCF method, both the coefficients of the determinants and the orbitals are variationally optimized and a full configuration-interaction (CI) calculation is done within a chosen *active space*. The active space may either be a "complete" active space (CAS) (*122*) or a "restricted" active space (RAS) (*123*). These calculations are therefore referred to as CASSCF or RASSCF calculations. In both types of calculations, a number of "windows" are chosen, which include certain subsets of orbitals. These windows correspond to a small subset of determinants which are included in the wavefunction. In the CASSCF calculation, the orbital space is subdivided into three spaces: active, inactive, and secondary. The inactive space typically includes core orbitals which are not expected to contribute significantly to static correlation; these orbitals are always doubly occupied in the calculation. The active space has orbitals which can take on occupancies

of zero, one, or two electrons in the individual configurations leading to the final wavefunction. The secondary orbitals are virtual orbitals which always have occupancies of zero.

The RASSCF calculation is similar in concept to the CASSCF calculation, although in the RASSCF case, the "active" space is further partitioned into three subspaces labelled RAS1, RAS2, and RAS3. In RAS1, the number of electron holes is restricted while in RAS3 the number of electrons is restricted. The orbitals in RAS2 can have occupations of zero, one, or two. An example of the procedure used to select the various RAS spaces is given in Appendix A. There are two advantages to the RASSCF method over the CASSCF method: (i) inclusion of the RAS3 space provides some estimate of the effect of dynamical electron correlation effects (whereas the CASSCF method accounts only for static correlation effects); (ii) generally it is possible to obtain results comparable to the CASSCF method using a RASSCF wavefunction composed of fewer determinants (*94*). For larger systems, the problem with both MCSCF methods is the steep scaling of the number of determinants (and hence computational time and memory) with the number of orbitals included in the active spaces. Typically 12-16 orbitals represents the maximum (*124*).

## Chapter 3: Measurement and Interpretation of Chemical Shift and Electric Field Gradient Tensors for Spin-n/2 Quadrupolar Nuclei

### 3.1 Introduction

The study of half-integer quadrupolar nuclei in the solid state *via* NMR spectroscopy has advanced tremendously over the past decade (*125*). There are two primary reasons for these advances. First, the increasing accessibility of high-field NMR spectrometers (17.6 T, 18.8 T, and beyond) has opened up the possibility of studying hitherto relatively inaccessible nuclei. For solid samples, half-integer spin quadrupolar nuclei benefit greatly from high applied magnetic field strengths due to the inverse relationship between the second-order quadrupolar broadening and $B_0$ (*84*, *125*, *126*). Indeed, high applied magnetic fields make possible the study of nuclei with low magnetogyric ratios, $\gamma$, which simply are not feasible at moderate field strengths. Recent work has taken advantage of the newly-available ultra-high magnetic field strengths to carry out solid-state NMR experiments on a variety of nuclei traditionally considered "difficult" to varying degrees, e.g., $^{25}$Mg (*127*, *128*), $^{35}$Cl (*129*), $^{67}$Zn (*130*, *131*), $^{71}$Ga (*132*), and $^{73}$Ge (*128*).

The second reason for the explosion of activity in the area of solid-state NMR of quadrupolar nuclei are the new developments aimed at averaging or refocusing the quadrupolar interaction such as the multiple-quantum magic-angle-spinning (MQMAS) experiment (*15*). This experiment has allowed for the acquisition of "high-resolution" NMR spectra of half-integer quadrupolar nuclei, e.g., $^{11}$B, $^{23}$Na, $^{17}$O, $^{27}$Al (*133*, *134*).

This is advantageous, for example, in the resolution of multiple magnetically or crystallographically non-equivalent nuclear sites. Although MQMAS methodology has undoubtedly had an enormous impact on solid-state NMR, these experiments are conducted under MAS conditions where the CS tensor is averaged to its isotropic value. The CS tensor is arguably the most important NMR parameter. With commercially available magnetic field strengths ever-increasing, the influence of the CS tensor will become increasingly important since it scales linearly with $B_0$. The magnitude and relative orientation of the CS tensors may be important, for example, in obtaining quantitative results from the rotational resonance (*135*) experiments recently introduced for half-integer quadrupolar nuclei (*136*, *137*), especially for nuclei with relatively small or moderate quadrupole moments such as $^{11}B$.

Furthermore, since many high-resolution solid-state NMR techniques for the observation of spin-n/2 quadrupolar nuclei involve MAS and are two-dimensional, there are inherent restrictions on the types of nuclei and chemical systems which may be studied by these advanced techniques. The broadening of the NMR spectrum of a stationary powdered sample due to the anisotropic nuclear spin interactions (typically primarily the quadrupolar interaction for quadrupolar nuclei) must be small in Hz, *i.e.*, less than achievable MAS rates, in order for MAS to be effective. Even if the quadrupolar interaction is sufficiently small such that MAS is beneficial for narrowing the central transition, multi-dimensional experiments on nuclei with spin-lattice relaxation time constants ($T_1$) of greater than a few seconds can quickly become prohibitively time-consuming. Signal-to-noise can also easily become a problem in such

situations. Thus, for much of the periodic table, elegant multi-dimensional MAS experiments such as MQMAS (*15*) and satellite-transition MAS (STMAS) (*138*) are simply not feasible. The difficulty in gleaning useful information from the solid-state NMR spectra of many nuclei is related to their relative receptivity and quadrupolar broadening factor. These parameters in turn are related to the natural abundance, nuclear quadrupole moment, spin, and magnetogyric ratio of the nuclei in question.

Many of the "difficult" nuclei have low magnetogyric ratios. Recent progress in solid-state NMR of low-$\gamma$ nuclei (*i.e.*, those whose resonance frequency is below $^{15}N$) have been summarized by Smith (*84*). Relevant properties of the nuclei of interest in the present chapter are presented in Table 3.1.

**Table 3.1:** NMR properties of selected spin-n/2 nuclei

| nucleus | spin ($I$) | NA / % | magnetogyric ratio ($\gamma$) /$10^7$ rad $T^{-1}$ $s^{-1}$ | quadrupole moment ($eQ$) / $fm^2$ (*139*) | relative receptivity[a] |
|---|---|---|---|---|---|
| $^{11}B$ | 3/2 | 80.42 | 8.5847 | 4.059 | 1 |
| $^{35}Cl$ | 3/2 | 75.53 | 2.6242 | -8.2 | $2.68 \times 10^{-2}$ |
| $^{37}Cl$ | 3/2 | 24.47 | 2.1844 | -6.46 | $5.01 \times 10^{-3}$ |
| $^{53}Cr$ | 3/2 | 9.55 | -1.5077 | -15 | $-6.40 \times 10^{-4}$ |
| $^{95}Mo$ | 5/2 | 15.72 | -1.7514 | -2.2 | $-2.49 \times 10^{-3}$ |
| $^{97}Mo$ | 5/2 | 9.46 | -1.7884 | 25.5 | $-1.60 \times 10^{-3}$ |

[a] The relative receptivity is defined as $(\gamma^3)(NA)(I(I+1))$, and has been adjusted to give the fractional contribution from just the central transition. Values have been normalized to $^{11}B$.

Of these nuclei, only $^{11}B$ is a "high-$\gamma$" nucleus and is certainly not considered as a difficult nucleus in solid-state NMR. Boron has a diverse structural chemistry and is particularly amenable to NMR studies. Boron-11 represents an ideal starting point for the characterization of EFG and CS tensors for quadrupolar nuclei as discussed in this chapter. Since $^{11}B$ is not a particularly difficult nucleus to observe, the key concepts involved in determining CS tensors for quadrupolar nuclei will be nicely demonstrated using boron NMR. Of its two naturally occurring isotopes, $^{11}B$ is best-suited to NMR spectroscopy. This is evidenced by the large number of isotropic shifts and indirect spin-spin coupling constants which have been reported (*140, 141, 142, 143, 144*). In particular, many boron-containing glasses have been examined by $^{11}B$ NMR (*133*g,h,i, *145*). The chemical shift range of boron in tricoordinate and tetracoordinate compounds extends over approximately 230 ppm (*144*). Relatively recent work on metallaboranes (*146*) has extended this range to over 350 ppm (*147, 148*). In spite of the surfeit of $^{11}B$ NMR data and the substantial range of chemical shifts, no boron chemical shift tensor has been characterized. Two compounds central to the study, trimesitylborane and triphenyl

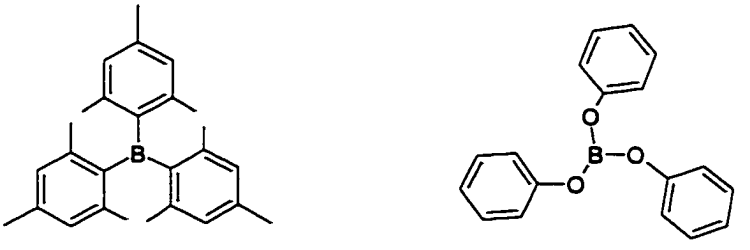


(a) (b)

Figure 3.1: Structures of (a) trimesitylborane and (b) triphenyl borate

borate, are shown in Figure 3.1. These compounds are of interest due to the nearly planar geometry about boron, which alludes to the possibility of a particularly anisotropic CS tensor.

While $^{11}B$ NMR studies of solids are straightforward, well-established and widespread, chlorine-35/37 are nuclei which have received relatively little attention in solid-state NMR. The relatively low values of $\gamma$ and moderately large quadrupole moments for these nuclei make them excellent candidates for high-field NMR studies. To date, single-crystal $^{35}Cl$ NMR studies have been carried out on $NaClO_3$ (*149*), $Mn(CO)_5Cl$ (*150*), tris sarcosine calcium chloride (*151*), $NH_4ClO_4$ (*152*), and betaine calcium chloride dihydrate (*153*). Perchlorate anions have been a popular focus of chlorine solid-state NMR studies due to the high local symmetry at chlorine (*154*, *155*, *156*, *157*, *158*, *159*). Studies of inorganic chlorides have been reported (*160*, *161*, *162*, *163*, *164*, *165*, *166*); in many cases, such as the alkali metal chlorides, the chlorine nuclear quadrupolar coupling constant is zero due to cubic symmetry. A limited number of organic or ammonium hydrochloride salts have been studied previously: $NH_4Cl$ (*161*), $C_4H_9NH_3Cl$ (*167*), and cocaine hydrochloride (*168*).

Due to large quadrupolar coupling constants, NMR studies of chlorine in compounds with covalently bound chlorine atoms are difficult in solution due to extremely efficient nuclear spin relaxation, and are untenable in the solid state using conventional pulsed FT techniques owing to extremely broad line shapes. Conversely, nuclear quadrupole resonance (NQR) methods (*169*) are difficult to apply when chlorine nuclei are in high-symmetry environments. Furthermore, they do not allow one to

characterize the chlorine magnetic shielding tensors. Oxychloro and chloride anions therefore represent an appealing situation for $^{35/37}$Cl solid-state NMR, where the high local symmetry guarantees relatively small quadrupolar coupling constants. The most insightful chlorine solid-state NMR study to date is that of Skibsted and Jakobsen (*159*). This study focusses on the chlorine NMR interaction tensors of the perchlorate anion in several inorganic perchlorates and establishes chlorine solid-state NMR as a viable and informative technique for the investigation of these types of materials. Their experiments show that the chlorine chemical shifts for a wide variety of perchlorate salts fall in the narrow range of ~ 980 to 1005 ppm relative to NaCl(aq) and that the $^{35}$Cl nuclear quadrupolar coupling constants range from 0.3 to 3.0 MHz.

In this chapter, the feasibility and utility of high-field chlorine NMR studies of solid organic hydrochloride salts is demonstrated. Chlorine NMR spectroscopy of such compounds represents an excellent probe of the local chlorine environment since any deviations from perfect cubic symmetry at chlorine will result in an observable quadrupolar coupling constant. In particular, Yesinowski *et al.* have remarked upon the potential application of high-field NMR techniques to investigate the relationship between the chlorine nuclear quadrupolar coupling tensor and the hydrogen bonding environment about chlorine in organic hydrochlorides (*168*). This relationship is explored by comparing the $^{35}$Cl NMR parameters to known crystal structures for the following set of compounds in which chloride anions exist in a variety of hydrogen-bonding environments (Figure 3.2): L-tyrosine hydrochloride (*170*), L-cysteine methyl ester hydrochloride (*171*), L-cysteine ethyl ester hydrochloride (*171*), quinuclidine

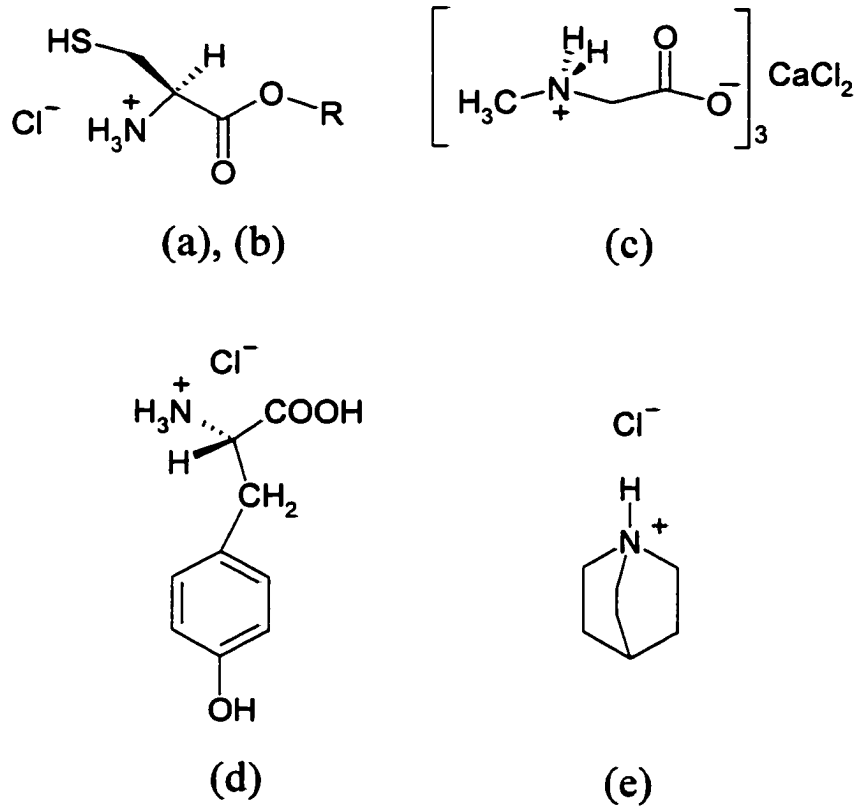


Figure 3.2: Structures of the hydrochloride salts studied by solid-state $^{35/37}$Cl NMR spectroscopy: (a) L-cysteine methyl ester hydrochloride (R = Me); (b) L-cysteine ethyl ester hydrochloride (R = Et); (c) tris sarcosine calcium chloride; (d) L-tyrosine hydrochloride; (e) quinuclidine hydrochloride.

hydrochloride (*172*), and tris sarcosine calcium chloride (*173*).

The final sections of this chapter focus on solid-state NMR of quadrupolar transition metal nuclei, in particular $^{95/97}$Mo and $^{53}$Cr. Hundreds of compounds have been studied in solution via $^{95}$Mo NMR (*174*); however, the number of solid-state $^{95}$Mo NMR studies remains quite limited (*84*). Recent $^{95}$Mo NMR studies of prototypal molybdenum compounds including hexacarbonylmolybdenum(0) and sodium molybdate dihydrate have demonstrated the utility of $^{95}$Mo solid-state NMR of powder samples for the

extraction of useful information on the $^{95}$Mo EFG and CS tensors (*175*). In this chapter, a combined high-field $^{95}$Mo solid-state NMR and ZORA-DFT study of the $^{95}$Mo CS and EFG tensors in the piano-stool complex mesitylenetricarbonylmolybdenum(0), **I** (Figure 3.3), is presented. This compound is of interest for several reasons. Arene molybdenum

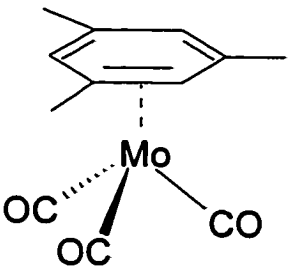


Figure 3.3:
Mesitylenetricarbonyl
molybdenum(0), **I**.

tricarbonyls have been investigated as co-catalysts in aromatic hydrocarbon hydrogenation (*176*) and phenylacetylene polymerization (*177*), and the related piano-stool complex methylcyclopentadienyl manganese tricarbonyl has found use as an anti-knock gasoline additive (*178*). Point-charge models indicate that the EFG at the central nucleus of piano-stool complexes of this type should be zero, or small, as is the case for perfectly tetrahedral and octahedral complexes (*179*, *180*, *181*). There is no requirement for the CS tensor to be perfectly isotropic in piano-stool complexes. While previous estimates of the $^{95}$Mo nuclear quadrupolar coupling constant, $C_Q(^{95}Mo)$, in **I** have been made in solution (*182*, *183*), measurement of the $^{95}$Mo NMR spectrum for a solid sample of **I** will allow for a detailed interpretation of the observed EFG tensor in the context of the known structure in the solid state as determined by X-ray diffraction (*184*).

Furthermore, solid-state NMR offers the possibility of characterizing a CS tensor for the central quadrupolar nucleus in a piano stool complex for the first time.

Chromium is an early transition metal element which continues to find extensive use in several areas of chemistry (*185*) including organic synthesis (*186*), non-linear optics (*187*), molecular magnetism (*188*), and superconductivity (*189*); however, NMR spectroscopy of chromium-53 is conspicuously underdeveloped, especially in the solid state (*190*, *191*). In contrast to $^{11}B$, $^{35/37}Cl$, and $^{95/97}Mo$, *there have been no solid-state NMR experiments reported for the $^{53}Cr$ nucleus in any diamagnetic compound.* As can been seen in Table 3.1, the relative receptivity and nuclear quadrupole moment of $^{53}Cr$ certainly make its observation in the solid state a challenge. Until 1988, only a small number of compounds had been studied in solution using $^{53}Cr$ NMR, e.g., hexacarbonylchromium(0) and some chromate salts (*192*, *193*, *194*). More recent solution studies have provided isotropic chemical shifts and line widths for over fifty pseudo-octahedral diamagnetic pentacarbonylchromium-carbene complexes (*195*), dichromate and halochromate anions, chromyl halides ($CrO_2X_2$), chromyl nitrate, and several complexes of the type $Cr(CO)_x(PF_3)_{6-x}$ (*196*). The use of supercritical solvents to reduce $^{53}Cr$ line widths has also been demonstrated recently (*197*).

In Smith's review (*84*), $^{53}Cr$ is represented by only one out of the 245 references. Previous solid-state $^{53}Cr$ NMR studies are very scarce (*194*) and limited to the study of paramagnetic, ferromagnetic, and antiferromagnetic compounds, e.g., $CdCr_2Se_4$ and $CuCr_2S_4$ (*198*), $CoCr_2S_4$ (*199*), $GdCrO_3$ (*200*), $ErCrO_3$ (*201*), CrFe (*202*), and $CrH_{0.93}$ (*203*). One NMR study of $^{51}Cr$, a radioactive isotope with no natural abundance, has also

been reported (*204*). Although no solid-state $^{53}Cr$ NMR spectrum of any diamagnetic compound has ever been reported, several $^{67}Zn$ ($I = 5/2$) NMR spectra have been reported (e.g., references *84, 205, 206, 207*); the Larmor frequency, natural abundance, and quadrupole moment of this nucleus are comparable to those of $^{53}Cr$. Given the viability of $^{67}Zn$ and $^{95}Mo$ solid-state NMR studies, an examination of the feasibility and utility of $^{53}Cr$ solid-state NMR is in order. Chromium-53 solid-state NMR spectra and their analyses for prototypal Cr(0) and Cr(VI) compounds are discussed in this chapter.

In summary, the work reported in this chapter aims to expand the applicability of solid-state NMR to include a variety of "difficult" nuclei which have not been exploited to their full potential. Furthermore, measurements of EFG and CS tensors in the context of molecular and electronic structures are analysed to provide important new information on a variety of chemical systems. Finally, wherever possible, the experimental results have been supplemented with *ab initio* or DFT calculations to provide a more complete interpretation.

## 3.2 Experimental and Computational Details

### *3.2.1 Samples*

Trimesitylborane (97%), triphenyl borate, borax, L-cysteine methyl ester hydrochloride, L-cysteine ethyl ester hydrochloride, and quinuclidine hydrochloride were purchased from Sigma-Aldrich and used without further purification. Crystals of tris sarcosine calcium chloride were obtained from an aqueous solution of sarcosine and $CaCl_2$ by slow evaporation as described by Ashida *et al.* (*173*). The identity and purity of

the product were confirmed by $^{13}C$ CP/MAS NMR spectroscopy. X-ray or neutron diffraction studies of the chlorine compounds (*170*, *171*, *172*, *173*) indicate that there is only one chlorine site and all spectra were analyzed as such.

Mesitylenetricarbonylmolybdenum(0), **1**, was kindly prepared by Richard Warren by refluxing molybdenum hexacarbonyl and mesitylene under nitrogen according to the method described by Angelici (*208*). The identity and purity of the product were confirmed by melting point, $^{1}H$ and $^{13}C$ solution NMR spectroscopy, as well as $^{13}C$ CP/MAS NMR spectroscopy.

Hexacarbonylchromium(0), potassium chromate, ammonium chromate, and cesium chromate were obtained from Alfa Aesar. Ammonium chromate was recrystallized from water prior to use. X-ray or neutron diffraction structures (*209*, *210*, *211*, *212*) indicate that each of these chromium compounds possesses only a single crystallographically distinct chromium site and all $^{53}Cr$ NMR spectra were analyzed accordingly.

### *3.2.2 Solid-State NMR Spectroscopy*

Solid-state NMR spectra were obtained on six different spectrometers: a Varian/Chemagnetics CMX Infinity 200 ($B_0 = 4.7$ T) at the University of Alberta; a Bruker AM300 ($B_0 = 7.05$ T) at the University of Alberta; a Bruker AMX400 ($B_0 = 9.4$ T) at Dalhousie University; a Bruker Avance DMX 400 ($B_0 = 9.4$ T) at the University of Calgary; a Varian Inova 750 ($B_0 = 17.63$ T) at the Environmental Molecular Sciences Laboratory (EMSL) in Washington; a Varian Inova 800 ($B_0 = 18.8$ T) at EMSL.

A variety of solid-state NMR probes were used. At 4.7 T, Chemagnetics 4 mm double resonance (DR), 5 mm triple-resonance (TR), and 7.5 mm DR MAS probes were used. At 7.05 T and on the Bruker Avance DMX 400 spectrometer, a modified Bruker Z32DR-MAS-7DB probe was used to acquire $^{53}Cr$ NMR spectra. This probe was modified by soldering in an extra capacitor, effectively lowering the tuning range to allow for the observation of the $^{53}Cr$ nucleus. A Bruker 4 mm broad-band MAS probe was used on the AMX400 system to observe $^{11}B$. A mid-bore (63 mm) Doty XC4 MAS probe was used to acquire all spectra on the Varian Inova spectrometers.

Compounds were powdered using a mortar and pestle and packed into zirconia ($ZrO_2$) or silicon nitride ($Si_3N_3$) rotors. For air-sensitive samples, rotors were packed under an inert atmosphere of nitrogen or argon in a glove box. For MAS NMR experiments, the magic angle was adjusted by maximizing the number of rotational echoes in the FID of a quadrupolar nucleus in a cubic environment (*53*). Typically, the $^{23}Na$ NMR signal of solid sodium nitrate or the $^{79}Br$ resonance of potassium bromide was used for this purpose. For the $^{35}Cl$ MAS NMR experiments at 18.8 T, the $^{35}Cl$ resonance of solid sodium chloride was used.

Boron-11 NMR experiments were carried out at applied magnetic field strengths of 4.7, 9.4, 17.63, and 18.8 T. Referencing and setup were done using solid powdered sodium borohydride. Solid $NaBH_4$ has a chemical shift of -42.06 ppm relative to the $^{11}B$ standard, liquid $F_3B{\cdot}O(C_2H_5)_2$ (*213*). Boron chemical shifts reported herein are therefore with respect to liquid $F_3B{\cdot}O(C_2H_5)_2$ at 0.00 ppm. Recycle delays of 2 to 20 s were used. For stationary samples, both one-pulse and quadrupolar echo ($\pi/2 - \tau_1 - \pi - \tau_2 - ACQ$) (*82,*

*126*) experiments were carried out. Typical $\pi/2$ pulse lengths for solid $NaBH_4$ were 2.0 - 4.0 μs. For one-pulse experiments, pulses of length 1.0 - 1.5 μs were used. The probes used at 9.4, 17.63, and 18.8 T caused a background in the $^{11}B$ spectrum as a result of boron nitride in the stators. At 17.63 T and 18.8 T, the intensity of this background was low compared with the signal of interest; the most effective method for removing the background signal from spectra obtained without quadrupolar echoes was simply to subtract the spectrum of an empty rotor from the spectrum of interest. In contrast, at 9.4 T, the $^{11}B$ background due to the probe swamped the sample signal; the quadrupolar echo sequence proved most effective in this case for suppressing the background signal. High-power proton decoupling was used for all boron NMR experiments except for those at 18.8 T.

Chlorine-35 solid-state NMR spectra were obtained at 18.8 T ($\nu_L(^{35}Cl) = 78.36$ MHz) and at 9.4 T ($\nu_L(^{35}Cl) = 39.18$ MHz). High-power proton decoupling was used on the 18.8 T system only. Experiments were set up using solid sodium chloride. The optimal central transition selective pulse was 5.75 μs on the 18.8 T system and 4.5 μs on the 9.4 T system. In practice, shorter pulse widths were sometimes used to provide more uniform excitation of the spectra. Due to broad signals and to avoid interference from probe ringing, echoes ($\pi/2 - \tau_1 - \pi - \tau_2$) were used for both stationary and MAS samples. QCPMG or spikelet echo experiments (Section 2.2.2) were carried out using the pulse sequence given in references 89 and 93. Phase cycling requirements are given in reference 89. Typically, M = 32 repeating units were used and the number of points acquired was adjusted so that the sideband separation was 1 - 10 kHz. Left shifting of the

FID prior to FT was typically used for all spectra except the QCPMG spectra, where acquisition exactly at the top of the echo is critical for obtaining reliable spectra. Recycle delays were 0.4 - 0.5 s for all compounds. Chlorine-37 spectra were obtained on the Bruker AMX instrument ($B_0 = 9.4$ T, $\nu_L(^{37}Cl) = 32.63$ MHz) with pulse widths of 2.75 μs. The $^{37}Cl$ NMR spectra were used in combination with the $^{35}Cl$ NMR spectra to refine the quadrupolar tensor parameters reported herein. Experimentally, the chlorine NMR spectra were referenced to the chlorine resonance of NaCl(s) at 0.00 ppm. To convert the chemical shifts so that they are with respect to the primary reference, an infinitely dilute solution of NaCl in $H_2O$, the chemical shift of the solid with respect to a very dilute solution was measured directly to give the conversion factor as:

$$\delta \text{ (rel. to NaCl in } H_2O\text{, inf. dilute)} = \delta \text{ (rel. to NaCl(s))} - 45.37 \text{ ppm} \qquad [3.1]$$

The chlorine chemical shift values reported in this thesis are with respect to an infinitely dilute solution of NaCl in $H_2O$ at 0.00 ppm. One should note that the $^{35}Cl$ chemical shifts for the chloride ion in $H_2O$ compared with $D_2O$ are significantly different (*214*). The chlorine NMR spectra shown in this chapter (scale in kHz) are with respect to solid NaCl at 0.0 kHz.

Molybdenum-95 solid-state NMR spectra were acquired on the Varian Inova spectrometer operating at a frequency of 52.025 MHz for $^{95}Mo$ ($B_0 = 18.8$ T). Chemical shifts were referenced to a 2 M aqueous solution of $Na_2MoO_4 \cdot 2H_2O$ at 0.00 ppm; this sample was also used to establish the non-selective $\pi/2$ pulse width as 7.0 μs. For solid mesitylenetricarbonylmolybdenum(0), spectra were acquired using an optimal central transition selective pulse of 2.3 μs, acquisition times of 85 to 100 ms, high-power proton

decoupling during acquisition, and recycle delays of 30 s. MAS rates of 4.000 and 11.000 kHz were employed, and an automated Doty Spin Rate Controller (version 1.06) was used to control the MAS rate to better than 1 Hz stability. Spectra are the sum of 2386 scans (4.000 kHz) and 2726 scans (11.000 kHz).

Chromium-53 solid-state NMR spectra were acquired on the AM300 ($\nu_L(^{53}Cr)$ = 16.93 MHz), Avance DMX400 ($\nu_L(^{53}Cr)$ = 22.6 MHz), and Inova ($\nu_L(^{53}Cr)$ = 45.21 MHz) spectrometers. Referencing and setup were performed using either a saturated solution of hexacarbonylchromium(0) in chloroform (at 0.00 ppm) or a saturated aqueous solution of cesium chromate (at 1798 ppm). The latter reference sample is much easier to observe. The non-selective $\pi/2$ pulse width was established as approximately 5.0 μs on the AM300 and DMX400 instruments, and 7.0 μs on the Inova. QCPMG experiments were carried out using selective $\pi/2$ and $\pi$ pulses, and typically M = 30 repeating units.

Spectra were processed using VNMR (*215*), NUTS (*216*), or WinNMR (*217*). Gaussian line broadening functions of 200 - 1000 Hz were applied to FIDs of stationary samples, 50 - 150 Hz to spectra of MAS samples, and 10 - 70 Hz to QCPMG spectra.

### *3.2.3 Spectral Simulations*

Most spectra were simulated using the WSOLIDS software package (*218*) which incorporates the space-tiling POWDER algorithm of Alderman *et al.* (*219*). Some spectra, including the QCPMG spectra, were simulated using the SIMPSON program (*220*). The simulations of QCPMG spectra take into account the possibility of incomplete or non-uniform spectral excitation by considering experimental parameters

such as the finite pulse widths and rf field strength used. For MAS spectra, summation of spinning sidebands into the centreband was carried out using WinNMR.

The issue of how a "best fit" was established deserves some mention here. In general, there are eight parameters which must be optimized in order to properly describe the NMR spectrum of a quadrupolar nucleus in a stationary powder sample: $\delta_{iso}$, $\Omega$, $\kappa$, $C_Q$, $\eta_Q$, and Euler angles $\alpha$, $\beta$, $\gamma$. Under MAS conditions, the CS tensor is averaged to its isotropic value and the spectrum requires three parameters to be fit: $\delta_{iso}$, $C_Q$, and $\eta_Q$. These three independent parameters are easily optimized by visual inspection since the dependence of the lineshape on $C_Q$ and $\eta_Q$ is well known (see Figure 2.4) and $\delta_{iso}$ simply reflects the horizontal position of the simulated spectrum. When fitting the spectrum of a quadrupolar nucleus in a stationary powder sample, $\delta_{iso}$, $C_Q$, and $\eta_Q$ are fixed and there remain 5 parameters to fit. If there is a diffraction structure of the compound under study available, some information about the Euler angles may be available from symmetry considerations. One of the most reliable methods to improve confidence in the final fit is to acquire spectra at more than one applied magnetic field strength, since the second-order quadrupolar and nuclear magnetic shielding interactions scale inversely and linearly, respectively, with $B_0$. The spectra are then fit using the same set of parameters.

In general, the final "best fit" is judged by visual inspection and is the result of a non-automated iterative variation of each of the parameters. Errors are similarly determined by visual inspection. One of the main reasons that this procedure is not automated is that, until recently, it has been difficult to account for various experimental conditions, such as rf field strength, which may adversely affect the utility of such a

procedure. For example, non-uniform excitation of a broad spectrum may change the relative intensities of various portions of an NMR powder pattern; however, the spectral positions of important discontinuities and inflection points will not be affected. Thus, an optimized fitting procedure may not fare well in such a case since relative intensities in the spectrum may not be important to obtaining accurate parameters. As mentioned above, the SIMPSON program, introduced in 2000, has the ability to account for some of these experimental conditions such as finite pulse lengths and rf field strengths, and has a built-in automated optimization procedure designed to give best-fit parameters along with errors. For the work reported in this thesis, however, this automated procedure has not been particularly useful.

### *3.2.4 Computational Details*

Calculations of nuclear magnetic shielding and electric field gradient tensors were carried out using Gaussian 98 for Windows (*221*) running on Dell Dimension computers (Pentium III, 550 MHz, 128 Mb SDRAM and Pentium III, 866MHz, 512 Mb RDRAM) or using Gaussian 98 (*95*) on a 43P Model 260 IBM RS6000 workstation with dual 200 MHz processors. Calculations of nuclear magnetic shielding tensors were generally done using the GIAO (Gauge-Including Atomic Orbitals) method (*222*). For comparison, both the restricted Hartree-Fock (RHF) method and density functional theory (DFT) using the B3LYP functional (*223*) were employed for most calculations. Locally-dense basis sets (*224*) were used for some calculations. The 3-21G, 6-31G, 6-311G*, and 6-311++G** basis sets were used, and are available within the Gaussian package. The LANL2DZ

basis set and effective core potential (*225*) was used on molybdenum and the 6-311++G** basis set was used on all other atoms for non-relativistic calculations on mesitylenetricarbonylmolybdenum(0).

For $^{95}$Mo, scalar relativistic ZORA-DFT calculations of nuclear magnetic shielding tensors were performed using the NMR module (*111, 112, 113, 114*) of the Amsterdam Density Functional (ADF) program (*226, 227*) running on the IBM RS6000 workstation. EFG tensors for molybdenum were also calculated using ADF (*118*). The calculations used the VWN (*228*) + Becke88 (*229*) and Perdew86 (*230*) generalized gradient approximation (GGA). The triple-polarized ADF ZORA V Slater-type basis sets available within the ADF package were used. Molecular orbital graphics were generated using the DENSF and ADFPLT programs in conjunction with ADF.

Nuclear quadrupolar coupling constants were determined from the calculated largest EFG component, $V_{zz}$, by means of equation 2.25. Conversion of $V_{zz}$ from atomic units to $Vm^{-2}$ was carried out by using the factor $9.7177 \times 10^{21}$ $Vm^{-2}$ per atomic unit (*231*). Quadrupole moments are given in Table 3.1. One should note that Gaussian 98 reports $V_{ZZ}$ with opposite sign to the convention used in equation 2.25; Gaussian output was corrected for this.

Calculated chlorine nuclear magnetic shielding tensors were converted to chemical shift tensors using the absolute shielding scale for chlorine (*232*). The absolute shielding constant for the primary reference, an infinitely dilute aqueous solution of NaCl, is $974 \pm 4$ ppm. Therefore, calculated shielding constants were converted to chemical shifts *via* the following equation:

$$\delta = 974 - \sigma \qquad [3.2]$$

where all quantities are in ppm. There are no established absolute shielding scales for boron, molybdenum, or chromium.

The geometry used for the calculations on trimesitylborane was taken from X-ray diffraction atomic coordinates (*233*) and the geometry for trimethylborate was taken from electron diffraction atomic coordinates (*234*). Carbon-hydrogen bond lengths were set to 1.09 Å (*235*). The geometry of ammonium chloride was taken from the solid-state neutron diffraction structure (*236*), with *r*(N-H) equal to 1.03 Å and an equilibrium nitrogen-chlorine distance of 1.933 Å. The geometry of sodium perchlorate used in the calculations employed a tetrahedral $ClO_4^-$ moiety with Cl-O bond lengths of 1.42 Å and a chlorine-sodium equilibrium internuclear distance of 3.54 Å (*237*, *238*), where the sodium atom lies in one of the O-Cl-O planes and bisects the O-Cl-O angle (model A from reference 237). The gas-phase equilibrium sodium-chlorine distance in NaCl is 2.3608 Å (*239*). The geometry of L-tyrosine hydrochloride was constructed from the neutron diffraction atomic coordinates (*170*).

The atomic coordinates for mesitylenetricarbonylmolybdenum(0) were taken from the X-ray crystal structure of Koshland *et al.* (*228*). Protons were added to the aromatic ring using a standard C-H bond length of 1.08 Å. Methyl groups were constructed using a perfect tetrahedral geometry and a C-H bond length of 1.09 Å. Analogous NMR and EFG calculations were performed on hexacarbonylmolybdenum(0) based on the X-ray structure of Mak (*240*). The "calculated" molybdenum isotropic chemical shift of **I** was determined using the ZORA-DFT isotropic molybdenum shielding constant for $Mo(CO)_6$,

$\sigma_{iso}$ = 1301 ppm, and the experimentally known isotropic molybdenum chemical shift of $Mo(CO)_6$ in $CHCl_3$ relative to the molybdenum chemical shift reference, 2 M sodium molybdate dihydrate, $\delta_{iso}$ = -1860 ppm (*174*, *241*).

## 3.3 Results and Discussion

The results and discussion for this chapter are divided into four major sections, based on the nuclei studied: $^{11}B$, $^{35/37}Cl$, $^{53}Cr$, and $^{95/97}Mo$.

### *3.3.1 Boron*

#### 3.3.1.1 Solid-state NMR

An example of the benefits of working at the highest possible field strengths when

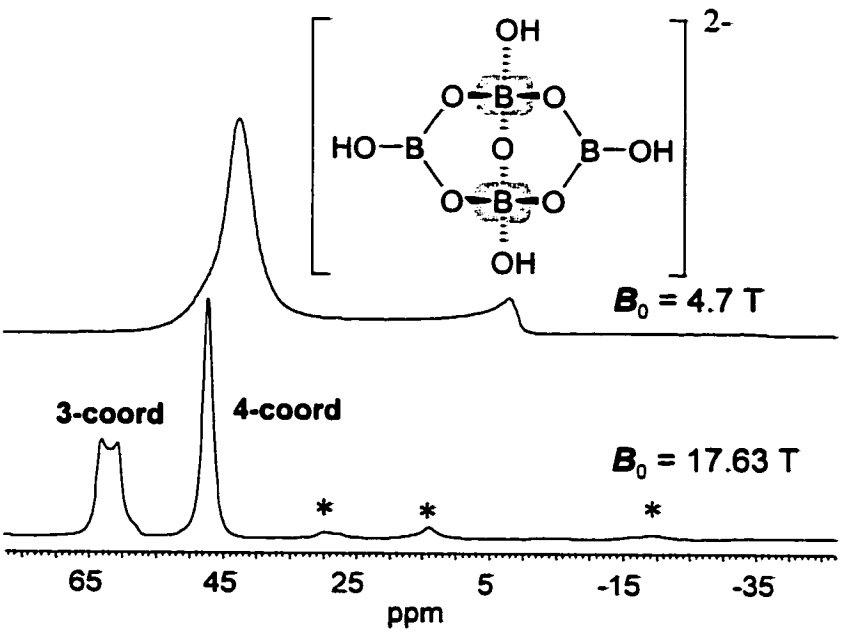


Figure 3.4: Boron-11 MAS NMR spectra of borax, providing an example of the site resolution which is available for quadrupolar nuclei at high magnetic field strengths. The isotropic chemical shift of the 4-coordinate site is 46 ± 1 ppm and that for the 3-coordinate site is 63 ± 1 ppm. Spinning sidebands are denoted by asterisks.

attempting to observe and interpret the NMR spectra of half-integer quadrupolar nuclei in the solid state is provided by the $^{11}B$ MAS NMR spectrum of borax. Shown in Figure 3.4 are $^{11}B$ MAS NMR spectra acquired at 4.7 and 17.63 T. Borax has both trigonally and tetrahedrally coordinated boron sites. At 4.7 T, broadening of the signal due to the trigonal boron sites results in a spectrum which is not resolved and which does not provide much useful information. However, at 17.63 T, the marked reduction in the second-order quadrupolar broadening results in a very well-resolved spectrum, with signals due to trigonal and tetrahedral boron sites easily assignable. Thus, the example of borax demonstrates the advantages of reducing the quadrupolar broadening by working at higher magnetic field strengths.

The other advantage of working at high fields is the increased role of the chemical shift tensor. Striking and definitive evidence for anisotropic boron shielding is found for

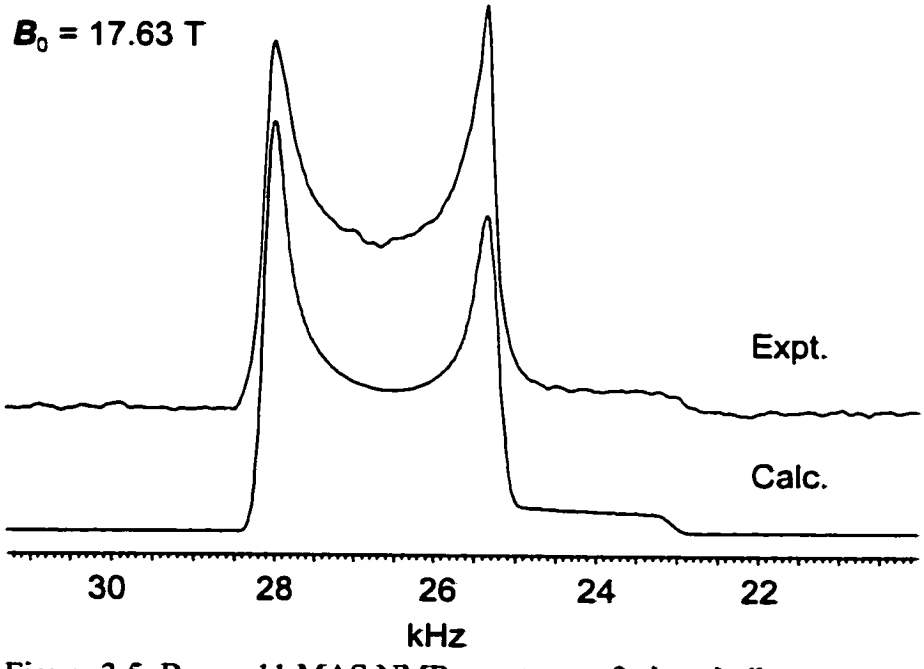


Figure 3.5: Boron-11 MAS NMR spectrum of trimesitylborane, acquired at 17.63 T. Also shown is the best-fit simulated spectrum. The scale is with respect to solid sodium borohydride at 0 kHz.

trimesitylborane. Shown in Figures 3.5 and 3.6 are experimental spectra of MAS and stationary powdered samples of trimesitylborane obtained with an external applied magnetic field of 17.63 T. Also shown are the best-fit simulated spectra, which were calculated using the parameters summarized in Table 3.2.

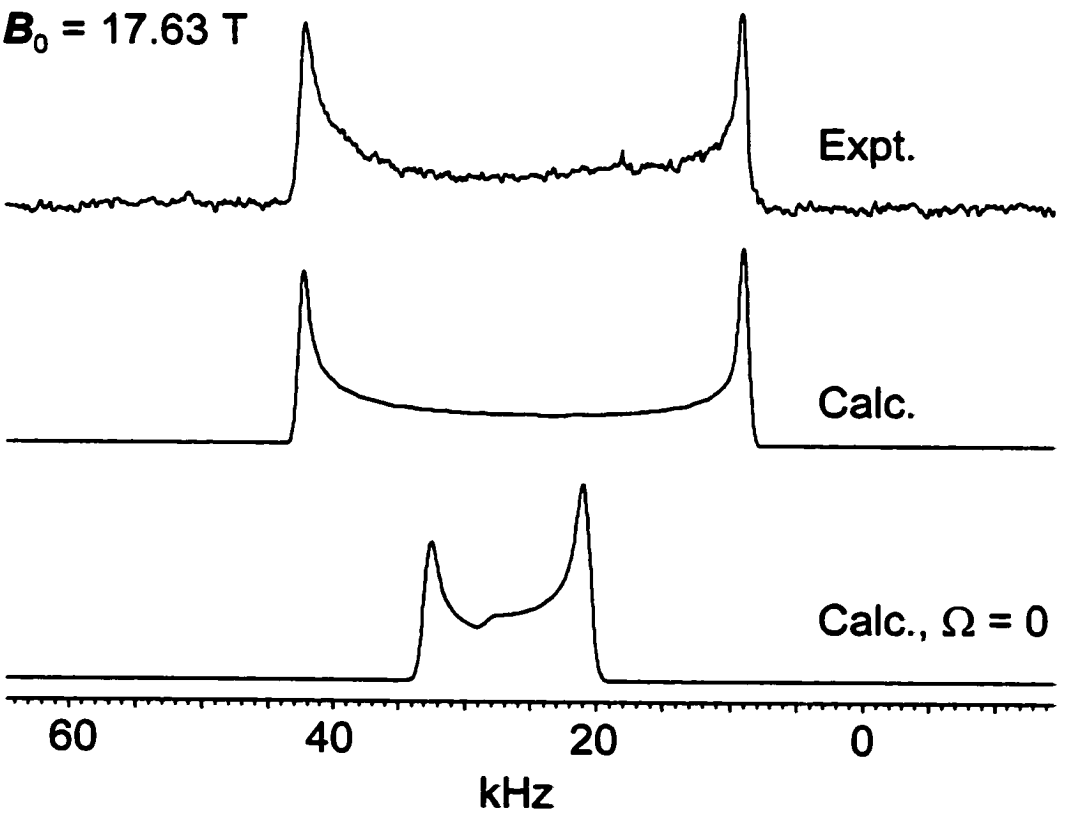


Figure 3.6: Boron-11 NMR spectrum of a stationary powdered sample of trimesitylborane. Also shown is the best-fit simulated spectrum which incorporates a span of 121 ppm. For comparison, a simulated spectrum under the assumption of an isotropic CS tensor is also shown.

**Table 3.2**: Experimental boron-11 chemical shift tensors and quadrupolar parameters for trimesitylborane and triphenyl borate.

| | trimesitylborane | triphenyl borate |
|---|---|---|
| $\delta_{iso}$ / ppm | 77.4 ± 0.5 | 17.9 ± 0.5 |
| $\Omega$ / ppm | 121 ± 1 | < 10 |
| $\kappa$ | 1.00 | 0.0 ± 0.3 |
| $C_Q$ / MHz | 4.75 ± 0.01 | 2.32 ± 0.02 |
| $\eta_Q$ | 0.00 | 0.00 |
| $\alpha$ | 0 | 0[a] |
| $\beta$ | 0 | 0 |
| $\gamma$ | 0 | 0 |

The precision of these parameters was determined by analyzing spectra of MAS and stationary samples obtained at both 17.63 T and 9.4 T (not shown). The isotropic chemical shift, quadrupolar coupling constant, and asymmetry parameter were first determined from spectra of MAS samples (Figure 3.5). Since the simulated spectra assume an infinite spinning rate, spinning sidebands were summed into the centreband during processing of the experimental spectrum to allow for an appropriate comparison of experimental and simulated spectra. There is an apparent discrepancy between the experimental and calculated intensities of the two prominent discontinuities in the spectra. The cause for the discrepancy is uncertain; however, probable reasons include a

[a] The Euler angles were set to zero for the best-fit simulation shown in Figure 3.8 although given the small span of the shielding tensor, its orientation with respect to the EFG tensor cannot be conclusively determined.

missetting of the magic angle or some variability in the MAS rate which would cause sideband intensity to be spread out over a larger spectral range than one would expect. Unexpected contributions to the spectrum from the satellite transition centrebands may also give rise to the unusual intensities observed experimentally. It is important to note that the discrepancy does not affect the values of $\delta_{iso}$, $C_Q$, or $\eta_Q$ or their errors (*cf.* Section 3.2.3).

The isotropic shift measured for solid trimesitylborane, 77.4 ± 0.5 ppm, is similar to the value reported in $CDCl_3$ solution, 79.0 ppm (*242*). A quadrupolar coupling constant of 4.75 MHz is in good agreement with the values determined for a series of trialkylboranes at 77 K *via* nuclear quadrupole resonance methods by Love (*243*) and discussed by Lucken (*169*); for example, the quadrupolar coupling constant in trimethylborane is 4.876 MHz. For $B(Mes)_3$ at 17.63 T, the second-order quadrupolar shift is -2.3 kHz (-9.7 ppm). The value of $\eta_Q$ was determined to be zero. Townes-Dailey analysis (*244*) indicates that the asymmetry parameter should be zero for the central atom in an isolated trigonal planar compound (*169*); the two in-plane components are equal. In the solid state, where crystal packing must be considered, experimental evidence indicates that in some cases, e.g., triethylborane ($\eta_Q = 0.009$) the asymmetry parameter can deviate very slightly from zero (*245*, *243*). Consideration of the geometry about the boron atom in trimesitylborane (*246*) (space group $C2/c$, $Z = 4$), as indicated by the X-ray crystal structure (*233*), shows that the boron atom and one mesityl group lie on a two-fold rotation axis; there is no true three-fold symmetry. An idealized trimesitylborane molecule would have $D_3$ point group symmetry. From the experimental value of $\eta_Q = 0$,

one may conclude that the largest component of the EFG tensor is perpendicular to the tricoordinate boron plane. This orientation is reproduced by *ab initio* calculations (*vide infra*).

Analysis of $^{11}B$ NMR spectra of stationary powdered trimesitylborane at 17.63 T (Figure 3.6) and 9.4 T (not shown) allows for the determination of the principal components of the boron chemical shift tensor ($\delta_{11} = \delta_{22} = 117.7$ ppm, $\delta_{33} = -3.3$ ppm) as well as its orientation relative to the EFG tensor. As shown in Figure 3.6 and Table 3.2, the span of the boron CS tensor was determined to be $121 \pm 1$ ppm. For comparison, a simulated spectrum for which the span was set to zero is also shown. Thus, at 17.63 T, where 121 ppm is equivalent to 29 kHz for $^{11}B$, anisotropic shielding accounts for more than half of the total breadth (35 kHz) of the powder pattern! Parameters obtained from the best-fit simulated spectrum for trimesitylborane indicate that the CS tensor is coincident with the EFG tensor and that the skew, $\kappa$, of the CS tensor is 1.0. This means that the in-plane components of the CS tensor are equal, as is the case for the EFG tensor. Although the electric field gradient and nuclear magnetic shielding tensors are fundamentally different properties, in the case of trimesitylborane these tensors are oriented such that their largest components are coincident. This is not always the case, even in situations of relatively high symmetry (*247, 248*).

Other definitive reports of anisotropic boron shielding measured using experimental solid-state NMR techniques are not available in the literature. Power has provided a qualitative estimate of the span of the boron CS tensor in solid $Ph_3P{\cdot}BH_3$ and finds it to be less than 50 ppm (*249*). A span on the order of 200 ppm has been

determined for gaseous BF (*250*) based on the spin-rotation data of Cazzoli *et al.* (*251*). Spin-rotation data are also available for a series of linear boron-containing molecules, FBO, ClBO, and FBS; however, the results have not been interpreted explicitly in terms of the span of the shielding tensor (*252*, *253*). The spans of the boron shielding tensors for these three linear triatomic molecules, as derived from the spin-rotation data, are approximately 210 - 220 ppm.

The case of trimesitylborane represents a very clear example of anisotropic boron shielding. The singularities of the stationary powder spectrum are very sharp. In particular, $^{11}B$-$^{11}B$ intermolecular homonuclear dipolar interactions are small due to the fact that the boron nucleus is quite sheltered from boron nuclei in adjacent molecules by the large mesityl groups. This is not the case for many compounds for which one might expect to detect anisotropic boron shielding. Additionally, many trigonally-coordinated boron atoms are bonded to nitrogen in compounds such as borazines. Under stationary conditions, heteronuclear $^{14}N$-$^{11}B$ dipolar interactions will cause the $^{11}B$ NMR spectrum to be broadened to an extent which renders the definitive characterization of boron CS tensors difficult even at field strengths as high as 17.63 T.

If compounds in which boron atoms may be subjected to significant $^{11}B$-$^{11}B$ homonuclear or $^{14}N$-$^{11}B$ heteronuclear dipolar couplings are excluded, other likely candidates for significant boron shielding anisotropy, beyond the boranes, are the borates, $B(OR)_3$. Shown in Figures 3.7 and 3.8 are the $^{11}B$ NMR spectra of MAS and stationary samples of solid powdered triphenyl borate along with best-fit simulations. As with trimesitylborane, the quadrupolar parameters (Table 3.2) were extracted from analysis of

the spectra of MAS samples at 9.4 T (Figure 3.7) and 17.63 T (not shown). The quadrupolar coupling constant, 2.32 MHz, is less than half the value of that for trimesitylborane. This reduction upon moving from a triarylborane to a triarylborate is supported by the measurements of Love (*243*), e.g. $C_Q(^{11}B)$ for $B(OH)_3$ is 2.56 MHz. In sharp contrast to the spectrum of stationary trimesitylborane, that of triphenyl borate derives most of its breadth from the quadrupolar interaction (Figure 3.8). At 17.63 T, the total breadth is only about 6 kHz, compared to 35 kHz for trimesitylborane. The isotropic shift, 17.9 ± 0.5 ppm, is in good agreement with the value reported in solution, 16.5 ppm (*254*). Based on the best-fit parameters obtained from analyses of the spectrum shown in Figure 3.8 (17.63 T) and a spectrum acquired at 9.4 T (not shown), the span of

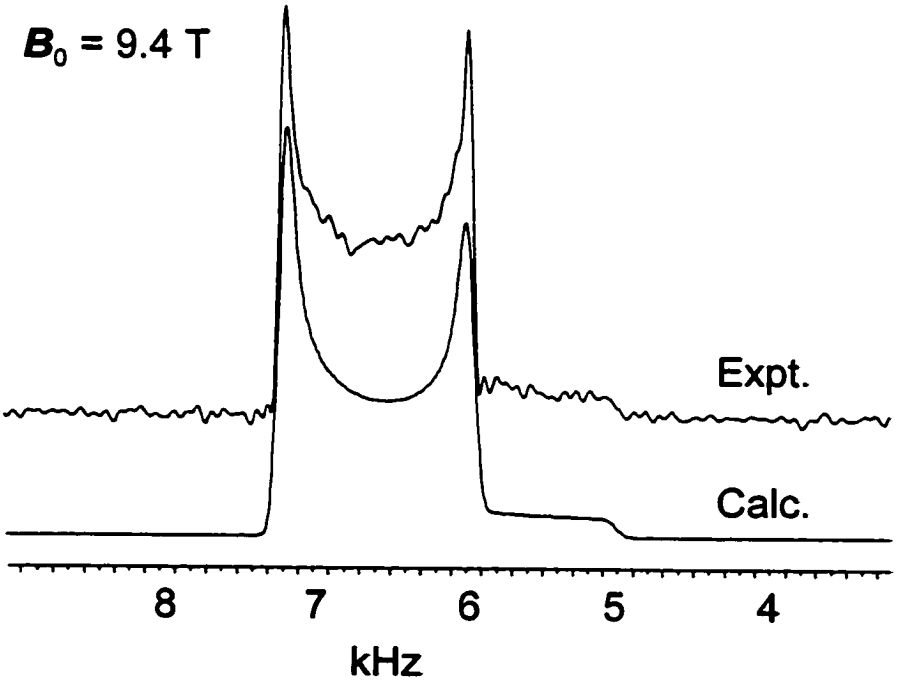


Figure 3.7: Boron-11 MAS NMR spectrum of triphenyl borate. Spinning sidebands have been summed into the experimental spectrum. Also shown is the best-fit simulated spectrum.

the boron CS tensor was determined to be less than 10 ppm. Also shown is a simulated spectrum for which the span was assumed to be zero. Although the span is an order of magnitude less than in trimesitylborane, the results presented in Figure 3.8 demonstrate that the span of the boron CS tensor in triphenyl borate is certainly non-zero. The simulated spectrum is not very sensitive to the skew or the orientation of the CS tensor with respect to the EFG tensor, as is to be expected when the span is small. Thus, from the experimental data alone one cannot conclusively determine the relative orientations of these tensors in triphenyl borate. However, given the coincident experimental orientation for trimesitylborane and results obtained from *ab initio* calculations (*vide infra*), the

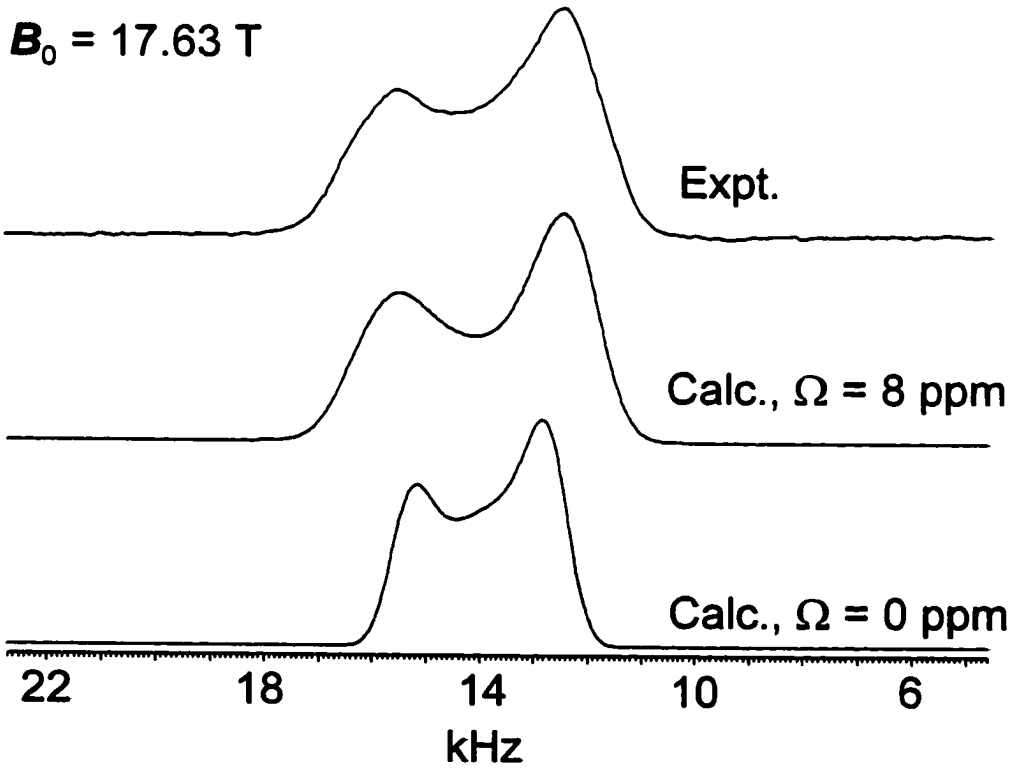


Figure 3.8: Boron-11 NMR spectrum of a stationary powdered sample of triphenyl borate. The best-fit simulated spectrum incorporates a CS tensor span of 8 ppm. Also shown is a simulated spectrum in the absence of an anisotropic CS tensor.

largest component of the EFG and nuclear magnetic shielding tensors, $V_{ZZ}$ and $\sigma_{33}$, are likely coincident for triphenyl borate as well.

The span of the boron CS tensor in triphenyl borate may be compared with those for the central atom in the analogous trigonally-coordinated carbon and nitrogen moieties $CO_3^{2-}$ and $NO_3^-$. The trend is that the span of the CS tensor of the central atom increases from boron (< 10 ppm in $B(OPh)_3$) to carbon (75 ppm in $CaCO_3$(*255*, *256*)) to nitrogen (231 ppm in $NH_4NO_3$ (*257*)), across the periodic table. A discussion of the carbon and nitrogen chemical shifts has been presented by Spiess (*256*).

A selection of tricoordinate and tetracoordinate boron compounds and their isotropic chemical shifts are presented in Figure 3.9. The chemical shifts shown here bridge most of the known range. Also shown is the boron CS tensor for trimesitylborane.

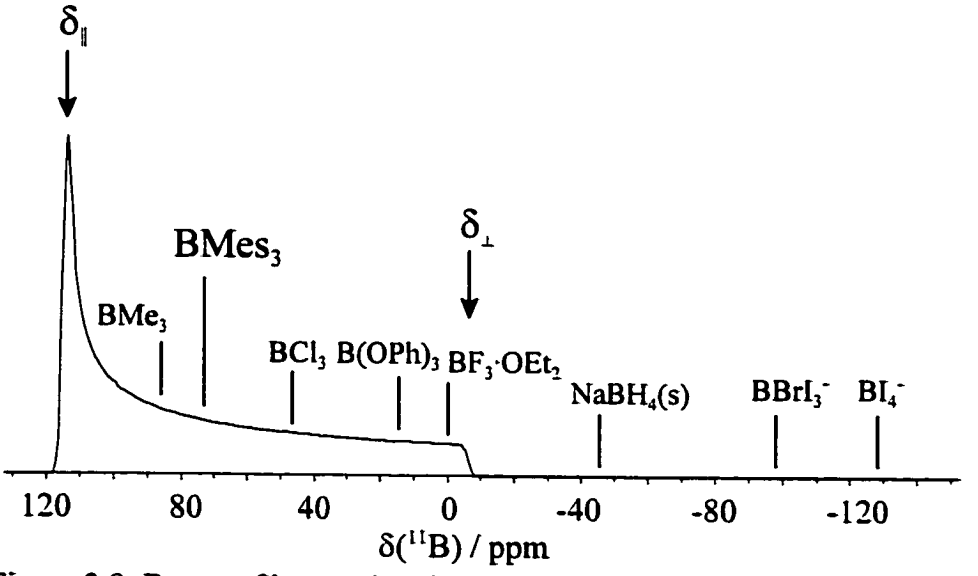


Figure 3.9: Range of boron chemical shifts for typical three- and four-coordinate boron compounds. Also shown is a simulated spectrum depicting the range covered by the axially symmetric anisotropic boron CS tensor measured experimentally for trimesitylborane.

Clearly, this tensor spans the range of most tricoordinate boron isotropic chemical shifts. Metallaboranes are not represented on this chemical shift scale. Some metallaboranes exhibit isotropic boron chemical shifts as large as 226 ppm (*148*); these are undoubtedly special compounds in which the boron nuclei are also expected to exhibit large shielding anisotropy.

3.3.1.2 *Ab Initio* Calculations

The results of *ab initio* calculations of the $^{11}B$ nuclear magnetic shielding and EFG tensors in trimesitylborane are presented in Table 3.3. Since there is no absolute shielding scale for boron, the calculated nuclear magnetic shielding tensors are discussed in terms of their span and skew rather than their principal components to allow for comparison with experiment. A reliable absolute shielding scale for boron would allow for a direct comparison of the experimental and calculated principal components.

**Table 3.3**: *Ab initio* and density functional theory calculations of the boron-11 nuclear magnetic shielding tensor and quadrupolar coupling parameters for trimesitylborane

| method | basis set[a] | $\sigma_{iso}$ / ppm | $\Omega$ / ppm | $\kappa$ | $C_Q$ / MHz | $\eta_Q$ |
|---|---|---|---|---|---|---|
| RHF | 6-31G | 56 | 112 | 0.91 | 5.02 | 0.00 |
| RHF | 6-311G*/3-21G | 66 | 104 | 0.90 | 4.63 | 0.00 |
| RHF | 6-311G* | 46 | 117 | 0.91 | 5.44 | 0.00 |
| RHF | 6-311++G** / 3-21G | 65 | 104 | 0.90 | 4.62 | 0.00 |
| DFT/B3LYP | 6-31G | 41 | 116 | 0.90 | 4.74 | 0.01 |
| DFT/B3LYP | 6-311G* / 3-21G | 54 | 109 | 0.88 | 4.26 | 0.01 |
| DFT/B3LYP | 6-311G* | 28 | 127 | 0.89 | 5.23 | 0.00 |
| DFT/B3LYP | 6-311++G** / 3-21G | 54 | 109 | 0.88 | 4.26 | 0.01 |
| expt.[b] | - | - | 121 | 1.00 | 4.75 | 0.00 |

The experimentally-determined tensors are reproduced very well by the calculations. At the RHF/6-311G* level, a span of 117 ppm is predicted while the B3LYP functional with the same basis set gives a span of 127 ppm. Both of these results are in excellent agreement with the experimental value of 121 ± 1 ppm. Trimesitylborane is a moderately-sized molecule with sixty-one atoms. Thus, the effect of locally-dense basis sets was investigated, e.g., where the boron atom and the carbon atoms directly bonded to boron are represented by a relatively large basis set (6-311G* or 6-311++G**

[a] The first listed basis set was used on boron and the carbon atoms directly bonded to boron. The second basis set listed was used on all remaining atoms. Where only one basis set is listed, this was applied to all atoms.

[b] Solid state (this work).

in this case) and the remaining atoms are represented by a relatively small basis set (3-21G in this case). The results show a decrease in the calculated span, from 117 to 104 ppm for the RHF calculation and from 127 to 109 ppm for the DFT calculation. All of the calculations predict a skew of ~ 0.9 for the boron shielding tensor, compared to the experimental value of 1.0. The predicted orientation of the shielding tensor is in agreement with the experimental chemical shift tensor orientation; $\delta_{33}$ is perpendicular to the tricoordinate boron plane (Figure 3.10) and the component of intermediate shielding, $\delta_{22}$, lies along the molecular $C_2$ axis.

The calculations presented here have been carried out on single gas-phase molecules while the experiments are performed in the solid state. Thus, the good agreement between theory and experiment suggests that intermolecular interactions involving the boron nuclei are weak. As previously mentioned, the bulky trimesityl substituents hamper boron-boron interactions. Bailey has demonstrated the reliability of the B3LYP functional and the MP2 method for the calculation of quadrupolar coupling

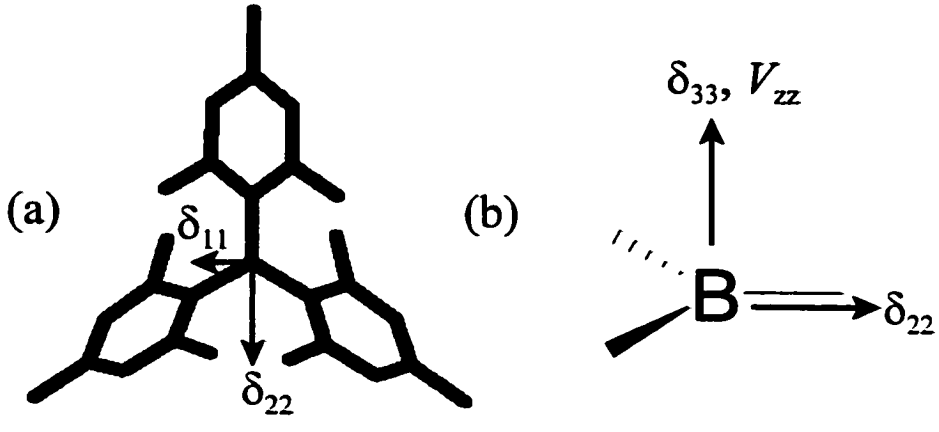


Figure 3.10: Orientations of the boron EFG and CS tensors for trimesitylborane from experiment and *ab initio* calculations. (a) Top view, along $\delta_{33}$. (b) Side view, along $\delta_{11}$.

constants in small molecules in the gas phase, where intermolecular effects are relatively unimportant (*258*). The calculated quadrupolar coupling constants reported here (Table 3.3) for trimesitylborane range from 4.26 to 5.44 MHz, and are all in reasonable accord with the experimental value of 4.75 MHz. The addition of diffuse functions makes essentially no difference to the calculated quadrupolar coupling constants (e.g., 6-311G*/3-21G compared with 6-311++G**/3-21G). All the calculations presented here predict an asymmetry parameter of zero, in agreement with experiment. The calculated orientation is consistent with the experimental conclusion that $V_{ZZ}$ is perpendicular to the tricoordinate boron plane (Figure 3.10). The results for trimesitylborane extend the good agreement between experimental and theoretical $^{11}B$ quadrupolar coupling constants obtained by Bailey (*258*).

Crystal structure data are unavailable for triphenyl borate and rather than using an *ab initio* optimized structure, calculations have been carried out on a model compound, trimethyl borate, for which electron diffraction data exist (*234*). Quantitative agreement between experimental and theoretical results is thus not expected; however, distinct differences between the boron shielding tensors of boranes and borates are expected. The results of these calculations are summarized in Table 3.4.

**Table 3.4**: *Ab initio* and density functional theory calculations of the boron-11 nuclear magnetic shielding tensor and quadrupolar coupling parameters for trimethyl borate as a model for triphenyl borate

| method | basis set | $\sigma_{iso}$ / ppm | $\Omega$ / ppm | $\kappa$ | $C_Q$ / MHz | $\eta_Q$ |
|---|---|---|---|---|---|---|
| RHF | 6-311G | 99 | 2.9 | 0.58 | 2.75 | 0.00 |
| RHF | 6-311++G** | 100 | 4.9 | -0.88 | 2.93 | 0.00 |
| DFT/B3LYP | 6-311G | 86 | 4.7 | 0.93 | 1.90 | 0.00 |
| DFT/B3LYP | 6-311++G** | 85 | 0.9 | 0.02 | 2.25 | 0.00 |
| expt[a] (*259*) ($B(OH)_3$) | - | - | - | - | 2.56 | 0.00[b] |
| expt[c] (triphenyl borate) | - | - | < 10 | $0.0 \pm 0.3$ | 2.32 | 0.00 |

The calculated shielding tensors exhibit spans ranging from 0.9 ppm (B3LYP/6-311++G**) to 4.9 ppm (RHF/6-311++G**) and support the experimental observation that $\Omega$ is less than 10 ppm. The calculated skews are not very consistent as the basis set and/or method of calculation is altered, ranging from -0.88 to 0.93; however, this is not surprising for a shielding tensor with such a small span. Indeed, the experimental value of $\kappa$ has a large uncertainty associated with it, $0.0 \pm 0.3$. While a very anisotropic boron CS tensor has been observed for trimesitylborane, the boron CS tensors of trialkyl- and

[a] Solid state.

[b] Assumed in original reference.

[c] Solid state (this work).

triarylborates are fortuitously nearly isotropic. A relatively small span for trimethylborate and a relatively large span for trimethylborane was predicted by Ebraheem and Webb in 1977 based on the results of semi-empirical CNDO/S calculations (*260*). IGLO calculations on $BF_3$ indicate that the in-plane boron shift tensor components are actually larger than the unique component which is perpendicular to the molecular plane ($\kappa < 0$) (*98*); GIAO calculations also give a negative skew. This result implies that indeed the borates are at a crossing-over point, where all three principal components of the boron CS tensor are serendipitously almost equal.

The calculated quadrupolar coupling constant for trimethyl borate, 2.25 MHz at the B3LYP/6-311++G** level, is in accord with the experimental value of 2.32 MHz in triphenyl borate. Once again, the asymmetry parameter is zero for all calculations. As for trimesitylborane, the calculations indicate that the largest component of the EFG tensor is perpendicular to the tricoordinate boron plane.

3.3.1.3 Rationalization of the difference in spans: comparison with $^{13}C$ shifts of carbocations

The explanation for the marked difference in the spans of the boron shielding tensors for a triarylborane compared to a triarylborate is not immediately obvious. Both boron atoms are in symmetrical trigonal planar environments bonded to first-row elements. Based on symmetry considerations alone, one might expect the spans to be comparable. In this section, *ab initio* calculations of the molecular electronic structures are presented and the difference in shielding tensors is rationalized in the context of

Ramsey's theory of nuclear magnetic shielding.

Several reports have described apparent correlations between the $^{13}C$ isotropic chemical shifts of trigonal planar carbon-centred cations and the $^{11}B$ isotropic chemical shifts of analogous tricoordinate neutral boron compounds (*261*). The IGLO *ab initio* method has been applied to the calculation of $^{13}C$ isotropic chemical shifts in various classical and non-classical carbocations (*98*, *262*). Kutzelnigg has presented an explanation for the large range of values for $\delta_{iso}(^{13}C)$ (*98*). As described in Chapter 2, the nuclear magnetic shielding tensor may be decomposed into diamagnetic ($\sigma^d$) and paramagnetic contributions ($\sigma^p$). For nuclei other than hydrogen, generally the paramagnetic term is the dominant factor in determining the anisotropy of the shielding tensor (*263*).

When virtual "rotation" of an occupied MO results in favourable overlap of this MO with a low-lying virtual MO, paramagnetic deshielding is observed for the direction of the axis of rotation. For example, in classical carbocations, rotation of occupied bonding orbitals about any direction in the plane of the carbocation leads to favorable overlap with an empty $p_z$ orbital which resides on the central carbon atom. This $\sigma \rightarrow \pi^*$ magnetic dipole allowed transition is of primary importance in determining the magnitude of the in-plane tensor components, and consequently, the isotropic chemical shift. For non-classical carbocations, the $p_z$ orbital is involved in bonding and thus is not available for the rotation of charge described above. Accordingly, non-classical carbocations have smaller isotropic chemical shifts than do classical carbocations. The difference in energy between the ground state and excited singlet states is critical in

deciding which virtual "rotations" will be important in determining $\sigma^p$. The closer in energy the occupied and virtual orbitals involved in the rotation are, the greater the (usually negative) paramagnetic contribution will be (*cf.* eq. 2.18).

Comparison of the *ab initio* calculated boron shielding tensors in trimesitylborane and trimethyl borate indicates that the component perpendicular to the tricoordinate plane, $\sigma_\perp$, varies little compared to the in-plane shielding components. For example, at the RHF/6-311G* level, $\sigma_\perp$ is 122 ppm for trimesitylborane and 96 ppm for trimethylborate. The average of the in-plane components, however, increases from 8 ppm in the borane to 101 ppm in the borate. As for carbocations, it is clear that the in-plane components are those which vary the most drastically from compound to compound and *thus these components determine the overall span of the shielding tensor as well as the isotropic shielding.* Tricoordinate boron compounds such as triarylboranes and triarylborates also have a virtual $p_z$ orbital available for magnetic dipole allowed transitions (rotations) which resides on boron. From a qualitative point of view, in borates the lone pairs on oxygen may be considered to donate strongly into the vacant orbital on boron, thus reducing its availability for the charge rotation discussed above. This would result in a reduction of $\sigma^p$. From a more quantitative standpoint, *ab initio* calculations (RHF/6-311G**) of the molecular orbitals for $B(CH_3)_3$ and $B(OH)_3$ in the $C_{3h}$ point group reveal that the e' → a" ($\sigma \rightarrow \pi^*$) transition, which involves the requisite rotation about an axis in the plane of the tricoordinate boron (Figure 3.11), has a smaller energy gap in the borane (0.59405 hartrees) than in $B(OH)_3$ (0.80555 hartrees). Thus, the same explanation is invoked to rationalize the drastic difference between the boron CS

tensors for trimesitylborane and triphenyl borate which has been observed experimentally. The boron nuclei in 4-coordinate boron compounds have smaller isotropic chemical shifts due to their different electronic structures, most importantly the lack of a virtual $p_z$ orbital.

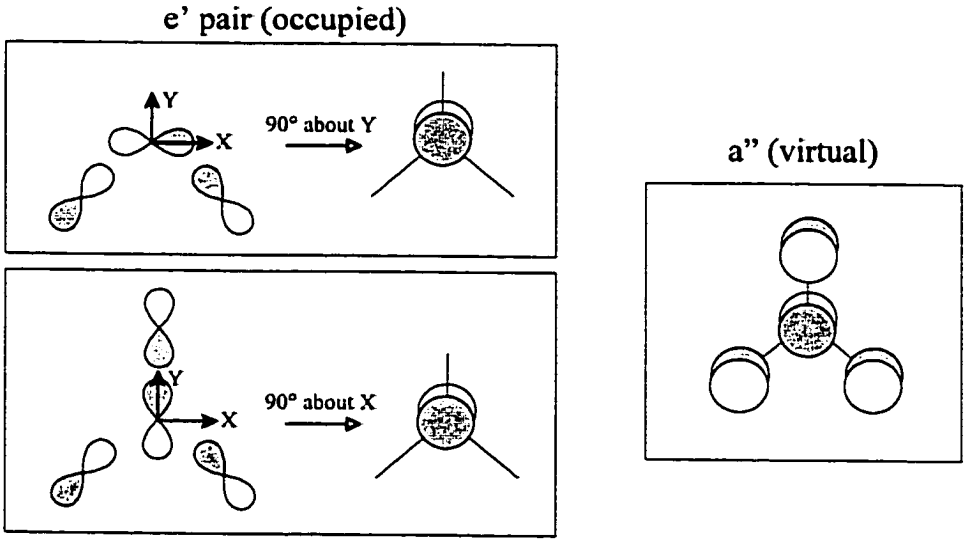


Figure 3.11: Molecular orbitals involved in $\sigma \rightarrow \pi^*$ magnetic dipole allowed transitions for planar tricoordinate boron compounds or carbocations in the $C_{3h}$ space group, e.g., $BMe_3$, $B(OH)_3$. The occupied degenerate e' pair orbitals on the left lie in the tricoordinate boron plane. Focussing solely on the central atom, rotation of the top e' orbital 90° about Y gives an orbital which overlaps constructively at boron with the virtual a" orbital shown on the right. Similarly, the bottom e' orbital may be rotated about X by 90° to give favorable overlap with a" at boron.

*3.3.2 Chlorine*

3.3.2.1 Cl-35 MAS NMR Spectra

Acquisition of $^{35}Cl$ MAS spectra of the central ½ ↔ -½ transition of compounds containing chloride ions with quadrupolar coupling constants of less than 4 MHz was straightforward on the 18.8 T magnet at MAS rates of 10 - 15 kHz. Signals were easily observed after a single scan. Spectra with well-defined second-order quadrupolar line shapes and good signal-to-noise ratios were generally obtained in approximately 30 minutes. Shown in Figure 3.12 are central transition spectra of MAS samples of (a) L-cysteine ethyl ester hydrochloride, (b) L-cysteine methyl ester hydrochloride and (c) L-tyrosine hydrochloride. The best-fit parameters for the simulated spectra are given in Table 3.5.

**Table 3.5:** Summary of $^{35}Cl$ NMR parameters for a series of organic hydrochloride salts

| Molecule | $C_Q$ / MHz | $\eta_Q$ | $\delta_{iso}$ / ppm | $\Omega$ / ppm | $\kappa$ |
|---|---|---|---|---|---|
| L-tyrosine HCl [a] | 2.23 ± 0.02 | 0.72 ± 0.03 | 48.3 ± 0.5 | < 150 | - |
| L-cysteine methyl ester HCl [a] | 2.37 ± 0.01 | 0.81 ± 0.03 | 47.2 ± 0.7 | ~ 30-60 | - |
| L-cysteine ethyl ester HCl [b] | 3.78 ± 0.02 | 0.03 ± 0.03 | 52.2 ± 0.5 | 47 ± 4 | -0.8 ± 0.2 |
| tris sarcosine $CaCl_2$ [c] | 4.04 ± 0.03 | 0.62 ± 0.02 | 13.7 ± 10.0 | < 150 | - |
| quinuclidine HCl [c] | 5.25 ± 0.02 | 0.05 ± 0.01 | 8.7 ± 10.0 | 50 ± 20 | - |

[a] Parameters determined from MAS and static Hahn-echo $^{35}Cl$ spectra acquired at 18.8 T.

[b] Parameters determined from MAS, Hahn-echo, and QCPMG $^{35}Cl$ spectra acquired at 18.8 T.

[c] Parameters determined from Hahn-echo $^{35}Cl$ spectra acquired at 18.8 T and 9.4 T, and Hahn-echo $^{37}Cl$ spectra acquired at 9.4 T.

The $^{35}Cl$ quadrupolar coupling constant for this series of compounds ranges from approximately 2 to 4 MHz, and the quadrupolar asymmetry parameter ranges from nearly zero to greater than 0.8. Conversely, the isotropic chemical shifts are fairly constant, all falling between 45 and 55 ppm. This small variation in the chemical shift is also found

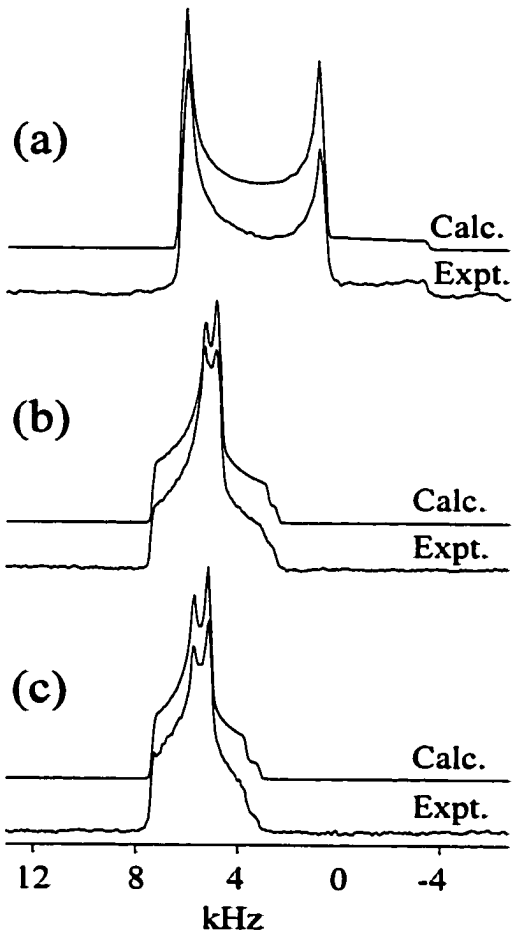


Figure 3.12: Experimental and calculated central transition region of the high-field ($B_0$ = 18.8 T) $^{35}Cl$ NMR spectra of MAS powder samples of (a) L-cysteine ethyl ester hydrochloride ($\nu_{rot}$ = 13.6 kHz); (b) L-cysteine methyl ester hydrochloride ($\nu_{rot}$ = 14.2 kHz); (c) L-tyrosine hydrochloride ($\nu_{rot}$ = 14.8 kHz). Best-fit parameters are given in Table 3.5.

for perchlorate salts (*159*), although the chemical shift ranges for the two classes of compounds are on the order of 1000 ppm apart. The variation in chemical shifts within either class of compounds, on the order of tens of ppm, represents less than 5 % of the total known chemical shift range for chlorine, 1500 ppm (*264*, *265*). The variation in $C_Q$ which has been measured for both the hydrochloride salts and the perchlorates is also relatively small, < 5 %, since values of up to -145.87 MHz are known (*232*, *266*). A more complete discussion of the dependence and sensitivity of the chlorine NMR interaction tensors on the local environment, in particular the hydrogen bonding about chlorine, is presented below. The spectra presented in Figure 3.12 are the first which explicitly demonstrate via sharp second-order quadrupolar line shapes the potential of $^{35}Cl$ MAS solid-state NMR for the study of organic hydrochloride salts. It is important to recognize that local sample heating induced by MAS is likely to slightly alter the chlorine nuclear quadrupolar coupling constant from that determined from a stationary sample.

Given the range of chlorine quadrupolar coupling constants determined using MAS NMR for chloride anions, 2 to 4 MHz, MQMAS (*15*) and STMAS (*138*) experiments on $^{35/37}Cl$ nuclei should be practical at high field strengths for identifying and characterizing non-equivalent chlorine sites in these types of compounds. Standard MAS and satellite transition spectroscopy (SATRAS) (*267*, *268*) experiments have already proven to be effective in the identification and characterization of multiple perchlorate sites exhibiting very small quadrupolar coupling constants, e.g., the two unique sites in $Mg(ClO_4)_2.6H_2O$ have $C_Q(^{35}Cl)$ values of 0.309 and 0.475 MHz (*159*).

3.3.2.2 Cl-35/37 NMR Spectra of Stationary Samples

For the majority of the hydrochloride salts studied herein, quantitative characterization of the chlorine chemical shift tensor proved to be difficult even at 18.8 T. This is simply due to the fact that the span of the chemical shift tensor typically amounts only to a few kHz (e.g., 50 ppm x 78.3 Hz $ppm^{-1}$ = 3.9 kHz), while the central transition spectra predicted based solely upon the quadrupolar interaction may be as wide as 100 kHz. However, for L-cysteine ethyl ester hydrochloride, a quantitative determination of the chlorine chemical shift tensor was possible. Shown in Figure 3.13 are experimental and simulated Hahn-echo and QCPMG $^{35}Cl$ spectra of L-cysteine ethyl ester hydrochloride, for which the chlorine CS tensor was determined to have a span of 47 ± 4 ppm and a skew of -0.8 ± 0.2 (Table 3.5). This corresponds to principal components of $\delta_{11}$ = 82, $\delta_{22}$ = 40, and $\delta_{33}$ = 35 ppm. Additionally, the simulations indicate that the largest components of the EFG and nuclear magnetic shielding tensors ($V_{ZZ}$ and $\sigma_{33}$) are at 90° with respect to one another. The simulation of the QCPMG spectrum is comparable to those where anisotropic chemical shift information has been extracted previously, e.g., $^{87}Rb$ spectra of $RbClO_4$ and $RbVO_3$ and $^{59}Co$ spectra of $(Co(NH_3)_5Cl)Cl_2$ (*89*). Although they are acquired at the same magnetic field strength, simulations of the QCPMG spectrum and the Hahn-echo spectrum in combination were useful to refine and establish accurately the EFG and CS parameters. Simulations of Hahn-echo and QCPMG spectra of L-tyrosine hydrochloride and L-cysteine methyl ester hydrochloride (not shown) did not allow for a precise determination of the chlorine chemical shift tensor in these compounds. Estimated limits on the span of the chlorine CS tensors are

given in Table 3.5.

While reports on the chlorine EFG tensor in organic hydrochlorides are scarce (*84*, *167*, *168*), information concerning the chlorine chemical shift tensor in such compounds is virtually non-existent. Even isotropic chemical shifts are rare for solid hydrochloride salts. One may, however, compare the span of 47 ppm in L-cysteine

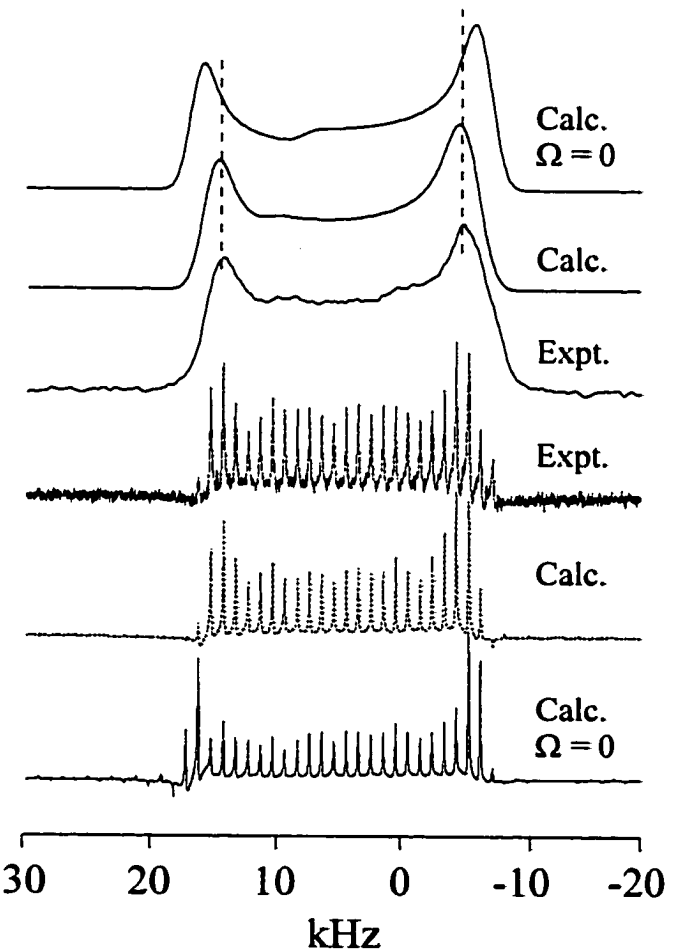


Figure 3.13: Experimental $^{35}$Cl NMR static echo (top) and QCPMG (bottom) spectra of L-cysteine ethyl ester hydrochloride, $B_0 = 18.8$ T, along with the best-fit simulated spectra. Also shown are simulated spectra for which a span of zero was used. Spikelets in the QCPMG spectra are spaced at 1 kHz intervals.

methyl ester hydrochloride to two known chlorine chemical shift tensor spans of oxychloro anions, both determined from single-crystal $^{35}Cl$ studies: $\Omega = 32.0 \pm 1.2$ ppm for $NH_4ClO_4$ (*152*), and $\Omega = 40 \pm 7$ ppm for $NaClO_3$ (*149*). The total range of chloride ion chemical shifts for the compounds studied in the present work is less than 50 ppm.

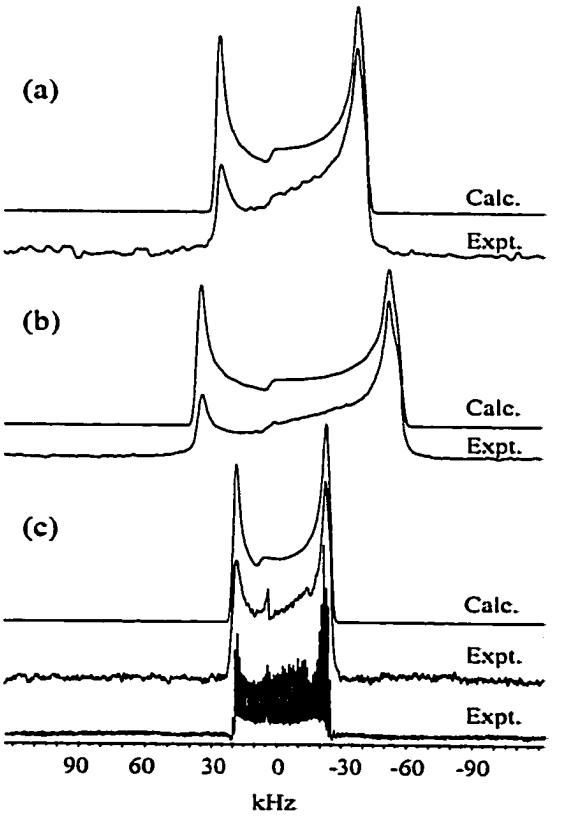


Figure 3.14: Experimental chlorine NMR static echo spectra of quinuclidine hydrochloride acquired for (a) $^{37}Cl$ at 9.4 T, (b) $^{35}Cl$ at 9.4 T, and (c) $^{35}Cl$ at 18.8 T, along with the best-fit simulations. Also shown in part (c) is the experimental $^{35}Cl$ QCPMG spectrum acquired at 18.8 T. The experimental spectra shown in parts (a) and (b) suffer from non-uniform excitation across the ~ 100 kHz breadth. The sharp feature at 4.1 kHz in part (c) is the isotropic resonance due to a small amount of solvated quinuclidine hydrochloride in the sample.

From solution NMR studies, chlorine chemical shifts of chloride ions are known to cover a fairly narrow range (~ 30 ppm) near zero ppm (*264*). Given that shielding constants for the chloride ion cover a fairly small range and lie within ~ 200 ppm of the diamagnetic free atom shielding for chlorine (1149 ppm (*269*)), it is likely that the chloride magnetic shielding tensor is dominated by the diamagnetic contribution; it is therefore reasonable to expect small shielding tensor spans.

Experimental and simulated chlorine Hahn-echo spectra of stationary samples of quinuclidine hydrochloride and tris sarcosine calcium chloride are shown in Figures 3.14 and 3.15, respectively. In part (a) of each Figure, the $^{37}Cl$ spectrum acquired at 9.4 T is shown; parts (b) and (c) show the $^{35}Cl$ spectra acquired at 9.4 T and 18.8 T. Also shown is the experimental QCPMG spectrum for quinuclidine hydrochloride. All of the spectra acquired at 9.4 T suffer to a certain extent from non-uniform rf excitation; nevertheless, fitting of the discontinuities in the spectra allows for the determination of $C_Q$ and $\eta_Q$. NMR of the $^{37}Cl$ nucleus affords narrower line shapes due to its smaller quadrupole moment relative to $^{35}Cl$; however, the lower natural abundance of $^{37}Cl$ results in spectra with lower signal-to-noise ratios relative to $^{35}Cl$. Analyses of both $^{37}Cl$ and $^{35}Cl$ NMR spectra allow for more accurate and precise determinations of the EFG tensor parameters (Table 3.5). In Figure 3.14c, the QCPMG sidebands were deliberately spaced at relatively small (1 kHz) intervals about the transmitter frequency to faithfully mimic the envelope of the powder pattern obtained using a simple Hahn echo pulse sequence.

The $^{35}Cl$ quadrupolar coupling constant in quinuclidine hydrochloride, 5.25 MHz, is the largest determined directly by chlorine nuclear magnetic resonance spectroscopy to

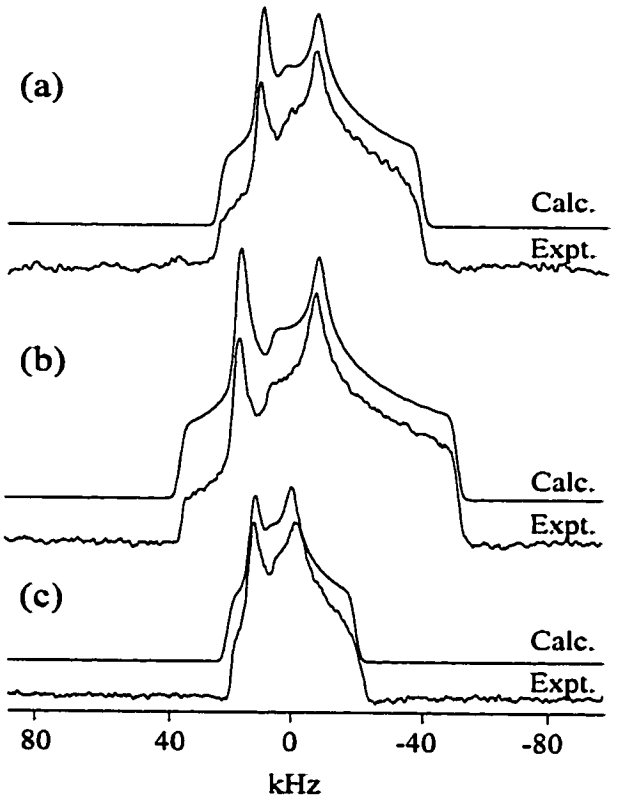


Figure 3.15: Experimental chlorine NMR static echo spectra of tris sarcosine calcium chloride acquired for (a) $^{37}Cl$ at 9.4 T, (b) $^{35}Cl$ at 9.4 T and (c) $^{35}Cl$ at 18.8 T, along with the best-fit simulations. The experimental spectra shown in parts (a) and (b) suffer from non-uniform excitation across the ~ 80 kHz breadth. An isotropic chemical shift tensor is assumed in the simulations shown. The effects of neglecting anisotropic magnetic shielding are more evident at 18.8 T (part (c)).

date. A comparable value, 5.027 MHz, has been determined for cocaine hydrochloride (*168*). Certainly NQR spectroscopy has been used to determine much larger quadrupolar coupling constants (*169*), e.g., $C_Q(^{35}Cl)$ in 1,2,4,5-tetrachloro-3,6-dinitrobenzene is 76.937 MHz (*270*) and $C_Q(^{35}Cl)$ in solid $Cl_2$ at 0 K is 108.975 MHz (*271*). A value of -145.87 MHz has been determined by molecular beam electric resonance spectroscopy

for the ground vibrational state of gaseous ClF (*266*). Large $C_Q$ values may also be determined indirectly by solid-state NMR methods. For example, residual spin-spin interactions between $^{35}Cl$ and $^{13}C$ in chloroketosulfones have been exploited to determine a $C_Q(^{35}Cl)$ of -73 MHz (*272*).

The chlorine isotropic chemical shifts for tris sarcosine calcium chloride and quinuclidine hydrochloride are identical within error, 8 - 14 ppm, but significantly different from those determined for L-tyrosine hydrochloride and the L-cysteine alkyl ester hydrochlorides. The neglect of anisotropy in the chlorine chemical shift tensor only becomes apparent in the spectra acquired at 18.8 T. For example, a span of 50 ppm was incorporated into the simulated spectrum of quinuclidine hydrochloride in order to achieve the best fit (Figure 3.14), although attempts at fitting this spectrum indicate that there is more than one solution. An isotropic chemical shift tensor was used in the simulated spectrum of tris sarcosine hydrochloride at 18.8 T (Figure 3.15c); deviations from the experimental spectrum which are clearly distinct from those arising due to non-uniform excitation of the powder pattern (*i.e.*, differences in the positions of the discontinuities rather than intensity differences) are apparent.

A single-crystal $^{35}Cl$ NMR study of tris sarcosine calcium chloride at 280 K (*151*) as well as an NQR study of a powder sample at 292 K (*273*) are available for comparison with the present high-field NMR results determined from a powder sample at ambient temperature (~ 296 K). No information concerning the chlorine CS tensor is reported in the two previous studies; the neglect of the CS interaction will introduce errors into the determination of $C_Q$. The single-crystal study reports $C_Q(^{35}Cl)$ as 4.10 MHz and $\eta_Q$ as

0.67, with errors in the tensor elements of less than 5 % (*151*). These values lie slightly outside the error limits on the values of 4.04 ± 0.03 MHz and 0.62 ± 0.02 determined herein, but nevertheless the agreement is quite good. The powder NQR study reports a quadrupolar frequency, $(e^2q_{ZZ}Q/2h)(1 + \eta_Q^2/3)^{1/2}$, of 2.160 MHz for $^{35}$Cl (*273*). To extract $C_Q$ (equivalent to $e^2q_{ZZ}Q/h$), one must make an assumption regarding the asymmetry parameter. Employing values ranging from 0.62 to 0.67 results in $C_Q(^{35}Cl)$ values of 4.067 to 4.029 MHz, in excellent agreement with the value obtained in the present work. One should be aware that temperature effects are likely to contribute to the slight discrepancies between the three studies. In fact, Erge *et al.* determined a temperature dependence of -0.75 kHz $K^{-1}$ in the range 120 - 260 K for the chlorine nuclear quadrupolar coupling constant in tris sarcosine calcium chloride (*151*).

#### 3.3.2.3 Chlorine NMR as a Probe of Hydrogen Bonding Environment

Based on the data reported herein, it is apparent that variations in the chlorine nuclear quadrupolar coupling constant are more easily measured than are variations in the chemical shift tensor. Nevertheless, the CS tensor may in fact be an equally sensitive probe of the chlorine environment. For example, McDermott and co-workers have illustrated the dependence of the carbon CS tensors in amino acids upon their protonation state (*274*), as well as the relationship between nitrogen CS tensors and hydrogen bonding in histidine and histidine-containing peptides (*275*).

Useful insights into the relative sensitivity of the chlorine chemical shift and EFG tensors to the local hydrogen bonding environment are afforded by *ab initio* calculations on a simple model system, $NH_4^+\cdots Cl^-$ (Figure 3.16). A series of calculations at the RHF/6-311++G** level has been carried out as a function of the nitrogen-chlorine separation (see Section 3.2.4 for details). In particular, the focus is on the span of the chlorine shift tensor and the nuclear quadrupolar coupling constant. Although the absolute values of these parameters are not significant due to the simplicity of the model system, instructive information may be obtained through the derivatives $\partial\sigma_{iso}(Cl)/\partial r$, $\partial\Omega(Cl)/\partial r$ and $\partial C_Q(^{35/37}Cl)/\partial r$, where $r$ is the nitrogen-chlorine separation. The slopes of the graphs shown in Figure 3.16 provide estimates of these derivatives near the equilibrium separation, $\partial\Omega(Cl)/\partial r = -111$ ppm Å$^{-1}$ and $\partial C_Q(^{35}Cl)/\partial r = -73$ MHz Å$^{-1}$. The calculations also indicate that $\partial\sigma_{iso}(Cl)/\partial r$ is 99 ppm Å$^{-1}$. A more in-depth computational study of the

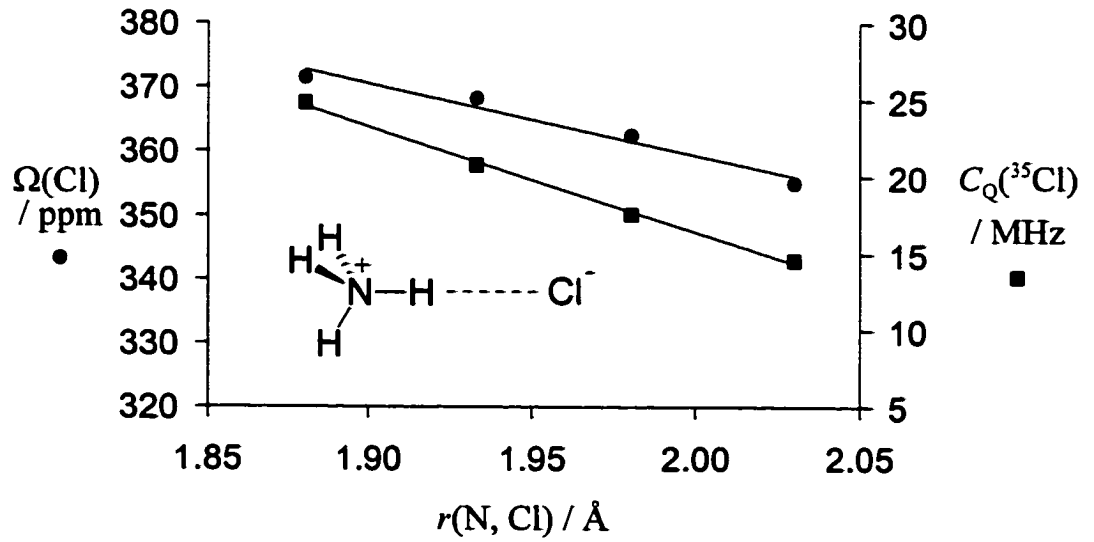


Figure 3.16: Ab initio chlorine chemical shift tensor spans (●) and $^{35}Cl$ quadrupolar coupling constants (■) for ammonium chloride as a function of the nitrogen-chlorine separation, $r$(N, Cl). Trendlines were determined by linear regression to have slopes of -111 ppm Å$^{-1}$ (span, ●) and -73 MHz Å$^{-1}$ ($C_Q(^{35}Cl)$, ■). The equilibrium value of $r$(N, Cl) is 1.933 Å.

nuclear quadrupolar coupling constants in $NH_4Cl$ has been provided by Halkier *et al.* (*276*).

Further information is gained by examining other simple model systems in the absence of hydrogen bonding. For example, calculations on $Na^+ \cdots Cl^-$ (RHF/6-311+G*) as a function of the sodium-chlorine distance indicate that for chlorine, $\partial\sigma_{iso}(Cl)/\partial r = 27$ ppm $Å^{-1}$, $\partial\Omega(Cl)/\partial r = -43$ ppm $Å^{-1}$, and $\partial C_Q(^{35}Cl)/\partial r = -23$ MHz $Å^{-1}$. The negative sign of $\partial C_Q(^{35}Cl)/\partial r$ for NaCl and the corresponding positive sign for $\partial V_{ZZ}(Cl)/\partial r$ (due to the negative $Q$ for $^{35}Cl$) are in agreement with higher-level calculations reported by Seth *et al.* (*277*). Finally, analogous calculations on a model perchlorate salt, $Na^+ \cdots ClO_4^-$, as a function of the sodium-chlorine separation, yield values of $\partial\sigma_{iso}(Cl)/\partial r = 0.07$ ppm $Å^{-1}$, $\partial\Omega(Cl)/\partial r = -28$ ppm $Å^{-1}$, and $\partial C_Q(^{35}Cl)/\partial r = 1.9$ MHz $Å^{-1}$. Based on these calculations, it appears that in the presence of a hydrogen bond, the EFG tensor is in fact more sensitive than $\sigma$ to changes in molecular and electronic structure around chlorine, e.g., for a change in $r$ of 1 Å in $NH_4^+ \cdots Cl^-$, the change in span represents just 7 % of the total chemical shift range while the change in $C_Q(^{35}Cl)$ represents nearly 50 % of the total range of known $^{35}Cl$ quadrupolar coupling constants! Notably, both derivatives for $NaClO_4$ are much smaller than for $NH_4Cl$. Recently, Chapman *et al.* have investigated some other NMR properties of N-H···Cl hydrogen bonds, e.g., the across hydrogen bond indirect nuclear spin-spin coupling constant, $^{2h}J_{iso}(^{35}Cl,^{15}N)$, in $NH_4Cl$ and pyridine hydrochloride using equation-of-motion coupled cluster singles and doubles (EOM-CCSD) calculations (*278*).

Halide ions represent some of the strongest hydrogen bond acceptors (*279*). Generally, a chloride ion is thought to have the ability to bind to a maximum of four strong donors, e.g., O-H and N-H donors (*279*, *280*). Beyond this, weaker donors such as C-H may play a role. Weak C-H···Cl interactions are found, for example, in quinuclidine hydrochloride (*172*). Presented in Figure 3.17 is a summary of chlorine quadrupolar coupling constants as a function of the total number of N-H···Cl, O-H···Cl, and S-H···Cl hydrogen bonds around the chloride ion in each of the compounds, as determined from

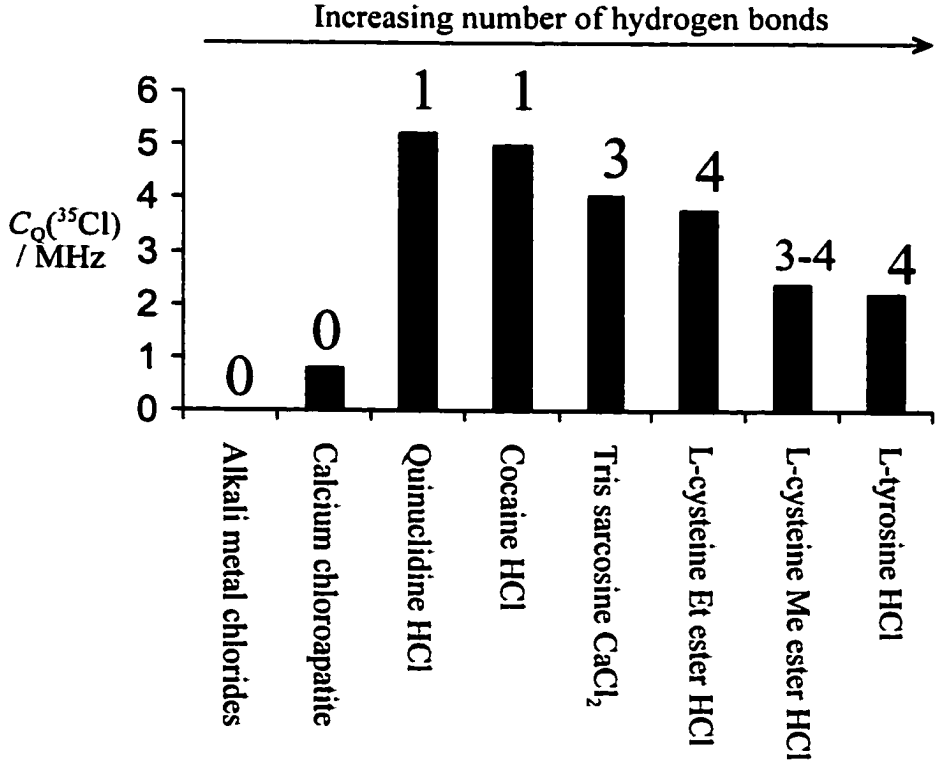


Figure 3.17: The variability in $^{35}Cl$ nuclear quadrupolar coupling constants as a function of the total number of N-H···Cl, O-H···Cl, and S-H···Cl hydrogen bonds to chlorine in a series of compounds containing chloride anions.

the crystal structures (*170*, *171*, *172*, *173*). The data shown indicate a possible trend: *as the number of hydrogen bonds to chlorine increases from one through four, the value of* $C_Q$ *decreases.* An isolated chloride anion should exhibit no EFG due to its spherical symmetry; similarly a chloride ion with no opportunities for hydrogen bonding may exhibit a very small quadrupolar coupling constant, e.g., $C_Q(^{35}Cl) = 0.8$ MHz for calcium chloroapatite (*168, 281*). As a single hydrogen bond is added, e.g., the case of quinuclidine hydrochloride, the symmetry is distorted and a large quadrupolar coupling constant results, 5.25 MHz. This is also the case for cocaine hydrochloride, where a single N-H···Cl hydrogen bond results in a value of $C_Q$ of 5.027 MHz (*168, 282*). The chloride anion in tris sarcosine hydrochloride possesses three hydrogen bonds to nitrogen atoms; this results in a reduced value of $C_Q$, 4.04 MHz.

The availability of X-ray crystal structures for the analogous compounds L-cysteine methyl ester hydrochloride and L-cysteine ethyl ester hydrochloride (*171*), in combination with the NMR data presented in Table 3.5, allows for a particularly insightful analysis of the effects of the local chlorine environment on the $^{35}Cl$ NMR parameters. The crystal structures of these two compounds are very similar, both crystallizing in the $P2_12_12_1$ space group, and both possessing three N-H···Cl bonds of comparable geometry. The only major difference reported in the structures of these compounds is the length of the S-H···Cl hydrogen bond. For the methyl ester, the authors conclude that there is no significant thiol-chloride hydrogen bond, whereas in the ethyl ester, a fairly strong interaction is deduced, based on the S-Cl internuclear distances. Interpretation of the observed chlorine quadrupolar coupling parameters for these

compounds in the context of the X-ray data suggests that the increased proximity of the thiol group is directly responsible for the *increase* in $C_Q$ from 2.36 to 3.79 MHz; this is in agreement with the negative values of $\partial C_Q(^{35}Cl)/\partial r$ reported above for $NH_4Cl$. Thus, the general trend shown in Figure 3.17 is not strictly obeyed for these two similar compounds. However, the asymmetry parameter changes quite drastically, from 0.03 in the ethyl ester, to 0.82 in the methyl ester, and may be a particularly useful parameter for comparison of the chloride sites in closely related compounds. Point charge models indicate that the EFG at a central nucleus in coordination complexes depends on the arrangement and number of the ligands; a similar dependence likely plays an important role in determining the chlorine EFG tensor for chloride ions involved in hydrogen bonding (*283*, *284*). Similarly, deuterium quadrupolar coupling constants in hydrogen bonded systems are known to be correlated with the hydrogen bond length and angle (*285*, *286*, *287*, *288*, *289*).

Neutron diffraction data are available for L-tyrosine hydrochloride (*170*). The availability of these type of data are extremely beneficial to NMR spectroscopists owing to the high precision to which hydrogen atom positions are reported. For example, the accurately-known structure of L-tyrosine hydrochloride has been used recently to establish a reliable method for measuring proton-carbon distances in high-speed MAS experiments (*290*, *291*). The availability of these data, including precisely known proton coordinates, have allowed a restricted-Hartree-Fock calculation of the chlorine CS and EFG tensors to be performed.

Fedotov *et al.* have performed DFT calculations of $^{35/37}$Cl NMR properties for some small chlorine-containing molecules (*292*). The system for which the present calculations have been carried out is shown in Figure 3.18a. This simplest unit incorporates the chloride anion and its four hydrogen bonding partners, *i.e.*, four distinct tyrosine units. Incorporation of all four of these units is essential to model the hydrogen bonding environment at chlorine. The results of the calculations, summarized in Table

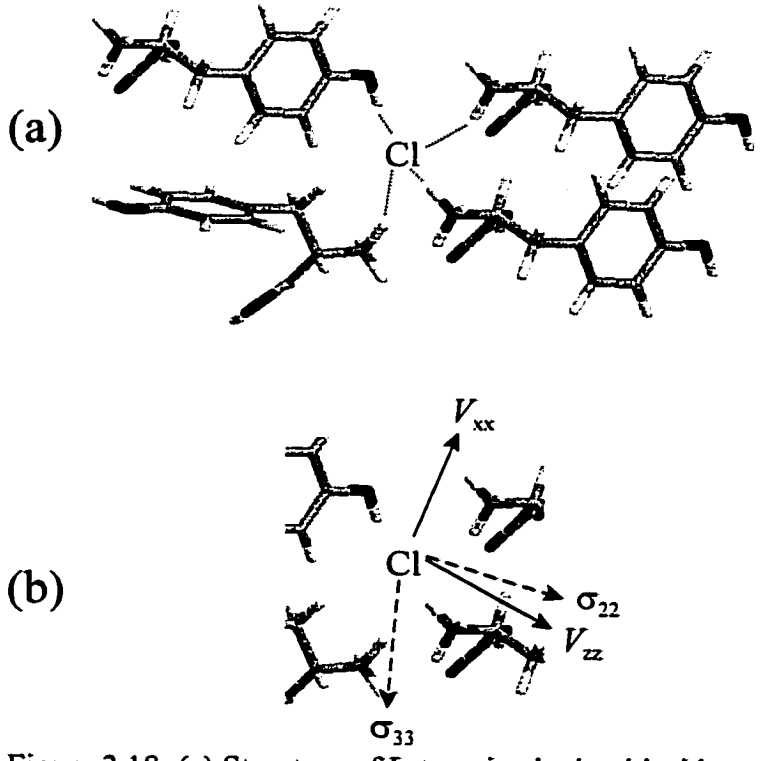


Figure 3.18: (a) Structure of L-tyrosine hydrochloride generated from neutron diffraction atomic coordinates. Each chloride anion is hydrogen bonded to four protons: one from an OH group and three from different $NH_3$ groups. (b) Detail of the structure shown in part (a), with only the atoms surrounding chlorine shown, for clarity. The calculated orientations of the chlorine nuclear magnetic shielding and electric field gradient tensors are indicated. The components shown all lie *approximately* in the plane of the page. $V_{yy}$ and $\sigma_{11}$ lie approximately perpendicular to the plane of the page.

3.6, are in good agreement with the experimental data for L-tyrosine hydrochloride.

The results of the second calculation, where the 6-311G basis set has been used on the OH and $NH_3$ groups in addition to the chloride anion, should be more reliable. The calculated quadrupolar coupling constant of 2.65 MHz is in reasonably good agreement with the experimental value of 2.23 ± 0.02 MHz. Perhaps more important is the fact that the calculated value falls well within the experimental range for chloride anions which have four hydrogen bonds (*i.e.*, ~ 2.2 - 3.8 MHz). The calculations also establish that $C_Q$ is positive; it is likely that this is true for all of the experimentally-determined quadrupolar coupling constants for chloride ions (Table 3.5). The Sternheimer antishielding effect (*293*), which modifies the EFG, is relatively large for the chloride ion ($(1 - \gamma_\infty) = 48$) (*294*); however, *ab initio* calculations take this effect into account and direct comparison between experimental and calculated values of $C_Q$ is appropriate (*139*, *295*).

Shown in Figure 3.18b are the calculated orientations of the nuclear magnetic shielding and EFG tensors for chlorine, with the indicated components lying approximately in the plane of the page. There is no obvious rationalization for the calculated orientation; for example, no component lies directly along one of the hydrogen bonds. Clearly further experimental and theoretical work will be required to determine the relationship between the tensor orientations and variations in hydrogen bonding environment. To obtain credible results, accurate knowledge of the hydrogen atom positions is imperative.

**Table 3.6**: Comparison of experimental and restricted Hartree-Fock $^{35}Cl$ NMR parameters for L-tyrosine hydrochloride

| basis set on Cl | basis set on OH, 3 x $NH_3$ | basis set on remaining atoms | $C_Q$ / MHz | $\eta_Q$ | $\sigma_{iso}$ / ppm | $\delta_{iso}$ / ppm | $\Omega$ / ppm | $\kappa$ |
|---|---|---|---|---|---|---|---|---|
| 6-311G | 3-21G | 3-21G | 2.95 | 0.77 | 990 | -16.3 | 84 | -0.27 |
| 6-311G | 6-311G | 3-21G | 2.68 | 0.59 | 985 | -11.4 | 69 | -0.10 |
| solid-state NMR | - | - | 2.23 ± 0.02 | 0.72 ± 0.03 | 926 | 48.3 ± 0.5 | < 150 | - |

Based on the data presented in Table 3.6, the span of the CS tensor is calculated to a reasonable accuracy, and the isotropic chemical shift falls in the approximate range known for chloride ions. The calculated isotropic chemical shifts are approximately 60 - 65 ppm less than the experimental value of 48.3 ppm. While such a discrepancy may seem large, especially given the small range of chemical shifts observed for the various compounds studied herein (~ 45 ppm), it is important to recognize that the total chlorine chemical shift range for diamagnetic compounds is nearly 1500 ppm. Thus, the 60 ppm difference between the calculated and experimental chemical shifts represents only 4 % of the possible shift range. Furthermore, gas-to-solid shifts are expected to be on this order of magnitude, e.g., the shift induced on going from HCl(g) to HCl dissolved in chloropentanes is 45 ppm (*232*).

### *3.3.3 Molybdenum*

#### 3.3.3.1 Molybdenum-95 NMR Spectroscopy

Shown in Figure 3.19 are $^{95}$Mo MAS spectra of mesitylenetricarbonyl-molybdenum(0), **I**, acquired on the 18.8 T magnet at spinning rates of 4 kHz and 11 kHz. The simulated spectra are based on the experimental parameters reported in Table 3.7.

**Table 3.7**: Summary of experimental and calculated molybdenum NMR parameters for mesitylenetricarbonylmolybdenum(0)[a].

| method | $C_Q(^{95}Mo)$ / MHz[b] | $\eta_Q$ | $\delta_{iso}$ / ppm | $\sigma_{iso}$ / ppm | $\Omega$ / ppm | $\kappa$ | ref. |
|---|---|---|---|---|---|---|---|
| Solid-state $^{95}$Mo NMR | (-)0.96 ± 0.15 | 0.30 ± 0.15 | -1885 ± 1 | - | 775 ± 30 | 0.87 ± 0.13 | this work |
| Solution dual-spin probe NMR | (-)1.0 | 0[c] | -1903 | - | - | - | 182 |
| Solution electric-field $^{95}$Mo NMR[d] | (-)0.954 ± 0.050 | (0)[c] | - | - | - | - | 183 |
| RHF | -0.17 | 0.06 | -391 | -168 | 133 | 0.83 | this work |
| non-relativistic DFT (B3LYP) | -0.13 | 0.06 | -460 | -99 | 85 | 0.85 | this work |
| ZORA-DFT | -1.55 | 0.34 | -1873 | 1314 | 740 | 0.58 | this work |

[a] The Euler angles relating the EFG and CS tensors used to simulate the experimental spectra are $\alpha = \beta = \gamma = 0°$.

[b] The negative sign for the experimental quadrupolar coupling constants is inferred from the ZORA-DFT value.

[c] Assumed $\eta_Q = 0$.

[d] Measurement made on mesitylene-$d_1$-tricarbonylmolybdenum(0).

The $^{95}$Mo quadrupolar coupling constant, ± (0.96 ± 0.15) MHz, is in good agreement with values which have been determined previously for **I** from solution studies via a dual-spin probe relaxation experiment, ± 1.0 MHz (*182*), and via a more precise electric-field NMR method, ± (0.954 ± 0.050) MHz (*183*). In the solution studies, a

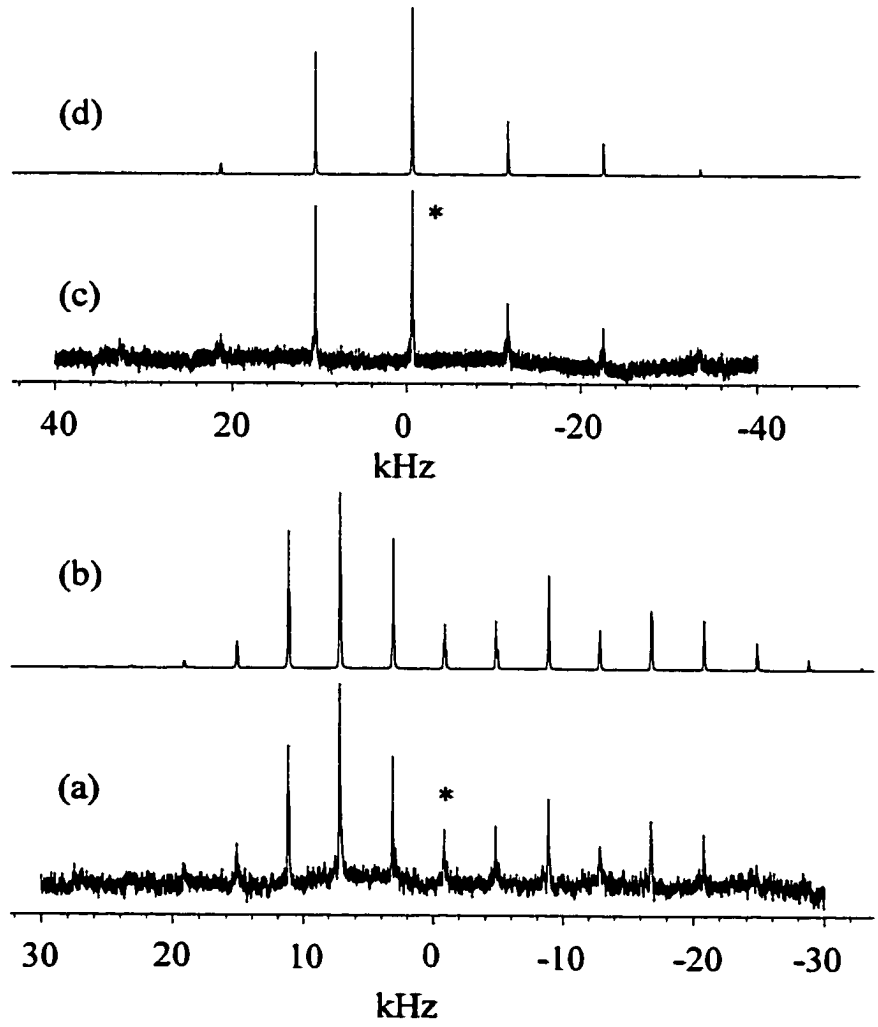


Figure 3.19: Molybdenum-95 central transition MAS NMR spectra of mesitylenetricarbonylmolybdenum(0) acquired at an external applied magnetic field strength of 18.8 T. In (a), an MAS rate of 4.000 kHz was used to acquire 2386 scans with a recycle delay of 30 s. In (c), an MAS rate of 11.000 kHz was used to acquire 2726 scans with a recycle delay of 30 s. Simulated spectra based on the parameters given in Table 3.7 are shown in (b) and (d). The centreband is denoted by an asterisk.

value of zero has been assumed for $\eta_Q$; in the solid state the value of $\eta_Q$ is $0.30 \pm 0.15$. This lack of axial symmetry of the EFG tensor arises from the fact that there is not a perfect $C_3$ axis for **I** in the solid state; molybdenum-carbon bond lengths and angles for the aromatic and carbonyl carbon atoms are all slightly different (*184*).

The solid-state isotropic molybdenum chemical shift, $-1885 \pm 1$ ppm, is approximately 20 ppm greater than the reported solution chemical shifts, -1907 ppm in $CH_2Cl_2$ (*296*) and -1903 ppm in $CDCl_3$ (*182*). Isotropic molybdenum solution chemical shifts for piano-stool complexes of the type (arene)$Mo(CO)_3$ are quite sensitive to substituent effects and generally fall in the range -1600 to -2000 ppm (*174*).

For a half-integer spin quadrupolar nucleus such as $^{95}Mo$, the quadrupolar interaction induces a second-order quadrupolar shift of the centre-of-gravity of the observed spectrum away from the true isotropic chemical shift (*32*, *297*), as discussed in Chapter 2 (see eq. 2.28). In the case of **I**, this second-order shift is -109 Hz or -2.1 ppm on the 18.8 T magnet. The shift is relatively small due to the low value of $C_Q(^{95}Mo)$ relative to the $^{95}Mo$ Larmor frequency. The inner satellite centreband is predicted to lie at +123 Hz (or +2.4 ppm) relative to the central transition centreband and the outer satellite centreband is predicted to lie at +493 Hz (or +9.5 ppm) relative to the central transition centreband. No signal from either of the satellite transitions is evident in the $^{95}Mo$ MAS spectra. This is not unexpected, as a "solid" $\pi/2$ pulse was used to selectively excite the central transition (see Chapter 2). Furthermore, the intensity of the satellite transitions would be distributed over a frequency range approximately 15 times larger than that of the central transition, thus making the satellite transitions more difficult to observe.

The most remarkable aspect of the spectra shown in Figure 3.19 is their close resemblance to a spinning sideband pattern typically observed for an isolated spin-1/2 nucleus with an approximately axially symmetric chemical shift tensor. This is the result of the relatively small value of the $^{95}$Mo quadrupolar coupling constant, and the substantial span of the molybdenum chemical shift tensor, which was determined to be 775 ± 30 ppm. The general appearance of the spectra shown in Figure 3.19 is therefore primarily a consequence of the chemical shift interaction rather than the quadrupolar interaction. Schurko *et al.* have presented static solid-state $^{27}$Al NMR spectra for $Cp^*_2Al$ ($Cp^*$ = pentamethylcyclopentadienide) which are the result of a small, axially symmetric ($\eta_Q = 0$) quadrupolar interaction and relatively large chemical shift anisotropy (*298*). Such spectra are not typically observed in the NMR of half-integer spin quadrupolar

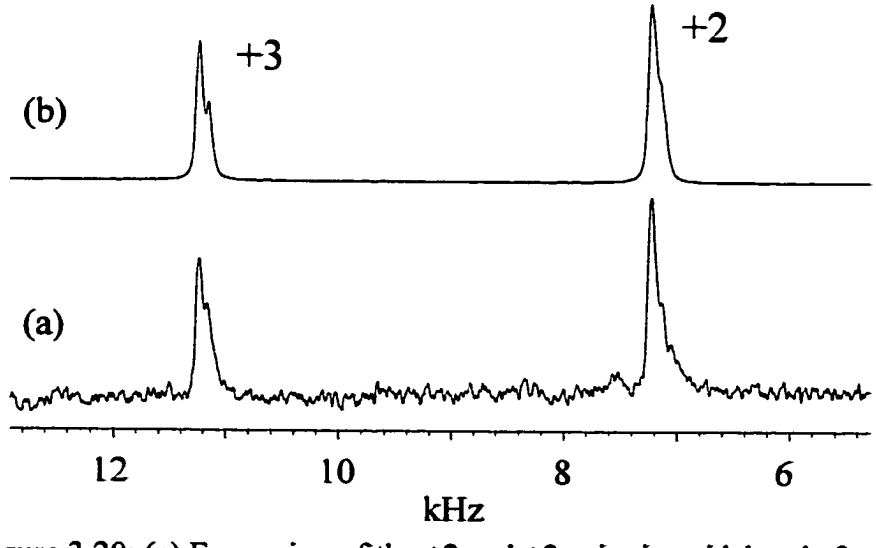


Figure 3.20: (a) Expansion of the +2 and +3 spinning sidebands from the $^{95}$Mo MAS NMR spectrum shown in Figure 3.19 ($B_0 = 18.8$ T; $\nu_{rot} = 4.000$ kHz). (b) Simulated spectrum based on the parameters given in Table 3.7. The fine structure in the spinning sidebands arises from the non-zero $^{95}$Mo quadrupolar interaction.

nuclei. More generally, the quadrupolar interaction will dominate the solid-state NMR spectra of quadrupolar nuclei, with the CS interaction acting as a minor contributor.

Whereas the anisotropic chemical shift interaction most strongly influences the spinning sideband pattern shown in Figure 3.19, the detailed lineshape exhibited by the centreband and each of the spinning sidebands depends intimately on the molybdenum quadrupolar interaction, *i.e.*, the values of $C_Q$ and $\eta_Q$. Shown in Figure 3.20 is an expansion of the +2 and +3 spinning sidebands of the 4 kHz $^{95}$Mo MAS spectrum. The asymmetry of the +2 sideband and the splitting of the +3 sideband are examples of the influence of the values of $C_Q$ and $\eta_Q$ on the spectrum. An expansion of the centreband of the $^{95}$Mo MAS NMR spectrum acquired at a spinning rate of 11 kHz is presented in Figure 3.21. The simulation further demonstrates the accuracy of the CS and EFG

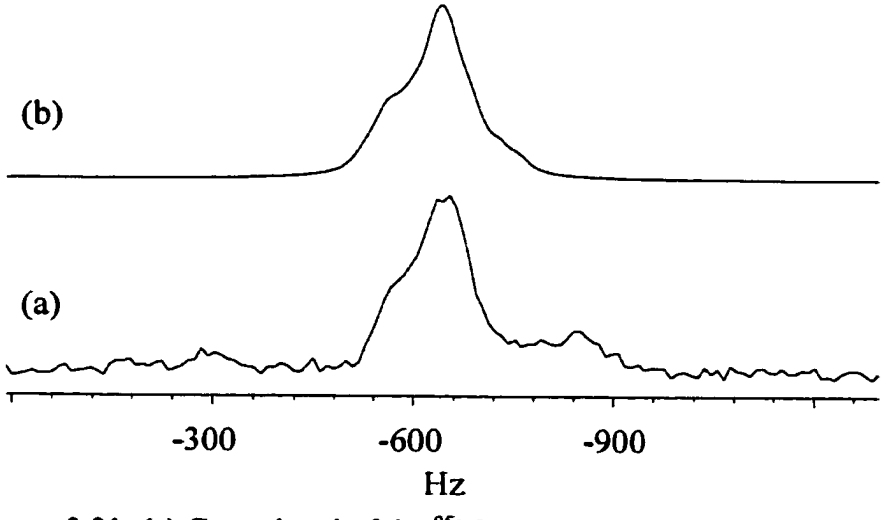


Figure 3.21: (a) Centreband of the $^{95}$Mo central transition MAS NMR spectrum of mesitylenetricarbonylmolybdenum(0) acquired at an external applied magnetic field strength of 18.8 T with an MAS rate of 11.000 kHz. A recycle delay of 30 s was used to acquire 2726 scans. (b) Simulation of spectrum shown in part (a), based on the parameters given in Table 3.7. The "bump" at -850 Hz is attributed to a trace impurity.

tensors parameters. A portion of the error reported for $C_Q$, ± 0.15 MHz, likely arises from the slightly different values of this parameter at MAS rates of 4 kHz and 11 kHz, due to frictional heating of the sample and the temperature dependence of $C_Q$. In refining the best-fit experimental parameters given in Table 3.7, the lineshapes of all spinning sidebands were examined in order to obtain a reliable fit.

Very small, or zero, quadrupolar coupling constants are expected on the basis of symmetry and point charge considerations for a quadrupolar nucleus at the centre of a tetrahedron or octahedron. For example, $C_Q(^{95}Mo)$ in solid hexacarbonylmolybdenum is 0.091 MHz (*175*). The fact that this hexacoordinate complex has a non-zero EFG tensor is a result of small deviations from perfect $O_h$ symmetry. Knop *et al.* have provided a detailed outline of other possible arrangements of point charges which give rise to zero electric field gradients (*179*, *180*). Akitt and McDonald revisited this topic and made specific reference to arene molybdenum tricarbonyls, for which the molybdenum is predicted to have a very small EFG (*181*). In addition to planarity of the arene ring, one of the key conditions which must be satisfied so that the EFG at Mo is zero or very small is that the molybdenum-carbonyl axis must form the magic angle, ~54.74°, with respect to the pseudo-$C_3$ symmetry axis of the molecule. In the present case, examination of the X-ray crystal structure of **I** shows that these three angles are 53.9°, 52.8°, and 54.3°, and that the six aromatic carbon atoms do not deviate from planarity by more than 0.009 Å (*184*). The measured $^{95}$Mo quadrupolar coupling constant, on the order of 1 MHz in the solid state and in solution, ostensibly results from a failure of the simple point-charge model as well as these small deviations from the required ideal geometry.

For comparison, $^{55}$Mn and $^{187}$Re quadrupolar coupling constants on the order of tens ($^{55}$Mn) to hundreds ($^{187}$Re) of megahertz have been determined by gas-phase microwave spectroscopic measurements on methylcyclopentadienyltricarbonylmanganese (*299*) and cyclopentadienyltricarbonylrhenium (*300*), and by nuclear quadrupole resonance spectroscopy at 77 K for a series of substituted cyclopentadienyl tricarbonyl manganese and rhenium complexes (*301*). These substantial values of $C_Q$ arise in large part due to the much larger values of the nuclear quadrupole moment for $^{55}$Mn and $^{187}$Re compared with $^{95}$Mo, but must also be partly due to deviations from the ideal geometry required for a small EFG at the central metal nucleus. For solid $C_5H_5Mn(CO)_3$, the angles between the Mn-CO bond and the pseudo-$C_3$ axis of the molecule are 56.1, 56.1, and 56.3 ° (*302*) and the observed $^{55}$Mn quadrupolar coupling constant is 65.20 MHz at 77 K (*301*). In the analogous rhenium complex, $C_5H_5Re(CO)_3$, angles of 52.7, 54.1, and 55.7° are formed in the solid state (*303*), and a $^{187}$Re quadrupolar coupling constant of 586.64 MHz is observed (*301*). In the case of **I** as well as the rhenium and manganese piano-stool complexes, the angles between the central metal nucleus, the centroid of the aromatic ring, and any of the aromatic carbon atoms is almost exactly 90°, thereby suggesting that the positions of the carbonyl groups are responsible for producing a sizable EFG at the metal nucleus in these cases.

Quadrupolar nuclei generally relax via the quadrupolar mechanism, *i.e.*, the interaction of the nuclear quadrupole moment with fluctuating electric field gradients at the nucleus. Brownlee *et al.* have measured the $^{95}$Mo spin-lattice relaxation time constant, $T_1$, at 4.7 T for a 0.5 M solution of **I** in $CDCl_3$ at 20°C to be 70.1 ms (*182*, *304*).

Presently, the possibility of relaxation in solution by the chemical shift anisotropy (CSA) mechanism has been investigated, given the relatively small value of $C_Q(^{95}Mo)$ and the relatively anisotropic molybdenum CS tensor. If relaxation by CSA were dominant, one would expect an inverse scaling of $T_1(^{95}Mo)$ with the square of $B_0$,

$$T_1^{-1}(\text{CSA}) = \frac{2}{15}\gamma^2 B_0^2 (\Delta\sigma)^2 \tau_c \quad , \qquad [3.3]$$

and $T_1(^{95}Mo)$ would be approximately 4.4 ms at 18.8 T. Here, $\Delta\sigma$ is a representation of the anisotropy of the CS tensor and $\tau_c$ is the rotational correlation time of the molecule. Measurements on a 0.5 M solution of **I** in $CDCl_3$ at 18.8 T produced a value of 66 ms for $T_1(^{95}Mo)$, which is within 6 % of the value reported at 4.7 T. Thus, while chemical shift anisotropy clearly dominates the *appearance* of the central transition $^{95}Mo$ MAS NMR spectrum at 18.8 T, the quadrupolar mechanism dominates the *relaxation* of the molybdenum nuclei as would be expected typically for a quadrupolar nucleus.

### 3.3.3.2 ZORA-DFT Calculations of $^{95}Mo$ NMR Interaction Tensors

Not surprisingly, the results of restricted Hartree-Fock (RHF) and non-relativistic DFT calculations of the $^{95}Mo$ EFG and CS tensors do not reproduce the experimental data (Table 3.7). In addition to being non-relativistic, these calculations employ an effective core potential on molybdenum. The shortcomings of these calculations are exemplified in the molybdenum CS tensor results, *i.e.*, the RHF calculated span of 133 ppm is only 17 % of the experimental value. The calculated values for the isotropic chemical shift, quadrupolar coupling constant, and quadrupolar asymmetry parameter are similarly poor.

Relativistic ZORA-DFT calculations of the $^{95}$Mo EFG and CS tensors are also presented in Table 3.7. These calculations were performed using the triple-zeta quality ZORA V basis set with polarization functions. The very good agreement obtained with all of the experimental parameters is exemplified, for example, by the span of the chemical shift tensor which is calculated as 740 ppm. This result is close to the experimental value of 775 ± 30 ppm. The calculations also indicate that the sign of $C_Q$ is negative. Overall, the improvement obtained upon including relativistic effects in the calculations of the molybdenum NMR parameters is dramatic; however one must also be aware of the fact that different basis sets were used to describe molybdenum in the non-relativistic and relativistic calculations.

Experimentally, it was found that the $^{95}$Mo NMR spectra could be successfully simulated with coincident CS and EFG tensors, *i.e.*, where $\delta_{33}$ and $V_{ZZ}$ are collinear and $\delta_{11}$ and $V_{XX}$ are collinear. The Euler angles which represent this relative orientation of the tensors, $\alpha = \beta = \gamma = 0°$, are used in the simulated spectra in Figures 3.19 - 3.21. The ZORA-DFT calculations, however, indicate an angle of 26° between $\delta_{33}$ and $V_{ZZ}$, as shown in Figure 3.22. While it is difficult to place error limits on the angles $\alpha$ and $\gamma$, spectral simulations indicate that experimentally, the angle $\beta$ between $\delta_{33}$ and $V_{ZZ}$ is 0° ± 10°, with 0° providing the best fit. If mesitylenetricarbonylmolybdenum(0) were perfectly $C_{3v}$ symmetric, $\delta_{33}$ and $V_{ZZ}$ would lie along the $C_3$ axis. If an approximate $C_3$ axis which passes through the molybdenum nucleus and the centroid of the aromatic ring is considered, the calculations place $V_{ZZ}$ at an angle of 168° with respect to the axis, and

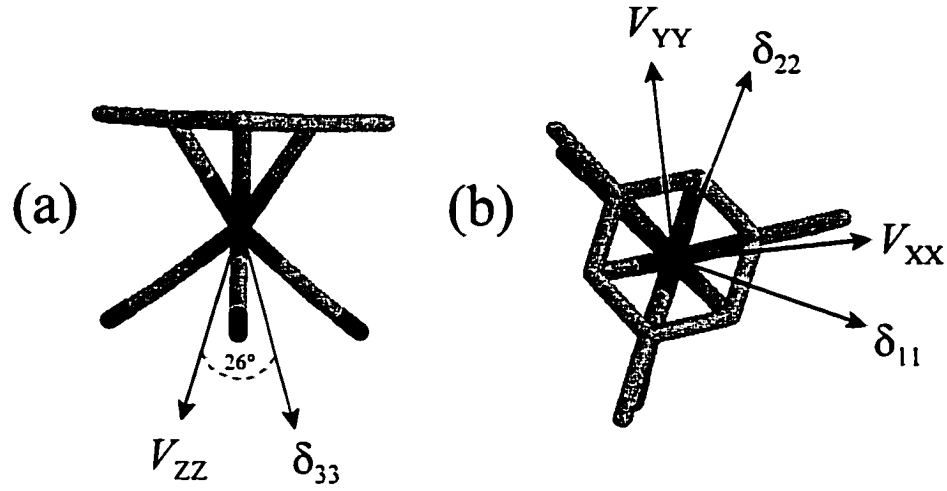


Figure 3.22: ZORA-DFT calculated orientations of the molybdenum CS and EFG tensors for **I** in the molecular frame of reference. Hydrogen atoms have been omitted for clarity. (a) Side view showing $V_{ZZ}$ and $\delta_{33}$ which lie approximately along the pseudo-$C_3$ axis of symmetry of the molecule. (b) Top view showing the remaining components of the molybdenum CS and EFG tensors. These components lie approximately in the plane of the page, with $V_{ZZ}$ and $\delta_{33}$ lying approximately perpendicular to the plane of the page. Experimentally, the EFG and CS tensors are coincident, with $V_{ZZ}$ and $\delta_{33}$ lying along the pseudo-$C_3$ axis.

$\delta_{33}$ at an angle of 166° with respect to the axis.

### 3.3.3.3 Interpretation of the molybdenum chemical shift tensor

The ZORA-DFT calculations provide some insight into the cause for the large chemical shift anisotropy observed for molybdenum in **I**. As discussed in Chapter 2, the nuclear magnetic shielding tensor may be considered as the sum of diamagnetic and paramagnetic parts. Contributions to the paramagnetic shielding are due to magnetic-dipole allowed mixing of occupied and virtual orbitals of appropriate symmetry. Furthermore, the relative importance of a contribution to the paramagnetic shielding from any given pair of occupied and virtual orbitals depends on the inverse of the energy gap

between them, and on there being large contributions to these MOs from the AOs on the nucleus of interest.

Schreckenbach has discussed the deshielding of the $^{57}Fe$ resonance in ferrocene in terms of relevant occupied and virtual MOs, and found that the dominant contributions arise solely from MOs which are largely composed of the metal *d* orbitals (*305*). The molybdenum chemical shifts for various compounds of the type $Mo(CO)_5PR_3$ (*306*) and $Mo(NH)_2X_2$ (*307*) have also been rationalized in terms of appropriate mixing of occupied and virtual molybdenum *d* orbitals. The role of *d* orbitals in determining transition metal nuclear magnetic shielding tensors has also been discussed more generally for $d^6$ octahedral and $d^8$ square planar complexes (*25*, *308*).

In the present case, the HOMO, HOMO-1, and HOMO-2 of **I** are all composed primarily of *d* AO contributions from Mo. This ZORA-DFT result is in agreement with the simple MO picture for a $d^6$ piano-stool complex (*309*). Examination of the LCAO coefficients for the three highest-energy occupied orbitals shows that they are primarily combinations of *d* orbitals rather than predominantly one type of *d* orbital. For example, the HOMO has a 32 % contribution from the $d_{z^2}$ orbital, 10 % from the $d_{x^2-y^2}$ orbital, and approximately 4 % from each of the $d_{xy}$ and $d_{xz}$ orbitals. There are a number of low-lying virtual MOs which have significant contributions from Mo *d* orbitals. In rationalizing the deshielding of the Mo nucleus in the xy-plane perpendicular to the pseudo-$C_3$ axis (z axis) of **I**, one must consider rotations of the occupied orbitals (HOMO, HOMO-1, HOMO-2) about either the x or y axis such that the resultant orbital overlaps favourably with a low-lying virtual orbital at Mo. Two such examples are presented in Figure 3.23.

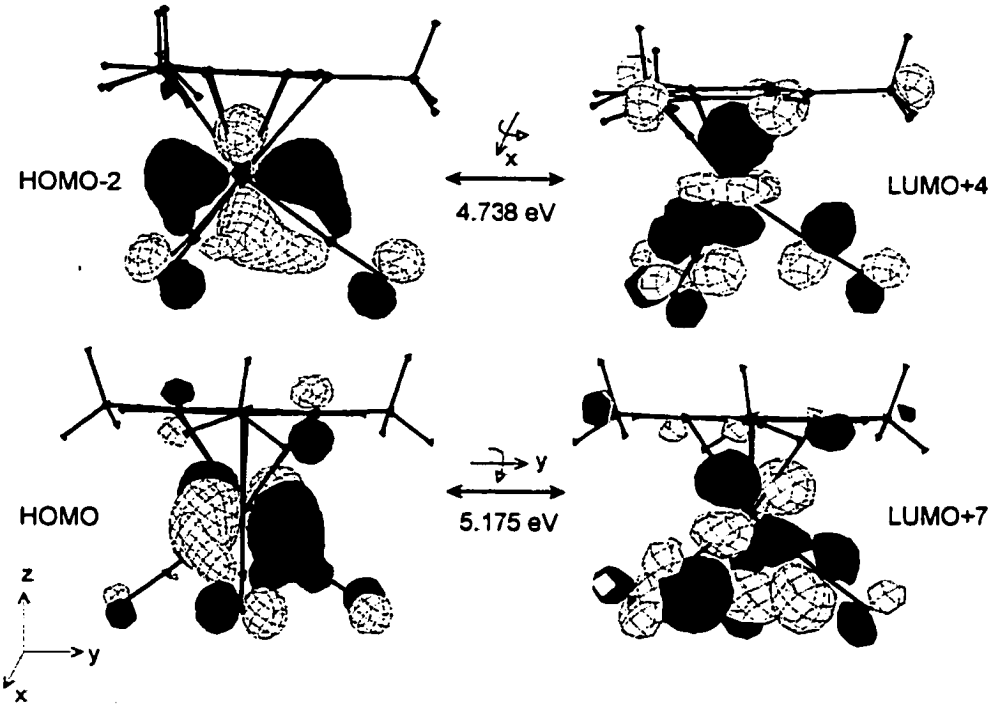


Figure 3.23: Selected molecular orbitals which contribute to the strong deshielding of the molybdenum nucleus observed perpendicular to the pseudo-$C_3$ axis of **1** (the xy plane). In order for deshielding to be observed in the xy plane, there must be symmetry-allowed mixing about the x and y axes of molybdenum-based occupied orbitals into molybdenum-based virtual orbitals. For example, mixing of the HOMO-2 orbital about the x axis at Mo results in favourable overlap with LUMO+4 at Mo. Similarly, rotation of the HOMO about the y axis at Mo results in favourable overlap with LUMO+7 at Mo. Energy gaps between the relevant orbitals are shown. Note that the axis system is for convenience of discussion and does not define the molybdenum *d* orbital axis system.

The HOMO-2 may be rotated about the x-axis to overlap favourably with the LUMO+4, and similarly the HOMO may be rotated about the y axis to overlap favourably with the LUMO+7. Other low-lying virtual orbitals with strong contributions from the molybdenum *d* orbitals, e.g., LUMO+3, LUMO+8, will also mix appropriately with the high-energy occupied orbitals to contribute to the deshielding of Mo in the xy plane; however, the LUMO and LUMO+1 have very small contributions from the Mo *d* orbitals.

In summary, mixing of the three highest occupied MOs with low-lying *d* orbital-dominated virtual orbitals produces a deshielding of Mo in the xy plane. This deshielding results in a particularly large span for the Mo CS tensor, since the shielding along the $C_3$ axis (z axis) is not affected by the rotations discussed above. Large chemical shift anisotropies are expected to be characteristic of other $d^6$ transition metal nuclei in piano-stool complexes, e.g., the $^{53}Cr$ nucleus in benzenetricarbonyl-chromium(0). The observation of a $^{55}Mn$ spin-rotation tensor with components on the order of 5 kHz in tricarbonyl(methylcyclopentadienyl)manganese (*299*) alludes to the existence of a sizable anisotropy in the manganese CS tensor, given the relationship between spin-rotation constants and nuclear magnetic shielding tensors (*23*, *310*, *311*).

### *3.3.4 Chromium*

Chromium-53 solid-state NMR results are summarized in Table 3.8.

#### 3.3.4.1 Hexacarbonylchromium(0)

The group 6 metal hexacarbonyl compounds, $Cr(CO)_6$, $Mo(CO)_6$, and $W(CO)_6$ are known to be isomorphous and crystallize in the space group *Pnma* (*230*, *312*, *313*, *314*). Oldfield *et al.* have presented a $^{13}C$ and $^{17}O$ solid-state NMR study of these three compounds (*315*). The structures possess a crystallographic mirror plane in which the central metal atom and two of the carbonyl moieties lie. For $Cr(CO)_6$, the chromium-carbon bond lengths vary over a small range, 1.9105 to 1.9185 Å, and bond angles are within 0.9°of the perfect octahedral angles of 90° and 180°(*209*). Such small, but significant, deviations from perfect octahedral symmetry in the solid state will in

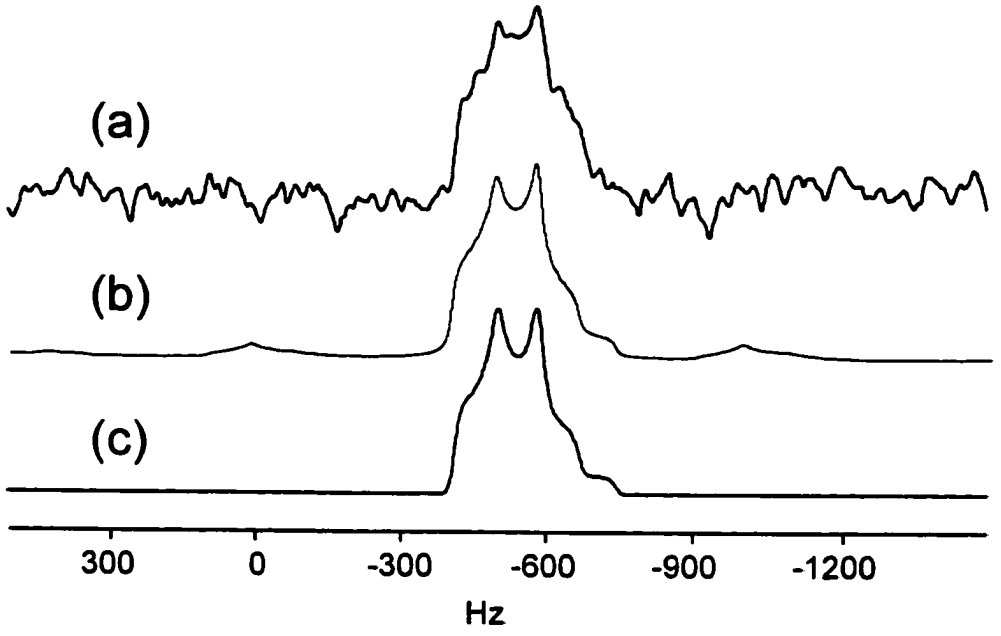


Figure 3.24: (a) Experimental $^{53}Cr$ MAS NMR spectrum of solid $Cr(CO)_6$ acquired using a pulse-acquire sequence ($\pi/2 = 6.0$ μs) with the transmitter set at 22.576 MHz ($B_0 = 9.4$ T). A recycle delay of 5.0 s was used to acquire 8549 scans with $\nu_{rot} = 500$ Hz. Also shown are the simulated spectra based on the parameters given in Table 3.8 and (b) using $\nu_{rot} = 500$ Hz and (c) assuming an infinite MAS rate.

principle result in a non-zero EFG tensor and asymmetry parameter for the metal nucleus.

The manifestation of these small structural distortions in solid powdered hexacarbonylchromium(0) is evident in the central transition portion of its $^{53}Cr$ MAS NMR spectrum (Figure 3.24), from which information about the chromium EFG tensor may be extracted (Table 3.8). A typical second-order quadrupolar powder pattern is observed (*316*, *317*). Under MAS conditions, sublimation of the sample was a significant problem, creating enough pressure to repeatedly displace the cap from the rotor. A low MAS rate, 500 Hz, was used to minimize sample heating; this was sufficient to almost completely concentrate all intensity from the spinning sidebands into the centreband, as evidenced by the small difference in the simulated spectra presented in Figure 3.24(b)

($\nu_{rot}$ = 500 Hz) and 1(c) ($\nu_{rot} = \infty$). Nevertheless, the relative intensities of the two main singularities of the second-order powder pattern are most successfully simulated when the finite spinning rate is considered. The $^{53}$Cr quadrupolar coupling constant is 348 kHz, a factor of 1.75 less than the result one obtains by multiplying the known $^{95}$Mo quadrupolar coupling constant for $Mo(CO)_6$ (89.3 kHz (*318*)) by the ratio of the $^{53}$Cr and $^{95}$Mo quadrupole moments (*139*) (-0.15 barn / -0.022 barn = 6.8). Although $Mo(CO)_6$ and $Cr(CO)_6$ are isomorphous, differences in the metal-carbon bond lengths between the two compounds are on the order of 0.15 Å; thus, significant differences are to be expected in the magnitude of the components of the EFG tensor at the metal nucleus. The $^{53}$Cr quadrupolar asymmetry parameter, 0.48, is substantially different from the corresponding $^{95}$Mo values reported for $Mo(CO)_6$ from powder (0.142 (*175*)) and single-crystal (0.151 (*318*)) $^{95}$Mo NMR measurements (see Table 3.8).

A $^{53}$Cr quadrupolar coupling constant of 356 kHz has been inferred from $T_1(^{53}Cr)$ measurements on $Cr(CO)_6$ dissolved in $CDCl_3$ at 40°C (*319*); this method relies on the assumption that the quadrupolar asymmetry parameter, $\eta_Q$, is exactly zero. The close correspondence between the solution and solid-state $^{53}$Cr quadrupolar coupling constants is fortuitous; the origins of a non-zero EFG tensor for a formally octahedral molecule in solution are likely due to intermolecular solvation effects rather than the structural deviations present in the solid.

**Table 3.8**: Summary of $^{53}Cr$ NMR parameters and comparison with $^{95}Mo$ NMR data for analogous molybdenum compounds

| compound | nucleus | $C_Q$ / MHz | $\eta_Q$ | $\delta_{iso}$ / ppm | $\Omega$ / ppm | $\kappa$ | Euler Angles ($\alpha$, $\beta$, $\gamma$)[a] |
|---|---|---|---|---|---|---|---|
| $Cr(CO)_6$ [b] | $^{53}Cr$ | 0.348 ± 0.008 | 0.48 ± 0.02 | -17 ± 1 | 23 ± 2 | 0.00 ± 0.05 | 100 ± 10°, 90 ± 5°, 55 ± 7° |
| $Mo(CO)_6$ | $^{95}Mo$ | 0.091 | 0.142 | -1854 ± 1 | 22 ± 2 | -0.09 | 90°, 90°, 50° [c] |
| | | 0.0893 ± 0.0002 | 0.151 ± 0.005 | -1854 ± 1 | 23 ± 0.4 | -0.026 | 90.7±0.6°,90.4±0.3°,49.6±0.8° [d] |
| $Cs_2CrO_4$ [b] | $^{53}Cr$ | 1.17 ± 0.05 | 0.00 | 1775 ± 3 | 90 ± 30 | 0.7 ± 0.3 | $\alpha$[e], 40 ± 10°, 0 ± 30° |
| $K_2CrO_4$ [b] | $^{53}Cr$ | 1.77 ± 0.05 | 0.39 ± 0.10 | 1765 ± 3 | 30 ± 10 | 0.00 | -40 ± 10°, 80 ± 5°, 0 ± 10° |
| $Na_2MoO_4 \cdot 2H_2O$ [c] | $^{95}Mo$ | 1.15 | 0.82 | 8 | ~ 200 | - | - |

[a] Euler angles define the rotations required to bring the electric field gradient tensor frame into coincidence with the principal axis system of the chemical shift tensor.

[b] This work

[c] Reference *175*.

[d] Reference *318*.

[e] The simulated spectrum is insensitive to the value of $\alpha$.

Although the $^{53}Cr$ and $^{95}Mo$ quadrupolar parameters are considerably different, analysis of the $^{53}Cr$ NMR spectrum of a stationary sample of $Cr(CO)_6$ (Figure 3.25) indicates that their respective chemical shift tensors are remarkably similar. The span of the chromium chemical shift tensor in $Cr(CO)_6$ is 23 ppm, which is *identical* to the span of the molybdenum chemical shift tensor in $Mo(CO)_6$ (*175*, *318*). The principal components of the chromium chemical shift tensor relative to a saturated solution of $Cr(CO)_6$ in chloroform are $\delta_{11}$ = -5.5 ppm, $\delta_{22}$ = -17.0 ppm, and $\delta_{33}$ = -28.5 ppm. Furthermore, the relative orientations of the metal CS and EFG tensors in the two

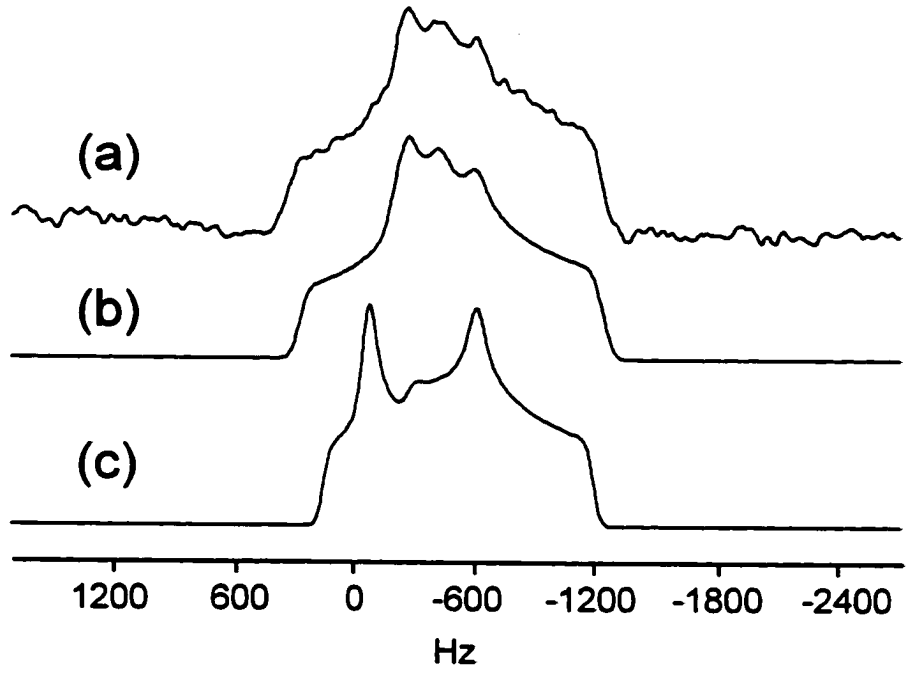


Figure 3.25: (a) Experimental $^{53}Cr$ NMR spectrum of solid $Cr(CO)_6$ acquired under stationary conditions using a pulse-acquire sequence ($\pi/2 \approx 5.0$ μs) with the transmitter set at 16.934 MHz ($B_0$ = 7.05 T). A recycle delay of 10.0 s was used to acquire 13122 scans (total experiment time 36.5 hours). Spectrum (b) is the best-fit simulation, incorporating an anisotropic chemical shift tensor, $\Omega$ = 23 ppm. The simulation shown in (c) is based solely on the quadrupolar interaction and assumes an isotropic chemical shift tensor.

hexacarbonyl compounds are *identical* within error. Simulation of the spectrum of a stationary sample of $Cr(CO)_6$ shown in Figure 3.25(a) is very sensitive to the magnitude and orientation of the chromium chemical shift tensor. For example, neglect of anisotropy in the CS tensor results in the simulated spectrum shown in Figure 3.25(c), which is clearly in disagreement with the experimental result shown in Figure 3.25(a).

While it is not possible to determine the absolute orientation of either the $^{53}Cr$ EFG or CS tensor based solely on the powder techniques used here, the absolute orientations of the $^{95}Mo$ NMR interaction tensors in the molecular framework are known for $Mo(CO)_6$ from the single-crystal study of Vosegaard and co-workers (*318*). Given the isomorphism of $Cr(CO)_6$ and $Mo(CO)_6$, one may reasonably conclude that the absolute orientations of the $^{53}Cr$ EFG and CS tensors in $Cr(CO)_6$ correspond to those found for $^{95}Mo$ in $Mo(CO)_6$, where the smallest component of the chemical shift tensor ($\delta_{33}$) and the intermediate component of the EFG tensor ($V_{YY}$) lie perpendicular to the mirror plane

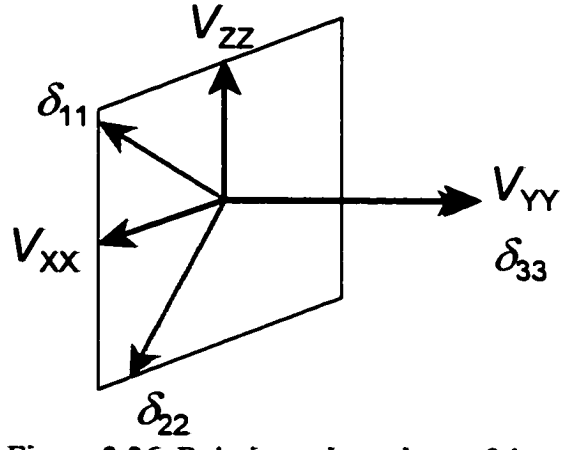


Figure 3.26: Relative orientations of the chromium EFG and CS tensors for chromium hexacarbonyl, determined from simulations of stationary $^{53}Cr$ NMR spectra.

defined by the *Pnma* space group symmetry (Figure 3.26).

Whereas the $^{53}Cr$ and $^{95}Mo$ EFG tensors in $Cr(CO)_6$ and $Mo(CO)_6$ reflect the small but significant structural differences between the two compounds (e.g., metal-carbon bond lengths), the remarkable correspondence of the chromium and molybdenum chemical shift tensors in their respective hexacarbonyl complexes is a testament to the sensitivity of the CS tensor to the overall crystal symmetry defined by the crystallographic space group.

3.3.4.2 Chromate(VI) Salts

Simulation of the $^{53}Cr$ NMR spectra of stationary samples of cesium chromate, $Cs_2CrO_4$ (not shown), and potassium chromate, $K_2CrO_4$ (Figure 3.27), allows for the extraction of the isotropic chemical shift and quadrupolar coupling parameters (Table

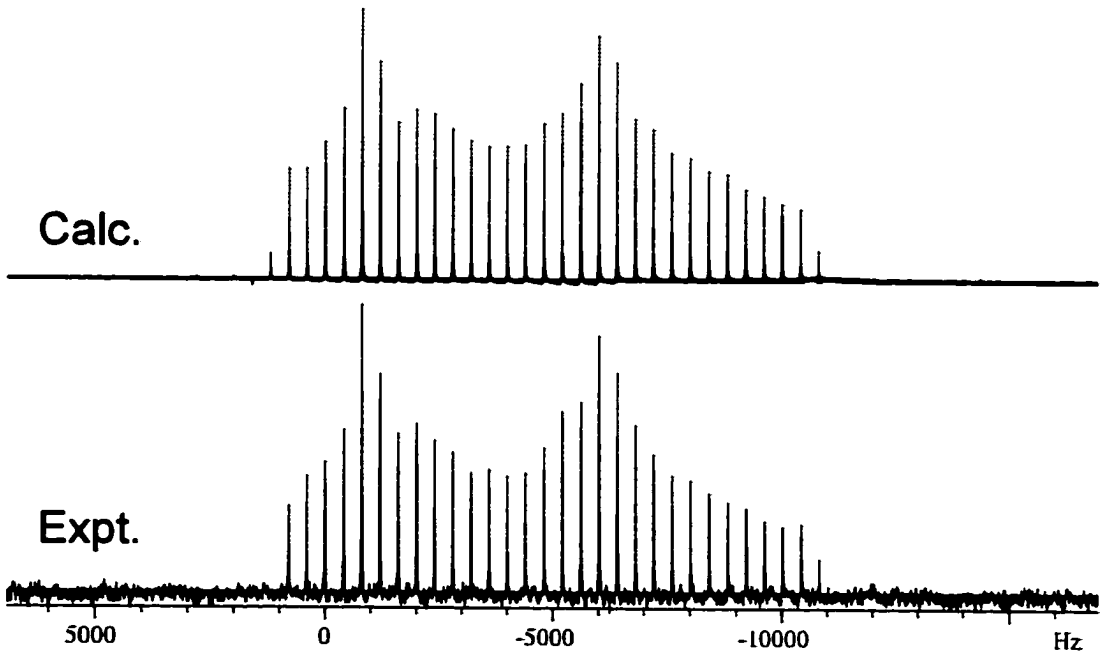


Figure 3.27: Chromium-53 solid-state NMR spectrum of a stationary sample of powdered potassium chromate, obtained at 18.8 T using the QCPMG pulse sequence. Also shown is the best-fit simulation.

3.8). For both of these chromate salts, quantitative determinations of the chemical shift tensor parameters were difficult due to the relatively small magnitude of the chromium shielding interaction. In the case of cesium chromate, the principal components of the chromium chemical shift tensor are $\delta_{11}$ = 1809.5 ppm, $\delta_{22}$ = 1796.0 ppm, and $\delta_{33}$ = 1719.5 ppm relative to $Cr(CO)_6$ in $CHCl_3$, and its orientation relative to the EFG tensor is given in Table 3.8. A span of 30 ± 10 ppm for the chromium CS tensor in potassium chromate was obtained from simulations of stationary spectra acquired at 9.4 and 18.8 T. Simulation of the $^{53}Cr$ QCPMG NMR spectrum in particular (Figure 3.27) was very sensitive to small changes in the magnitude and orientation of the chromium chemical shift tensor. The isotropic chromium chemical shifts of chromate salts are known from solution studies to be on the order of 1800 ppm larger than in chromium(0) complexes such as $Cr(CO)_6$ (*193, 194*). The same is found in the solid state, with $Cs_2CrO_4$ being 1793 ppm less shielded than $Cr(CO)_6$. A similar shift difference is found for the analogous molybdenum compounds, e.g., $Cs_2MoO_4$ is 1832 ppm less shielded than $Mo(CO)_6$ (*320*).

In agreement with $^{95}Mo$ data on hexacarbonylmolybdenum(0) and sodium molybdate(VI) dihydrate (see Table 3.8), the $^{53}Cr$ quadrupolar coupling constants are several times larger in the tetrahedral anions than in the octahedral complexes. However, the $^{53}Cr$ quadrupolar coupling constants in solid $K_2CrO_4$ (1.75 MHz) and $Cs_2CrO_4$ (1.17 MHz) differ substantially with data derived from $T_1(^{53}Cr)$ measurements carried out in solution. For example, employing a $T_1$ value extrapolated to infinite dilution, Haid *et al.* report $C_Q(^{53}Cr)$ to be 750 kHz for aqueous $K_2CrO_4$ (*321*). The non-zero value in solution

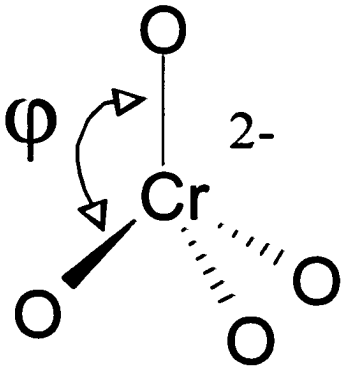


Figure 3.28: Distortion of
the chromate tetrahedron.

likely arises from solvation effects whereas the principal cause of the large $C_Q$ values in the solid state is due to forced distortion of the chromate tetrahedron in the crystal lattice. For example, in the solid state it is noted that upon changing the chromate counterion from cesium to potassium, an increase in the $^{53}Cr$ quadrupolar coupling constant of 50 % results. Furthermore, preliminary results on solid ammonium chromate indicate a quadrupolar coupling constant on the order of 2.5 MHz, over twice as large as that for cesium chromate. Consideration of the X-ray structures of $K_2CrO_4$ (*210*) and $(NH_4)_2CrO_4$ (*211*) and the neutron diffraction structure of $Cs_2CrO_4$ (*212*) suggests that deviation of the O-Cr-O bond angle, φ, from the perfect tetrahedral angle of 109.47° may be correlated with the observed $^{53}Cr$ quadrupolar coupling constants. The largest deviations for each of these compounds are 0.53° (Cs), 0.77° (K), and 2.43°($NH_4$) (Figure 3.28). The increasing trend in bond angle deviation, Cs < K < $NH_4$ clearly parallels the observed increase in the $^{53}Cr$ quadrupolar coupling constants, 1.17 < 1.75 < ~2.5 MHz. Unquestionably, the $^{53}Cr$ quadrupolar coupling constant in solid chromate salts is an extremely sensitive probe of

small deviations from perfect tetrahedral symmetry of the chromate anion.

The question arises as to why the report of $^{53}Cr$ solid-state NMR spectra for prototypal chromium compounds has taken so long. Previous attempts may have been thwarted by an unfortunate choice of compound or recycle delay. As pointed out by Smith (*84*), relaxation times for quadrupolar nuclei with large quadrupole moments are not guaranteed to be short (e.g, milliseconds or less); recycle delays on the order of several seconds have indeed been necessary in the case of $^{53}Cr$ and $^{95}Mo$. For example, the $T_1(^{95}Mo)$ in hexacarbonylmolybdenum(0) is 15.9 s (*318*). Applications of $^{53}Cr$ NMR are limited to relatively symmetric species due to the large quadrupole moment of this nucleus; however, the advent of "ultra-high" field spectrometers, e.g., 18.8 T and 21.1 T, will result in much improved $^{53}Cr$ NMR sensitivity, thereby allowing for the study of a wider range of compounds. Cross-polarization from $^{1}H$ in compounds where protons are present will undoubtedly benefit future $^{53}Cr$ solid-state NMR studies; CP to $^{95}Mo$ has already been shown to be beneficial (*76*). Lipton *et al.* have recently presented a general strategy for the NMR observation of spin-*n*/2 quadrupolar nuclei in dilute environments (*322*) which will certainly be valuable in future $^{53}Cr$ solid-state NMR studies.

## 3.4 Conclusions

The work presented in this chapter has demonstrated the feasibility and utility of studying several traditionally "difficult" spin-n/2 quadrupolar nuclei in the solid state. While much emphasis in the NMR community has been placed on the acquisition of "high-resolution" solid-state NMR spectra of quadrupolar nuclei in recent years, the results described herein clearly attest to the advantages of analyzing broad-line NMR spectra of stationary samples, where the magnitudes and orientations of both the EFG and CS tensors are accessible; these are exactly the parameters which are so intimately related to the local molecular and electronic structure surrounding a given nucleus. The interplay between experiment and theory when relating NMR interaction tensors to structural properties has also been effectively demonstrated in this chapter.

The $^{11}$B NMR results demonstrate that the CS interaction does, in some cases, play a dominant role in the solid-state NMR spectra of quadrupolar nuclei. This work has provided the first experimental characterization of a boron chemical shift tensor, for trimesitylborane. In analogy with $^{13}$C chemical shifts of carbocations, it has also been shown that the in-plane $^{11}$B chemical shift tensor components, which are largely responsible for differences in the isotropic chemical shift and the span of the shift tensor, vary greatly between boranes and borates. This phenomenon has been rationalized in terms of a simple molecular orbital picture. The boron results have direct implications in the interpretation of $^{11}$B NMR spectra of borate glass materials, given the similarity in local structure about boron in glasses and in the model borates and boranes discussed herein.

The viability of studying solid organic hydrochloride salts using high-field $^{35/37}Cl$ NMR techniques has been established. In particular, the chlorine nuclear quadrupolar coupling constant has been found to be characteristic of the hydrogen bonding environment of the chloride ion. For the first time, anisotropic chlorine nuclear magnetic shielding has been observed from a powder sample, in L-cysteine ethyl ester hydrochloride. The success of the chlorine work foreshadows further high-field $^{35/37}Cl$ NMR studies of larger and more complex organic and biological hydrochloride compounds. Chlorine NMR is well-suited to provide information on the local structure about chloride ions in such compounds in terms of the nuclear quadrupolar coupling constant and asymmetry parameter.

The present work has also provided direct solid-state NMR evidence for a small EFG at the central nucleus of a piano-stool compound, **I**, as predicted previously by point charge arguments and inferred from narrow solution NMR line widths. In contrast to the small quadrupolar interaction, a particularly anisotropic molybdenum CS tensor has been measured. The large deshielding of the molybdenum nucleus in the plane perpendicular to the pseudo-$C_3$ axis of **I** has been shown to arise from mixing of appropriate *d* orbital-dominated occupied and virtual MOs. The utility of the ZORA-DFT method in accounting for relativistic corrections in the calculation of EFG and CS tensors for transition metal nuclei has been demonstrated through favourable comparisons with the experimental data. The molybdenum work illustrates the utility of quadrupolar transition-metal NMR in the solid state, but also cautions against underestimating the importance of the chemical shift interaction in quadrupolar nuclei. The ability to measure

the CS tensor for a quadrupolar nucleus, and understand its origins, becomes increasingly crucial as higher magnetic field strengths become commercially available.

Finally, the first $^{53}Cr$ solid-state NMR spectra of diamagnetic Cr(0) and Cr(VI) compounds have been presented and interpreted in terms of the $^{53}Cr$ EFG and CS tensor interactions. Given the difficulties associated with NMR spectroscopy of the $^{53}Cr$ nucleus, these results provide encouraging evidence that nearly the entire periodic table is accessible to NMR spectroscopists not only in principle, but also in practice. Future work on expanding the types of nuclei which are available for useful and practical study by modern solid-state NMR methodologies is outlined in Chapter 6.

# Chapter 4: Insights into Indirect Nuclear Spin-Spin Coupling Tensors from Computational Chemistry and Experiment

## 4.1 Introduction and History

The indirect spin-spin coupling between nuclei is of fundamental importance in magnetic resonance spectroscopy (*44*, *323*, *324*). Recent applications which have received attention in the literature range from the identification of hydrogen bonding networks in nucleic acid base pairs (*325*, *326*) and in proteins (*327*, *328*, *329*, *330*) to probing binary semiconducting compounds (*331*, *332*) and high-temperature superconductors (*333*). In isotropic fluids, indirect nuclear spin-spin coupling constants (also widely known as "scalar" coupling constants) are important in providing information about the secondary and tertiary structure of biological macromolecules (*334*, *335*, *336*). The largest known isotropic coupling constant is $^1J(^{199}Hg, ^{199}Hg) = 284100 \pm 860$ Hz for a $[Hg\text{-}Hg]^{2+}$ crown ether complex (*337*). This corresponds to what is likely the largest reduced isotropic coupling constant, $^1K_{iso} = 72085 \times 10^{20}$ N $A^{-2}m^{-3}$.

While isotropic coupling constants, $J_{iso}$, are routinely measured in solution and in the solid state, experimentally it is difficult to measure reliable values of the anisotropy in **J** because the Hamiltonians describing the anisotropic **J**-interaction and the direct-dipolar interaction involve tensors of the same form (*35*, *50*). As discussed in Chapter 2, one cannot independently measure the anisotropic **J** tensor and the direct dipolar coupling tensor. In addition, the direct dipolar interaction is often at least an order of magnitude

larger than the anisotropic **J**-interaction. Because of this close relationship between the direct dipolar interaction and $\Delta J$, anisotropy in the **J** tensor has sometimes been termed the "pseudo-dipolar" interaction (*338*). Numerous NMR experiments, both solution- and solid-state, have been devised to measure the direct dipolar coupling constants, which depend upon the inverse cube separation of the two nuclei (*cf.* eq. 2.32) (*339*, *340*). What seems to be consistently ignored when these experiments are applied is the fact that anisotropy in the indirect spin-spin coupling will also contribute to the apparent dipolar coupling constant measured. It is essential to have a better understanding of the indirect spin-spin coupling, and in particular the magnitude of $\Delta J$, in order to have confidence in any internuclear separations derived from NMR measurements.

To determine $\Delta J$, the value of the direct dipolar contribution, $R_{DD}$, must be known independently of the NMR experiment. Complete **J** tensors can be characterized by studying the NMR spectra of single crystals (*341*), solid powder samples (*50*, *342*), or samples oriented in liquid crystalline solvents (*343*). Another less well-recognized source of spin-spin coupling tensor information is the hyperfine structure observed in molecular beam (*40*, *49*) or high-resolution microwave (*344*) spectroscopy experiments. The importance of experimental data from the latter experiments, with few exceptions, has been completely overlooked.

Experimental trends concerning $J_{iso}$ have been recognized for some time (*345*, *346*, *347*, *348*, *349*); however, periodic trends concerning $\Delta J$ are less clear. There has been some evidence that $\Delta J$ increases when one or more heavy nuclei are involved (*332*, *338c*, *341*, *342*, *350*, *351*, *352*, *353*) (e.g., $\Delta J$ ($^{199}$Hg, $^{31}$P) = 4.0 ± 0.5 kHz in

$Hg(PPh_3)_2(NO_3)_2$ (*341b*)), but there have also been indications that $\Delta J$ could be important for light nuclei (e.g., $\Delta J(^{19}F, ^{13}C) = 350$ Hz in $^{13}CH_3F$ (*354*)). Methyl fluoride in particular has attracted a great deal of attention. For example, although the currently accepted value for $\Delta J(^{19}F, ^{13}C)$ is 350 Hz, previously reported values include $404 \pm 31$ Hz (*355*), measured using liquid crystal techniques, and $-1200 \pm 1200$ Hz, measured *via* $^{13}C$ NMR in a solid argon matrix at 15 K (*51*).

Pople and Santry (*356*) developed approximate formulae for each of the mechanisms which contribute to **J** (see Chapter 2) within the context of a simple valence electron molecular orbital theory. One of the main conclusions from this classic paper is that the Fermi contact term is generally the most important mechanism for spin-spin coupling, particularly if protons are involved. The orbital and spin-dipolar terms were found to be most important when there is multiple bonding between the two coupled nuclei. Buckingham and Love (*357*) extended the Pople-Santry work to investigate the full coupling tensor in terms of LCAO coefficients and singlet-triplet excitation energies. They were especially interested in determining the mechanisms which are responsible for anisotropy in the **J** tensor. According to molecular orbital theory as employed by Buckingham and Love, the FC x SD term can make a significant contribution to the anisotropy of the electron-coupled nuclear spin-spin interactions. It should be noted that only a few molecules were investigated and used to draw general conclusions in this early study. Other than thallium fluoride, there were no reliable experimental data on isolated molecules in the gas phase available in the mid- to late-1960s for comparison with the calculated results.

In 1967, Pople and co-workers developed a finite perturbation theory for calculating spin-spin coupling constants (*358*). This technique was used with INDO semi-empirical self-consistent molecular orbital methods to calculate indirect spin-spin coupling constants in numerous molecules. As implemented by Pople and co-workers, only the Fermi-contact mechanism was considered. Others (*359*) incorporated the remaining mechanisms. Although these semi-empirical methods often reproduced experimental trends, particularly for couplings involving protons, the results for pairs of heavier nuclei were often suspect. Early attempts to use the finite perturbation approach with non-empirical SCF calculations using minimal basis sets to calculate $J_{iso}$ failed (*360*).

Thus, reliable first-principles calculations of **J** tensors have been challenging and generally confined to relatively small molecules containing first-row elements (*94*, *361*). For many years, difficulties were encountered even in reproducing the correct sign of $J_{iso}$ in a molecule as simple and light as hydrogen fluoride (see Table 16 of ref. *411*). Recently, there have been substantial improvements in first-principles calculations of **J** couplings (*94*, *109*, *361*, *362*, *363*, *364*, *365*, *366*, *367*). Particularly promising results have recently been obtained using multiconfigurational self-consistent field (MCSCF) linear response methods with large correlation-consistent basis sets. With the exception of recent papers by Jokisaari and co-workers (*343 b-d*), judgements concerning the quality of the calculations have been based on a comparison of **isotropic** spin-spin coupling constants (calculated and observed). The role of medium effects is generally not considered, with some important exceptions (*368*).

While *ab initio* techniques may yield results which are in excellent agreement with available experimental data, they are time consuming and limited to small systems composed of relatively light atoms. Density functional theory (DFT) methods for calculating NMR properties allow for relatively large or heavy systems to be treated more rapidly (*369*). Malkina *et al.* have described their implementation of a DFT method for calculating **J** tensors using Gaussian-type orbitals (*370*). An alternative implementation was subsequently applied with Slater-type basis sets to demonstrate the feasibility of calculating **J** couplings to transition metal nuclei (*371*, *372*). Recently, several new DFT techniques for calculating **J** tensors have been developed, including a zeroth-order regular approximation (ZORA) DFT method (*373*, *374*, *375*). These recent implementations have included the spin-dipolar (SD) term in the calculations; this term, which can not be neglected *a priori*, had been omitted in earlier DFT treatments.

The work presented in this Chapter endeavours to provide a combined experimental and theoretical foundation for periodic trends in indirect spin-spin coupling tensors. Both *ab initio* and DFT computational methods will be employed. Comparison of calculated results with experimental data, where available, provides some insights into the utility of the computational techniques. Finally, a discussion of the prospects of making the first experimental measurement of the antisymmetric part of the **J** tensor are discussed. As presented in Chapter 2, it has long been known that for powdered samples containing tightly coupled (AB) spin systems observed under conditions of magic-angle spinning, $\mathbf{J}^{antisym}$ should affect the observed spectrum (*52*, *376*). Nevertheless, no experimental determinations of $\mathbf{J}^{antisym}$ exist.

## 4.2 Computational and Experimental Details

### *4.2.1 Computational Details*

MCSCF and ZORA-DFT methods were used for the calculation of **J** tensors.

Calculations of **J** tensors for light diatomics were carried out using MCSCF methods and complete active space self-consistent field (CASSCF) (*122*) or restricted active space SCF (RASSCF) (*123*) wavefunctions on an IBM RS 6000 workstation running the Dalton (*96*) quantum chemistry program. The largest possible balanced active spaces were chosen based on the MP2 natural orbital occupation numbers (*377*) (see Appendix A).

The complete active spaces, basis sets, and equilibrium bond lengths employed in the MCSCF calculations on diatomics are summarized in Table 4.1. The cc-pV5Z and aug-cc-pVQZ basis sets have been used for most calculations (*96*, *378*), and in cases where this was not possible (Na, K), the largest feasible uncontracted basis sets were used (*379*). Equilibrium bond lengths for the diatomics listed in Table 4.1 were obtained from the compilation of Huber and Herzberg (*239*), except for KNa (*380*) and ClF (*381*).

**Table 4.1**: Equilibrium bond lengths, complete active spaces, inactive orbitals, basis sets, and total number of orbitals used for the MCSCF calculation of **J** tensors.

| | $r_e$ / Å | CAS/inactive | basis set | number of orbitals |
|---|---|---|---|---|
| HF | 0.91682 | 6331/1000 | cc-pV5Z | 146 |
| $^{7}$LiH | 1.5957 | 6332/0000 | cc-pV5Z | 146 |
| $^{7}$LiF | 1.563864 | 6331/1000 | cc-pV5Z | 182 |
| $^{23}$NaF | 1.925947 | 7331/1000 | 20s12p4d / cc-pV5Z | 167 |
| $^{39}$KF | 2.171457 | 6330/2000 | 26s17p1d / cc-pV5Z | 173 |
| $^{35}$ClF | 1.628332 | 7330/2000 | aug-cc-pVQZ | 164 |
| $^{23}Na_2$ | 3.0788 | 41113111/20001000 | 20s12p4d | 152 |
| $^{39}$K$^{23}$Na | 3.499035 | 5331/6110 | 26s17p1d / 20s12p4d | 158 |
| $^{11}$BF | 1.26259 | 5321/1000 | cc-pV5Z | 182 |
| $^{27}$AlF | 1.654369 | 7331/1000 | aug-cc-pVQZ | 164 |
| H$^{35}$Cl | 1.27455 | 6331/1000 | aug-cc-pVQZ | 130 |

Rovibrational corrections to some of the MCSCF-calculated coupling constants were carried out as originally suggested by Buckingham (*382*). For any molecular property, *P*:

$$P(eq) = P(v,J) - \left(v+\frac{1}{2}\right)\left(\frac{B_e}{\omega_e}\right)\left[\left(\frac{\partial^2 P}{\partial \xi^2}\right)_{\xi=0} - 3a\left(\frac{\partial P}{\partial \xi}\right)_{\xi=0}\right] - 4(J^2+J)\left(\frac{B_e}{\omega_e}\right)^2\left(\frac{\partial P}{\partial \xi}\right)_{\xi=0} \quad [4.1]$$

Here, $P$(eq) is the property at the equilibrium bond length, $r_e$, and $P(v, J)$ is the property for a particular rovibrational state; note that here $J$ refers to the rotational state of the molecule and is not related to the indirect spin-spin coupling tensor. The rotational

constant at the equilibrium bond length, $B_e$, is equal to $h / 8\pi^2 I_e$ (in Hz), $I_e$ is the moment of inertia at the equilibrium bond length; $\omega_e$ is the harmonic vibrational frequency; $\xi$ is the reduced displacement from equilibrium, $(r-r_e) / r_e$, and $a$ is the cubic force constant:

$$a = -1 - \frac{\alpha_e \omega_e}{6B_e^2} \qquad [4.2]$$

First and second derivatives are estimated by carrying out additional MCSCF calculations in the region of the equilibrium bond length. The goal is to find the rovibrational average of $R_{DD}$, which is equivalent to $c_3$(direct) (*vide infra*).

The procedure employed follows that of Bass *et al.* (*383*) and Tipping and Ogilvie (*384*); a similar procedure was outlined by Schlier (*402*). The quantity to be averaged is:

$$\left\langle \frac{1}{r^3} \right\rangle = \frac{1}{r_e^3} \frac{1}{\left(1 + \langle \xi \rangle\right)^3} \qquad [4.3]$$

Expansion of $(1 + \langle\xi\rangle)^{-3}$ using the MacLaurin series and substitution of the result into equation 2.32 gives, to fourth order,

$$R_{DD}(v,J) = \left(\frac{\gamma_1 \gamma_2 \hbar}{2\pi} \frac{\mu_0}{4\pi}\right) \frac{1}{r_e^3} \left(1 - 3\langle\xi\rangle + 6\langle\xi\rangle^2 - 10\langle\xi\rangle^3 + 15\langle\xi\rangle^4\right) \qquad [4.4]$$

The rovibrationally-averaged quantities, $\langle\xi\rangle^n$ (n = 1, 2, 3, 4), depend on $v$ and the rotational angular momentum quantum number $J$. The lengthy expressions for $\langle\xi\rangle^n$ are given by Tipping and Ogilvie (*384*). These expressions depend on the Dunham coefficients $a_0$ through $a_6$ (*385*), which describe the shape of the potential energy well near the equilibrium bond length. These coefficients in turn depend on the spectroscopic constants of the diatomic molecule, including $B_e$ and $\omega_e$, for example. These values were obtained from the compilation of Huber and Herzberg, available online from the NIST

Chemistry Webbook (*239*). Analytical equations for the Dunham coefficients $a_0$, $a_1$, $a_2$, and $a_3$ are available (*344*); unfortunately such equations are not readily available for the higher-order terms $a_4$, $a_5$, and $a_6$. Since most models adequately describe the potential well in the region of $r_e$, a recursive relationship applying to the Morse potential (*384*) was used to determine suitable values for $a_4$ through $a_6$. The results obtained by this method are in very close agreement with the $\langle\xi\rangle^n$ values reported by Bass *et al.* for hydrogen fluoride (*383*). Determining $R_{DD}(v, J)$ in this manner allows the application of equation 2.50 to determine $\Delta J$.

Indirect nuclear spin-spin coupling tensors for the interhalogen diatomics were calculated using the CPL coupling module (*120*, *121*, *371*, *372*) of the Amsterdam Density Functional program (*226*, *227*) running on an IBM RS6000 workstation or a PC with an AMD Athlon microprocessor. The couplings are calculated based on the relativistic ZORA-DFT implementation described in references *120* and *121*. The Fermi-contact (FC), SD, diamagnetic and paramagnetic spin-orbit (DSO and PSO) coupling mechanisms were included in the calculations. In the ZORA-DFT implementation, the FC and SD terms are not separated, and this sum term is labelled "FC+SD". The FC+SD term contains the well-known FCxSD cross term, and also part of the (FC+SD)-PSO cross term. Likewise, the "PSO" term that is computed contains the remaining part of the (FC+SD)-PSO cross term. Note that the (FC+SD)-PSO term is exactly zero in the nonrelativistic or scalar relativistic limit where no spin-orbit coupling is present. However, it has been demonstrated that, e.g., for TlI, it can represent the largest individual contribution to the isotropic coupling constant (*121*, *386*) and only upon

inclusion of relativistic spin-orbit coupling (and the respective cross terms) can reasonable agreement with experiment be achieved.

All DFT calculations used the VWN (*228*) + Becke88 (*229*) and Perdew86 (*230*) generalized gradient approximation (GGA) as described in reference 121. Relativistic spin-orbit calculations were performed for all diatomic molecules (so-GGA), and scalar relativistic calculations (scalar-GGA) were carried out for some molecules for comparison purposes. The triple-polarized ADF ZORA IV and ZORA V Slater-type basis sets available within the ADF package were used for the diatomics. A missing 5d polarization function with exponent 1.900 was added to the iodine basis set, which was found to yield slightly improved results for the computed coupling tensors. Experimental equilibrium bond lengths were obtained from the compilation of Huber and Herzberg (*239*), except for ClF (*381*), $Cl_2$ (*387*), and $I_2$ (*388*). A theoretical bond length of 2.987 Å was used for $At_2$ (*389*).

Some calculations for $F_2$ and ClF were also carried out using the MCSCF method. Restricted active space (RAS) wave functions were chosen based on the MP2 natural orbital occupation numbers. The $D_{\infty h}$ symmetry of $F_2$ was represented in the $D_{2h}$ point group in Dalton. The RAS used for $F_2$ was 10001000(inactive), 00000000(RAS1), 21101110(RAS2), 32213221(RAS3), where the eight digits refer to orbitals of $A_g$, $B_{3u}$, $B_{2u}$, $B_{1g}$, $B_{1u}$, $B_{2g}$, $B_{3g}$, and $A_u$ symmetries, respectively. The $C_{\infty v}$ symmetry of ClF was represented in the $C_{2v}$ point group in Dalton. The RAS used for ClF was 4110(inactive), 0000(RAS1), 3220(RAS2), 4331(RAS3), where the four digits refer to orbitals of $A_1$, $B_1$, $B_2$, and $A_2$ symmetries, respectively. The cc-pCVQZ basis set was used for $F_2$, and the

aug-cc-pVQZ basis set was used for ClF. For both molecules, up to two electrons were allowed to be excited into RAS3. The procedure used to select the active spaces is presented in Appendix A.

For calculations of the **J** tensors in the methyleneimine dimer, the experimental gas-phase geometry of the methyleneimine monomer was used (*390*, *391*) and the N-N distance and N-H···N bond angle in the planar dimer were systematically varied in order to gain a thorough understanding of the effects of the hydrogen bond geometry on the properties of the $^{2h}$**J**(N, N) tensor. Both MCSCF and ZORA-DFT calculations were carried out for this system. The MCSCF calculations make use of the $C_s$ point group symmetry of the planar dimer. The wave function was constructed using the following restricted active space (RAS): (40/00/10,2/32), where the orbitals are of a' and a" symmetries respectively, and the orbital spaces are listed in the order (inactive / RAS1 / RAS2 / RAS3). Two electrons were allowed to be excited into RAS3. The cc-pCVDZ basis set has been used in all calculations; this corresponds to a total of 102 orbitals. Due to computational limitations inherent to the MCSCF technique and inherent to Dalton, the use of larger basis sets was not feasible for this model system. To carry out an MCSCF calculation of all of the indirect spin-spin coupling tensors in the model system required approximately 45 hours of CPU time for each geometry; this time was reduced to 11 hours for each geometry if only the $^{2h}$**J**(N, N) tensor was calculated. ZORA-DFT calculations were carried out using ADF and the ZORA V basis set on all atoms, as described above for the diatomics.

MCSCF calculations of the **J** couplings in urea were carried out using the

geometry reported in reference *392*. The calculations employed $C_{2v}$ symmetry and a RAS of 3100 / 0000 / 5421 / 4321. The cc-pCVTZ basis set was used on all atoms.

### *4.2.2 Experimental Details*

Hexa-(*p*-tolyl)ditin, **II**, was kindly synthesized by Kris Harris following a procedure adapted from references *393*, *394*, and *395*.

Tin-119 and tin-117 one-dimensional VACP/MAS NMR spectra of powdered samples of **II** were acquired on a Chemagnetics CMX Infinity 200 spectrometer operating at a frequency of 74.63 MHz for $^{119}$Sn and 71.31 MHz for $^{117}$Sn. A 4 mm DR MAS probe was used for all experiments. Tetracyclohexylditin was used as a setup sample and chemical shift reference, $\delta_{iso}$ = -97.35 ppm (*396*, *397*). Typical experimental parameters for $^{119}$Sn and $^{117}$Sn CP/MAS experiments were: 40 s recycle delay, 2.40 μs π/2 pulse, 5.0 ms contact time, 92 ms acquisition time, 4096 scans recorded. High-power proton decoupling was used for all experiments.

Two-dimensional *J*-resolved $^{119}$Sn MAS NMR spectra (*398*, *399*) were acquired using similar parameters, with 16 points acquired in the indirect dimension, a spectral window of 200 Hz in the indirect dimension, and 128 scans per increment. Resolution in the indirect dimension is limited by the acquisition time, which is in turn limited by how long the probe can withstand high-power proton decoupling.

## 4.3 The Link Between Molecular Beam Hyperfine Data and NMR J Tensors

### *4.3.1 MCSCF Calculations on Light Diatomics*

To illustrate the procedure for extracting $J_{iso}$ and $\Delta J$ from hyperfine data, the case of $^{35}Cl$-$^{19}F$, which has been extensively investigated experimentally (*400*), will be discussed. The hyperfine Hamiltonian for a diatomic molecule, e.g., $^{35}Cl$-$^{19}F$, in the absence of any external fields is given in equation 2.51. It is well known that the nuclear spin-rotation constants $c_{Cl}$ and $c_F$ are related to the nuclear magnetic shielding tensors (*23, 41b, 311, 401*) and it is understood in the literature that $c_4$ corresponds to $J_{iso}$. *What is not generally recognized is the significance of $c_3$, in particular the indirect spin-spin coupling contribution to $c_3$.* As discussed in Chapter 2, the forms of the direct dipolar coupling tensor (**D**) and the **ΔJ** tensor are identical. As a result of these similarities, it is impossible to separately observe the two contributions to the effective dipolar coupling constant, $R_{eff}$ (*35, 44, 50, 338, 341, 342, 343*). The hyperfine parameter $c_3$ is equivalent to $R_{eff}$ (also sometimes denoted as $d_T$ (*402*)). In analogy with the separation of $R_{eff}$ into two contributions as presented in equation 2.50, it is convenient to separate $c_3$ into a direct and an indirect contribution,

$$c_3 = c_3(direct) + c_3(indirect) \qquad [4.5]$$

The direct contribution to $c_3$ ($R_{DD}$) can be determined if the rovibrationally-averaged bond length is known. Thus, knowledge of the effective bond length and of $c_3$ (including its sign) also implies knowledge of $\Delta J$. Pyykkö and Wiesenfeld (*403*) recognized the validity of this separation. So far, this technique has been successfully applied to thallium fluoride, where $\Delta J$ is actually larger than $R_{DD}$ (*404*). In this case, $c_4$ =

$J(^{205}\mathrm{Tl},^{19}\mathrm{F})_{iso}$ = -13.3 ± 0.7 kHz and $c_3$ = 3.50 ± 0.15 kHz. Since $c_3$ (direct) can be calculated from the bond length to be 7.19 ± 0.07 kHz, the indirect contribution must be -3.69 ± 0.15 kHz. Associating $c_3$(indirect) with -$\Delta J$/3 yields $\Delta J(^{205}\mathrm{Tl},^{19}\mathrm{F})$ = 11.1 ± 0.5 kHz for the $v = 0$ state (this number is also given by Buckingham and Love (*357*)).

At first glance, the determination of the anisotropy of the **J** tensor seems trivial. However, unlike for TlF, in most cases the direct coupling contribution swamps the $\Delta J$ contribution; additionally, the observed effect of $\Delta J$ is reduced by a factor of three (see equation 2.50) (*405*). Thus, in order to extract reliable information from the experimentally-determined $c_3$ values, rovibrational corrections to the direct contribution are in many cases essential.

Since experimental $c_3$ values are determined for a particular rovibrational state (typically $v = 0$ and $J = 1$), and the direct dipolar coupling is calculated based on an equilibrium bond length, the rovibrationally-averaged value of the direct dipolar coupling must be calculated, from which $\Delta J$ can be determined:

$$\Delta J(v,J) = -3\left[c_3(v,J) - R_{DD}(v,J)\right] \qquad [4.6]$$

To demonstrate the utility of the approach described above for determining the anisotropy of indirect spin-spin coupling tensors, a series of diatomic molecules has been selected: HF, LiH, LiF, NaF, KF, KNa, $Na_2$, BF, AlF, HCl, and ClF. For some of these molecules, precise experimental hyperfine data are available: HF (*406*), LiH (*407*), LiF (*408*), KF (*409*), $Na_2$ (*410*), and ClF (*400a*). For the calculation of $J_{iso}$, hydrogen fluoride has already been well-studied by Helgaker *et al.* (*119*), although no discussion of the anisotropy of the **J** tensor was presented. Their MCSCF study of the basis-set

dependence of nuclear spin-spin coupling constants for HF and $H_2O$ indicates that the best results are obtained for basis sets of the cc-pVXZ type, supplemented with tight *s* functions. The results for HF presented herein are for comparison purposes and to ensure the reproducibility of the previously reported results. To ensure the reliability of the MCSCF technique for calculating $\Delta J$ as well as $J_{iso}$ beyond HF, calculations of **J** tensors for LiH, LiF, KF, $Na_2$, and ClF were carried out and the results compared to the experimental data. The results in Table 4.2 indicate that the calculations perform very well; both the isotropic coupling constants and the anisotropies are in very good agreement with the experimental data. Given the history of the calculation of $J_{iso}$ in small molecules (*361*, *411*), the accuracy of these calculated results is encouraging. It is also important to point out that in the past most comparisons between experiment and theory have been based solely on $J_{iso}$, when in fact **J** is a second-rank tensor. This is the first time accurate **J** tensor data from molecular beam experiments have been compared with state-of-the-art first principles calculations.

**Table 4.2**: Calculated and experimental hyperfine data for $^{7}$LiH, $^{7}$LiF, $^{39}$KF, $^{23}Na_2$, and $^{35}$ClF.

| | | calc. $(v, J)^a$ | expt. $(v, J)^b$ |
|---|---|---|---|
| $^{7}$LiH | $c_3 = R_{eff}$ | - | 11346 ± 7 |
| | $c_3(\text{dir}) = R_{DD}$ | 11327 | - |
| | $-3c_3(\text{ind}) = \Delta J$ | -13 | -57 ± 21 |
| | $c_4 = J_{iso}$ | 151 | 135 ± 10 |
| $^{7}$LiF | $c_3 = R_{eff}$ | - | 11324 ± 9 |
| | $c_3(\text{dir}) = R_{DD}$ | 11382 | - |
| | $-3c_3(\text{ind}) = \Delta J$ | 176.9 | 173.2 ± 27.7 |
| | $c_4 = J_{iso}$ | 199 | 172.3 ± 3.2 |
| $^{39}$KF | $c_3 = R_{eff}$ | - | 472 ± 4 |
| | $c_3(\text{dir}) = R_{DD}$ | 514 | - |
| | $-3c_3(\text{ind}) = \Delta J$ | 109.5 | 125.7 ± 5.1 |
| | $c_4 = J_{iso}$ | 78.2 | 57.8 ± 1.3 |
| $^{23}Na_2$ | $c_3 = R_{eff}$ | - | 302.6 ± 5.0 |
| | $c_3(\text{dir}) = R_{DD}$ | 286.7 | - |
| | $-3c_3(\text{ind}) = \Delta J$ | -30 | -48 ± 15 |
| | $c_4 = J_{iso}$ | 1245 | 1067 ± 7 |
| $^{35}$ClF | $c_3 = R_{eff}$ | - | 2859 ± 9 |
| | $c_3(\text{dir}) = R_{DD}$ | 2557 | - |
| | $-3c_3(\text{ind}) = \Delta J$ | -800 | -907 ± 27 |
| | $c_4 = J_{iso}$ | 829 | 840 ± 6 |

[a] For LiF and KF, $v = 0, J = 0$; for LiH and ClF, $v = 0, J = 1$; for $Na_2$, $v = 0$.

[b] References are given in the text.

The good agreement for both $J_{iso}$ and $\Delta J$ shown in Table 4.2 lends support to the notion that all contributions to **J** are calculated with reasonable accuracy. For example, the calculated $\Delta J\,(v=0, J=0)$ of 176.9 Hz for $^{7}$LiF is well within the experimental error (173.2 ± 27.7 Hz); the calculated $J_{iso}$ for $^{35}$ClF of 829 Hz is in notably good agreement with the experimental value of 840 ± 6 Hz. It is expected that the results for KF and $Na_2$ will be less accurate. Although the number of basis functions used is comparable to the number used for the other molecules, the basis sets for K and Na are not of the cc-pVXZ (correlation-consistent) type (Table 4.1). It is interesting to note that as the constituent atoms become heavier, the relative importance of the FC mechanism tends to decrease (*vide infra*); this is fortunate since the FC contribution is difficult to calculate, in part due to the cusp problem associated with using Gaussian-type orbitals (*361a,c, 412*). Rovibrational corrections to $R_{DD}(r_e)$ were a few percent or less in all cases. It is important to make these corrections, however, to ensure that the experimental data are being compared to the appropriate calculated values.

**Table 4.3:** Calculated equilibrium contributions to the isotropic portion of the indirect spin-spin coupling tensor for a series of diatomic molecules.

| Molecule | % DSO | % PSO | % SD | % FC | $J_{iso}$ / Hz | $K_{iso}$ / $10^{20}$ N $A^{-2}$ $m^{-3}$ |
|---|---|---|---|---|---|---|
| HF | -0.05 | 38.83 | -0.48 | 61.69 | 476.09 | 4.21 |
| $^{7}$LiH | 0.02 | -0.06 | 0.07 | 99.98 | 152.47 | 3.27 |
| $^{7}$LiF | -0.01 | -4.23 | 0.12 | 104.11 | 193.10 | 4.39 |
| $^{23}$NaF | 0.00 | -17.48 | 0.25 | 117.22 | 193.98 | 6.48 |
| $^{39}$KF | 0.00 | -13.17 | -0.16 | 113.34 | 76.59 | 14.5 |
| $^{23}Na_2$ | 0.00 | 0.00 | 0.00 | 100.00 | 1243.6 | 148 |
| $^{39}K^{23}$Na | 0.00 | 0.00 | 0.00 | 100.00 | 479.89 | 323 |
| $^{11}$BF | 0.17 | 34.29 | 4.23 | 61.31 | -249.24 | -6.87 |
| $^{27}$AlF | 0.01 | 23.17 | 6.94 | 69.88 | -627.13 | -21.3 |
| $^{35}$ClF | 0.01 | 73.89 | 37.69 | -11.60 | 832.24 | 75.0 |
| H$^{35}$Cl | -0.01 | 21.86 | 0.01 | 78.15 | 58.87 | 5.00 |

Having established the reliability of the MCSCF **J** calculations for molecules as large as ClF, the calculation of **J** tensors was carried out for the remaining molecules: NaF, KNa, BF, AlF, and HCl. The choice of molecules is of course limited by computational resources and the availability of suitably large basis sets. Results are summarized in Tables 4.3 and 4.4, and Figures 4.1 and 4.2. Unfortunately, reliable experimental hyperfine data are only available for comparison for a limited number of small diatomics (*48*). With this in mind, the chosen molecules should provide some insights into any periodic trends in indirect spin-spin coupling. Data are available for

sodium fluoride (*413*); however the errors are quite large. Also, a value for $J_{iso}$ of 306 ± 30 Hz has been reported for KNa (*414*). This value was obtained by an optical pumping technique, and a corresponding $c_3$ value was not reported.

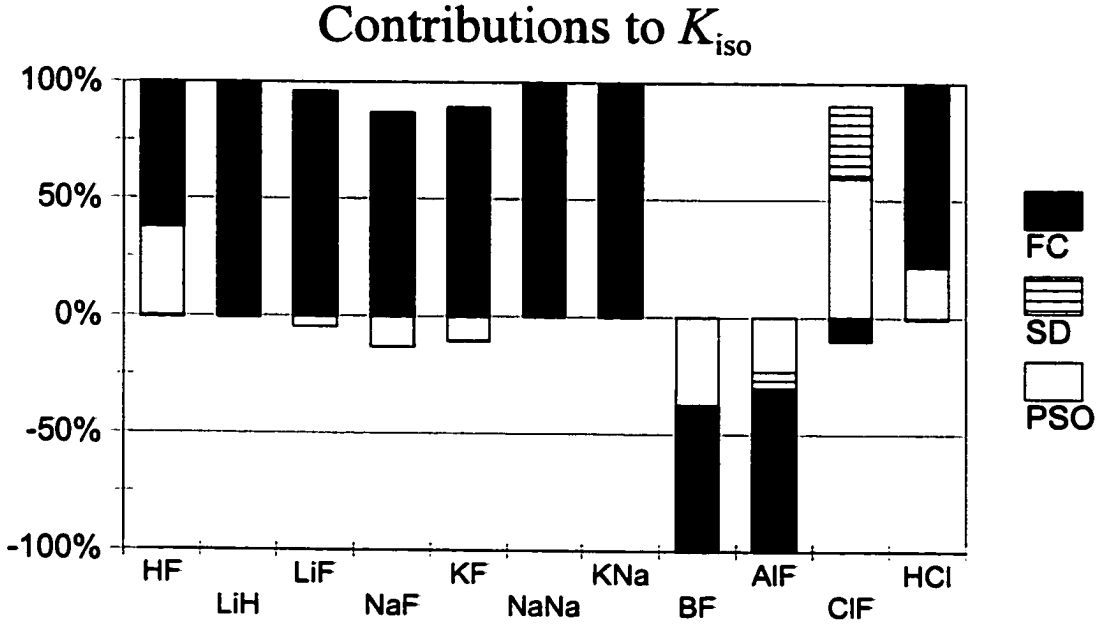


Figure 4.1: Graphical representation of the percentage contributions of each of the spin-spin coupling mechanisms to the total calculated reduced coupling constant, $K_{iso}$. Data are given in Table 4.3. In each case, the DSO contribution is too small to appear in the graph.

**Table 4.4**: Calculated equilibrium contributions to the anisotropy in the indirect spin-spin coupling tensors for a series of diatomic molecules.

| Molecule | % DSO | % PSO | % SD | % SD x FC | $\Delta J$ / Hz | $\Delta K$ / $10^{20}$ N $A^{-2}$ $m^{-3}$ |
|---|---|---|---|---|---|---|
| HF | 185.99 | -262.75 | -47.7 | 224.43 | 115.98 | 1.03 |
| $^{7}$LiH | -34.54 | -1.16 | -0.55 | 136.14 | -12.39 | -0.27 |
| $^{7}$LiF | 11.23 | 18.28 | -3.09 | 73.58 | 177.43 | 4.04 |
| $^{23}$NaF | 2.81 | 23.32 | -2.06 | 75.93 | 494.19 | 16.51 |
| $^{39}$KF | 2.57 | 29.68 | -2.99 | 70.74 | 109.22 | 20.68 |
| $^{23}Na_2$ | -3.64 | 0.10 | 0.02 | 103.53 | -29.88 | -3.55 |
| $^{39}K^{23}Na$ | -1.88 | 0.14 | -0.10 | 101.82 | -10.85 | -7.31 |
| $^{11}$BF | 7.82 | 63.63 | -9.49 | 38.05 | 468.9 | 12.92 |
| $^{27}$AlF | 4.45 | 76.42 | -10.3 | 29.42 | 555.51 | 18.84 |
| $^{35}$ClF | -1.53 | 109.99 | -36.5 | 28.05 | -805.68 | -72.65 |
| $H^{35}Cl$ | 32.41 | -32.38 | -5.97 | 105.94 | 61.18 | 5.19 |

Shown in Table 4.3 are $J_{iso}$, $K_{iso}$, and a breakdown of these quantities into the various contributing mechanisms for the complete series of diatomics studied herein. The percentage contributions are also displayed graphically in Figure 4.1. The results for HF are in agreement with those reported by Helgaker *et al.* (*119*). For the alkali metal fluorides, MF (M = $^{7}$Li, $^{23}$Na, $^{39}$K), there are several trends which are apparent. First, the reduced isotropic spin-spin coupling increases with the atomic number of the alkali metal atom, ranging from 4.4 x$10^{20}$ N $A^{-2}$ $m^{-3}$ in LiF to 14.5 x$10^{20}$ N $A^{-2}$ $m^{-3}$ in KF. The dominant contribution to the isotropic part of the coupling is from the Fermi contact

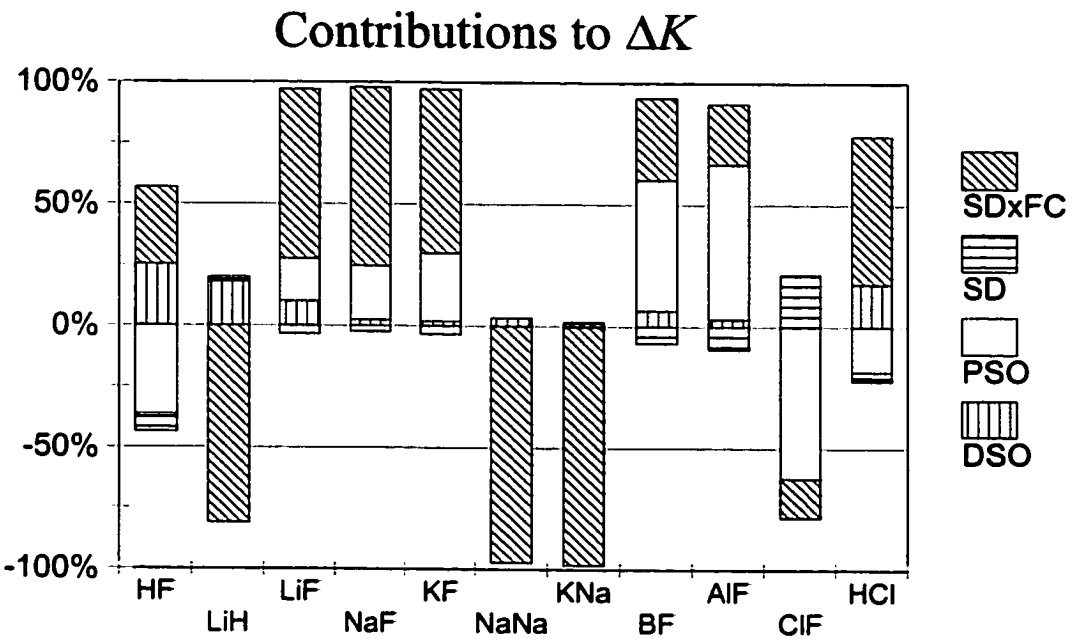


Figure 4.2: Graphical representation of the percentage contributions of each of the spin-spin coupling mechanisms to the total calculated anisotropy in the reduced coupling tensor, $\Delta K$. Data are given in Table 4.4.

mechanism, as expected from the arguments of Pople and Santry (*356*). The only other notable contribution to $K_{iso}$ for the alkali metal halides is due to the paramagnetic spin-orbit (PSO) mechanism; its effect is to oppose the FC contribution and its relative importance seems to increase as the atomic number of the alkali metal increases. The DSO and SD contributions combined amount to less than 0.2% of the total isotropic coupling. In contrast, the early results of Buckingham and Love (*357*) indicate a significant negative spin-dipolar contribution to $K_{iso}$ for the alkali metal fluorides.

No accurate experimental data are available for the lighter group 13 fluorides, BF, AlF, and GaF. Examination of the calculated results (Table 4.3) for $K_{iso}$ provides an indication of what happens as the atomic number of the group 13 element is increased. In

contrast with the alkali metal halides, the $K_{iso}$ values are negative; the magnitudes of $K_{iso}$ for the two groups are fairly similar, with the group 13 fluorides exhibiting slightly larger values for a given row of the periodic table. Most interesting is the relative importance of the various coupling mechanisms to $K_{iso}$. The FC mechanism, while still the most significant, now only constitutes 60 - 70% of the total coupling, even in boron fluoride. The PSO and SD mechanisms are seen to play more prominent roles than in the alkali metal fluorides. The results for BF are of particular interest in the context of the work of Pople and Santry (*356*). Their treatment included an average energy approximation, and as a result, the spin-orbital contribution was automatically zero for any molecule without

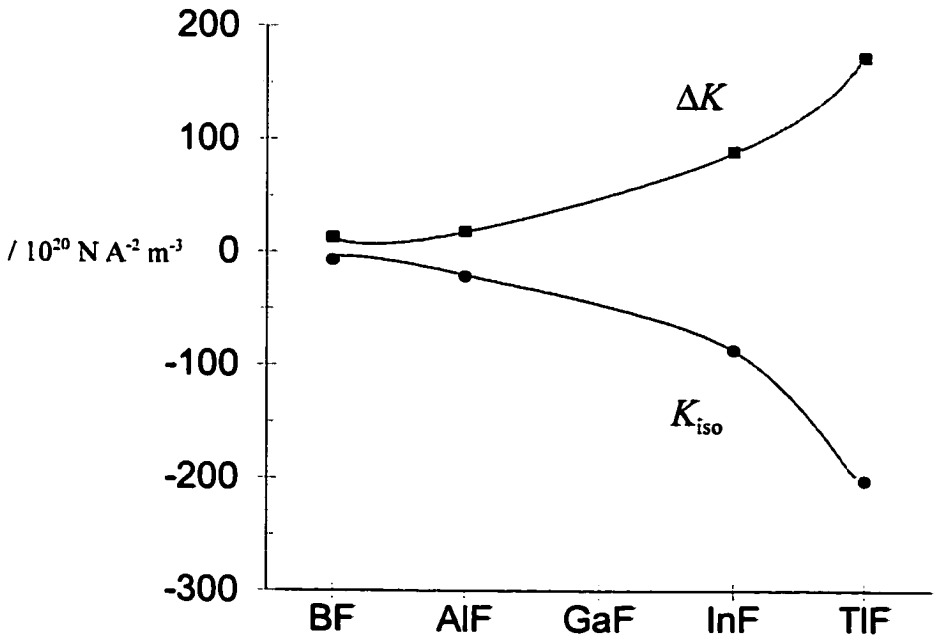


Figure 4.3: This plot demonstrates the variations in $K_{iso}$ and $\Delta K$ for the group 13 fluorides. Calculated values ($r_e$) are given for $^{11}$BF and $^{27}$AlF. The data for $^{205}$TlF ($v = 0, J = 1$) and $^{115}$InF ($v = 0, J = 1$) are experimentally determined; see the text for further details. The dotted lines are not fits, but rather serve to accentuate the apparent trend.

π-bond character. These results demonstrate that interpretation of the coupling constants only in terms of the FC mechanism is inappropriate, even for a molecule as light as BF, where the MCSCF data reveal a PSO contribution to $J_{iso}$ of 34%.

Shown in Figure 4.3 is the dependence of both $K_{iso}$ and $\Delta K$ on atomic number for the group 13 fluorides, with experimental data used for $^{205}$TlF ($v = 0, J = 1$) (*404*) and for $^{115}$InF ($v = 0, J = 1$) (*415*). Results for gallium fluoride can be easily interpolated. Anisotropy in the **K** tensor has also been extracted from existing data in the literature for $^{205}Tl^{35}Cl$ ($v = 0, J = 2$) (*416*), $^{205}Tl^{81}Br$ ($v = 0, J = 2$) (*417*), and $^{205}Tl^{127}I$ ($v = 0, J = 3$) (*418*); the results have been plotted along with those for $^{205}Tl^{19}F$ in Figure 4.4. These data clearly indicate increasing trends in the absolute values of $K_{iso}$ and $\Delta K$ as the atomic number of the halide bonded to thallium increases.

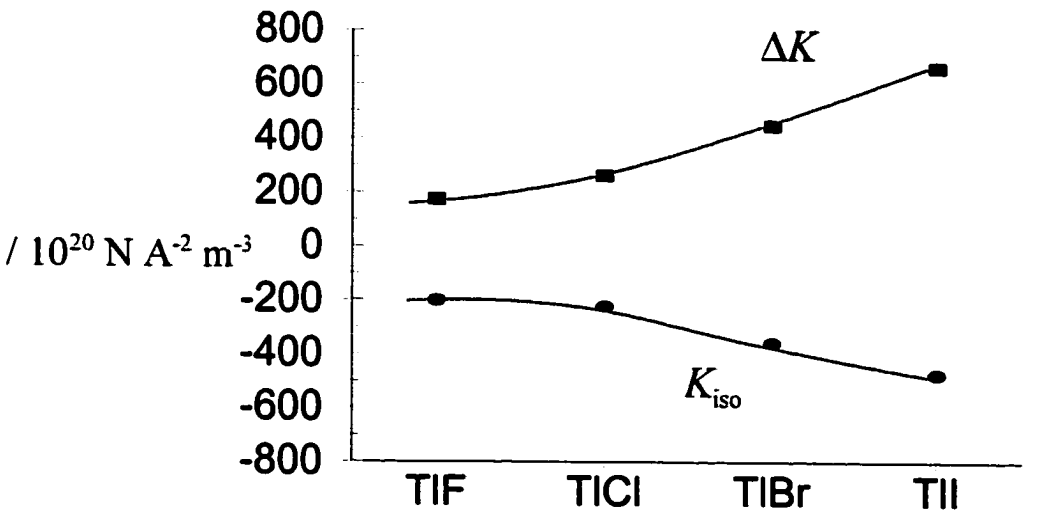


Figure 4.4: Experimental values for $K_{iso}$ and $\Delta K$ for the thallium halides, deduced from the results of high-resolution rotational spectroscopy, are shown. The values are for the particular rovibrational states given in the text. The dotted lines serve as guides to the trends.

Comparison of chlorine monofluoride and hydrogen chloride (Table 4.3) indicates the dramatic effect of replacing H with F on the **K** tensor and on the relative importance of the various contributing mechanisms. The isotropic coupling for liquid HCl has been measured as 38 Hz (*419*); therefore medium effects will play a role in any comparison with the calculated value of ~59 Hz. For HCl, the Fermi contact contribution is foremost, as it is in HF. For ClF however, the FC mechanism becomes almost insignificant, making up only about 12% of the total coupling! Instead, it is the paramagnetic spin-orbit mechanism which dominates (74%), and the spin-dipolar mechanism contributes 38% of the total coupling. These results suggest that the interpretation of any spin-spin coupling constant entirely on the basis of the Fermi contact mechanism is exceedingly dangerous, and reinforces what has been emphasized in the past: large $\Delta J$ values imply significant non-FC contributions to **J** (*341a,b, 343*). The results for ClF are also useful for exploring trends in $K_{iso}$ and the various contributions across a row of the periodic table. For example, inspection of the results for the second-row fluorides (NaF, AlF, and ClF), allows for the proposal of certain trends. The PSO contribution is seen to steadily increase, initially small and negative in NaF, and becoming positive and dominant in ClF. Similarly, the SD mechanism is negligible in NaF, but accounts for an increasing percentage of $K_{iso}$ as the atomic number of the atom bonded to fluorine increases. The FC contribution steadily decreases across this row for the diatomic fluorides. The absolute value of $K_{iso}$ itself increases across the row, beginning at roughly 10 $x10^{20}$ N $A^{-2}$ $m^{-3}$ for NaF and increasing to ~ 20 $x10^{20}$ N $A^{-2}m^{-3}$ for AlF and 75 $x10^{20}$ N $A^{-2}$ $m^{-3}$ for ClF.

The trends and comparisons discussed thus far have been based primarily on the

isotropic spin-spin coupling. Unfortunately, this is where most discussions of indirect spin-spin coupling terminate. As emphasized earlier, **J** is a second-rank tensor quantity and as such requires two independent components for its complete characterization in a linear molecule. Shown in Table 4.4 are the calculated results for the spin-spin coupling anisotropies, $\Delta J$, and the corresponding reduced values, $\Delta K$, for HF, LiH, LiF, NaF, KF, $Na_2$, KNa, BF, AlF, HCl, and ClF. In addition, these values have been decomposed into their constituent contributions and summarized graphically in Figure 4.2. The first aspects of these results which are particularly striking are the relatively large anisotropies in **J** for HF and LiF since these are both small, light molecules for which one might intuitively expect a fairly isotropic coupling tensor. For HF, the anisotropy in **J** is about 25% of $J_{iso}$. For LiF, this relative anisotropy ratio (*411*) increases to 92%! This value is in good agreement with the rovibrationally-averaged experimental ratio of 101%. Shown in Table 4.5 are the calculated relative anisotropy ratios for all of the molecules studied herein. Examination of the $\Delta K$ results (Table 4.4) for the alkali metal fluorides reveals that the anisotropy increases as the atomic number increases, and that the SD x FC mechanism is the most important in each case. All mechanisms (except FC) contribute significantly to $\Delta K$, and the PSO mechanism becomes increasingly important for the heavier diatomics. The early calculations of Buckingham and Love (*357*) yielded a similar trend for the total $\Delta K$; however, their results for LiF, NaF, KF, and RbF suggested that the spin-orbital mechanisms (DSO + PSO) were decidedly more important than the FC x SD cross term.

**Table 4.5**: Theoretical relative anisotropy ratios, $\Delta J/J_{iso}$ and $\Delta J/R_{DD}$, as determined from MCSCF calculations at the equilibrium bond length.

| | $\Delta J/J_{iso}$ (%) | $\Delta J/R_{DD}$ (%) |
|---|---|---|
| HF | 24.4 | 0.08 |
| $^{7}$LiH | -8.4 | -0.12 |
| $^{7}$LiF | 91.9 | 1.55 |
| $^{23}$NaF | 255 | 11.8 |
| $^{39}$KF | 143 | 21.2 |
| $^{23}Na_2$ | -2.4 | -10.4 |
| $^{39}K^{23}Na$ | -2.3 | -31.4 |
| $^{11}$BF | -189 | 2.61 |
| $^{27}$AlF | -88.6 | 8.53 |
| $^{35}$ClF | -96.8 | -31.5 |
| $H^{35}Cl$ | 104 | 1.08 |

Inspection of the $\Delta K$ data for the group 13 fluorides shows that, as for the LiF, NaF, KF series, the anisotropy becomes larger as the atomic number of the atom bonded to fluorine increases. In accord with the relative contributions to $K_{iso}$, the PSO mechanism is more important for the group 13 fluorides than for the alkali metal fluorides. The group 13 halides are of particular interest owing to the accurate experimental data available for thallium fluoride and indium fluoride. As mentioned above, $^{205}Tl^{19}F$ exhibits an extremely large spin-spin coupling anisotropy, ($\Delta K = 173 \times 10^{20}$ N A$^{-2}$ m$^{-3}$). Although accurate *ab initio* calculations of the **J** tensor for TlF are not currently feasible, the trend in $\Delta K$ illustrated by the results for BF and AlF in Table 4.4

indicates that the theoretical predictions are in line with the experimental anisotropy observed for InF and TlF (see Figure 4.3). The results for BF are in contrast with one of the conclusions of Buckingham and Love (*357*), who indicate that for molecules containing light atoms, the FC x SD term is the most important contribution to $\Delta K$. The present results demonstrate that for BF, the paramagnetic spin-orbit mechanism is the origin of more than 60% of the total anisotropy.

The results for ClF are very important in the context of the present work. This is due to the fact that this molecule exhibits an exceptionally large indirect spin-spin coupling anisotropy for a compound composed of only first- and second-row elements (see expt. data, Table 4.2), and is within the reach of high-level MCSCF calculations. Owing to the accuracy of the calculated results (Table 4.2), confidence can be placed in the overall accuracy of the method. This is very useful since the calculations provide the contributions from each individual mechanism, while experiments can only yield the two principal components of the total **J** tensor ($J_\perp$ and $J_\parallel$). Such a breakdown into the various contributions is indispensable in the interpretation of spin-spin couplings. In an attempt to update the results of Pople and Santry on the isotropic couplings and of Buckingham and Love on the anisotropic couplings, a summary of the trends observed is presented in Figure 4.5. Only for the diatomics composed solely of *s*-block elements does the FC mechanism completely dominate, making the $\Delta J$ values essentially negligible. The trends in Figure 4.5 are investigated further through a systematic study of the interhalogen diatomics (*vide infra*).

It is now common practice by many scientists to refer to indirect spin-spin

coupling constants as *scalar* coupling constants (*324*, *420*). This is clearly misleading. Also, the contribution that $\Delta J$ makes to the dipole-dipole relaxation mechanism is either not recognized or ignored even though this was identified by Blicharski in 1972 (*256*, *421*). In fact, relaxation *via* the indirect spin-spin coupling tensor is entirely analogous to relaxation by the direct dipolar interaction; the two cannot be separated.

As mentioned in the Introduction, one of the important applications of the understanding of spin-spin coupling mechanisms is the accurate measurement of internuclear distances. Since the contributions to $R_{eff}$ from $\Delta J$ and $R_{DD}$ are inseparable, knowledge of periodic trends in the $\Delta J/R_{DD}$ ratio is essential if one wishes to determine

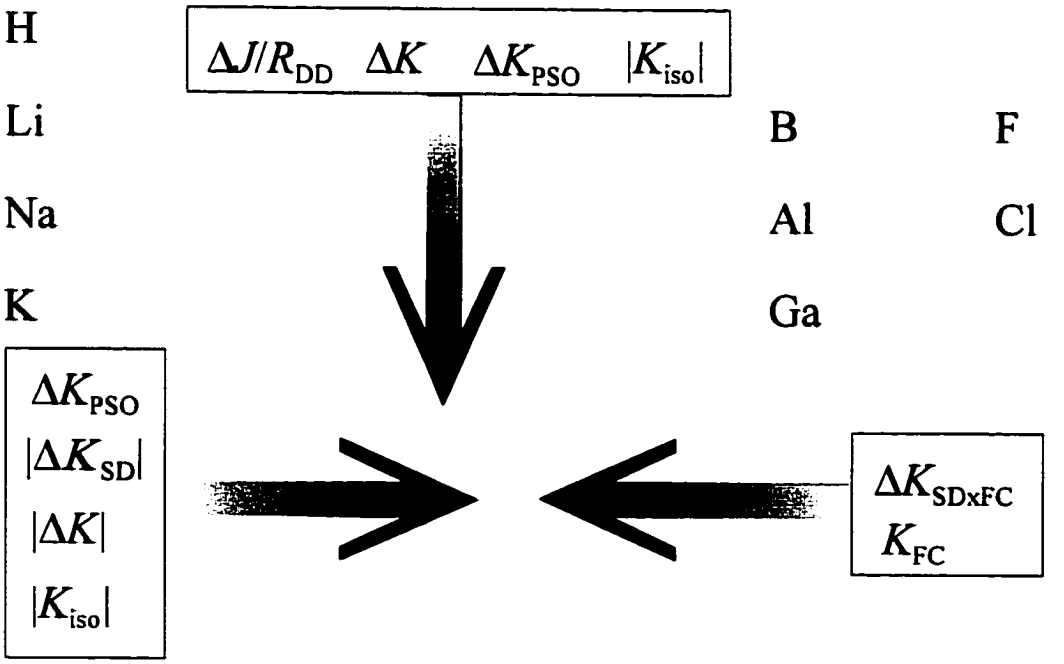


Figure 4.5: A summary of some of the observations made in the present work on diatomic fluorides, FX. A partial periodic table (indicating the nature of X) orients the reader. The large arrows indicate the direction of increasing magnitude of the properties listed at the base of the arrow. For example, $\Delta K_{SDxFC}$ and $K_{FC}$ increase from right to left across the periodic table as X is changed.

reliable internuclear distances from any NMR experiment. Although the case of the thallium halides is extreme, it demonstrates the fact that dipolar recoupling experiments should be interpreted with caution. Shown in Table 4.5 are the $\Delta J/R_{DD}$ percentages for the molecules examined herein. Some nuclei which are commonly involved in heteronuclear recoupling experiments are represented in this table: $^{19}F$ (*422*), $^{11}B$ (*423*), and $^{27}Al$ (*424*), for example. Buckingham and Love (*357*) concluded that for molecules containing light atoms (*i.e.*, up to fluorine), the anisotropy in the indirect spin-spin coupling should be less than 1% of the anisotropy in the direct dipolar tensor, $-3R_{DD}$; the present results confirm this conclusion. Although it could be argued that the $\Delta J$ contribution is negligible compared to the direct dipolar contribution for HF, LiH, BF, LiF, and HCl, it is clear that its effect cannot be ignored for the other molecules presented. However, one must also bear in mind that the $\Delta J$ term is always reduced by a factor of three when contributing to $R_{eff}$. In real systems, the combination of rovibrational averaging of $R_{eff}$ and unknown $\Delta J$ contributions should be given serious consideration in the interpretation of NMR data to yield internuclear distances. In the solid state, molecular librations in the lattice will also affect the observed dipolar coupling constant. As pointed out by Brouwer *et al.* (*422*), the $\Delta J$ contribution is generally negligible in cases where the dipolar coupling occurs between nuclei of two separate molecules.

Shown in Table 4.6 are the reduced spin-spin coupling tensors and relative anisotropy ratios for another series of diatomics for which there are precise experimental data available, but for which MCSCF calculations are not feasible at present due to computational limitations.

**Table 4.6:** Reduced spin-spin coupling tensors and relative anisotropy ratios derived from available experimental hyperfine data

| | $K_{iso}$ / $10^{20}$ N A$^{-2}$ m$^{-3}$ | $\Delta K$ / $10^{20}$ N A$^{-2}$ m$^{-3}$ | $\Delta J/J_{iso}$ (%) | $\Delta J/R_{DD}$ (%) | Ref.[a] |
|---|---|---|---|---|---|
| $^{7}Li^{79}Br$ | 5.15 | 18.1 | 351 | 19 | *425* |
| $^{23}Na^{79}Br$ | 9.76 | 43.9 | 450 | 69 | *426* |
| $^{7}Li^{127}I$ | 6.65 | 18.4 | 277 | 25 | *427* |
| $^{133}CsF$ | 41.8 | 46.5 | 111 | 60 | *428* |
| $^{133}Cs^{35}Cl$ | 39.4 | 67.9 | 172 | 167 | *429* |
| $^{115}InF$ | -86.4 | 89.9 | -104 | 66 | *415* |
| $^{35}ClF$ | 75.7 | -81.8 | -108 | -35 | *266* |
| $^{79}BrF$ | 171 | -206 | -120 | -113 | *430* |
| $^{127}IF$ | 252 | -257 | -102 | -179 | *430* |
| $^{205}TlF$ | -202 | 173 | -85.6 | 156 | *404* |
| $^{205}Tl^{35}Cl$ | -224 | 262 | -117 | 400 | *416* |
| $^{205}Tl^{81}Br$ | -361 | 448 | -124 | 800 | *417* |
| $^{205}Tl^{127}I$ | -474 | 664 | -140 | 1470 | *418* |

Chlorine monofluoride is also included for comparison with BrF and IF. Values for $\Delta J$ were determined from the experimental $c_3$ values and from the rovibrationally-averaged direct-dipolar coupling constants. $\Delta J$ is significant compared to $R_{DD}$ for all of these molecules. The results confirm some of the trends observed as a consequence of the MCSCF calculations on smaller molecules. For example, in addition to the series of thallium halides, the spin-spin couplings in the halofluorides (ClF, BrF, and IF) clearly demonstrate that as the atomic number of the halide bonded to fluorine increases, both

[a]Reference to original hyperfine data.

components of the tensor increase in magnitude (see Figure 4.6), while $\Delta J/J_{iso}$ remains relatively constant, and $\Delta J/R_{DD}$ increases.

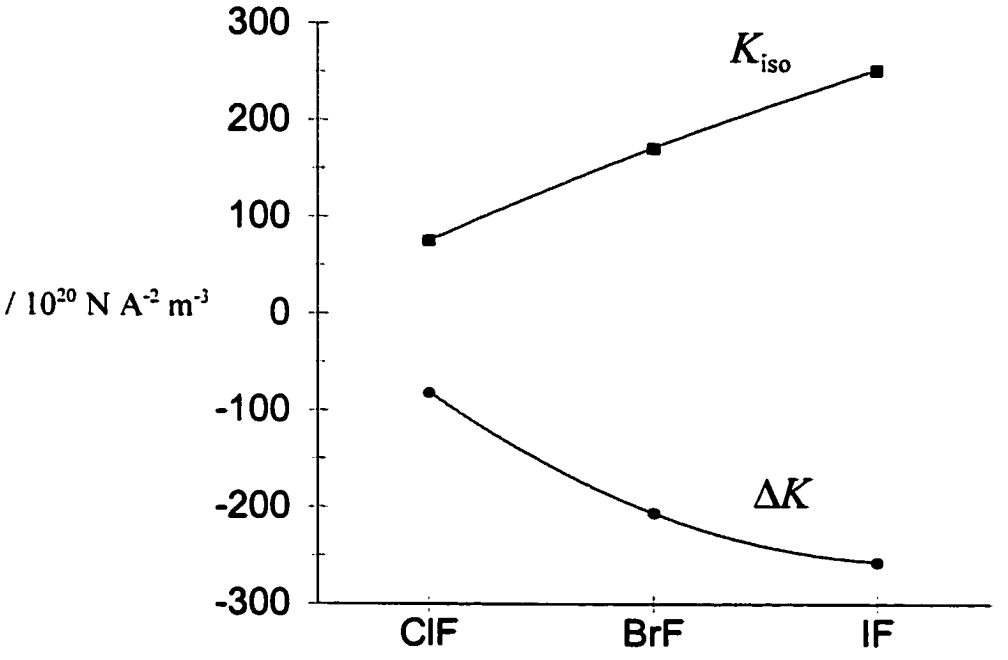


Figure 4.6: Experimental values for $K_{iso}$ and $\Delta K$ for ClF, BrF, and IF, which have been calculated from experimental hyperfine data. The values are for the particular rovibrational states given in the text. The dotted lines serve as guides to the trends.

*4.3.2 ZORA-DFT Calculations for Interhalogen Diatomics*

As an extension of the work presented in the previous section to examine periodic trends in **J** tensors involving heavier nuclei, the interhalogen diatomics have been examined using the relativistic ZORA-DFT computational method.

Shown in Table 4.7 are the available magnetic hyperfine data for the ground $^1\Sigma_g^+$ electronic state of molecular iodine, $I_2$ (*431*). Stimulated Raman spectroscopy has provided the hyperfine parameters $d$ and $\delta$. The parameter $d$ is equal to the effective dipolar coupling constant, $R_{eff}$, and the parameters $\delta$ and $c_4$ are equal to $J_{iso}$ (*41*, *48*, *49*). Wallerand *et al.* (*431*) were able to determine values for $c_3$ and $c_4$ for two rovibrational states ($v = 0, J = 13$ and $v = 0, J = 15$). The rovibrationally-averaged value of the direct dipolar coupling constant, $R_{DD}$, is determined using the equilibrium bond length of 2.66614 Å (*388*) and the averaging procedure described in section 4.2. As shown in Table 4.7, there is a slight rotational dependence of the two hyperfine constants; however, the values for the two rotational states are identical within experimental error. Analogous experimental data have also been discussed for the excited electronic $B^3\Pi_{0u}^+$ state of iodine (*432*, *433*). The iodine data are particularly interesting from an NMR spectroscopist's point of view, since coupling between magnetically equivalent nuclei is not typically observed in NMR experiments. It is important to note that the negative experimental value of $\Delta J$ implies that the largest component of the **J** tensor lies perpendicular to the bond axis rather than along it (Figure 4.7). This orientation for **J** is consistent for all of the interhalogen couplings discussed herein (*vide infra*).

**Table 4.7**: Experimental and calculated[a] indirect nuclear spin-spin coupling data for the ground $^1\Sigma_g^+$ electronic state of iodine, $^{127}I_2$.

| Method | Basis set or rovibrational state | $c_3$ / Hz | $R_{DD}$ / Hz | $\Delta J$ / Hz | $c_4$ (= $J_{iso}$) / Hz | $\Delta K$ / $10^{20}$ N A$^{-2}$ m$^{-3}$ | $K_{iso}$ / $10^{20}$ N A$^{-2}$ m$^{-3}$ |
|---|---|---|---|---|---|---|---|
| scalar-GGA | ZORA IV | - | - | -6536 | 6254 | -1345 | 1287 |
| scalar-GGA | ZORA V | - | - | -5663 | 5418 | -1165 | 1115 |
| so-GGA | ZORA IV | - | - | -5535 | 4791 | -1139 | 986 |
| so-GGA | ZORA V | - | - | -4941 | 4263 | -1017 | 877 |
| experiment | $v = 0, J = 13$ | 1528 ± 18 | 257 | -3814 ± 54 | 3708 ± 22 | -785 ± 11 | 763 ± 5 |
| experiment | $v = 0, J = 15$ | 1519 ± 18 | 257 | -3787 ± 54 | 3701 ± 23 | -779 ± 11 | 762 ± 5 |

[a] Calculated values are at the equilibrium bond length.

Molecular beam magnetic resonance spectroscopy was applied in 1980 by Yokozeki and Muenter (*434*) to provide values of $c_3$ and $c_4$ similar to those shown in Table 4.7; however, the Raman study has improved the precision to which these parameters are known. In 1981, Pyykkö and Wiesenfeld (*435*) attempted to calculate the **K** coupling tensors for molecular iodine using a relativistically parameterized extended Hückel (REX) calculation, and compared their results to the molecular beam data (*434*). The REX method provided a value of -99.7 x $10^{20}$ N $A^{-2}m^{-3}$ for $K_{iso}$ which is clearly of the wrong sign and magnitude when compared to the experimental data (Table 4.7).

The indirect nuclear spin-spin coupling tensor for molecular iodine therefore represents a stringent test of the ZORA-DFT method, especially given the very small errors associated with the experimental data. It is important to emphasize that the

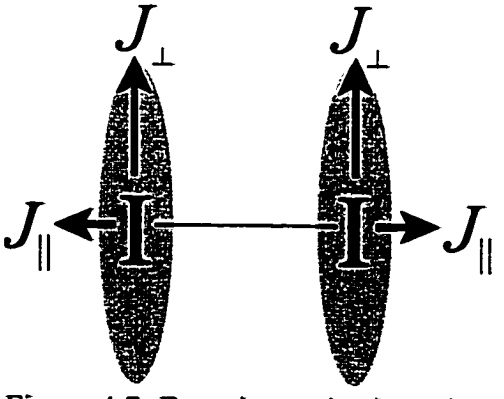


Figure 4.7: Experimental orientation of the **J**($^{127}$I, $^{127}$I) tensor for molecular iodine in its ground electronic state. The larger component of the coupling tensor lies perpendicular to the bond axis, $J_{\perp} = 4979$ Hz, and the smaller component lies along the bond axis, $J_{\parallel} = 1165$ Hz (values for the $v = 0$, $J = 13$ state).

experimental data are for relatively isolated molecules in the gas phase (1 mTorr pressure) and the resulting lack of intermolecular effects make the data ideal for comparisons with calculated results, which are carried out on isolated single molecules. The results of scalar and spin-orbit relativistic calculations of the **K** tensor for iodine are presented in Table 4.7. The fact that the sign and order of magnitude of both $K_{iso}$ and $\Delta K$ are reproduced by the calculations is an important success. For the scalar relativistic calculation on $I_2$ with the ZORA IV basis set, the isotropic and anisotropic coupling constants are overestimated by approximately 70 %. However, the improvement obtained when spin-orbit relativistic effects are included and the ZORA V basis set is used is remarkable; the calculated equilibrium value of $J_{iso}$, 4263 Hz, overestimates the experimental $v = 0$ values by only 15 %. Similarly, the agreement between the experimental and calculated values of $\Delta J$ improves substantially when spin-orbit relativistic effects are included. The remaining overestimation of the isotropic and anisotropic coupling constants by the calculations can likely be attributed to deficiencies of the density functional. It has previously been noted that with standard GGA functionals, the PSO term tends to be overestimated in magnitude, and thus the coupling constants of systems in which the PSO term clearly dominates are often too large (*121*, *370*, *371*, *372*, *436*). The missing treatment of the self-interaction correction (SIC) is an important factor here (*436*).

REX calculations were carried out by Pyykkö and Wiesenfeld for $Cl_2$ and $Br_2$ in addition to iodine; however, they conclude their section on the dihalogens by stating that it is difficult to say whether the REX results are meaningful, and that they consider the

issue of the sign and magnitude of dihalogen coupling constants unsettled (*435*). In an effort to resolve the issues of the sign, magnitude, and periodic trends in the spin-spin coupling tensors of the dihalogen molecules, so-GGA ZORA calculations of the **J** tensors for all five homonuclear dihalogen molecules have been performed (Table 4.8). While relativistic effects are surely minor for a molecule as light as fluorine, the same computational methods have been applied to all of the molecules for consistency. The reduced spin-spin coupling constants, $K_{iso}$, as well as the reduced anisotropic coupling constants, $\Delta K$, increase in magnitude for $Cl_2$ through $At_2$. Fluorine is an exception to this trend; $K_{iso}$ for fluorine is larger than that for $Cl_2$, but smaller than that for $Br_2$. The earlier REX calculations (*435*) provide $K_{iso}$ values of $-17.0 \times 10^{20}$ N $A^{-2}m^{-3}$ for $Cl_2$ and $+24.1 \times 10^{20}$ N $A^{-2}m^{-3}$ for $Br_2$. Buckingham and Love's (*357*) LCAO calculation of the **K** coupling tensor for $F_2$ gives $K_{iso} = -95.4 \times 10^{20}$ N $A^{-2}m^{-3}$ and $\Delta K = 13.9 \times 10^{20}$ N $A^{-2}m^{-3}$; all of these early data are clearly in disagreement with the results presented in Table 4.8.

**Table 4.8**: Summary of calculated[a] indirect nuclear spin-spin coupling tensors for homonuclear dihalogens.

| Molecule | $J_{iso}$ / Hz | $\Delta J$ / Hz | $K_{iso}$ / $10^{20}$ N A$^{-2}$ m$^{-3}$ | $\Delta K$ / $10^{20}$ N A$^{-2}$ m$^{-3}$ | % PSO for $K_{iso}$ | % FC + SD (+PSO cross term) for $K_{iso}$ |
|---|---|---|---|---|---|---|
| $^{19}F_2$ | 13182 | -13484 | 123.9 | -126.7 | 67 | 33 |
| $^{19}F_2$ (MCSCF/RAS) | 12676 | -11821 | 119.1 | -111.1 | 63 | 37 |
| $^{35}Cl_2$ | 119 | -138 | 102.8 | -118.8 | 78 | 22 |
| $^{81}Br_2$ | 4109 | -4461 | 466.1 | -506.4 | 75 | 25 |
| $^{127}I_2$ | 4263 | -4941 | 877 | -1017 | 79 | 21 |
| $At_2$ | - | - | 2738 | -2735 | 100 | 0 |

[a] so-GGA method, with ZORA V basis set on all atoms, except where otherwise indicated.

To confirm the result obtained using ZORA-DFT methods for fluorine, a MCSCF calculation using a RAS wave function was performed. The comparison of the two methods shown in Table 4.8 is very encouraging. Although there are no experimental data for comparison with the calculated coupling tensors in $F_2$, the DFT and MCSCF methods are in remarkable agreement both with respect to the isotropic and anisotropic portions of the coupling tensor, and also with respect to the relative importance of the coupling mechanisms to $K_{iso}$. For all of the diatomics except astatine, the relative importance of the PSO and FC+SD terms to $K_{iso}$ is approximately constant. The PSO term is the dominant contributor at ~ 70 - 80 %, demonstrating again that caution should be exercised when attempting to interpret spin-spin couplings solely in terms of the Fermi-contact mechanism. The dominance of the PSO term seems to increase slightly as the atomic number of the halogen is increased. Calculations for $Cl_2$, $Br_2$, $I_2$, and $At_2$ using the relativistic scalar-GGA and so-GGA methods indicate that the improvement in $J_{iso}$ induced by adding the spin-orbit relativistic correction increases from 2 % in $Cl_2$ to 11 % in $Br_2$ to 21 % in $I_2$ to 52 % in $At_2$ (*437*).

To further examine the dependence of the reduced coupling tensor on the nature of the halogen atom in interhalogen compounds, results for heteronuclear diatomic halogens are presented in Table 4.9. Experimental data are available for comparison with ClF (*266*), and BrF and IF (*430*). ZORA-DFT results for ClF, BrF, and IF were presented in reference *121*. Results for the other diatomics in Table 4.9 further confirm the relative importance of the PSO and FC+SD coupling mechanisms. In Ramsey's original formalism for spin-spin coupling tensors (*40*), all of the coupling mechanisms except the

Fermi-contact mechanism depend on the expectation value of the inverse cube of the electron-nuclear distance, $\langle r^{-3} \rangle$. This quantity in turn varies periodically with the atomic number, $Z^{(N)}$, of the nucleus in question (*346*, *438*). Attempts have been made to correlate known reduced coupling constants with the square of the atomic number in a series of molecules where one nucleus is fixed, e.g., fluorine (*348*, *439*). In the present work, the atomic numbers of both coupled nuclei are varied. Shown in Figure 4.8 are the calculated values of $K_{iso}$ and $\Delta K$ for all of the interhalogens plotted as a function of the product of the atomic numbers of the nuclei involved, $Z^{(1)}Z^{(2)}$. A good linear correlation is observed, with values of the correlation coefficient $R^2$ in excess of 0.99 for both $K_{iso}$ and $\Delta K$, including the data for $F_2$. As noted above, the values for $F_2$ are higher than one would predict based on a simple $Z^{(1)}Z^{(2)}$ dependence. This discrepancy may be rationalized by considering that the expectation value $\langle r^{-3} \rangle$ for fluorine, 7.546 a.u., is *greater* than that for chlorine, 6.7095 a.u. (*440*).

**Table 4.9**: Summary of calculated[a] equilibrium indirect nuclear spin-spin coupling tensors for heteronuclear dihalogens. Experimental values of $J_{iso}$ and $\Delta J$ are included for comparison[b].

| Molecule | Experimental $J_{iso}$ / Hz | $J_{iso}$ / Hz | Experimental $\Delta J$ / Hz | $\Delta J$ / Hz | $K_{iso}$ / $10^{20}$ N $A^{-2}$ $m^{-3}$ | $\Delta K$ / $10^{20}$ N $A^{-2}$ $m^{-3}$ | % PSO for $K_{iso}$ | % FC + SD (+ PSO cross term) for $K_{iso}$ |
|---|---|---|---|---|---|---|---|---|
| $^{35}Cl^{19}F$ | 840 | 969 | -907 | -1143 | 87.4 | -103.1 | 78 | 22 |
| $^{35}Cl^{19}F$[c] | 840 | 722 | -907 | -774 | 65.1 | -69.8 | 79 | 21 |
| $^{35}Cl^{81}Br$ | - | 711 | - | -788 | 222.9 | -246.9 | 75 | 25 |
| $^{35}Cl^{127}I$ | - | 678 | - | -801 | 286.1 | -337.8 | 78 | 22 |
| $^{81}Br^{19}F$ | 5240 | 5648 | -6306 | -6420 | 184.4 | -209.6 | 75 | 25 |
| $^{81}Br^{127}I$ | - | 3993 | - | -4538 | 610 | -693.4 | 76 | 24 |
| $^{127}I^{19}F$ | 5730 | 4908 | -5856 | -6223 | 215.8 | -273.6 | 80 | 20 |

[a] so-GGA method, with ZORA V basis set on all atoms, except where otherwise indicated.

[b] Experimental data are for the $v = 0, J = 1$ rovibrational state. References are given in the text.

[c] MCSCF/RAS calculation.

It is interesting to note that reliable experimental coupling tensors are available from Cederberg and co-workers for several alkali metal halides involving heavy nuclei, e.g., LiI (*427*), CsF (*428*), CsCl (*429*); the values of both $K_{iso}$ and $\Delta K$ for these molecules are generally significantly less than those for the interhalogen compounds discussed presently. This is in agreement with the periodic trends evident from the MCSCF calculations (Figure 4.5) on a series of lighter diatomics, i.e, that the absolute values of both $K_{iso}$ and $\Delta K$ increase from left to right across the periodic table.

Jameson and Osten have presented a comprehensive analysis of isotope effects on spin-spin coupling, including the effects of bond extension on **K** (*441*, *442*). In particular, the possible effects of lone pairs on the derivatives of the spin-spin coupling constant with respect to bond length, $(\partial K_{iso} / \partial r)_{r_e}$, are discussed. For a Se-H bond, for example, it is postulated that a possible negative Fermi-contact contribution to this derivative may arise as a result of lone pairs with *s* character. Since it is the PSO term which is dominant for the interhalogen couplings discussed here, it is of interest to determine the dependence of these couplings on bond length. Presented in Table 4.10 are the calculated derivatives of the isotropic and anisotropic reduced spin-spin coupling constants for all of the interhalogen diatomics. Shown in Figure 4.9 is an example of the plots which were generated to determine the derivatives of the coupling constants near the equilibrium bond length. The data shown are for iodine, which has an equilibrium bond length of 2.66614 Å (*239*). For comparison, it is noted that the derivatives $(\partial K_{iso} / \partial r)_{r_e}$ for the interhalogens are all one to two orders of magnitude larger than the corresponding values summarized by Jameson (*442*) for couplings involving hydrogen,

e.g., for the phosphorus-hydrogen spin pair in phosphine, $(\partial K_{iso} / \partial r)_{re}$ is -42.2 × $10^{20}$ N $A^{-2}m^{-3}$ per Å and for the tin-hydrogen spin pair in $SnH_3^-$, $(\partial K_{iso} / \partial r)_{re}$ is -58.0 ± 4.0 × $10^{20}$ N $A^{-2}m^{-3}$ per Å.

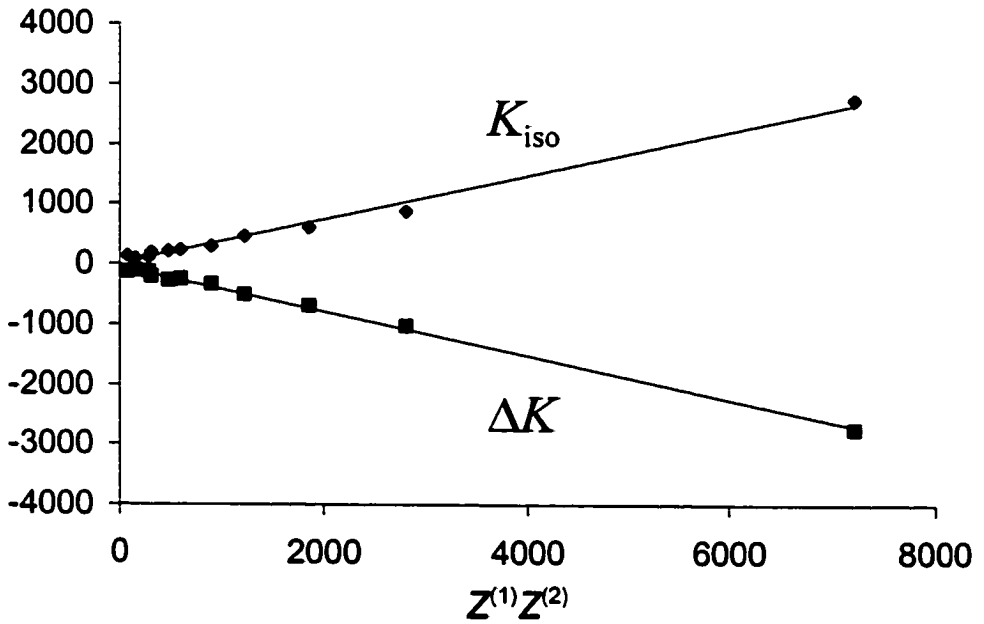


Figure 4.8: Calculated trends in the reduced isotropic ($K_{iso}$) and anisotropic ($\Delta K$) portions of the indirect nuclear spin-spin coupling tensors for interhalogen diatomics. The so-GGA ZORA DFT data are plotted as a function of the product of the atomic numbers of the coupled nuclei, $Z^{(1)}Z^{(2)}$. The units for the coupling constants are $10^{20}$ N $A^{-2}m^{-3}$. The data, including those for $F_2$, were fit to the following linear equations: $K_{iso} = 0.3669(Z^{(1)}Z^{(2)}) + 6.552$, $R^2 = 0.9908$ and $\Delta K = -0.3674(Z^{(1)}Z^{(2)}) - 47.019$, $R^2 = 0.9972$. For convenience, the atomic numbers of the halogens are: 9 for fluorine, 17 for chlorine, 35 for bromine, 53 for iodine, and 85 for astatine.

**Table 4.10**: Calculated[a] derivatives of the isotropic and anisotropic portions of the indirect nuclear spin-spin coupling tensors for diatomic halogens[b].

| Molecule | $r_e$ / Å | $(\partial K_{iso} / \partial r)_{re}$ m = slope / $10^{20}$ N A$^{-2}$ m$^{-3}$ per Å | $(\partial(\Delta K) / \partial r)_{re}$ m = slope / $10^{20}$ N A$^{-2}$ m$^{-3}$ per Å |
|---|---|---|---|
| $F_2$ | 1.41193 | 492 | -317 |
| $F_2$ (MCSCF/RAS) | 1.41193 | 536 | -303 |
| ClF | 1.628332 | 338 | -248 |
| ClF (MCSCF/RAS) | 1.628332 | 270 | -185 |
| BrF | 1.75894 | 521 | -401 |
| IF | 1.90975 | 475 | -320 |
| $Cl_2$ | 1.9885 | 317 | -245 |
| ClBr | 2.13606 | 504 | -420 |
| $Br_2$ | 2.28105 | 816 | -782 |
| ClI | 2.32087 | 475 | -375 |
| BrI | 2.46898 | 810 | -800 |
| $I_2$ | 2.66614 | 982 | -1097 |

In addition to the small rotational dependence of the coupling tensor for $I_2$ shown in Table 4.7, the vibrational dependence of the coupling tensor for BrF is also known experimentally (*430*). Experimentally for BrF, $K_{iso}$ increases from 171(9) × $10^{20}$ N A$^{-2}$ m$^{-3}$ for the $v = 0$ vibrational state to 228(30) × $10^{20}$ NA$^{-2}$m$^{-3}$ for the $v = 1$ state. The

[a] so-GGA method, with ZORA V basis set on all atoms, unless otherwise indicated.

[b] Results are fit to the linear equation $K = mr + b$, with correlation coefficient $R^2$. Values of $R^2$ are greater than 0.999 for all molecules.

data for the two states convincingly demonstrate that $K_{iso}$ increases as the bond length is increased, which is the calculated trend for all of the diatomics in Table 4.10, *i.e.*, $(\partial K_{iso} / \partial r)_{re}$ is positive. The experimental values of $\Delta K$ in BrF are -206(25) × $10^{20}$ N $A^{-2}$ $m^{-3}$ for $v = 0$ and -183(27) × $10^{20}$ N $A^{-2}m^{-3}$ for $v = 1$. The apparent bond length dependence ($(\partial(\Delta K) / \partial r)_{re} > 0$) is in contradiction with the calculated derivative;

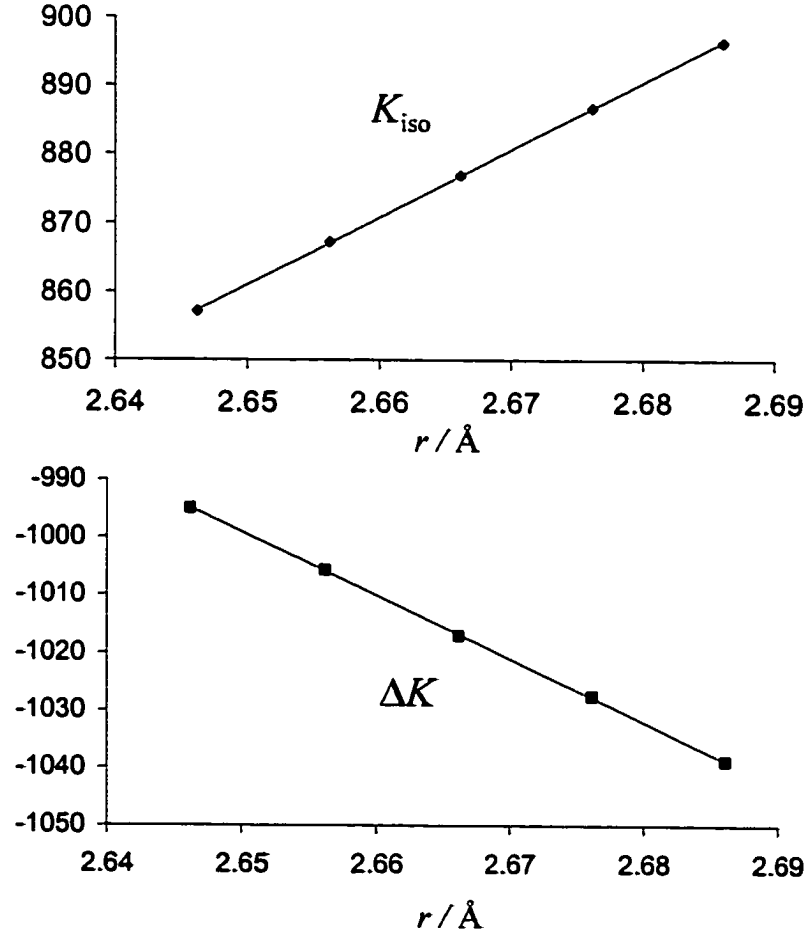


Figure 4.9:Plots of the reduced isotropic (top) and anisotropic (bottom) portions of the indirect nuclear spin-spin coupling tensors for iodine as a function of bond length. The equilibrium bond length for iodine is 2.66614 Å. The units for the coupling constants are $10^{20}$ N $A^{-2}m^{-3}$. The data were fit to a linear equation to yield the following relationships (see Table 4.10): $K_{iso} = 982(r / Å) - 1741$ and $\Delta K = -1097(r / Å) + 1908$.

however, the error bars on the experimental values overlap. For iodine, the experimental data for the two rotational states are identical within error. The calculated derivatives are $(\partial K_{iso} / \partial r)_{re} = 982 \times 10^{20}$ N A$^{-2}$m$^{-3}$ per Å and $(\partial(\Delta K) / \partial r)_{re} = -1097 \times 10^{20}$ N A$^{-2}$m$^{-3}$ per Å. It is important to recognize that the ZORA-DFT derivatives for all of the compounds, $(\partial K_{iso} / \partial r)_{re} > 0$ and $(\partial(\Delta K) / \partial r)_{re} < 0$, are in agreement with the MCSCF derivatives determined for $F_2$ and ClF.

## 4.4 Application: Probing Hydrogen Bonds via J Tensors

One of the most spectacular developments in NMR in recent years has been the observation of unexpectedly large *J* couplings (~ 7-10 Hz) between heavy nuclei (*i.e.*, non-hydrogen atoms) across hydrogen bonds. The first such reports were concerned with $^{15}N$-$^{15}N$ *J* coupling in RNA (*325*) and DNA (*443*). Subsequently, an abundance of these couplings have been detected (*326*, *444*, *445*, *446*, *447*, *448*). In addition to $^{2h}J(^{15}N, ^{15}N)$, many reports of *J* couplings across hydrogen bonds involving other nuclei have been reported, e.g., $^{h}J(^{15}N, ^{13}C)$ (*449*, *328*, *450*, *451*), $^{2h}J(^{1}H, ^{13}C)$ (*452*), $^{2h}J(^{1}H, ^{1}H)$ (*453*), $^{2h}J(^{31}P, ^{1}H)$ and $^{3h}J(^{31}P, ^{15}N)$ (*454*, *455*).

In this section, the results of MCSCF and ZORA-DFT calculations of the complete $^{2h}\mathbf{J}(^{15}N, ^{15}N)$ tensor[a] for a simple model system, the dimer of methyleneimine (Figure 4.10), are presented. Use of this system models the $^{2h}\mathbf{J}(N, N)$ tensor of nucleic

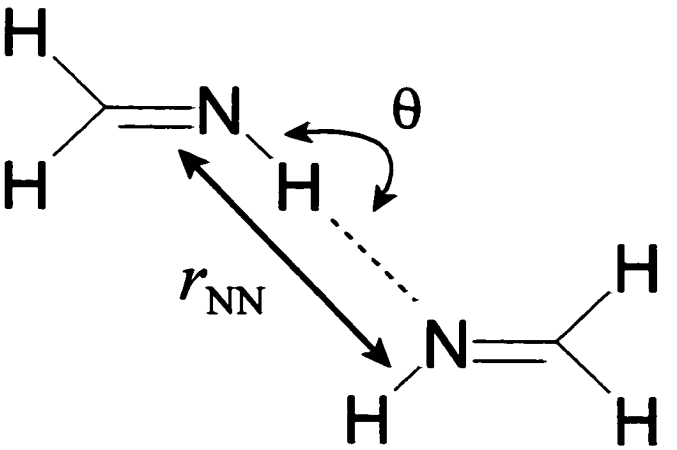


Figure 4.10: Methyleneimine dimer model for nucleic acid base pairs used for the calculation of $^{2h}\mathbf{J}(N, N)$ tensors.

[a]All results reported herein are for $^{15}N$-$^{15}N$ couplings.

acid base pairs, the building blocks of DNA and RNA. It must be emphasized that accurate high-level *ab initio* calculations of complete **J** tensors for much larger molecular fragments are impractical at this time. Also, from a more fundamental point of view, it is advantageous to study relatively simple model systems where the effects of specific variables such as hydrogen bond length and bond angle may be systematically investigated. There have been few previous computational studies of couplings between nitrogen atoms across hydrogen bonds (*326*, *329*, *456*, *457*, *458*, *459*). Of these studies, only Pecul and co-workers have employed the MCSCF approach to calculating $^{2h}J_{iso}$(N, N) (*459*).

Shown in Figure 4.11 is a plot of the isotropic and anisotropic portions of $^{2h}$**J**(N, N) as a function of the nitrogen-nitrogen separation ($r_{NN}$), with the N-H···N angle fixed at 180°. The magnitude of the isotropic portion decays exponentially as a function of $r_{NN}$ (eq. 1, $R^2 = 0.9959$); however, the fit tends to get worse for very small values of $r_{NN}$. The datum for $r_{NN} = 2.02$ Å has not been included in the fits (eqs. 4.7 and 4.8) because at this separation, one of the nitrogen-hydrogen distances is reduced to less than the equilibrium value.

$$^{2h}J_{iso}(N, N) / Hz = 9640 \exp(-2.73\, r_{NN}) \quad [4.7]$$

$$r_{NN} / Å = -0.37 \ln(^{2h}J_{iso}(N, N)) + 3.36 \quad [4.8]$$

Calculations using the ZORA-DFT method on the same system yields the following relationships:

$$^{2h}J_{iso}(N, N) / Hz = 9516 \exp(-2.77\, r_{NN}) \quad [4.9]$$

$$r_{NN} / Å = -0.36 \ln(^{2h}J_{iso}(N, N)) + 3.31 \quad [4.10]$$

which are in remarkably good agreement with the MCSCF results.

An analogous correlation between hydrogen bond length in proteins and $^{3h}J_{iso}$(N, C) has been described by Cornilescu *et al.* (*451*), based on experimental data. Typical N-N separations across nucleic acid base pairs are approximately 2.8 - 2.9 Å, although there are cases where the separation can be anomalously small, e.g., 2.2 - 2.6 Å (*460*). The correlations obtained in equations 4.7 - 4.10 are reasonable when compared to existing experimental data. For example, the experimentally observed value of $^{2h}J_{iso}$(N, N) in Watson-Crick base pairs ranges from approximately 6 to 8 Hz and in Hoogsteen base pairs from about 7 to 10 Hz (*326*). Employing equation 4.7 and standard N-N separations (2.8 - 2.9 Å) gives values of 3.5 - 4.6 Hz for $^{2h}J_{iso}$(N, N). Using a typical value of 7 Hz for $^{2h}J_{iso}$(N, N) in equation 4.8 yields a short but certainly reasonable N-N

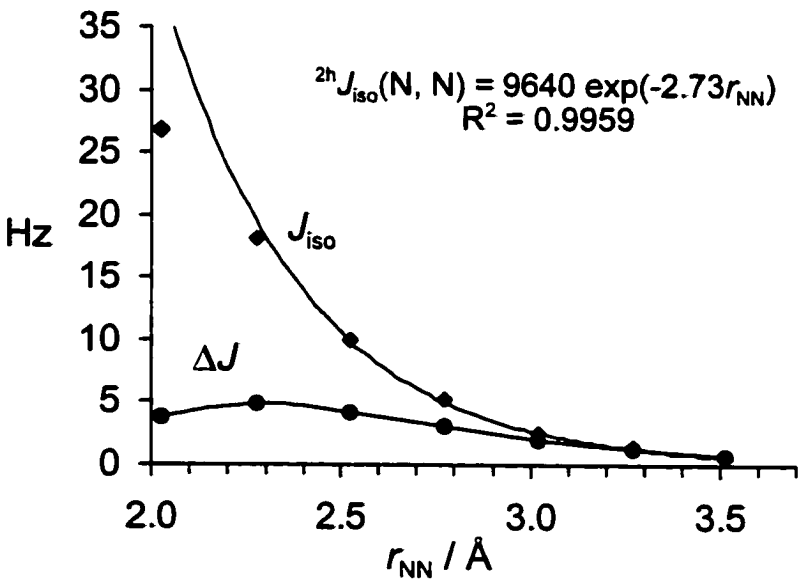


Figure 4.11: MCSCF results for $^{2h}$J(N,N) for the methyleneimine dimer as a function of nitrogen-nitrogen distance.

distance of 2.64 Å.

Although the reliability of calculated **J** tensors has increased greatly in the past several years, it should be emphasized that the computational results should not be regarded as being accurate to better than 10%. Regardless of the computational technique and model system employed, if such a level of accuracy were desired, rovibrational corrections would be required to account for the fact that the calculations are performed at the equilibrium geometry while experimental data are inevitably for molecules in particular rovibrational states. Additionally, quantitative comparison between experiment and theory necessitates a consideration of medium effects on the coupling tensor (*362*). The main intent here is to study *trends* in the **J** tensor as a function of hydrogen bond geometry. Independent of the nitrogen-nitrogen distance, the FC mechanism dominates (97-99%) the isotropic coupling. The dominance of the FC term was also noted by Del Bene *et al.* (*457*) and Pecul *et al.* (*459*). It is important to note, however, that despite this dominance, the anisotropic portion of $^{2h}$**J**(N, N) is not insignificant compared to $^{2h}J_{iso}$(N, N) (Figure 4.11). In fact, for very long hydrogen bonds, the magnitude of $\Delta J$ equals and even surpasses the magnitude of the isotropic portion. Contributions to $\Delta J$ are dominated by the FC x SD cross term. The asymmetry of the **J** tensor, $\eta_J$, decreases smoothly from 0.47 to 0.20 as the nitrogen-nitrogen distance is increased over the range shown in Figure 4.11.

It has been suggested that the dominant factor in determining the value of $^{2h}J_{iso}$(N, N) is the nitrogen-nitrogen distance (*457*, *459*). To test this hypothesis, calculations of $^{2h}$**J**(N, N) as a function of the N-H···N bond angle, while holding the $N_{donor}$-H and $N_{acceptor}$···H separations fixed at 1.02 Å and 1.75 Å, respectively, have been

performed. The results are presented in Figure 4.12. When the angle is reduced from 180° to 170°, there is a slight decrease in the value of $^{2h}J_{iso}$(N, N). However, as the angle is diminished further, to 140°, $^{2h}J_{iso}$(N, N) increases to 8.3 Hz. The FC mechanism dominates the **J** tensor regardless of the N-H···N bond angle. The value of $\Delta J$ is less sensitive to the bond angle than is $J_{iso}$, and remains constant at about 3 Hz. Majumdar and co-workers (*445*) have reported a comparatively small value for $^{2h}J_{iso}$(N, N) in an A-A mismatch segment of DNA (2.45 Hz); it has been proposed (*445*, *447*) that the reason for the reduced value of the coupling constant is due to an unusual hydrogen bond geometry. In addition to the possibility that the N-N distance in the A-A mismatch is simply longer than in typical nucleic acid base pairs, consideration of the data presented in Figure 4.12 indicates that a slight deviation from linearity of the hydrogen bond (~ 170°) could also contribute to the reduced value of $^{2h}J_{iso}$(N, N).

Although the anisotropy of $^{2h}$**J**(N, N) is small for all of the geometries considered

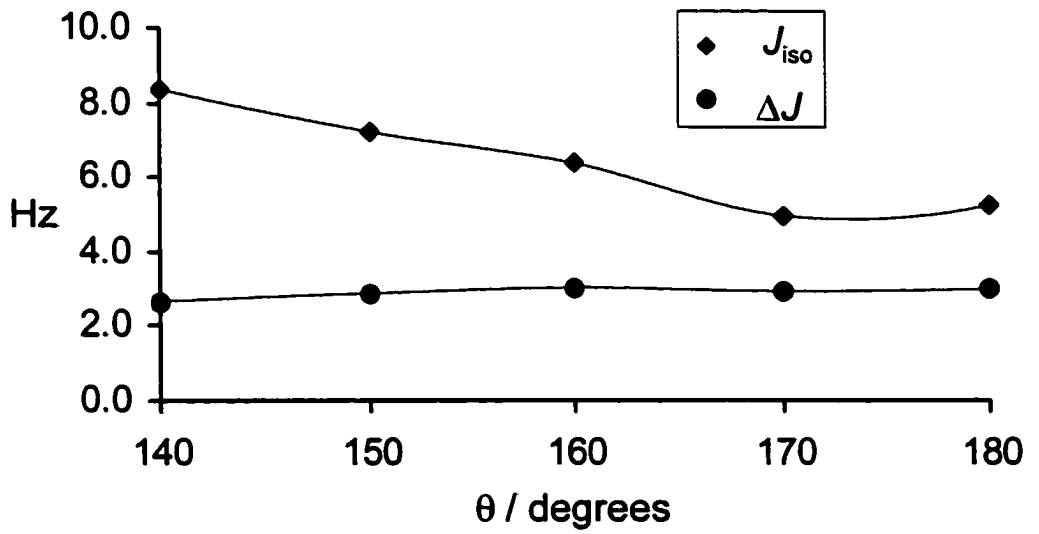


Figure 4.12: MCSCF results for the variation in $^{2h}$**J**(N,N) for the methyleneimine dimer as a function of the angle θ.

here, it is nevertheless important to specify the orientation of the tensor in the molecular framework. For a nitrogen-nitrogen separation of 3.02 Å in a linear hydrogen bond, the principal components of the symmetric part of the $^{2h}$J(N, N) tensor are: $J_{11} = 0.93$ Hz, $J_{22} = 1.07$ Hz, $J_{33} = 2.00$ Hz. In its PAS, the tensor is oriented such that $J_{22}$ is perpendicular to the dimer plane and $J_{33}$ is approximately along the vector connecting the two nitrogen nuclei.

As a testament to the remarkable magnitude of $^{2h}J_{iso}$(N, N) observed in nucleic acid base pairs, consider that prior to the observation of these couplings, one of the largest known two-bond nitrogen-nitrogen couplings was through covalent bonds in urea, $^{2}J_{iso}$(N, N) = ± 5.1 Hz (*461*). The largest $^{2h}J_{iso}$(N, N) reported to date is 11.0 ± 1.0 Hz between the imidazole rings of histidine bases in sperm whale apomyoglobin, pH = 4.9 (*444*). Given that the largest known two-bond proton-proton coupling is found in formaldehyde ($^{2}J_{iso}$(H, H) = 41 Hz) (*462*, *463*), it is reasonable to assume that $^{2}J_{iso}$(N, N) is relatively large in urea since these two compounds have similar geometries. MCSCF calculations of $^{2}$J(N, N) in urea indicate that $^{2}J_{iso}$(N, N) is + 5.9 Hz, thus providing the sign of this coupling and showing good agreement with experiment. The calculations show that the coupling is dominated by the FC mechanism; however, given the N-N distance of 2.3 Å (*392*), it is clear that the simple correlation between $^{2h}J_{iso}$(N, N) and $r_{NN}$ shown in Figure 4.11 and eq. 4.7 - 4.10 cannot be extended to include two-bond N-N couplings in σ-bonded systems.

## 4.5 Experimental Investigations of Antisymmetry in J

### *4.5.1 Practical Considerations*

The theory describing $\mathbf{J}^{antisym}$ was published many years ago; however, as mentioned in Chapter 2, there have been no previous measurements of the antisymmetric part of the **J** tensor. The work presented in this section addresses the *practical* aspects of how one would go about measuring $\mathbf{J}^{antisym}$, followed by the first attempt to make such a measurement. The theory laid out by Andrew and Farnell (*52*) alone does not provide much insight into what types of chemical systems may actually lead to an experimental observation of $\mathbf{J}^{antisym}$. In this section, the discussion represents one possible strategy for the measurement of $\mathbf{J}^{antisym}$, focussed solely on the methods outlined by Andrew and Farnell.

A useful starting point is to consider the spectral frequencies observed in the solid-state NMR spectrum of an isolated spin pair derived in Chapter 2. There are several requirements which must be satisfied to ensure the feasibility of measuring $\mathbf{J}^{antisym}$. Even if all the requirements are satisfied, there is no guarantee that $A$ will be of significant magnitude to be measured unambiguously. The requirements may be divided into those which concern the nuclear spin interactions of the nucleus to be observed, and those that describe the structural and symmetry properties of the molecule to be studied. The following discussion aims to demonstrate that after consideration of all requirements, there is a very limited number of molecules known which *may* allow for the observation of $\mathbf{J}^{antisym}$. The discussion is focussed on powdered samples; however, measurement of $\mathbf{J}^{antisym}$ from a single crystal has the same general requirements.

It is interesting to note that $\mathbf{J}^{antisym}$ contains no contribution from the FC

mechanism (Table 2.1). The anisotropic symmetric part of **J** does not contain a direct contribution from the FC mechanism; however, it does in principle contain a contribution from the FC x SD cross term which is related to the FC term. Measurement of $\mathbf{J}^{antisym}$ would therefore represent some of the most convincing experimental evidence for non-FC contributions to **J**.

The most basic requirement following the theory of Andrew and Farnell is that one must have a chemical system for which there is an effectively isolated pair of spin-1/2 nuclei. Isotopes such as $^{1}H$, $^{19}F$, and possibly $^{203/205}Tl$ will likely not be suitable due to strong homonuclear dipolar couplings. Quadrupolar nuclei are not feasible candidates due to the typically dominant quadrupolar interaction; however it is possible that another method for measuring antisymmetric **J** coupling may involve quadrupolar nuclei as the quadrupolar interaction was taken advantage of to measure the antisymmetric part of the CS tensor by Wi and Frydman (*22*). In the present work, suitable nuclei include e.g., $^{13}C$, $^{15}N$, $^{29}Si$, $^{31}P$, $^{77}Se$, $^{111/113}Cd$, $^{123/125}Te$, $^{115/117/119}Sn$, $^{199}Hg$, $^{203/205}Tl$, $^{207}Pb$.

The next requirement is that a chemical system must be found for which the two nuclei are strongly *J*-coupled and for which their isotropic chemical shift difference is as small as possible. This requirement may be understood by considering equations 2.61 - 2.62, where it may be seen that the influence of *A* on the spectrum increases as the magnitude of *A* increases relative to the chemical shift difference. A pair of crystallographically and magnetically equivalent nuclei, which constitute an $A_2$ spin pair and give rise to identical chemical shifts, is not a suitable spin pair since *J* coupling between these nuclei will not manifest itself in the NMR spectrum. Hence, what is needed is an isolated pair of spin-1/2 nuclei which are nearly (but not exactly)

crystallographically equivalent, so they will have very similar isotropic chemical shifts, but are likely to have a large indirect nuclear spin-spin coupling interaction.

One must consider the question of how large $J_{iso}$ and $A$ must be compared to the chemical shift difference such that the general case presented in Figure 2.5 may be approximated by one of the two situations presented in Figure 2.6. In the general case, the separation of the two inner peaks of the AB pattern is given by

$$2C - |J_{iso}| \qquad [4.11]$$

whereas if the approximation may be made that both $J_{iso}$ and $A$ are much greater than the difference in isotropic chemical shift for the two sites, the splitting is given by:

$$\sqrt{J_{iso}^2 + A^2} - J_{iso} \qquad J_{iso}, A >> (\sigma_B - \sigma_A) \qquad [4.12]$$

Since no measurements of $A$ have been made to date, it would not be prudent to invoke equation 4.12, thereby making a drastic assumption about the magnitude of $A$. Although Abragam states that the components of $\mathbf{J}^{antisym}$ are expected to be negligible relative to the symmetric part of **J** (*78*), MCSCF calculations on $ClF_3$ and $OF_2$ have indicated that the magnitudes of the components of the $\mathbf{J}^{antisym}$ tensor are comparable to those of the principal components of the $\mathbf{J}^{sym}$ tensor in these compounds (*464*). Thus, a spin pair with a large value of $J_{iso}$ favours the likelihood of there being an antisymmetric component of substantial magnitude. An appropriate molecule will thus have an isotropic spin-spin coupling constant which is preferably several times larger than the difference in the isotropic chemical shifts. Since the chemical shift difference is smaller in Hz at lower applied magnetic field strengths, the observation of $A$ will be facilitated by carrying out the NMR measurements at the *lowest* possible applied magnetic field strengths.

The requirement that $J_{iso}$ be several times larger than the chemical shift differences rules out many spin pairs including $^{13}C$ and $^{15}N$ since e.g., in a magnetic field of 4.7 T, the value of $^{1}J_{iso}(^{13}C,^{13}C)$ would have to be well in excess of 50 Hz for a spin pair with a chemical shift difference of 1 ppm. Such a situation is not likely given that one-bond carbon-carbon coupling constants are typically on the order of 50 Hz.

The molecule under study must be of sufficiently low symmetry about the bond axis of the coupled nuclei to ensure that the antisymmetric component of **J** is not forced to be zero by symmetry. According to the symmetry rules developed by Buckingham *et al.* (*47*), the symmetry at the coupled nuclei may be at most $C_3$. In such a situation, there are two antisymmetric components of the **J** tensor which are zero, and one which is (in principle) non-zero. If the symmetry of the system is lower, there is a positive consequence that this reduction in symmetry will likely lead to an increase in the magnitude of $A$.

Practically, one must be concerned with the chemical shift anisotropy of the nuclei in the AB pair. Heavier nuclei such as $^{199}Hg$ and $^{207}Pb$ tend to have substantial CS tensor spans. When carrying out a MAS NMR experiment on a powdered sample, this fact introduces the additional complication that the spectral intensity is distributed over a large spectral width in the form of spinning sidebands. Thus, not only would a large span reduce the effective signal-to-noise of the NMR spectrum, but it would also complicate the appearance and interpretation of the spectrum. Hence it is preferable to find a system for which the nuclei have relatively small CS tensor spans. This requirement is not critical, especially if a single-crystal NMR experiment is to be performed. However, this discussion is focussed on measurements made on powdered samples.

While the anisotropy of the symmetric part of the $\boldsymbol{\sigma}$ tensor may pose a challenge in the acquisition of high-quality NMR spectra of the AB spin pair, the antisymmetric part of $\boldsymbol{\sigma}$ will not hamper or influence the measurement of $A$. Whereas the presence of a significant $A$ will influence the splitting between two lines in the spectrum, the influence of $\boldsymbol{\sigma}^{\text{antisym}}$ only serves to generally shift the apparent positions of the principal components of the symmetric part of the CS tensor (*cf.* eq. 2.15); the splitting due to **J** will not be altered.

At this point it is useful to summarize properties of a molecule which may be suitable for the measurement of $A$ (Table 4.11).

**Table 4.11**: Some requirements for the observation of the antisymmetric part of **J**

| Property | Rationale |
|---|---|
| Pair of isolated spin-1/2 nuclei | No complications from quadrupolar interaction |
| Large $J_{iso}$ compared to chemical shift difference | Large $A$ is more likely if $J_{iso}$ is large; $A$ becomes easier to measure as its magnitude relative to the chemical shift difference increases. |
| Small CS tensor span | Simplified spectrum with good signal-to-noise |
| Symmetry no greater than $C_3$ about the AB spin pair | $A$ is not forced to be zero by symmetry |

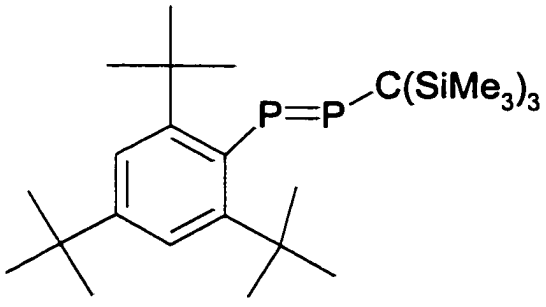


Figure 4.13: An unsymmetrically-substituted diphosphine.

A small selection of molecules may now be presented as potential candidates for the measurement of *A*. Shown in Figure 4.13 is an unsymmetrically-substituted diphosphine prepared by Cowley and co-workers (*465*). This molecule, and its $^{31}P$-$^{31}P$ spin pair, generally satisfy the requirements in Table 4.11. The two phosphorus atoms are crystallographically distinct, with isotropic solution chemical shifts of 533.1 and 530.0 ppm, and an isotropic *J* coupling of 619.7 Hz. Thus, at 4.7 T where the Larmor frequency of $^{31}P$ is 81.03 MHz, the *J* coupling is about 2.5 times larger than the chemical shift difference between two phosphorus nuclei. The symmetry of the molecule is low enough that *A* is non-zero in principle.

Another candidate is presented in Figure 4.14. The cation of the compound $\{[Hg_2(18\text{-crown-}6)_2(Me_2SO)(\mu\text{-}Me_2SO)]\}_2(O_3SCF_3)_4$ has two crystallographically equivalent pairs of crystallographically non-equivalent mercury atoms (*337*) . The value of $^1J_{iso}(^{199}Hg,^{199}Hg)$ measured in dichloromethane solution is 220300 ± 790 Hz, one of the largest known isotropic coupling constants (*337*). The chemical shift difference between the two mercury sites in the 18-crown-6 complex is 509 ppm. Therefore, at an applied magnetic field strength of 4.7 T, $J_{iso}$ is twelve times larger than the chemical shift

difference. There are no symmetry elements about the non-equivalent mercury nuclei (although the two halves of the molecule are related by an inversion centre). One drawback to this mercury compound is that CS tensor spans on the order of 3000 ppm are expected (*466*).

Unfortunately, there remains one further consideration which must be addressed in order to extract information on $A$. As described in Chapter 2, evidence for $A$ is most easily extracted in the limit where $A$ is much larger than both $J_{iso}$ and the chemical shift difference. A slightly more likely possibility is where both $A$ and $J_{iso}$ are much larger

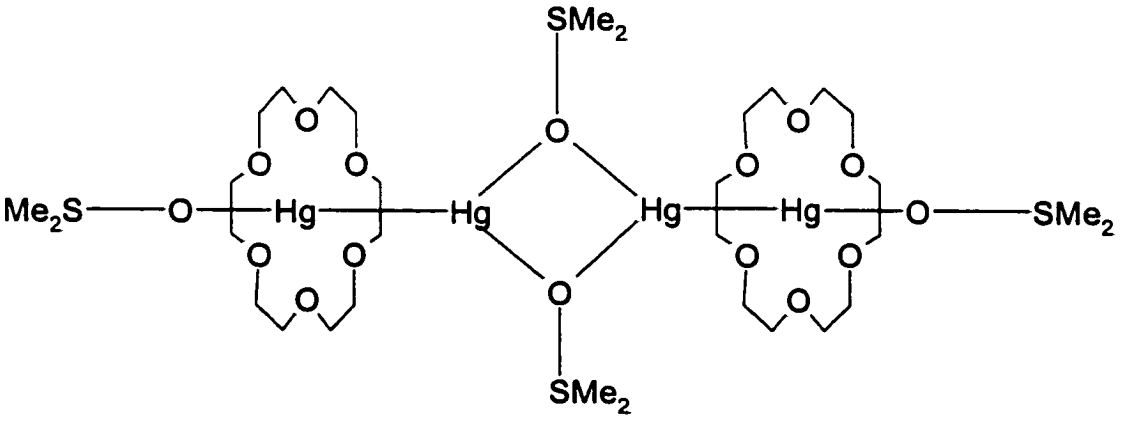


Figure 4.14: The cation of a $[Hg\text{-}Hg]^{2+}$ crown ether complex.

than the chemical shift difference. In both of these cases, the four lines in the NMR spectrum are defined by only two parameters ($A$ and $J_{iso}$) since the chemical shift difference is negligible. However, the assumption that $A$ is much larger than the chemical shift difference cannot be justified. Therefore, one must resort to the general description of the four-line spectrum where all three parameters, $J_{iso}$, $A$, and the chemical shift difference are required to properly describe the line positions. This presents a problem: the spectrum can always be fit by only two parameters, namely $J_{iso}$ and the chemical shift difference, if one assumes a negligible value for $A$. This corresponds to

the standard description of an AB spin system found in NMR textbooks, where antisymmetry in **J** is ignored. At a single magnetic field strength, the three parameters $A$, $J_{iso}$, and $\sigma_A$-$\sigma_B$ are underdetermined by the spectral positions of only four lines in the spectrum. The only parameter one may unambiguously extract from the general spectrum is $J_{iso}$ since it is always the splitting between the outer pairs of lines.

One potential solution is to use an isotope which is not 100% naturally abundant, such as $^{199}$Hg, so that the isotropic chemical shift difference for two sites may be determined independently from the resonances of the uncoupled nuclei. This would leave the four lines due to the coupled nuclei from which $J_{iso}$ and $A$ may be determined. The problem with this approach is that, as estimated from the well-known equations describing the intensities of the four transitions for an AB spin system (*73*), the two outer lines of the spectrum will have much less than 1 % of the intensity of the two central lines when the spin system is so tightly coupled that $J_{iso}$ is much greater than the chemical shift difference between the two nuclei. This incredibly small intensity, combined with the fact that only about 3 % of the mercury pairs contain two $^{199}$Hg nuclei which give rise to the AB pattern, unfortunately means that there is very little hope of observing the outer two lines of the AB pattern.

How then will it be possible to determine $A$? The fact that the spectrum underdetermines the desired parameters seems to rule out any possibility of measuring $A$. Extra information must be somehow introduced into the spectrum to provide enough data to unambiguously determine the three parameters. One possible solution is a system in which *at least two spin-1/2 isotopes of the atom to be observed are present in sufficient natural abundance and there is also an isotope(s) of zero spin of sufficient natural*

*abundance*. If this condition is satisfied, then the isotropic chemical shift difference is determined from the spin-active nuclei which are adjacent to spin-zero nuclei, the value of $J_{iso}$ is determined from the AX coupling to spin-1/2 isotope other than the one under observation (this circumvents the requirement to observe the outer two lines of very weak intensity), and finally, the value of $A$ may be extracted from the splitting of the inner two lines of the AB pattern according to equations 4.11 and 2.62. The implicit assumption made here is that the reduced coupling constants for different isotopes of the same element are independent of primary isotope effects (*441*, *442*). This is a reasonable assumption given the small magnitude of reported primary isotope effects on coupling constants; however the assumption may break down if very light nuclei are to be examined or if very precise measurements of $A$ coupling constants of small magnitude are desired.

There are only three elements which satisfy all of the requirements described so far: cadmium, tin, and tellurium (Table 4.12). Tellurium is not very appealing due to the low natural abundance of $^{123}$Te. Cadmium and tin remain as the only two possibilities.

**Table 4.12:** Possible candidate elements and isotopes for which homonuclear antisymmetric **J** coupling may be observed.

| Element | Isotope | NA / % |
|---|---|---|
| Cadmium | 111 | 12.75 |
| | 113 | 12.26 |
| Tin | 115 | 0.35 |
| | 117 | 7.61 |
| | 119 | 8.58 |
| Tellurium | 123 | 0.87 |
| | 125 | 6.99 |

*4.5.2 Tin-119 Solid-State NMR of Hexa(p-tolyl)ditin*

Now that the possible candidates for the observation of homonuclear antisymmetric **J** coupling have been narrowed down to two elements, suitable compounds must be identified. Tin-tin bonds are relatively common compared to cadmium-cadmium bonds. However, many ditin compounds of the type $R_3Sn\text{-}SnR_3$ possess magnetically equivalent tin atoms which are related by an inversion centre. Others have $C_{3v}$ symmetry, which by symmetry require $A$ to be zero (*47*). A singular candidate that satisfies all requirements is hexa(*p*-tolyl)ditin (**II**), which has two crystallographically non-equivalent tin atoms (Figure 4.15). Solution $^{119}Sn$ NMR in $CDCl_3$ has provided a value of $\delta_{iso} = -141.9$ ppm for the chemically equivalent tin atoms, and a value of $^1J_{iso}(^{119}Sn,^{119}Sn)$ of 4570 Hz (*467*).

The $^{119}Sn$ CP/MAS NMR spectrum of solid powdered **II** is presented in Figure

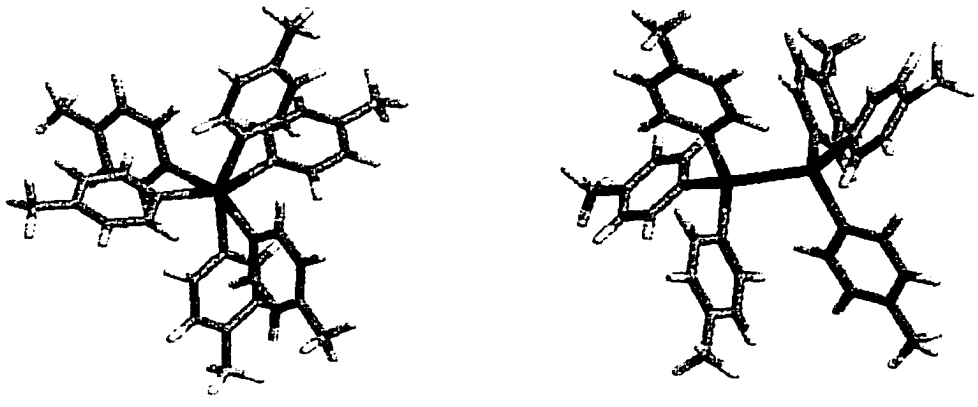


Figure 4.15: Structure of hexa(*p*-tolyl)ditin. (a) View along the tin-tin bond. (b) Side view.

4.16. At first glance, this spectrum appears much more complicated than the simple four-line ideal spectra presented in Chapter 2. This is due to the fact that the $^{119}$Sn isotope is not 100 % abundant. Tin-119 CP NMR spectra of a stationary sample of **II** indicate a CS tensor span for tin of less than 200 ppm; thus it was possible to spin the sample at a sufficiently fast rate to concentrate most of the spectral intensity into the centrebands. The expanded spectrum shown in Figure 4.16(b) contains the information required to make a determination of *A*. The isotropic chemical shifts of the uncoupled $^{119}$Sn nuclei are easily determined from the spectrum to be -142.5 and -154.2 ppm. Coupling to the $^{117}$Sn nucleus (designated as (i) and (ii)) is easily measured from the splittings indicated in Figure 4.16(b) to be 4175 ± 20 Hz, which may be converted to a value of $^{1}J_{iso}(^{119}Sn,^{119}Sn)$

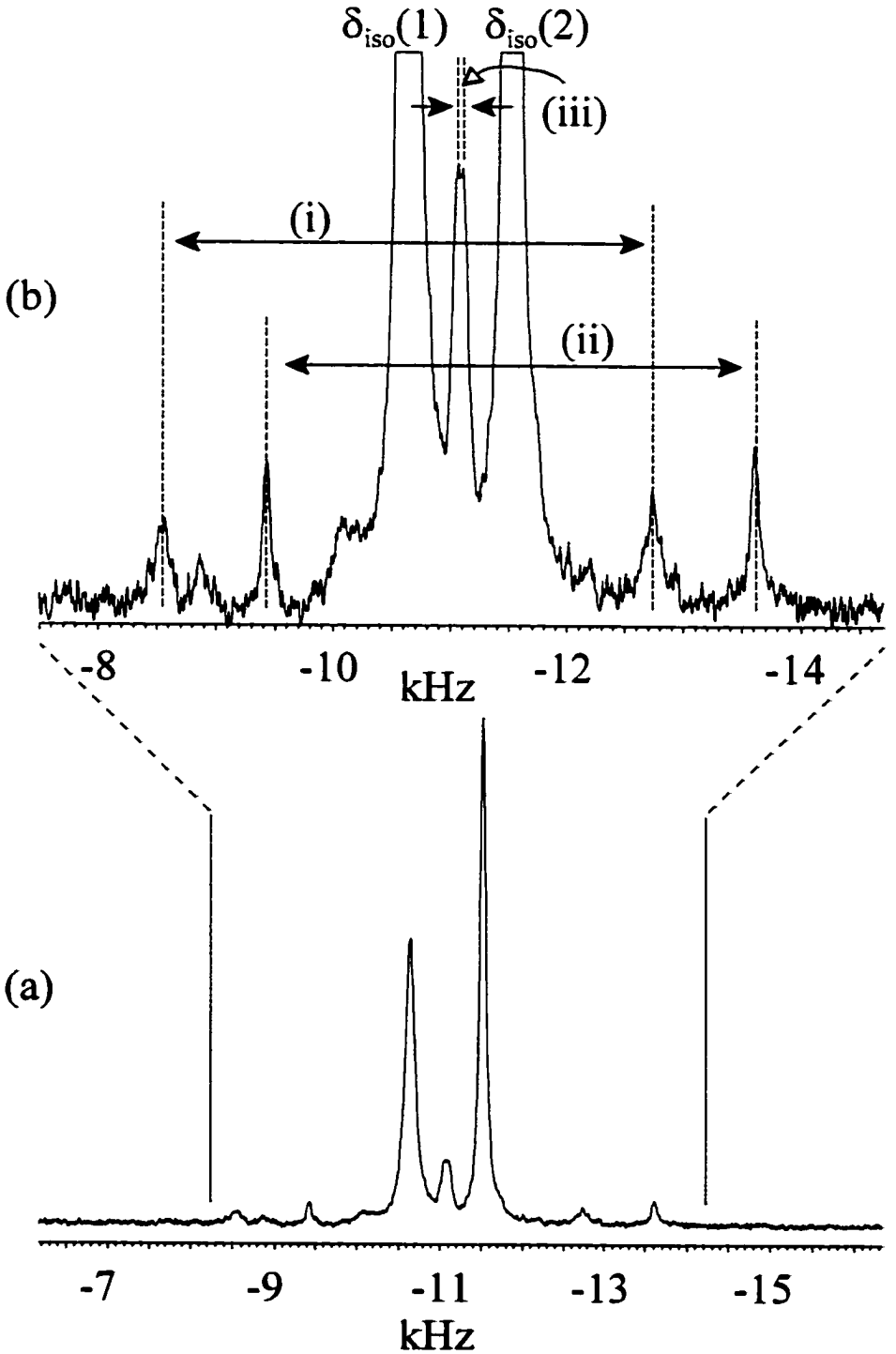


Figure 4.16: (a) Tin-119 VACP/MAS spectrum of hexa(*p*-tolyl)ditin obtained at 4.7 T. (b) Expansion of the spectrum shown in part a. The splitting (i) is equal to $^{1}J_{iso}(^{119}Sn, ^{117}Sn)$ for site 1 and the splitting (ii) is $^{1}J_{iso}(^{119}Sn, ^{117}Sn)$ for site 2. The splitting (iii) is $2C - |J_{iso}(^{119}Sn, ^{119}Sn)|$.

of 4370 Hz. Hence, at 4.7 T, the value of $^1J_{iso}(^{119}Sn,^{119}Sn)$ is five times greater than the isotropic chemical shift difference for the two sites. The splitting between the two inner lines is equal to $2C - |J_{iso}|$. From equations 2.62 and 4.11, it may be predicted that this splitting will be 86 Hz in the absence of a contribution from $A$. Certainly excellent resolution is required to observe this splitting. The one-dimensional $^{119}Sn$ CP/MAS NMR spectrum does not afford sufficient resolution of the two inner peaks of the AB pattern. However, the splitting is identical to 86 Hz within experimental error. The conclusion may be drawn that $A$ is not substantial, *i.e.*, certainly not on the same order of magnitude as $J_{iso}$ in this case.

In an effort to improve the resolution of the splitting of the inner two lines, a two-dimensional $J$-resolved $^{119}Sn$ NMR experiment was performed. This experiment has the ability to increase the apparent resolution due to homonuclear $J$ coupling compared with the standard one-dimensional spectrum. This is accomplished because heteronuclear dipolar interactions as well as anisotropic chemical shifts are refocussed at the top of the echo, thereby providing better resolution in the indirect (F1) dimension (*398*).

Shown in Figure 4.17 is a 2D-$J$ resolved $^{119}Sn$ CP/MAS NMR spectrum of hexa(*p*-tolyl)ditin. The projection of this spectrum onto the isotropic dimension corresponds to the one-dimensional CP/MAS spectrum shown in Figure 4.16. In the indirect $J$-resolved dimension, the splitting $2C - |J_{iso}(^{119}Sn,^{119}Sn)|$ is much better resolved than it is in the isotropic dimension, and therefore provides a more accurate measurement. The precision of the measurement in the indirect dimension is limited by the number of points which define the spectrum. In the spectrum shown in Figure 4.17, 16 points define the 200 Hz spectral window in the indirect dimension, thereby providing

one data point every 12.5 Hz. The splitting $2C - |J_{iso}(^{119}Sn,^{119}Sn)|$ is 85.0 ± 12.5 Hz, in agreement with the result estimated from the 1D spectrum, and also in agreement with the splitting expected in the absence of antisymmetric $J$ coupling.

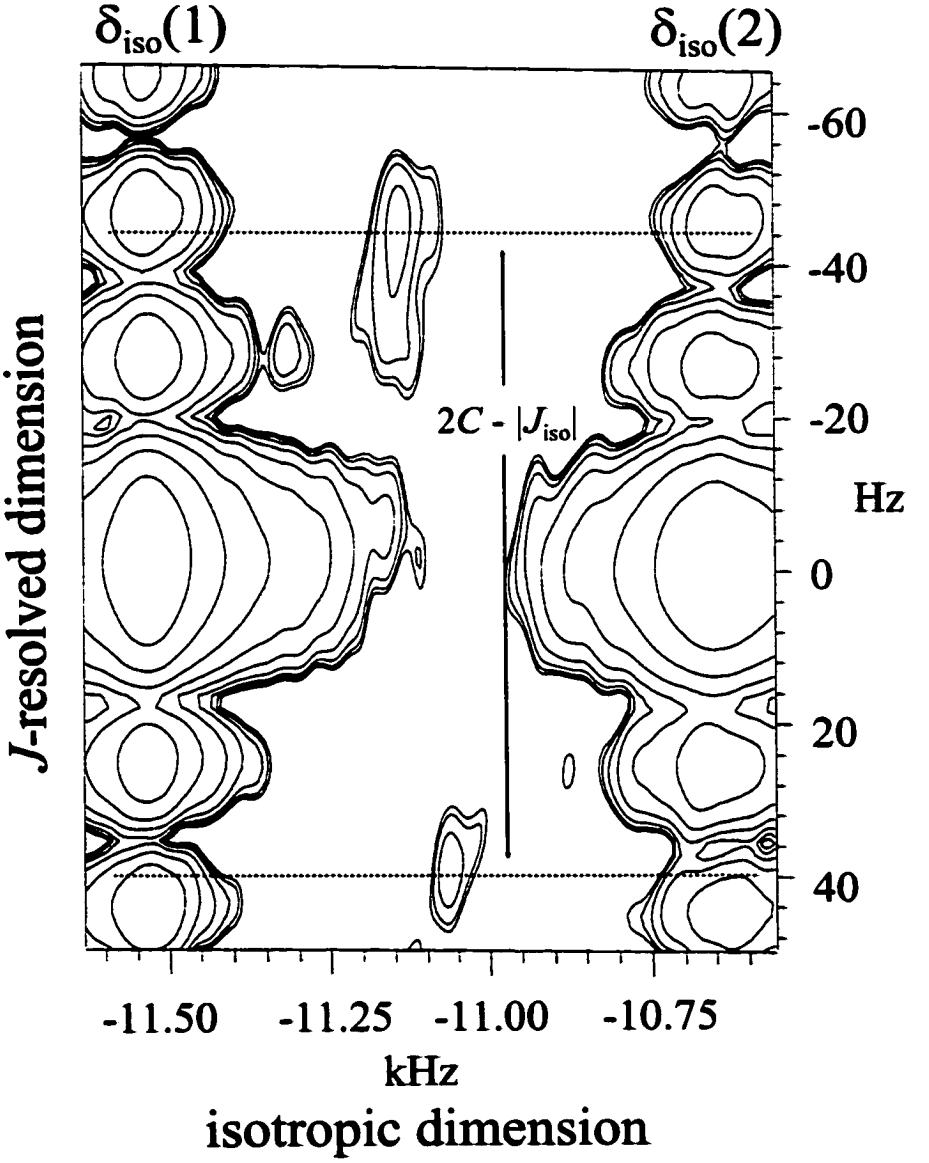


Figure 4.17: 2D-$J$ resolved $^{119}Sn$ CP/MAS NMR spectrum of hexa(*p*-tolyl)ditin. The isotropic chemical shifts of the uncoupled nuclei in sites 1 and 2 are indicated. The splitting $2C$-$|J_{iso}(^{119}Sn,^{119}Sn)|$ is easily resolved in the second dimension.

**Table 4.13**: Tin-119 NMR parameters determined for hexa(*p*-tolyl)ditin, **II**.

| Parameter | Value |
|---|---|
| $\delta_{iso}$ (1) / ppm | -142.5 ± 0.5 |
| $\delta_{iso}$ (2) / ppm | -154.2 ± 0.5 |
| $J_{iso}(^{119}Sn,^{119}Sn)$ / Hz | 4370 ± 75 |
| $A(^{119}Sn,^{119}Sn)$ / Hz | < \|315\| |

The error in the measurement of $2C$ - $|J_{iso}(^{119}Sn,^{119}Sn)|$, 12.5 Hz, allows an upper limit of ±315 Hz to be placed on the value of $A(^{119}Sn,^{119}Sn)$. Results are summarized in Table 4.13. In this case, the antisymmetric part of **J** is not forced to zero by symmetry; however, the relatively high symmetry of **II** apparently is enough to ensure $A$ is very small. A small value for $A$ in this case could also arise from a fortuitous cancellation of contributions from competing coupling mechanisms, e.g., PSO and SD.

## 4.6 Conclusions

The work presented in this chapter clearly emphasizes the three-dimensional orientation-dependent nature of the indirect nuclear spin-spin coupling interaction, and the type of information which is available from experiment and theory.

The little-appreciated link between the hyperfine Hamiltonian and the NMR spin-spin coupling Hamiltonian has been developed in the terminology and symbolism familiar to NMR spectroscopists. In particular, the parameters $c_3$ and $c_4$ yield the complete experimental indirect spin-spin coupling tensor, *i.e.*, both the isotropic and the anisotropic parts, for an isolated molecule in the gas phase. In conjunction with *ab initio* and relativistic DFT calculations, this relationship has been exploited fully for the first time to establish periodic trends in one-bond spin-spin coupling ***tensors*** for select spin pairs across the periodic table. Several findings improve upon or contrast with earlier work where fewer data were used to reach conclusions. One of the most significant conclusions is that the Fermi-contact mechanism is not dominant in the general case; the paramagnetic spin-orbit and spin-dipolar mechanisms are found to be important if not dominant contributors to the spin-spin coupling tensors for a variety of spin pairs. This conclusion has major implications relating to the standard text-book interpretation of spin-spin coupling constants.

The excellent agreement between the experimental and calculated coupling tensors presented in this chapter is among the first such demonstrations, especially using modern quantum chemistry techniques and for such a wide variety of spin pairs. The excellent agreement between the MCSCF and DFT methods for the light interhalogen diatomics is particularly encouraging. Furthermore, the relativistic ZORA-DFT results

for molecular iodine attest to the applicability of this computational method for calculating heavy-atom spin-spin coupling tensors.

The investigation of $^{2h}$**J**(N, N) in the methyleneimine dimer has provided insight into the relative importance of the various coupling mechanisms and the dependence of both the isotropic and anisotropic portions on local molecular structure. The nitrogen-nitrogen distance is dominant in determining $^{2h}J_{iso}$(N, N) across hydrogen bonds; however, if highly accurate correlations are to be made between $^{2h}J_{iso}$(N, N) and local molecular structure, consideration of the hydrogen bond angle is also necessary. $^{2h}J_{iso}$(N, N) provides a measure of hydrogen bond strength insofar as it is related to hydrogen bond length. The general conclusions reached regarding the properties of $^{2h}$**J**(N, N) and the dependence of $^{2h}J_{iso}$(N, N) on local molecular structure should be applicable to similar systems of biological relevance, specifically nucleic acid base pairs.

Finally, the practical requirements for the observation of antisymmetric **J** coupling have been described for the first time. Although a somewhat esoteric property, the antisymmetric rank-1 part of **J** remains as the only part of the four most important NMR interaction tensors (CS, **J**, **D**, EFG) which has yet to be observed experimentally. The experimental work presented in this chapter illustrates one strategy by which the first measurement may be made. An upper limit of ±315 Hz has been placed on $A(^{119}\text{Sn}, ^{119}\text{Sn})$ in hexa-(*p*-tolyl)ditin. At this stage, however, a definitively non-zero measurement of $A$ remains elusive.

## Chapter 5: Concluding Remarks and Outlook

The research presented in this thesis is of a fundamental nature. The conclusions reached provide evidence that in the context of NMR spectroscopy, such research is critical to the development of a more complete understanding of important concepts (Sections 3.4 and 4.6). Fundamental research is also crucial in the establishment and evolution of new applications. The focus of the work presented herein has been to apply modern experimental and theoretical methods to measure and interpret anisotropic NMR interactions, including chemical shift, indirect spin-spin coupling, direct dipolar coupling, and electric field gradient tensors, for chemical systems representative of various groups of the periodic table. The specific future applications of fundamental NMR research, such as that presented in this thesis, obviously cannot be predicted. However, the following concluding remarks illustrate recent examples of NMR applications where knowledge and understanding of NMR interaction tensors play, or will play, a crucial role.

Recently, there has been an apparent merging of the traditional areas of solution- and solid-state NMR. The convergence of ideas from the two historically distinct areas of research has most successfully been manifested in the rapidly developing field of NMR spectroscopy in dilute liquid crystalline solvents (*468*). While solution NMR has enjoyed success in the characterization of structure and dynamics for diverse species, one of the most exciting aspects of the new liquid crystal NMR technique is that advantage is taken of residual dipolar couplings as well as residual anisotropic chemical shift

interactions (*469*) to refine the structures of biomolecules. These are the types of anisotropic interactions for which the fundamental studies reported in Chapter 3 have provided benchmark values and interpretations for several nuclei whose potential has yet to be fully exploited in NMR. Additionally, the theoretical calculations of *J*-couplings across hydrogen bonds reported in Chapter 4 provide valuable information which may be used to help in structure determination about hydrogen bonds in biomolecules.

The past year has seen NMR studies carried out at the two extremes of applied magnetic field strengths: $^{27}$Al NMR studies of solids at 40 T ($^{1}$H frequency of 1700 MHz) (*470*), and solution NMR of small molecules in microtesla fields ($^{1}$H frequency of ~ 100 Hz) (*471*). The research reported in this thesis bears direct implications on NMR spectra acquired at such extreme applied magnetic field strengths. As demonstrated in Chapter 3, chemical shift tensors have the potential to completely dominate the appearance of the solid-state NMR spectra of transition metal nuclei in inorganic and organometallic complexes. Thus, at field strengths as high as 40 T, a thorough understanding of the CS interaction in quadrupolar nuclei becomes critical. In contrast, in microtesla fields, all chemical shift information is lost and the *J*-coupling interaction becomes dominant. In a commentary in *Science*, R. F. Service makes the claim that "*J*-coupling could revolutionize medical imaging by making the machines [...] cheap enough for the doctors's office" (*472*). The research into the 2$^{nd}$-rank tensor properties of **J**, as well as periodic trends in **J**, presented in Chapter 4 will have a greater impact as lower magnetic fields strengths come into vogue.

The outlook for increased application of the tensor properties of NMR parameters, rather than simply their isotropic values, is optimistic. Central to this

continued growth are technological developments in the form of larger NMR magnets, theoretical advances which render the accurate calculation and interpretation of NMR interaction tensors more and more feasible and useful to spectroscopists, and the ongoing thrust to develop increasingly accurate and precise NMR techniques for structural determination of a variety of chemical species such as biological macromolecules. Fundamental research in NMR and computational chemistry will continue to act as the foundation for these advances.

## Chapter 6: Ongoing and Future Research Directions

There are several possible directions which future research could take, based on the results reported in this thesis. Some representative examples are discussed below.

### 6.1 Chemical Shift Tensors for Transition Metal Nuclei

As with the $^{95}$Mo and $^{53}$Cr solid-state NMR results presented in Chapter 3, the opportunity to make precise determinations of chemical shift tensors for many transition metal nuclei exists. One promising example is $^{99}$Ru ($I = 5/2$, NA = 12.72 %, $Q = 7.9$ fm$^2$), which remains as one of the few transition metal nuclei which has not been investigated in any substantial way by solid-state NMR (*84*). Solid-state NMR of $^{99}$Ru should be less difficult than for $^{53}$Cr, if compounds of appropriately high symmetry are chosen for study. Several candidates are found in the work by Gaemers *et al.*, who have carried out some solution $^{99}$Ru NMR studies (*473*). Numerous pseudo-octahedral

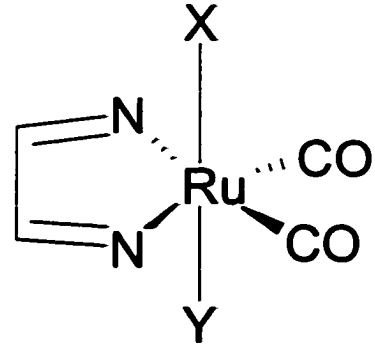


Figure 6.1: Generic structure of pseudo-octahedral ruthenium compounds to be studied by solid-state $^{99}$Ru NMR spectroscopy.

organometallic compounds of the type shown in Figure 6.1 have given narrow solution line widths, e.g., as low as 25 Hz for $X = CH_3$ and $Y = Br$. Such narrow line widths imply a small EFG at ruthenium, which bodes well for the observation of $^{99}Ru$ in the solid state.

Observation and interpretation of $^{99}Ru$ EFG and CS tensors will increase the body of knowledge available for quadrupolar transition metal nuclei. To date, no ruthenium CS tensor has been measured. Relativistic ZORA-DFT calculations are expected to be of great benefit in the interpretation of the data.

Synthesis of the compounds of the type shown in Figure 6.1 has been initiated in the Wasylishen lab by Kris Ooms.

## 6.2 J coupling in Biologically Relevant Systems

As mentioned in Chapter 5, a great deal of recent activity in the area of biomolecular structure determination relies on the measurement of residual dipolar coupling constants in dilute liquid crystalline media. These residual dipolar coupling constants are proportional to the full direct dipolar coupling constant (eq. 2.32) and hence to internuclear distances as well as bond vector orientations. However, as described in section 2.1.6, any observed dipolar coupling constant is in fact an effective dipolar coupling constant which contains a contribution from $\Delta J$. To date, the influence of $\Delta J$ on the biomolecular structure refinements has not been addressed in the literature. Although the influence of $\Delta J$ is expected to be small for the light atoms involved in molecules such as peptides, ignoring its effect completely will introduce small unknown errors into the NMR-derived structures.

A future research project will employ the computational methods described in Chapter 4 to provide reliable estimates of one-bond $\Delta J$ values for small compounds which model larger peptides and DNA fragments, such as glycylglycine (Figure 6.2) and a nucleic acid base pair. Knowledge of these values may allow for appropriate corrections to be made to observed residual dipolar coupling constants in biomolecular structure determination. Work in this direction is currently underway.

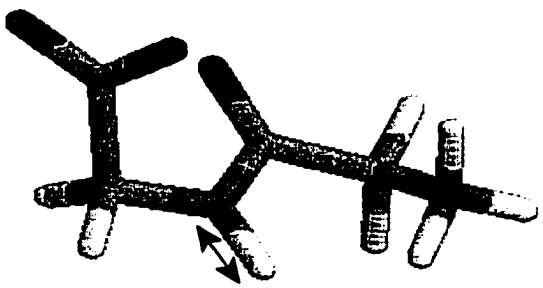

$\Delta J(^{15}N, ^{1}H)$

Figure 6.2: Glycylglycine, a candidate for calculating one-bond spin-spin coupling anisotropies, e.g., for the amide nitrogen-proton spin pair.

## 6.3. Experimental Evidence for Antisymmetry in NMR Interaction Tensors

The experimental attempts to measure the antisymmetric part of **J** in Chapter 4 allowed for an upper limit to be placed on the antisymmetric coupling constant. However, now that the practical methodology for measuring $A$ has been described, the limitation becomes the identification and synthesis of an appropriate compound for which $A$ will be significantly non-zero. As described in Chapter 4, compounds with tin-tin bonds are the most promising candidates. In the Wasylishen lab, Kris Harris has begun

the synthesis of 1,1,2,2-tetra-*t*-butyl-1,2-bis(2,4,6-triisopropylphenyl)ditin. This compound satisfies all of the requirements for the observation of antisymmetric **J** coupling, and has the additional advantage over hexa-(*p*-tolyl)ditin of lower symmetry about the tin-tin axis.

Another candidate for observing antisymmetric **J** coupling is $\{[HB(3,5\text{-}Me_2pz)_3]Cd\}_2$ (pz = pyrazolyl ring), for which a particularly large isotropic $^{113}Cd$-$^{111}Cd$ coupling constant of 20646 Hz has been observed in solution (*474*). Many other systems are also currently being considered.

* * * *

Finally, several other projects have been completed which have not been discussed in this thesis (see Appendix B), and several more are currently in progress. Research can be addictive, with each new discovery leading to a new set of even more intriguing questions and challenges.

*The farther one travels,*
*the less one knows...*
*the less one really knows.*

- George Harrison (1943-2001)
in The Beatles' "The Inner Light"

## Appendix A: Restricted active space selection for ClF

The process by which the restricted active space is chosen in a Dalton calculation of **J** tensors is presented here. A similar process is used for complete active space calculations. Chlorine monofluoride is used as an example.

The first step in the process is to generate Hartree-Fock orbital energies and MP2 natural orbital occupation numbers for the molecule. This is done by running an MP2 calculation partway through until the natural orbitals are generated in the output file. For heteronuclear diatomic molecules, which are represented in the $C_{2v}$ point group in Dalton, there are four orbital symmetries: $A_1$, $B_1$, $B_2$, and $A_2$. For ClF at the equilibrium bond length, with the cc-pVQZ basis set, the orbital energies and occupation numbers are given in Tables A1 - A8. The energies have been rounded to 4 decimal places and the occupation numbers to 5 decimal places for convenience. The columns of the tables have no significance; the energies and occupation numbers are listed in order from left to right across the rows.

**Table A1:** Hartree-Fock orbital energies for ClF, symmetry 1 ($A_1$)

| | | | | |
|---|---|---|---|---|
| -104.938 | -26.3560 | -10.6556 | -8.1231 | -1.6402 |
| -1.1057 | -0.7009 | 0.0365 | 0.078 | 0.1184 |
| 0.1857 | 0.2569 | 0.3327 | 0.3550 | 0.47 |
| 0.6377 | 0.6437 | 0.6818 | 0.7986 | 0.8794 |
| 0.9412 | 1.0044 | 1.2042 | 1.4641 | 1.7118 |
| 1.7173 | 1.7829 | 1.8421 | 2.0429 | 2.0612 |
| 2.1651 | 2.1677 | 2.4357 | 2.4903 | 2.6044 |
| 2.8951 | 3.1050 | 4.1068 | 4.2240 | 4.4079 |
| 4.4551 | 4.663 | 4.6781 | 4.7259 | 4.7648 |
| 5.3608 | 5.4327 | 5.4403 | 5.6688 | 5.7886 |
| 5.8780 | 6.2699 | 6.9568 | 8.2865 | 13.64 |
| 13.8535 | 13.9942 | 14.4272 | 15.9502 | 16.281 |
| 16.7461 | 17.4245 | 24.6039 | 54.557 | |

**Table A2:** Hartree-Fock orbital energies for ClF, symmetry 2 ($B_1$)

| | | | | |
|---|---|---|---|---|
| -8.119 | -0.7265 | -0.4934 | 0.0922 | 0.2035 |
| 0.3263 | 0.4525 | 0.6560 | 0.8052 | 0.8132 |
| 0.9246 | 1.1551 | 1.7044 | 1.7264 | 1.8254 |
| 1.8532 | 2.0238 | 2.121 | 2.2075 | 2.4782 |
| 2.9688 | 3.7141 | 4.2618 | 4.4276 | 4.6214 |
| 4.6474 | 4.8561 | 4.9476 | 5.5446 | 5.5926 |
| 5.9662 | 6.4483 | 6.8711 | 13.219 | 13.671 |
| 14.0324 | 15.8354 | 16.0827 | 17.212 | |

**Table A3:** Hartree-Fock orbital energies for ClF, symmetry 3 ($B_2$)

| | | | | |
|---|---|---|---|---|
| -8.119 | -0.727 | -0.4934 | 0.0922 | 0.2035 |
| 0.3263 | 0.4525 | 0.656 | 0.8052 | 0.8132 |
| 0.9246 | 1.1551 | 1.7044 | 1.7264 | 1.8254 |
| 1.8532 | 2.0238 | 2.121 | 2.2075 | 2.4782 |
| 2.9688 | 3.7141 | 4.2618 | 4.4276 | 4.6214 |
| 4.6474 | 4.8561 | 4.9476 | 5.5446 | 5.5926 |
| 5.9662 | 6.4483 | 6.8711 | 13.219 | 13.6713 |
| 14.0324 | 15.8354 | 16.0827 | 17.212 | |

**Table A4:** Hartree-Fock orbital energies for ClF, symmetry 4 ($A_2$)

| | | | | |
|---|---|---|---|---|
| 0.2569 | 0.6377 | 0.6818 | 0.9412 | 1.7118 |
| 1.7829 | 1.8421 | 2.0612 | 2.1651 | 2.6044 |
| 4.2240 | 4.4551 | 4.6630 | 4.6781 | 4.7259 |
| 5.4403 | 5.7886 | 5.878 | 13.6400 | 13.8535 |
| 15.9502 | 16.7461 | | | |

**Table A5:** Natural orbital occupation numbers for ClF, symmetry 1 ($A_1$)

| | | | | |
|---|---|---|---|---|
| 2.00000 | 1.99937 | 1.99937 | 1.99858 | 1.98614 |
| 1.97610 | 1.93843 | 0.05530 | 0.01639 | 0.01079 |
| 0.00922 | 0.00542 | 0.00491 | 0.00482 | 0.00251 |
| 0.00138 | 0.00129 | 0.00087 | 0.00072 | 0.00059 |
| 0.00055 | 0.00055 | 0.00042 | 0.00042 | 0.00039 |
| 0.00037 | 0.00027 | 0.00025 | 0.00019 | 0.00018 |
| 0.00015 | 0.00013 | 0.00012 | 0.00012 | 0.00010 |
| 0.00008 | 0.00008 | 0.00007 | 0.00007 | 0.00006 |
| 0.00006 | 0.00005 | 0.00005 | 0.00004 | 0.00003 |
| 0.00002 | 0.00002 | 0.00002 | 0.00002 | 0.00001 |
| 0.00001 | 0.00001 | 0.00001 | 0.00001 | 0.00001 |
| 0.00001 | 0.00001 | 0.00001 | 0.00001 | 0.00000 |
| 0.00000 | 0.00000 | 0.00000 | 0.00000 | |

**Table A6:** Natural orbital occupation numbers for ClF, symmetry 2 ($B_1$)

| | | | | |
|---|---|---|---|---|
| 1.99880 | 1.97101 | 1.95635 | 0.02286 | 0.00987 |
| 0.00817 | 0.00450 | 0.00138 | 0.00113 | 0.00082 |
| 0.00065 | 0.00055 | 0.00042 | 0.00040 | 0.00030 |
| 0.00021 | 0.00016 | 0.00015 | 0.00014 | 0.00013 |
| 0.00011 | 0.00008 | 0.00008 | 0.00007 | 0.00006 |
| 0.00005 | 0.00003 | 0.00002 | 0.00002 | 0.00002 |
| 0.00001 | 0.00001 | 0.00001 | 0.00001 | 0.00001 |
| 0.00000 | 0.00000 | 0.00000 | -0.00003 | |

**Table A7:** Natural orbital occupation numbers for ClF, symmetry 3 ($B_2$)

| | | | | |
|---|---|---|---|---|
| 1.99880 | 1.97101 | 1.95635 | 0.02286 | 0.00987 |
| 0.00817 | 0.00450 | 0.00138 | 0.00113 | 0.00082 |
| 0.00065 | 0.00055 | 0.00042 | 0.00040 | 0.00030 |
| 0.00021 | 0.00016 | 0.00015 | 0.00014 | 0.00013 |
| 0.00011 | 0.00008 | 0.00008 | 0.00007 | 0.00006 |
| 0.00005 | 0.00003 | 0.00002 | 0.00002 | 0.00002 |
| 0.00001 | 0.00001 | 0.00001 | 0.00001 | 0.00001 |
| 0.00000 | 0.00000 | 0.00000 | -0.00003 | |

**Table A8:** Natural orbital occupation numbers for ClF, symmetry 4 ($A_2$)

| | | | | |
|---|---|---|---|---|
| 0.01639 | 0.00491 | 0.00138 | 0.00087 | 0.00055 |
| 0.00042 | 0.00027 | 0.00019 | 0.00018 | 0.00012 |
| 0.00008 | 0.00007 | 0.00006 | 0.00005 | 0.00003 |
| 0.00002 | 0.00002 | 0.00001 | 0.00001 | 0.00001 |
| 0.00001 | 0.00001 | | | |

As described in Section 2.3, there are four orbital spaces which must be chosen in a RAS calculation: inactive, RAS1, RAS2, and RAS3. Usually the RAS1 space is empty. One of the most important factors in choosing an appropriate set of orbitals to include in a given active space window is that all of the orbital symmetries are treated equally in terms of where the energy or occupation number cutoffs are made.

The inactive orbitals are chosen on the basis of the HF energies. From a simple MO picture, a good choice for the inactive orbitals are the core orbitals, *i.e.* the $1s^2$ orbitals which are associated with fluorine and the $1s^2$ and $2s^22p^6$ orbitals which are associated with chlorine. This corresponds to a total of six doubly occupied orbitals; four of $\sigma$ symmetry and two of $\pi$ symmetry. These orbitals may be easily identified as the four low-lying orbitals of $A_1$ symmetry (Table A1) and one each from the orbitals of $B_1$ and $B_2$ symmetries (Tables A2 and A3). The appropriateness of this selection of orbitals is exemplified in the fact that for the first three orbital symmetries, an obvious cutoff point in the energies is approximately -8.1 au. The fourth symmetry ($A_2$) has no orbitals in the inactive space. This selection of inactive orbitals is represented as "4110".

The RAS2 space is generally chosen to include the remainder of those orbitals with negative HF energies which have not already been included in the inactive space. Referring to Tables A1 - A4, there are 3 from $A_1$, 2 from $B_1$, 2 from $B_2$, and zero from $A_2$. This selection of the RAS2 space is represented as "3220".

The RAS3 space is chosen to include as many virtual orbitals as possible within the limitations of the computational resources. The orbitals are chosen on the basis of the MP2 natural orbital occupation numbers. Referring to Tables A5 - A8, it may be noted

that all orbitals with occupations close to 2.00 have already been assigned to orbital spaces: the first 7 orbitals in $A_1$, the first 3 orbitals in $B_1$ and $B_2$, and zero orbitals in $A_2$. A critical requirement in choosing the orbitals which go into RAS3 is to select an appropriate occupation number cutoff point. For example, it is not appropriate to include an orbital with occupation number 0.00491 and exclude an orbital with occupation number 0.00482. Observation of the occupation numbers for the first three orbital symmetries (Tables A5 - A7) indicates that there is a relatively large gap in the occupation numbers between ~ 0.009 and ~ 0.005. Thus an appropriate RAS3 space includes 4 orbitals of $A_1$ symmetry, 3 orbitals of $B_1$ symmetry, 3 orbitals of $B_2$ symmetry, and 1 orbital of $A_2$ symmetry. Inclusion of more orbitals of $A_2$ symmetry would not be appropriate since the occupation number of the next orbital is 0.00491 and the choice has been made to exclude orbitals which are on the high-energy side of the gap identified in the occupation numbers of the first three symmetries. The RAS3 space is represented as "4331". In practice, the RAS3 space is the most difficult to select. Often one encounters difficulties with the size of the calculation, or convergence problems.

The results of the RAS calculation on ClF described above are presented in Table 4.9.

## Appendix B: List of Publications

### B.1 Publications based on material presented in this thesis

David L. Bryce and Roderick E. Wasylishen "A $^{95}$Mo and $^{13}$C Solid-State NMR and Relativistic DFT Investigation of Mesitylenetricarbonylmolybdenum(0) - A Typical Transition Metal Piano-Stool Complex" *Phys. Chem. Chem. Phys.* **2002**, *4*, 3591-3600.

David L. Bryce, Roderick E. Wasylishen, Jochen Autschbach, and Tom Ziegler "Periodic Trends in Indirect Nuclear Spin-Spin Coupling Tensors: Relativistic Density Functional Calculations for Interhalogen Diatomics" *J. Am. Chem. Soc.* **2002**, *124*, 4894-4900.

David L. Bryce and Roderick E. Wasylishen "The First Chromium-53 Solid-State Nuclear Magnetic Resonance Spectra of Diamagnetic Chromium(0) and Chromium(VI) Compounds" *Phys. Chem. Chem. Phys.* **2001**, *3*, 5154-5157.

David L. Bryce, Myrlene Gee, and Roderick E. Wasylishen "High-Field Chlorine NMR Spectroscopy of Solid Organic Hydrochloride Salts: A Sensitive Probe of Hydrogen Bonding Environment" *J. Phys. Chem. A* **2001**, *105*, 10413-10421.

David L. Bryce and Roderick E. Wasylishen "Modeling $^{2h}J_{iso}$(N, N) in Nucleic Acid Base Pairs: Ab Initio Characterization of the $^{2h}$J(N, N) Tensor in the Methyleneimine Dimer as a Function of Hydrogen Bond Geometry" *J. Biomol. NMR* **2001**, *19*, 371-375.

David L. Bryce, Roderick E. Wasylishen, and Myrlene Gee "Characterization of Tricoordinate Boron Chemical Shift Tensors: Definitive High-Field Solid-State NMR Evidence for Anisotropic Boron Shielding" *J. Phys. Chem. A* **2001**, *105*, 3633-3640.

David L. Bryce and Roderick E. Wasylishen "Indirect Nuclear Spin-Spin Coupling Tensors in Diatomic Molecules: A Comparison of Results Obtained by Experiment and First Principles Calculations" *J. Am. Chem. Soc.* **2000**, *122*, 3197-3205.

## B.2 Other publications resulting from Ph.D. research

David L. Bryce and Roderick E. Wasylishen "Evaluation of the Influence of Anisotropic Indirect Nuclear Spin-Spin Coupling Tensors on Effective Residual Dipolar Couplings for Model Peptides" *J. Biomol. NMR* **2002**, submitted for publication.

Roderick E. Wasylishen and David L. Bryce "A Revised Absolute Magnetic Shielding Scale for Oxygen" *J. Chem. Phys.* **2002**, submitted for publication.

Juha Vaara, Jukka Jokisaari, Roderick E. Wasylishen, and David L. Bryce "Spin-Spin Coupling Tensors as Determined by Experiment and Computational Chemistry" *Prog. Nucl. Magn. Reson. Spectrosc.* **2002**, accepted.

David L. Bryce and Roderick E. Wasylishen "Insight into the Structure of Silver Cyanide from $^{13}C$ and $^{15}N$ Solid-State NMR Spectroscopy" *Inorg. Chem.* **2002**, *41*, 4131-4138.

David L. Bryce and Roderick E. Wasylishen "Interpretation of Indirect Nuclear Spin-Spin Coupling Tensors for Polyatomic Xenon Fluorides and Group 17 Fluorides: Results from Relativistic Density Functional Calculations" *Inorg. Chem.* **2002**, *41*, 3091-3101.

David L. Bryce and Roderick E. Wasylishen "Ab Initio Characterization of Through-Space Indirect Nuclear Spin-Spin Coupling Tensors for Fluorine-X (X=F,C,H) Spin Pairs" *J. Mol. Struct.* **2002**, *602-603*, 463-472.

David L. Bryce, Guy M. Bernard, Myrlene Gee, Michael D. Lumsden, Klaus Eichele, and Roderick E. Wasylishen "Practical Aspects of Modern Routine Solid-State Multinuclear Magnetic Resonance Spectroscopy: One-Dimensional Experiments" *Can. J. Anal. Sci. Spectrosc.* **2001**, *46*, 46-82.

David L. Bryce and Roderick E. Wasylishen "Ab Initio Calculations of NMR Parameters For Diatomic Molecules: An Exercise In Computational Chemistry" *J. Chem Educ.* **2001**, *78*, 124-133.

David L. Bryce and Roderick E. Wasylishen "Symmetry Properties of Indirect Nuclear Spin-Spin Coupling Tensors: First Principles Results for $ClF_3$ and $OF_2$" *J. Am. Chem. Soc.* **2000**, *122*, 11236-11237.

Roderick E. Wasylishen, David L. Bryce, Corey J. Evans, and Michael C. L. Gerry "Hyperfine Structure in the Rotational Spectrum of GaF. A Comparison of Experimental and Calculated Spin-Rotation and Electric Field Gradient Tensors" *J. Mol. Spectrosc.* **2000**, *204*, 184-194.

David L. Bryce and Roderick E. Wasylishen "Dipolar-Chemical Shift and Rotational Resonance $^{13}C$ NMR Studies of the Carboxyl-Methylene Spin Pair in Solid Phenylacetic Acid and Potassium Hydrogen Bisphenylacetate" *J. Phys. Chem. A* **2000**, *104*, 7700-7710.

David L. Bryce and Roderick E. Wasylishen "Rotational Resonance in Solid State NMR", in *Encyclopedia of Spectroscopy and Spectrometry*; Lindon, J. C., Tranter, G. E., and Holmes, J. L., Eds.; Academic Press: New York, **2000**; pp 2136-2144.

David L. Bryce and Roderick E. Wasylishen "Beryllium-9 NMR Study of Solid Bis(2,4-pentanedionato-O,O')beryllium and Theoretical Studies of $^{9}Be$ Electric Field Gradient and Chemical Shielding Tensors. The First Evidence for Anisotropic Beryllium Shielding" *J. Phys. Chem. A* **1999**, *103*, 7364-7372.

**References and Notes**


1. The first observed nuclear magnetic resonance was for the lithium nuclei of lithium chloride. Rabi, I. I.; Zacharias, J. R.; Millman, S.; Kusch, P. *Phys. Rev.* **1938**, *53*, 318.

2. Ramsey describes the early history of magnetic resonance, including several failed attempts in the 1920s and 1930s to observe nuclear magnetic resonance. Ramsey, N. F. *Phys. Perspect.* **1999**, *1*, 123.

3. Purcell, E. M.; Torrey, H. C.; Pound, R. V. *Phys. Rev.* **1946**, *69*, 37.

4. Bloch, F.; Hansen, W. W.; Packard, M. *Phys. Rev.* **1946**, *69*, 127.

5. Proctor, W. G.; Yu, F. C. *Phys. Rev.* **1950**, *77*, 717.

6. (a) Hahn, E. L.; Maxwell, D. E. *Phys. Rev.* **1952**, *88*, 1070. (b) Gutowsky, H. S.; McCall, D. W.; Slichter, C. P. *J. Chem. Phys.* **1953**, *21*, 279.

7. Andrew, E. R.; Bradbury, A.; Eades, R. G. *Nature (London)* **1958**, *182*, 1659.

8. Andrew, E. R.; Bradbury, A.; Eades, R. G. *Nature (London)* **1959**, *183*, 1802.

9. Lowe, I. J. *Phys. Rev. Lett.* **1959**, *2*, 285.

10. Ernst, R. R. *Angew. Chem. Int. Ed. Engl.* **1992**, *31*, 805.

11. Hartmann, S. R.; Hahn, E. L. *Phys. Rev.* **1962**, *128*, 2042.

12. Pines, A.; Gibby, M. G.; Waugh, J. S. *J. Chem. Phys.* **1973**, *59*, 569.

13. Schaefer, J.; Stejskal, E. O. *J. Am. Chem. Soc.* **1976**, *98*, 1031.

14. Fyfe, C. A. *Solid-State NMR for Chemists*; C. F. C. Press: Guelph, 1983.

15. (a) Medek, A.; Harwood, J. S.; Frydman, L. *J. Am. Chem. Soc.* **1995**, *117*, 12779. (b) Medek, A.; Frydman, L. *J. Braz. Chem. Soc.* **1999**, *10*, 263.

16. Haeberlen, U. In *High Resolution NMR in Solids: Selective Averaging*, Advances in Magnetic Resonance, Supplement 1; Waugh, J. S., Ed.; Academic Press: New York, 1976.

17. Mehring, M. *Principles of High Resolution NMR in Solids*, 2nd ed.; Springer-Verlag: Berlin, 1983.

18. Munowitz, M. *Coherence and NMR*; John Wiley & Sons: New York, 1988; Appendix C.

19. Ding, S. W.; Ye, C. H. *Chem. Phys. Lett.* **1990**, *170*, 277.

20. Anet, F. A. L.; O' Leary, D. J.; Wade, C. G.; Johnson, R. D. *Chem. Phys. Lett.* **1990**, *171*, 401.

21. Chenon, M. T.; Coupry, C.; Werbelow, L. G. *J. Phys. Chem.* **1992**, *96*, 561.

22. Wi, S.; Frydman, L. *J. Chem. Phys.* **2002**, *116*, 1551.

23. (a) Ramsey, N. F. *Phys. Rev.* **1950**, *77*, 567. (b) Ramsey, N. F. *Phys. Rev.* **1950**, *78*, 699. (c) Ramsey, N. F. *Phys. Rev.* **1951**, *83*, 540. (d) Ramsey, N. F. *Phys. Rev.* **1952**, *86*, 243.

24. *Nuclear Magnetic Shieldings and Molecular Structure*; Tossell, J.A., Ed.; Series C: Mathematical and Physical Sciences - Vol. 386, NATO ASI Series; Kluwer Academic Publishers: Dordrecht, 1993.

25. Jameson, C. J. In *Multinuclear NMR*; Mason, J., Ed.; Plenum Press: New York, 1987; Chapter 3.

26. Grutzner, J. B. In *Recent Advances In Organic NMR Spectroscopy*; Lambert, J. B., Rittner, R., Eds.; Norell Press: Landisville, NJ, 1987; chapter 2.

27. Mason, J. *Solid State Nucl. Magn. Reson.* **1993**, *2*, 285.

28. Cohen, M. H.; Reif, F. In *Solid State Physics*, Volume 5; Seitz, F. and Turnbull, D. Eds.; Academic Press: New York, 1957; p. 321.

29. Pound, R. V. *Phys. Rev.* **1950**, *79*, 685.

30. For an extension of Pound's work, see: Volkoff, G. M.; Petch, H. E.; Smellie, D. W. L. *Can. J. Phys.* **1952**, *30*, 270.

31. Duer, M. J.; Farnan, I. In *Solid-State NMR Spectroscopy: Principles and Applications*; Duer, M. J., Ed.; Blackwell Science: Osney Mead, Oxford, UK: 2002; Chapter 4.

32. Samoson, A. *Chem. Phys. Lett.* **1985**, *119*, 29.

33. Man, P. P. In *Encyclopedia of Nuclear Magnetic Resonance*; Grant, D. M. and Harris, R. K., Eds.; John Wiley & Sons.: Chichester, UK, 1996; pp. 3838-3848.

34. Vega, A. J. In *Encyclopedia of Nuclear Magnetic Resonance*; Grant, D. M. and Harris, R. K., Eds.; John Wiley & Sons: Chichester, UK, 1996; p.3869-3889.

35. Wasylishen, R. E. In *Encyclopedia of Nuclear Magnetic Resonance*; Grant, D. M., Harris, R. K., Eds.; John Wiley & Sons: Chichester, UK, 1996; pp. 1685-1695.

36. Ishii, Y.; Terao, T.; Hayashi, S. *J. Chem. Phys.* **1997**, *107*, 2760.

37. Carravetta, M.; Eden, M.; Johannessen, O. G.; Luthman, H.; Verdegem, P. J. E.; Lugtenburg, J.; Sebald, A.; Levitt, M. H. *J. Am. Chem. Soc.* **2001**, *123*, 10628.

38. Ishii, Y. *J. Chem. Phys.* **2001**, *114*, 8473.

39. Case, D. A. *J. Biomol. NMR* **1999**, *15*, 95.

40. Ramsey, N. F. *Phys. Rev.* **1953**, *91*, 303.

41. (a) Ramsey, N. F. In *Nuclear Moments and Statistics, Experimental Nuclear Physics*, Volume 1; Segrè, E., Ed.; John Wiley & Sons, Inc.: New York, 1953; Part III. (b) Ramsey, N. F. *Molecular Beams*; Oxford University Press: London, 1956. (c) Zorn, J. C.; English, T. C. *Molecular Beam Electric Resonance Spectroscopy*, In *Advances in Atomic and Molecular Physics*, Volume 9; Bates, D. R., Ed.; Academic Press: New York, 1973; pp. 243-321.

42. Norman F. Ramsey, in addition to developing the widely-used theories of indirect spin-spin coupling and nuclear magnetic shielding, was also involved in the development and application of the molecular beam electric resonance method to the study of hyperfine structure in diatomic molecules. See Ramsey, N. F. *Spectroscopy with Coherent Radiation: Selected papers of Norman F. Ramsey with commentary*, World Scientific Series in 20th Century Physics, Volume 21; World Scientific Publishing Co. Pte. Ltd.: Singapore; 1998.

43. Jameson, C. J. In *Phosphorus-31 NMR Spectroscopy in Stereochemical Analysis: Organic Compounds and Metal Complexes*, Methods in Stereochemical Analysis Volume 8; Verkade, J. G. and Quin, L. D., Eds.; VCH: Deerfield Beach, Florida: 1987; Chapter 6.

44. Jameson, C. J. In *Multinuclear NMR*; Mason, J., Ed.; Plenum Press: New York, 1987; Chapter 4.

45. Pyykkö, P. *Theor. Chem. Acc.* **2000**, *103*, 214.

46. Raynes, W. T. *Magn. Reson. Chem.* **1992**, *30*, 686.

47. Buckingham, A. D.; Pyykkö, P.; Robert, J. B.; Wiesenfeld, L. *Mol. Phys.* **1982**, *46*, 177.

48. (a) Demaison, J.; Hüttner, W.; Starck, B.; Buck, I.; Tischer, R.; Winnewisser, M. In *Landolt-Börnstein: Numerical Data and Functional Relationships in Science and*

*Technology*; Hellwege, K.-H., Hellwege, A. M., Eds.; New Series, Group II: Atomic and Molecular Physics, Volume 6: Molecular Constants; Springer-Verlag: Berlin, 1974; section 2.9. (b) Demaison, J.; Dubrulle, A.; Hüttner, W.; Tiemann, E. In *Landolt-Börnstein: Numerical Data and Functional Relationships in Science and Technology*; Hellwege, K.-H., Hellwege, A. M., Eds.; New Series, Group II: Atomic and Molecular Physics, Volume 14a: Molecular Constants; Springer-Verlag: Berlin, 1982; section 2.9.

49. Dyke, T. R.; Muenter, J. S. In *International Review of Science: Molecular Structure and Properties, Physical Chemistry, Series Two, Volume 2*, Buckingham, A. D., Ed.; Butterworths: London, 1975; Chapter 2.

50. VanderHart, D. L.; Gutowsky, H. S. *J. Chem. Phys.* **1968**, *49*, 261.

51. Zilm, K. W.; Grant, D. M. *J. Am. Chem. Soc.* **1981**, *103*, 2913.

52. Andrew, E. R.; Farnell, L. F. *Mol. Phys.* **1968**, *15*, 157.

53. Bryce, D. L.; Bernard, G. M.; Gee, M.; Lumsden, M. D.; Eichele, K.; Wasylishen, R. E. *Can. J. Anal. Sci. Spectrosc.* **2001**, *46*, 46.

54. Smith, M. E.; Strange, J. H. *Meas. Sci. Technol.* **1996**, *7*, 449.

55. Schmidt-Rohr, K.; Spiess, H. W. *Multidimensional Solid-State NMR and Polymers*; Academic Press: London, 1994.

56. Duer, M. J. *Solid-State NMR Spectroscopy: Principles and Applications*; Duer, M. J., Ed.; Blackwell Science: Osney Mead, Oxford, UK: 2002.

57. Stejskal, E. O.; Memory, J. D. *High Resolution NMR in the Solid State: Fundamentals of CP/MAS*; Oxford University Press: New York, 1984.

58. Fyfe, C. A.; Wasylishen, R. E. In *Solid State Chemistry Techniques*; Cheetham, A. K. and Day, P., Eds.; Clarendon Press: Oxford, 1987; Chapter 6.

59. Sebald, A. *NMR Basic Princ. Prog.* **1994**, *31*, 91.

60. Burum, D. P. In *Encyclopedia of Nuclear Magnetic Resonance*; Grant, D. M. and Harris, R. K., Eds.; John Wiley & Sons: Chichester, UK, 1996; p. 1535.

61. Ernst, R. R.; Bodenhausen, G.; Wokaun, A. *Principles of Nuclear Magnetic Resonance in One and Two Dimensions: The International Series of Monographs on Chemistry*, Volume 14; Breslow, R., Goodenough, J. B., Halpern, J., Rowlinson, J. S., Eds.; Clarendon Press: Oxford, 1987; Section 4.5.

62. Geen, H.; Titman, J. J.; Spiess, H. W. *Chem. Phys. Lett.* **1993**, *213*, 145.

63. Hediger, S.; Signer, P.; Tomaselli, M.; Ernst, R. R.; Meier, B. H. *J. Magn. Reson.* **1997**, *125*, 291.

64. Hediger, S.; Meier, B. H.; Ernst, R. R. *J. Chem. Phys.* **1995**, *102*, 4000.

65. Hediger, S.; Meier, B. H.; Ernst, R. R. *Chem. Phys. Lett.* **1993**, *213*, 627.

66. Andrew, E. R.; Newing, R. A. *Proc. Phys. Soc.* **1958**, *72*, 959.

67. Andrew, E. R. In *Encyclopedia of Nuclear Magnetic Resonance*; Grant, D. M. and Harris, R. K., Eds.; John Wiley & Sons: Chichester, UK, 1996; p. 2891.

68. Andrew, E. R. *Phil. Trans. R. Soc. Lond.* **1981**, *A299*, 505.

69. Bennett, A. E.; Rienstra, C. M.; Auger, M.; Lakshmi, K. V.; Griffin, R. G. *J. Chem. Phys.* **1995**, *103*, 6951.

70. VanderHart, D. L.; Campbell, G. C. *J. Magn. Reson.* **1998**, *134*, 88.

71. Gan, Z.; Ernst, R. R. *Solid State Nucl. Magn. Reson.* **1997**, *8*, 153.

72. Ernst, M.; Bush, S.; Kolbert, A. C.; Pines, A. *J. Chem. Phys.* **1996**, *105*, 3387.

73. Harris, R. K. *Nuclear Magnetic Resonance Spectroscopy*; Longman: UK, 1987.

74. Fukushima, E.; Roeder, S. B.W. *Experimental Pulse NMR: A Nuts and Bolts Approach*; Addison-Wesley Publishing Company, Inc.: Massachusetts, 1981.

75. Slichter, C. P. *Principles of Magnetic Resonance*, Springer Series in Solid-State Sciences 1, 3rd ed.; Springer-Verlag: Berlin, 1990; Sections 3.3 and 3.4.

76. Edwards, J. C. and Ellis, P. D. *Magn. Reson. Chem.* **1990**, *28*, S59.

77. Samoson, A.; Lippmaa, E. *Phys. Rev. B* **1983**, *28*, 6567.

78. Abragam, A. *The Principles of Nuclear Magnetism*; Oxford University Press: Oxford, 1961.

79. Man, P. P.; Klinowski, J.; Trokiner, A.; Zanni, H.; Papon, P. *Chem. Phys. Lett.* **1988**, *151*, 143.

80. Eichele, K.; Chan, J. C. C.; Wasylishen, R. E.; Britten, J. F. *J. Phys. Chem. A* **1997**, *101*, 5423.

81. Woo, A. J.; Han, D.-Y.; Cho, S. H. *Bull. Korean Chem. Soc.* **2000**, *21*, 233.

82. Hahn, E. L. *Phys. Rev.* **1950**, *80*, 580.

83. Chan, J. C. C. *Concepts Magn. Reson.* **1999**, *11*, 363.

84. Smith, M. E. *Annu. Rep. NMR Spectrosc.* **2000**, *43*, 121.

85. Kunwar, A. C.; Turner, G. L.; Oldfield, E. *J. Magn. Reson.* **1986**, *69*, 124.

86. Bodart, P. R.; Amoureux, J.-P.; Dumazy, Y.; Lefort, R. *Mol. Phys.* **2000**, *98*, 1545.

87. (a) Carr, H. Y.; Purcell, E. M. *Phys. Rev.* **1954**, *94*, 630. (b) Meiboom, S.; Gill, D. *Rev. Sci. Instr.* **1958**, *29*, 688.

88. Cheng, J. T.; Ellis, P. D. *J. Phys. Chem.* **1989**, *93*, 2549.

89. Larsen, F. H.; Jakobsen, H. J.; Ellis, P. D.; Nielsen, N. Chr. *J. Phys. Chem. A* **1997**, *101*, 8597.

90. Larsen, F. H.; Jakobsen, H. J.; Ellis, P. D.; Nielsen, N. Chr. *Mol. Phys.* **1998**, *95*, 1185.

91. Larsen, F. H.; Jakobsen, H. J.; Ellis, P. D.; Nielsen, N. Chr. *J. Magn. Reson.* **1998**, *131*, 144.

92. Larsen, F. H.; Lipton, A. S.; Jakobsen, H. J.; Nielsen, N. Chr.; Ellis, P. D. *J. Am. Chem. Soc.* **1999**, *121*, 3783.

93. Larsen, F. H.; Skibsted, J.; Jakobsen, H. J.; Nielsen, N. Chr. *J. Am. Chem. Soc.* **2000**, *122*, 7080.

94. Helgaker, T.; Jaszuński, M.; Ruud, K. *Chem. Rev.* **1999**, *99*, 293.

95. *Gaussian 98* (Revision A.4), M. J. Frisch, G. W. Trucks, H. B. Schlegel, G. E. Scuseria, M. A. Robb, J. R. Cheeseman, V. G. Zakrzewski, J. A. Montgomery, R. E. Stratmann, J. C. Burant, S. Dapprich, J. M. Millam, A. D. Daniels, K. N. Kudin, M. C. Strain, O. Farkas, J. Tomasi, V. Barone, M. Cossi, R. Cammi, B. Mennucci, C. Pomelli, C. Adamo, S. Clifford, J. Ochterski, G. A. Petersson, P. Y. Ayala, Q. Cui, K. Morokuma, D. K. Malick, A. D. Rabuck, K. Raghavachari, J. B. Foresman, J. Cioslowski, J. V. Ortiz, B. B. Stefanov, G. Liu, A. Liashenko, P. Piskorz, I. Komaromi, R. Gomperts, R. L. Martin, D. J. Fox, T. Keith, M. A. Al-Laham, C. Y. Peng, A. Nanayakkara, C. Gonzalez, M. Challacombe, P. M. W. Gill, B. G. Johnson, W. Chen, M. W. Wong, J. L. Andres, M. Head-Gordon, E. S. Replogle and J. A. Pople, Gaussian, Inc., Pittsburgh PA, 1998.

96. "Dalton, an *ab initio* electronic structure program, Release 1.0 (1997)", written by Helgaker, T., Jensen, H. J. Aa., Jørgensen, P., Olsen, J., Ruud, K., Ågren, H., Andersen, T., Bak, K. L., Bakken, V., Christiansen, O., Dahle, P., Dalskov, E. K., Enevoldsen, T., Fernandez, B., Heiberg, H., Hettema, H., Jonsson, D., Kirpekar,

S., Kobayashi, R., Koch, H., Mikkelsen, K. V., Norman, P., Packer, M. J., Saue, T., Taylor, P.R., Vahtras, O.

97. "ACES II, an *ab initio* program system", authored by Stanton, J. F., Gauss, J., Watts, J. D., Lauderdale, W. J., Bartlett, R. J., also containing modified versions of the MOLECULE Gaussian integral program of Almlöf, J. and Taylor, P. R., the ABACUS integral derivative program written by Helgaker, T., Jensen, H. J. Aa., Jørgensen, P., Taylor, P. R., and the PROPs property integral code of Taylor, P. R.

98. Kutzelnigg, W.; Fleicher, U.; Schindler, M. *NMR Basic Princ. Prog.* **1990**, *23*, 165.

99. Webb, G. A. In *Nuclear Magnetic Shieldings and Molecular Structure*; Tossell, J.A., Ed.; Series C: Mathematical and Physical Sciences - Vol. 386, NATO ASI Series; Kluwer Academic Publishers: Dordrecht, 1993; pp. 1-25.

100. Fleischer, U.; van Wüllen, C.; Kutzelnigg, W. In *Encyclopedia of Computational Chemistry*; Schleyer, P. v. R., Ed.; John Wiley and Sons; Chichester, 1998; pp.1827-1835.

101. O'Reilly, D. E. *Prog. Nucl. Magn. Reson. Spectrosc.* **1967**, *2*, 1.

102. Lipscomb, W. N. *Adv. Magn. Reson.* **1966**, *2*, 137.

103. Ditchfield, R. *Mol. Phys.* **1974**, *27*, 789.

104. Wolinski, K.; Hinton, J. F.; Pulay, P. *J. Am. Chem. Soc.* **1990**, *112*, 8251.

105. Kutzelnigg, W. *Isr. J. Chem.* **1980**, *19*, 193.

106. Schindler, M.; Kutzelnigg, W. *J. Chem. Phys.* **1982**, *76*, 1919.

107. Hansen, A. E.; Bouman, T. D. *J. Chem. Phys.* **1985**, *82*, 5035.

108. Keith, T. A.; Bader, R. F. W. *Chem. Phys. Lett.* **1992**, *194*, 1.

109. Autschbach, J.; Ziegler, T. In *Encyclopedia of Nuclear Magnetic Resonance*, Supplement; Grant, D. M. and Harris, R. K., Eds.; John Wiley & Sons: Chichester, in press.

110. Malkin, V. G.; Malkina, O. L.; Salahub, D. R. *Chem. Phys. Lett.* **1996**, *261*, 335.

111. Schreckenbach, G.; Ziegler, T. *J. Phys. Chem.*, **1995**, *99*, 606.

112. Schreckenbach, G.; Ziegler, T. *Int. J. Quantum Chem.*, **1997**, *61*, 899.

113. Wolff, S. K.; Ziegler, T. *J. Chem. Phys.*, **1998**, *109*, 895.

114. Wolff, S. K.; Ziegler, T.; van Lenthe, E.; Baerends, E. J. *J. Chem. Phys.* **1999**, *110*, 7689.

115. Chang, Ch.; Pelissier, M.; Durand, Ph. *Phys. Scr.* **1986**, *34*, 394.

116. Heully, J.-L.; Lindgren, I.; Lindroth, E.; Lundqvist, S.; Mårtensson-Pendrill, A.-M. *J. Phys. B* **1986**, *19*, 2799.

117. van Lenthe, E.; Baerends, E. J.; Snijders, J. G. *J. Chem. Phys.* **1993**, *99*, 4597.

118. van Lenthe, E.; Baerends, E. J. *J. Chem. Phys.* **2000**, *112*, 8279.

119. Helgaker, T.; Jaszuński, M.; Ruud, K.; Górska, A. *Theor. Chem. Acc.* **1998**, *99*, 175.

120. Autschbach, J.; Ziegler, T. *J. Chem. Phys.* **2000**, *113*, 936.

121. Autschbach, J.; Ziegler, T. *J. Chem. Phys.* **2000**, *113*, 9410.

122. Roos, B. O. *Adv. Chem. Phys.* **1987**, *69*, 399.

123. Vahtras, O.; Ågren, H.; Jørgensen, P.; Jensen, H. J. Aa.; Padkjær, S. B.; Helgaker, T. *J. Chem. Phys.* **1992**, *96*, 6120.

124. Levine, I. R. *Quantum Chemistry*, 5th ed.; Prentice Hall: Upper Saddle River, New Jersey, 2000; Section 13.21.

125. Smith, M. E.; van Eck., E. R. H. *Prog. Nucl. Magn. Reson. Spectrosc.* **1999**, *34*, 159.

126. Freude, D.; Haase, J. *NMR Basic Princ. Prog.* **1993**, *29*, 1.

127. Kroeker, S.; Neuhoff, P. S.; Stebbins, J. F. *J. Non-Cryst. Sol.* **2001**, *293*, 440.

128. Stebbins, J. F.; Du, L. S.; Kroeker, S.; Neuhoff, P.; Rice, D.; Frye, J.; Jakobsen, H. J. *Solid State Nucl. Magn. Reson.* **2002**, *21*, 105.

129. Bryce, D. L.; Gee, M.; Wasylishen, R. E. *J. Phys. Chem. A* **2001**, *105*, 10413.

130. Lipton, A. S.; Buchko, G. W.; Sears, J. A.; Kennedy, M. A.; Ellis, P. D. *J. Am. Chem. Soc.* **2001**, *123*, 992.

131. Lipton, A. S.; Smith, M. D.; Adams, R. D.; Ellis, P. D. *J. Am. Chem. Soc.* **2002**, *124*, 410.

132. Massiot, D.; Vosegaard, T.; Magneron, N.; Trumeau, D.; Montouillout, V.; Berthet, P.; Loiseau, T.; Bujoli, B. *Solid State Nucl. Magn. Reson.* **1999**, *15*, 159.

133. For recent examples, see: (a) Wu, G. *Biochem. Cell Biol.* **1998**, *76*, 429. (b) Kanehashi, K.; Saito, K.; Sugisawa, H. *Chem. Lett.* **2000**, *6*, 588. (c) Bull, L. M.; Bussemer, B.; Anupõld, T.; Reinhold, A.; Samoson, A.; Sauer, J.; Cheetham, A. K.; Dupree, R. *J. Am. Chem. Soc.* **2000**, *122*, 4948. (d) Smith, L. J.; Eckert, H.; Cheetham, A. K. *J. Am. Chem. Soc.* **2000**, *122*, 1700. (e) Bodart, P. R.; Amoureux, J. P.; Pruski, M.; Bailly, A.; Fernandez, C. *Magn. Reson. Chem.* **1999**, *37*, S69. (f) Wang, S. H.; Stebbins, J. F. *J. Am. Ceram. Soc.* **1999**, *82*, 1519. (g) Hwang, S.-J.; Fernandez, C.; Amoureux, J. P.; Han, J.-W.; Cho, J.; Martin, S. W.; Pruski, M. *J. Am. Chem. Soc.* **1998**, *120*, 7337. (h) Stebbins, J. F.; Zhao, P. D.; Kroeker, S. *Solid State Nucl. Magn. Reson.* **2000**, *16*, 9. (i) Hwang, S.-J.; Fernandez, C.; Amoureux, J. P.; Cho, J.; Martin, S. W.; Pruski, M. *Solid State Nucl. Magn. Reson.* **1997**, *8*, 109.

134. (a) Chan, J. C. C. *J. Magn. Reson.* **1999**, *140*, 487. (b) Pruski, M.; Bailly, A.; Lang, D. P.; Amoureux, J. P.; Fernandez, C. *Chem. Phys. Lett.* **1999**, *307*, 35. (c) Wu, G.; Yamada, K. *Chem. Phys. Lett.* **1999**, *313*, 519. (d) Wu, G. *Chem. Phys. Lett.* **2000**, *322*, 513. (e) Wi, S.; Frydman, L. *J. Chem. Phys.* **2000**, *112*, 3248. (f) Wu, G.; Wasylishen, R. E. *Mol. Phys.* **1998**, *95*, 1177.

135. Bryce, D. L.; Wasylishen, R. E. In *Encyclopedia of Spectroscopy and Spectrometry*; Lindon, J. C., Tranter, G. E., Holmes, J. L., Eds.; Academic Press: London, 2000; pp. 2136-2144.

136. Baldus, M.; Rovnyak, D.; Griffin, R. G. *J. Chem. Phys.* **2000**, *112*, 5902.

137. Nijman, M.; Ernst, M.; Kentgens, A. P. M.; Meier, B. H. *Mol. Phys.* **2000**, *98*, 161.

138. Gan, Z. *J. Am. Chem. Soc.* **2000**, *122*, 3242.

139. Pyykkö, P. *Mol. Phys.* **2001**, *99*, 1617.

140. Mann, B. E. In *NMR and the Periodic Table*; Harris, R. K., Mann, B. E., Eds.; Academic Press: London, 1978; Section 4C.

141. Kennedy, J. D. In *Multinuclear NMR*; Mason, J., Ed.; Plenum Press: New York, 1987; Chapter 8.

142. Kidd, R. G. In *NMR of Newly Accessible Nuclei: Chemically and Biochemically Important Elements*, Vol. 2; Laszlo, P., Ed.; Academic Press: New York, 1983; Chapter 3.

143. Wrackmeyer, B. In *Annual Reports on NMR Spectroscopy*, Vol. 20; Webb, G. A., Ed.; Academic Press: London, 1988; pp. 61-203.

144. Nöth, H.; Wrackmeyer, B. In *NMR Basic Principles and Progress*, Vol. 14; Diehl, P., Fluck, E., Kosfeld, R., Eds.; Springer-Verlag: Berlin, 1978.

145. See for example: (a) Bray, P. J. *Inorg. Chim. Acta* **1999**, *289*, 158. (b) Eckert, H. *Prog. Nucl. Magn. Reson. Spectrosc.* **1992**, *24*, 159. (c) Chan, J. C. C.; Bertmer, M.; Eckert, H. *J. Am. Chem. Soc.* **1999**, *121*, 5238. (d) Bray, P. J.; Petersen, G. L. *Z. Naturforsch*, **1998**, *53a*, 273. (e) Kirkpartick, R. J.; Brow, R. K. *Solid State Nucl. Magn. Reson.* **1995**, *5*, 9. (f) Youngman, R. E.; Zwanziger, J. W. *J. Am. Chem. Soc.* **1995**, *117*, 1397. (g) van Wüllen, L.; Züchner, L.; Müller-Warmuth, W.; Eckert, H. *Solid State Nucl. Magn. Reson.* **1996**, *6*, 203. (h) van Wüllen, L.; Gee, B.; Züchner, L.; Bertmer, M.; Eckert, H. *Ber. Bunsenges. Phys. Chem.* **1996**, *100*, 1539. (i) Bertmer, M.; Züchner, L.; Chan, J. C. C.; Eckert, H. *J. Phys. Chem. B* **2000**, *104*, 6541. (j) Chan, J. C. C.; Bertmer, M.; Eckert, H. *Chem. Phys. Lett.* **1998**, *292*, 154. (k) Silver, A. H.; Bray, P. J. *J. Chem. Phys.* **1958**, *29*, 984.

146. For a review of metallaborane chemistry, see: Fehlner, T. P. *Organometallics* **2000**, *19*, 2643.

147. Fehlner, T. P. *Collect. Czech. Chem. Commun.* **1999**, *64*, 767.

148. (a) Khattar, R.; Puga, J.; Fehlner, T. P.; Rheingold, A. L. *J. Am. Chem. Soc.* **1989**, *111*, 1877. (b) Rath, N. P.; Fehlner, T. P. *J. Am. Chem. Soc.* **1987**, *109*, 5273. (c) Housecroft, C. E.; Buhl, M. L.; Long, G. J.; Fehlner, T. P. *J. Am. Chem. Soc.* **1987**, *109*, 3323. (d) Miller, V. R.; Weiss, R.; Grimes, R. N. *J. Am. Chem. Soc.* **1977**, *99*, 5646. (e) Venable, T. L.; Grimes, R. N. *Inorg. Chem.* **1982**, *21*, 887. (f) Lei, X.; Shang, M.; Fehlner, T. P. *J. Am. Chem. Soc.* **1999**, *121*, 1275. (g) Bandyopadhyay, A.; Shang, M.; Jun, C. S.; Fehlner, T. P. *Inorg. Chem.* **1994**, *33*, 3677. (h) Lei, X.; Shang, M.; Fehlner, T. P. *Inorg. Chem.* **1998**, *37*, 3900.

149. Kawamori, A.; Itoh, J. *J. Phys. Soc. Jpn.* **1963**, *18*, 1614.

150. Spiess, H. W.; Sheline, R. K. *J. Chem. Phys.* **1971**, *54*, 1099.

151. Erge, Th.; Michel, D.; Petersson, J.; Windsch, W. *Phys. Stat. Sol. (A)* **1989**, *114*, 705.

152. Bastow, T. J.; Stuart, S. N. *J. Phys.: Condens. Matter* **1989**, *1*, 4649.

153. Holzer, K.-P.; Häcker, U.; Petersson, J.; Michel, D.; Kluthe, S. *Solid State Commun.* **1995**, *94*, 275.

154. Jurga, S.; Seliger, J.; Blinc, R.; Spiess, H. W. *Phys. Lett. A* **1986**, *116*, 295.

155. Jurga, S.; Harbison, G. S.; Blümich, B.; Spiess, H. W.; Fujara, F.; Olinger, A. *Ber. Bunsenges. Phys. Chem.* **1986**, *90*, 1153.

156. Furukawa, Y.; Ikeda, R. *Ber. Bunsenges. Phys. Chem.* **1993**, *97*, 1143.

157. Ono, H.; Ishimaru, S.; Ikeda, R.; Ishida, H. *Chem. Phys. Lett.* **1997**, *275*, 485.

158. Ono, H.; Ishimaru, S.; Ikeda, R.; Ishida, H. *Bull. Chem. Soc. Jpn.* **1999**, *72*, 2049.

159. Skibsted, J.; Jakobsen, H. J. *Inorg. Chem.* **1999**, *38*, 1806.

160. Kanda, T. *J. Phys. Soc. Jpn.* **1955**, *10*, 85.

161. Weeding, T. L.; Veeman, W. S. *J. Chem. Soc., Chem. Commun.* **1989**, 946.

162. Lefebvre, F. *J. Chim. Phys.* **1992**, *89*, 1767.

163. Jelinek, R.; Stein, A.; Ozin, G. A. *J. Am. Chem. Soc.* **1993**, *115*, 2390.

164. Bastow, T. J.; Stuart, S. N.; McDugle, W. G.; Eachus, R. S.; Spaeth, J. M. *J. Phys.: Condens. Matter* **1994**, *6*, 8633.

165. Becker, K. D. *J. Chem. Phys.* **1978**, *68*, 3785.

166. Kirkpatrick, R. J.; Yu, P.; Hou, X.; Kim, Y. *Am. Mineral.* **1999**, *84*, 1186.

167. Hattori, M.; Onoda, Y.; Erata, T.; Smith, M. E.; Hattori, M.; Ohki, H.; Ikeda, R. *Z. Naturforsch.* **1994**, *49a*, 291.

168. Yesinowski, J. P.; Buess, M. L.; Garroway, A. N.; Ziegeweid, M.; Pines, A. *Anal. Chem.* **1995**, *67*, 2256.

169. Lucken, E. A. C. *Nuclear Quadrupole Coupling Constants*; Academic Press: London, 1969.

170. Frey, M. N.; Koetzle, T. F.; Lehmann, M. S.; Hamilton, W. C. *J. Chem. Phys.* **1973**, *58*, 2547.

171. Görbitz, C. H. *Acta Chem. Scand.* **1989**, *43*, 871.

172. Kurahashi, M.; Engel, P.; Nowacki, W. *Z. Krist.* **1980**, *152*, 147.

173. Ashida, T.; Bando, S.; Kakudo, M. *Acta Cryst.* **1972**, *B28*, 1560.

174. Malito, J. *Annu. Rep. NMR Spectrosc.* **1997**, *33*, 151.

175. Eichele, K.; Wasylishen, R. E.; Nelson, J. H. *J. Phys. Chem. A* **1997**, *101*, 5463.

176. Pasynkiewicz, S.; Jankowski, J. *Appl. Organomet. Chem.* **1995**, *9*, 335.

177. Belen Mula, M.; Beaumont, A. J.; Doyle, K. O.; Gallagher, M. L.; Rooney, A. D. *J. Mol. Catal. A: Chemical* **1999**, *148*, 23.

178. Vreugdenhil, A. J.; Butler, I. S. *Appl. Spectrosc.* **1995**, *49*, 482.

179. Knop, O.; Palmer, E. M.; Robinson, R. W. *Acta Cryst.* **1975**, *A31*, 19.

180. Knop, O. *Acta Cryst.* **1976**, *A32*, 147.

181. Akitt, J. W.; McDonald, W. S. *J. Magn. Reson.* **1984**, *58*, 401.

182. Brownlee, R. T. C.; O'Connor, M. J.; Shehan, B. P.; Wedd, A. G. *Aust. J. Chem.* **1986**, *39*, 931.

183. Huis, L.; Pouwels, P. J. W.; MacLean, C. *Mol. Phys.* **1990**, *70*, 879.

184. Koshland, D. E.; Myers, S. E.; Chesick, J. P. *Acta Cryst.* **1977**, *B33*, 2013.

185. House, D. A. *Adv. Inorg. Chem.* **1997**, *44*, 341.

186. (a) Bolm, C.; Muñiz, K. *Chem. Soc. Rev.* **1999**, *28*, 51. (b) Avalos, M.; Babiano, R.; Cintas, P.; Jiménez, J. L.; Palacios, J. C. *Chem. Soc. Rev.* **1999**, *28*, 169. (c) Dötz, K. H.; Tomuschat, P. *Chem. Soc. Rev.* **1999**, *28*, 187. (d) Hegedus, L. S. *Acc. Chem. Res.* **1995**, *28*, 299.

187. Whittall, I. R.; McDonagh, A. M.; Humphrey, M. G.; Samoc, M. *Adv. Organomet. Chem.* **1998**, *42*, 291.

188. (a) Mallah, T.; Thiébaut, S.; Verdaguer, M.; Veillet, P. *Science* **1993**, *262*, 1554. (b) Ferlay, S.; Mallah, T.; Ouahès, R.; Veillet, P.; Verdaguer, M. *Nature* **1995**, *378*, 701. (c) Sato, O.; Iyoda, T.; Fujishima, A.; Hashimoto, K. *Science* **1996**, *271*, 49.

189. (a) Snowling, D. C. H.; Grovenor, C. R. M. *J. Mater. Chem.* **1993**, *3*, 473. (b) Martin, C.; Hervieu, M.; Maignan, A.; Michel, C.; Raveau, B.; Daturi, M.; Letouzé, F. *Physica C* **1997**, *292*, 32. (c) Letouzé, F.; Martin, C.; Michel, C.; Hervieu, M.; Maignan, A.; Seshadri, R.; Raveau, B. *Eur. Phys. J. Appl. Phys.* **1998**, *1*, 285.

190. Minelli, M.; Enemark, J. H.; Brownlee, R. T. C.; O'Connor, M. J.; Wedd, A. G. *Coord. Chem. Rev.* **1985**, *68*, 169.

191. Granger, P. In *The Encyclopedia of Nuclear Magnetic Resonance*; Grant, D. M. and Harris, R. K., Eds.; John Wiley & Sons: Chichester, UK, 1996; pp. 3889-3900.

192. Egozy, Y.; Loewenstein, A. *J. Magn. Reson.* **1969**, *1*, 494.

193. Epperlein, B. W.; Krüger, H.; Lutz, O.; Nolle, A.; Mayr, W. *Z. Naturforsch.* **1975**, *30a*, 1237.

194. Brevard, C.; Pregosin, P. S.; Thouvenot, R. In *Transition Metal Nuclear Magnetic Resonance, Studies in Inorganic Chemistry, Volume 13*; Pregosin, P. S., Ed.; Elsevier: Amsterdam, 1991, and references therein.

195. Hafner, A.; Hegedus, L. S.; deWeck, G.; Hawkins, B.; Dötz, K. H. *J. Am. Chem. Soc.* **1988**, *110*, 8413.

196. Dove, M. F. A.; Lloyd Jones, E. M.; Clark, R. J. *Magn. Reson. Chem.* **1989**, *27*, 973.

197. Gaemers, S.; Groenevelt, J.; Elsevier, C. J. *Eur. J. Inorg. Chem.* **2001**, 829.

198. (a) Abelyashev, G. N.; Berzhanskij, V. N.; Sergeev, N. A.; Fedotov, Yu. V. *Phys. Lett. A* **1988**, *133*, 263. (b) Abelyashev, G. N.; Berzhansky, V. N.; Polulyakh, S. N.; Sergeev, N. A. *Physica B* **2000**, *292*, 323.

199. Derkachenko, V. N.; Kovtun, N. M.; Proporenko, V. K.; Safarov, A. F.; Shemyakov, A. A.; Eivazov, E. A. *Izv. Akad. Nauk SSR, Neorg. Mater.* **1984**, *20*, 1270.

200. Karnachev, A. S.; Klechin, Yu. I.; Kovtun, N. M.; Moskvin, A. S.; Solov'ev, E. E.; Tkachenko, A. A. *Zh. Eksp. Teor. Fiz.* **1983**, *85*, 670. (English translation: *Sov. Phys. JETP* **1983**, *58*, 390.)

201. Karnachev, A. S.; Kovtun, N. M.; Kurkin, M. I.; Solov'ev, E. E.; Tkachenko, A. A. *Zh. Eksp. Teor. Fiz.* **1983**, *85*, 224. (English translation: *Sov. Phys. JETP* **1983**, *58*, 130).

202. Dubiel, S. M.; Lütgemeier, H. *Phys Lett.* **1981**, *84A*, 396, and references therein.

203. Poźniak, J. K.; Nowak, B.; Tkacz, M. *Z. Phys. B* **1997**, *104*, 255.

204. Boysen, J.; Kettschau, A.; Brewer, W. D. *Phys. Lett.* **1983**, *95A*, 502.

205. (a) Wu, G. *Chem. Phys. Lett.* **1998**, *298*, 375. (b) Sham, S.; Wu, G. *Can. J. Chem.* **1999**, *77*, 1782.

206. (a) Larsen, F. H.; Lipton, A. S.; Jakobsen, H. J.; Nielsen, N. Chr.; Ellis, P. D. *J. Am. Chem. Soc.* **1999**, *121*, 3783. (b) Lipton, A. S.; Buchko, G. W.; Sears, J. A.; Kennedy, M. A.; Ellis, P. D. *J. Am. Chem. Soc.* **2001**, *123*, 992.

207. Vosegaard, T.; Andersen, U.; Jakobsen, H. J. *J. Am. Chem. Soc.* **1999**, *121*, 1970.

208. Angelici, R. J. *J. Chem. Educ.* **1968**, *45*, 119.

209. (a) Jost, A.; Rees, B.; Yelon, W. B. *Acta Cryst.* **1975**, *B31*, 2649. (b) Rees, B.; Mitschler, A. *J. Am. Chem. Soc.* **1976**, *98*, 7918.

210. McGinnety, J. *Acta Cryst.* **1972**, *B28*, 2845.

211. Gatehouse, B. M.; Leverett, P. *J. Chem. Soc. (A)* **1969**, 1857.

212. Morris, A. J.; Kennard, C. H. L.; Moore, F. H.; Smith, G.; Montgomery, H. *Cryst. Struct. Comm.* **1981**, *10*, 529.

213. Hayashi, S.; Hayamizu, K. *Bull. Chem. Soc. Jpn.* **1989**, *62*, 2429.

214. Loewenstein, A.; Shporer, M.; Lauterbur, P. C.; Ramirez, J. E. *J. Chem. Soc., Chem. Commun.* **1968**, 214.

215. *VNMR*, Version 6.1B, Varian Inc., 1998.

216. *NUTS - NMR Utility Transform Software for Windows 95/NT*, 2D Version, Acorn NMR, 1998.

217. WIN-NMR, Version 6.0, Copyright Bruker-Franzen Analytik GmbH.

218. Eichele, K.; Wasylishen, R. E. *WSOLIDS NMR Simulation Package*, Version 1.17.26, 2000.

219. Alderman, D. W.; Solum, M. S.; Grant, D. M. *J. Chem. Phys.* **1986**, *84*, 3717.

220. Bak, M.; Rasmussen, J. T.; Nielsen, N. Chr. *J. Magn. Reson.* **2000**, *147*, 296.

221. *Gaussian 98*W (Revision A.7), M. J. Frisch, G. W. Trucks, H. B. Schlegel, G. E. Scuseria, M. A. Robb, J. R. Cheeseman, V. G. Zakrzewski, J. A. Montgomery, R. E. Stratmann, J. C. Burant, S. Dapprich, J. M. Millam, A. D. Daniels, K. N. Kudin, M. C. Strain, O. Farkas, J. Tomasi, V. Barone, M. Cossi, R. Cammi, B. Mennucci, C. Pomelli, C. Adamo, S. Clifford, J. Ochterski, G. A. Petersson, P. Y. Ayala, Q. Cui, K. Morokuma, D. K. Malick, A. D. Rabuck, K. Raghavachari, J. B. Foresman, J. Cioslowski, J. V. Ortiz, B. B. Stefanov, G. Liu, A. Liashenko, P. Piskorz, I. Komaromi, R. Gomperts, R. L. Martin, D. J. Fox, T. Keith, M. A. Al-Laham, C. Y. Peng, A. Nanayakkara, C. Gonzalez, M. Challacombe, P. M. W. Gill, B. G. Johnson, W. Chen, M. W. Wong, J. L. Andres, M. Head-Gordon, E. S. Replogle and J. A. Pople, Gaussian, Inc., Pittsburgh PA, 1998.

222. (a) Ditchfield, R. *Mol. Phys.* **1974**, *27*, 789. (b) Wolinski, K.; Hinton, J. F.; Pulay, P. *J. Am. Chem. Soc.* **1990**, *112*, 8251.

223. Becke, A. D. *J. Chem. Phys.* **1993**, *98*, 5648.

224. (a) Chesnut, D. B.; Moore, K. D. *J. Comput. Chem.* **1989**, *10*, 648. (b) Chesnut, D. B.; Rusiloski, B. E.; Moore, K. D.; Egolf, D. A. *J. Comput. Chem.* **1993**, *14*, 1364.

225. Hay, P. J.; Wadt, W. R. *J. Chem. Phys.* **1985**, *82*, 270.

226. ADF 2000.01. Theoretical Chemistry, Vrije Universiteit, Amsterdam, http://www.scm.com.

227. (a) Baerends, E. J.; Ellis, D. E.; Ros, P. *Chem. Phys.* **1973**, *2*, 41. (b) Versluis, L.; Ziegler, T. *J. Chem. Phys.* **1988**, *88*, 322. (c) te Velde, G.; Baerends, E. J. *J. Comput. Phys.* **1992**, *99*, 84. (d) Fonseca Guerra, C.; Snijders, J. G.; te Velde, G.; Baerends, E. J. *Theor. Chem. Acc.* **1998**, *99*, 391.

228. Vosko, S. H.; Wilk, L.; Nusair, M. *Can. J. Phys.* **1980**, *58*, 1200.

229. Becke, A. D. *Phys. Rev. A* **1988**, *38*, 3098.

230. Perdew, J. P. *Phys. Rev. B* **1986**, *33*, 8822; **1986**, *34*, 7406.

231. Mills, I.; Cvitaš, T.; Homann, K.; Kallay, N.; Kuchitsu, K. *Quantities, Units and Symbols in Physical Chemistry*, 2nd ed., International Union of Pure and Applied Chemistry Physical Chemistry Division; Blackwell Science: Oxford, 1993.

232. Gee, M.; Wasylishen, R. E.; Laaksonen, A. *J. Phys. Chem. A* **1999**, *103*, 10805.

233. Blount, J. F.; Finocchiaro, P.; Gust, D.; Mislow, K. *J. Am. Chem. Soc.* **1973**, *95*, 7019.

234. Gundersen, G.; Jonvik, T.; Seip, R. *Acta Chem. Scand. A* **1981**, *35*, 325.

235. Jeffrey, G. A.; Ruble, J. R.; McMullan, R. K.; Pople, J. A. *Proc. R. Soc. Lond. A* **1987**, *414*, 47.

236. Levy, H. A.; Peterson, S. W. *Phys. Rev.* **1952**, *86*, 766.

237. Strømme, K. O. *Acta. Chem. Scand.* **1974**, *A28*, 515.

238. Braekken, H.; Harang, L. *Z. Krist.* **1930**, *75*, 538.

239. Huber, K. P.; Herzberg, G. "Constants of Diatomic Molecules" (data prepared by J.W. Gallagher and R.D. Johnson, III) in *NIST Chemistry WebBook, NIST Standard Reference Database Number 69*; Mallard, W. G. and Linstrom, P. J., Eds.; February 2000, National Institute of Standards and Technology: Gaithersburg MD, 20899 (http://webbook.nist.gov).

240. Mak, T. C. W. *Z. Kristallogr.* **1984**, *166*, 277.

241. Alyea, E. C.; Somogyvari, A. *Transition Met. Chem.* **1987**, *12*, 310.

242. Brown, N. M. D.; Davidson, F.; Wilson, J. W. *J. Organomet. Chem.* **1981**, *209*, 1.

243. Love, P. *J. Chem. Phys.* **1963**, *39*, 3044.

244. Townes, C. H.; Dailey, B. P. *J. Chem. Phys.* **1949**, *17*, 782.

245. Dehmelt, H. G. *Z. Physik.* **1952**, *133*, 528.

246. Although individual trimesitylborane molecules are chiral, the crystals are racemic due to their mirror plane symmetry.

247. Schurko, R. W.; Wasylishen, R. E.; Foerster, H. *J. Phys. Chem. A* **1998**, *102*, 9750.

248. Bryce, D. L.; Wasylishen, R. E. *J. Phys. Chem. A* **1999**, *103*, 7364.

249. Power, W. P. *J. Am. Chem. Soc.* **1995**, *117*, 1800.

250. Wasylishen, R. E.; Bryce, D. L.; Evans, C. J.; Gerry, M. C. L. *J. Mol. Spectrosc.* **2000**, *204*, 184.

251. Cazzoli, G.; Cludi, L.; Degli Esposti, C.; Dore, L. *J. Mol. Spectrosc.* **1989**, *134*, 159.

252. Gatehouse, B.; Müller, H. S. P.; Gerry, M. C. L. *J. Mol. Spectrosc.* **1998**, *190*, 157.

253. Gatehouse, B. *Chem. Phys. Lett.* **1998**, *288*, 698.

254. Henderson, W. G.; Mooney, E. F. In *Annual Review of NMR Spectroscopy*, Vol. 2; Mooney, E. F., Ed.; Academic Press: London, 1969; p. 219.

255. Lauterbur, P. C. *Phys. Rev. Lett.* **1958**, *1*, 343.

256. Spiess, H. W. In *NMR Basic Principles and Progress*, Vol. 15; Diehl, P., Fluck, E., Kosfeld, R., Eds.; Springer-Verlag: Berlin, 1978; pp 55-214.

257. (a) Gibby, M. G.; Griffin, R. G.; Pines, A.; Waugh, J. S. *Chem. Phys. Lett.* **1972**, *17*, 80. (b) Anderson-Altmann, K. L.; Grant, D. M. *J. Phys. Chem.* **1993**, *97*, 11096. This paper gives nitrate nitrogen CS tensor principal components for five solid phases of $NH_4NO_3$. The span for phase IV at 18°C, 231 ppm, is discussed here.

258. Bailey, W. C. *J. Mol. Spectrosc.* **1997**, *185*, 403.

259. (a) Bray, P. J.; Edwards, J. O.; O'Keefe, J. G.; Ross, V. F.; Tatsuzaki, I. *J. Chem. Phys.* **1961**, *35*, 435. (b) Silver, A. H. *J. Chem. Phys.* **1960**, *32*, 959.

260. Ebraheem, K. A. K.; Webb, G. A. *Org. Magn. Reson.* **1977**, *10*, 258.

261. (a) Olah, G. A.; Rasul, G.; Surya Prakash, G. K. *J. Org. Chem.* **2000**, *65*, 5956. (b) Nöth, H.; Wrackmeyer, B. *Chem. Ber.* **1974**, *107*, 3070. (c) Spielvogel, B. F.; Nutt, W. R.; Izydore, R. A. *J. Am. Chem. Soc.* **1975**, *97*, 1609. (d) Wrackmeyer, B. *Z. Naturforsch.* **1980**, *35b*, 439.

262. Schindler, M. *J. Am. Chem. Soc.* **1987**, *109*, 1020.

263. Jameson, C. J.; Gutowsky, H. S. *J. Chem. Phys.* **1964**, *40*, 1714.

264. Akitt, J. W. In *Multinuclear NMR*; Mason, J., Ed.; Plenum: New York, 1987; Chapter 17.

265. Lindman, B.; Forsén, S. *NMR Basic Princ. Prog.* **1976**, *12*, 1.

266. Fabricant, B.; Muenter, J. S. *J. Chem. Phys.* **1977**, *66*, 5274.

267. Jäger, C. *NMR Basic Princ. Prog.* **1994**, *31*, 133.

268. Skibsted, J.; Nielsen, N. C.; Bildsøe, H.; Jakobsen, H. J. *J. Magn. Reson.* **1991**, *95*, 88.

269. Malli, G.; Fraga, S. *Theor. Chim. Acta* **1966**, *5*, 275.

270. Wigand, S.; Weiden, N.; Weiss, A. *Ber. Bunsenges. Phys. Chem.* **1989**, *93*, 913.

271. Nakamura, N.; Chihara, H. *J. Phys. Soc. Jpn.* **1967**, *22*, 201.

272. Eichele, K.; Wasylishen, R. E.; Grossert, J. S.; Olivieri, A. C. *J. Phys. Chem.* **1995**, *99*, 10110.

273. Blinc, R.; Mali, M.; Osredkar, R.; Seliger, J. *J. Chem. Phys.* **1975**, *63*, 35.

274. Gu, Z.; McDermott, A. *J. Am. Chem. Soc.* **1993**, *115*, 4282.

275. Wei, Y.; de Dios, A. C.; McDermott, A. E. *J. Am. Chem. Soc.* **1999**, *121*, 10389.

276. Halkier, A.; Jaszuński, M.; Jørgensen, P. *Phys. Chem. Chem. Phys.* **1999**, *1*, 4165.

277. Seth, M.; Pernpointer, M.; Bowmaker, G. A.; Schwerdtfeger, P. *Mol. Phys.* **1999**, *96*, 1767.

278. Chapman, K.; Crittenden, D.; Bevitt, J.; Jordan, M. J. T.; Del Bene, J. E. *J. Phys. Chem. A* **2001**, *105*, 5442.

279. Desiraju, G. R.; Steiner, T. *The Weak Hydrogen Bond*, IUCr Monographs on Crystallography 9; Oxford University Press: Oxford, 1999; Section 3.3.

280. Jeffrey, G. A; Saenger, W. *Hydrogen Bonding In Biological Structures*; Springer-Verlag: Berlin, 1991.

281. Yesinowski, J. P.; Eckert, H. unpublished data, California Institute of Technology, 1985.

282. Gabe, E. J.; Barnes, W. H. *Acta Cryst.* **1963**, *16*, 796.

283. Hee Han, O.; Oldfield, E. *Inorg. Chem.* **1990**, *29*, 3666.

284. Akitt, J. W.; Mann, B. E. *NMR and Chemistry: An introduction to modern NMR spectroscopy*, 4th ed.; Stanley Thornes Ltd: Cheltenham, UK, 2000; pp. 113-114.

285. Berglund, B.; Vaughan, R. W. *J. Chem. Phys.* **1980**, *73*, 2037.

286. Brown, T. L.; Butler, L. G.; Curtin, D. Y.; Hiyama, Y.; Paul, I. C.; Wilson, R. B. *J. Am. Chem. Soc.* **1982**, *104*, 1172.

287. Clymer, J. W.; Ragle, J. L. *J. Chem. Phys.* **1982**, *77*, 4366.

288. Camus, S.; Harris, K. D. M.; Johnston, R. L. *Chem. Phys. Lett.* **1997**, *276*, 186.

289. Fung, B. M. In *Critical Evaluation of Chemical and Physical Structural Information*; Lide, D. R., Jr. and Paul, M. A., Eds.; National Academy of Sciences: Washington, D. C., 1974; pp. 436-448.

290. van Rossum, B.-J.; de Groot, C. P.; Ladizhansky, V.; Vega, S.; de Groot, H. J. M. *J. Am. Chem. Soc.* **2000**, *122*, 3465.

291. van Rossum, B.-J. *Proefschrift*, Universiteit Leiden, 2000.

292. Fedotov, M. A.; Malkina, O. L.; Malkin, V. G. *Chem. Phys. Lett.* **1996**, *258*, 330.

293. (a) Sternheimer, R. M. *Phys. Rev.* **1954**, *95*, 736. (b) Sternheimer, R. M. *Phys. Rev.* **1966**, *146*, 140.

294. Slichter, C. P. *Principles of Magnetic Resonance*, Springer Series in Solid-State Sciences 1, 3rd ed.; Springer-Verlag: Berlin, 1990; p. 502.

295. Pyykkö, P. *Z. Naturforsch.* **1991**, *47a*, 189.

296. Masters, A. F.; Brownlee, R. T. C.; O'Connor, M. J.; Wedd, A. G. *Inorg. Chem.* **1981**, *20*, 4183.

297. Freude, D.; Haase, J.; Klinowski, J.; Carpenter, T. A.; Ronikier, G. *Chem. Phys. Lett.* **1985**, *119*, 365.

298. Schurko, R. W.; Macdonald, C. L. B.; Cowley, A. H. 43rd Rocky Mountain Conference on Analytical Chemistry, NMR Symposium, **2001**, Abstract #261.

299. Indris, O.; Stahl, W. *Mol. Phys.* **2000**, *98*, 1495.

300. Drouin, B. J.; Cassak, P. A.; Kukolich, P. G. *J. Chem. Phys.* **1998**, *108*, 8878.

301. Semin, G. K.; Kuznetsov, S. I.; Bryukhova, E. V.; Khotsyanova, T. L. *J. Organomet. Chem.* **1996**, *508* 129.

302. Fitzpatrick, P. J.; Le Page, Y.; Sedman, J.; Butler, I. S. *Inorg. Chem.* **1981**, *20*, 2852.

303. Huang, Y.; Butler, I. S.; Gilson, D. F. R. *Inorg. Chem.* **1992**, *31*, 4762 .

304. Brownlee, R. T. C.; O'Connor, M. J.; Shehan, B. P.; Wedd, A. G. *J. Magn. Reson.* **1985**, *61*, 516.

305. Schreckenbach, G. *J. Chem. Phys.* **1999**, *110*, 11936.

306. Ruiz-Morales, Y.; Ziegler, T. *J. Phys. Chem. A* **1998**, *102*, 3970.

307. Bühl, M. *Chem. Eur. J.* **1999**, *5*, 3514.

308. Griffith, J. S.; Orgel, L. E. *Trans. Faraday Soc.* **1957**, *53*, 601.

309. Albright, T. A. *Acc. Chem. Res.* **1982**, *15*, 149.

310. Bryce, D. L.; Wasylishen, R. E. *J. Chem. Educ.* **2001**, *78*, 124.

311. Flygare, W. H. *Chem. Rev.* **1974**, *74*, 653.

312. Mak, T. C. W. *Z. Kristallogr.* **1984**, *166*, 277.

313. Adams, D. M.; Taylor, I. D. *J. Chem. Soc., Faraday Trans. 2* **1982**, *78*, 1051.

314. Rüdorff, W.; Hofmann, U. *Z. Phys. Chem.* **1935**, *B28*, 351. Although an incorrect space group was assigned, this early work establishes the isomorphism of the group 6 metal hexacarbonyls.

315. Oldfield, E.; Keniry, M. A.; Shinoda, S.; Schramm, S.; Brown, T. L.; Gutowsky, H. S. *J. Chem. Soc., Chem. Commun.* **1985**, 791.

316. (a) Kundla, E.; Samoson, A.; Lippmaa, E. *Chem. Phys. Lett.* **1981**, *83*, 229. (b) Samoson, A.; Kundla, E.; Lippmaa, E. *J. Magn. Reson.* **1982**, *49*, 350.

317. Frydman, L. *Annu. Rev. Phys. Chem.* **2001**, *52*, 463.

318. Vosegaard, T.; Skibsted, J.; Jakobsen, H. J. *J. Phys. Chem. A* **1999**, *103*, 9144.

319. Brownlee, R. T. C.; Shehan, B. P. *J. Magn. Reson.* **1986**, *66*, 503.

320. Mastikhin, V. M.; Lapina, O. B.; Maximovskaya, R. I. *Chem. Phys. Lett.* **1988**, *148*, 413.

321. Haid, E.; Köhnlein, D.; Kössler, G.; Lutz, O.; Schich, W. *J. Magn. Reson.* **1983**, *55*, 145.

322. Lipton, A. S.; Sears, J. A.; Ellis, P. D. *J. Magn. Reson.* **2001**, *151*, 48.

323. Thomas, W. A. *Prog. Nucl. Magn. Reson. Spectrosc.* **1997**, *30*, 183.

324. Eberstadt, M.; Gemmecker, G.; Mierke, D. F.; Kessler, H. *Angew. Chem. Int. Ed. Engl.* **1995**, *34*, 1671.

325. Dingley, A. J.; Grzesiek, S. *J. Am. Chem. Soc.* **1998**, *120*, 8293.

326. Dingley, A. J.; Masse, J. E.; Peterson, R. D.; Barfield, M.; Feigon, J.; Grzesiek, S. *J. Am. Chem. Soc.* **1999**, *121*, 6019.

327. Cordier, F.; Grzesiek, S. *J. Am. Chem. Soc.* **1999**, *121*, 1601.

328. Cornilescu, G.; Hu, J. S.; Bax, A. *J. Am. Chem. Soc.* **1999**, *121*, 2949.

329. Scheurer, C.; Brüschweiler, R. *J. Am. Chem. Soc.* **1999**, *121*, 8661.

330. Cordier, F.; Rogowski, M.; Grzesiek, S.; Bax, A. *J. Magn. Reson.* **1999**, *140*, 510.

331. Patnaik, R. C.; Hota, R. L.; Tripathi, G. S. *Phys. Rev. B* **1998**, *58*, 3924.

332. Tomaselli, M.; deGraw, D.; Yarger, J. L.; Augustine, M. P.; Pines, A. *Phys. Rev. B* **1998**, *58*, 8627.

333. Slichter, C. P.; Corey, R.; Curro, N.; Haase, J.; Milling, C.; Morr, D.; Schmalian, J.; Stern, R. *Mol. Phys.* **1998**, *95*, 897.

334. Marino, J. P.; Schwalbe, H.; Griesinger, C. *Acc. Chem. Res.* **1999**, *32*, 614.

335. Case, D. A. *Curr. Opin. Struct. Biol.* **2000**, *10*, 197.

336. Mollova, E. T.; Pardi, A. *Curr. Opin. Struct. Biol.* **2000**, *10*, 298.

337. Malleier, R.; Kopacka, H.; Schuh, W.; Wurst, K.; Peringer, P. *Chem. Commun.* **2001**, 51.

338. (a) Slichter, C. P. *Principles of Magnetic Resonance*, 3rd ed., Springer Series in Solid-State Sciences; Fulde, P., Ed.; Springer: Berlin, 1990; p. 142. (b) Emsley, J. W.; Lindon, J. C. *NMR Spectroscopy Using Liquid Crystal Solvents*; Pergamon Press: Oxford, 1975. (c) Anisotropy in the indirect spin-spin coupling is also sometimes denoted as *B* and termed the "pseudo-dipolar - dipolar interference term". See: Sears, R. E. J.; Ni, Q. W. *J. Chem. Phys.* **1994**, *100*, 4708.

339. (a) Hodgkinson, P.; Emsley, L. *J. Magn. Reson.* **1999**, *139*, 46. (b) *Nature Structural Biology: NMR Special Issue*, October 1997, Volume 4 supplement. (c) Garbow, J. R.; Gullion, T. In *Carbon-13 NMR Spectroscopy of Biological Systems*; Beckmann, N., Ed.; Academic Press: New York, 1995; pp. 65-115. (d) Kiihne, S. R.; Geahigan, K. B.; Oyler, N. A.; Zebroski, H.; Mehta, M. A.; Drobny, G. P. *J. Phys. Chem. A.* **1999**, *103*, 3890. (e) Smith, S. O. *Magn. Reson. Rev.* **1996**, *17*, 1. (f) Baldus, M.; Iuliucci, R. J.; Meier, B. H. *J. Am. Chem. Soc.* **1997**, *119*, 1121.

340. Dusold, S.; Sebald, A. *Annu. Rep. Nucl. Magn. Reson. Spectrosc.* **2000**, *41*, 185.

341. (a) Lumsden, M. D.; Eichele, K.; Wasylishen, R. E.; Cameron, T. S.; Britten, J. F. *J. Am. Chem. Soc.* **1994**, *116*, 11129. (b) Lumsden, M. D.; Wasylishen, R. E.; Britten, J. F. *J. Phys. Chem.* **1995**, *99*, 16602. (c) Nolle, A. *Z. Physik. B* **1979**, *34*, 175. (d) Tutunjian, P. N.; Waugh, J. S. *J. Chem. Phys.* **1982**, *76*, 1223; *J. Magn. Reson.* **1982**, *49*, 155. (e) Eichele, K.; Wu, G.; Wasylishen, R. E.; Britten, J. F. *J. Phys. Chem.* **1995**, *99*, 1030.

342. (a) Haubenreisser, U.; Sternberg, U.; Grimmer, A.-R. *Mol. Phys.* **1987**, *60*, 151. (b) Penner, G. H.; Power, W. P.; Wasylishen, R. E. *Can. J. Chem.* **1988**, *66*, 1821. (c) Power, W. P.; Lumsden, M. D.; Wasylishen, R. E. *J. Am. Chem. Soc.* **1991**, *113*, 8257. (d) Wasylishen, R. E.; Wright, K. C.; Eichele, K.; Cameron, T. S. *Inorg. Chem.* **1994**, *33*, 407.

343. (a) Lounila, J.; Jokisaari, J. *Prog. Nucl. Magn. Reson. Spectrosc.* **1982**, *15*, 249. (b) Vaara, J.; Kaski, J.; Jokisaari, J. *J. Phys. Chem. A* **1999**, *103*, 5675. (c) Kaski, J.; Vaara, J.; Jokisaari, J. *J. Am. Chem. Soc.* **1996**, *118*, 8879. (d) Kaski, J.; Lantto, P.; Vaara, J.; Jokisaari, J. *J. Am. Chem. Soc.* **1998**, *120*, 3993.

344. Gordy, W.; Cook, R. L. *Microwave Molecular Spectra, Techniques of Chemistry*, Volume XVII; John Wiley and Sons: New York, 1984.

345. Pyykkö, P. and Wiesenfeld, L. *Mol. Phys.*, **1981**, *43*, 557.

346. Jameson, C. J.; Gutowsky, H. S. *J. Chem. Phys.* **1969**, *51*, 2790.

347. McFarlane, W. *Quart. Rev.* **1969**, *23*, 187.

348. Dalling, D. K.; Gutowsky, H. S. *J. Chem. Phys.* **1971**, *55*, 4959.

349. Wasylishen, R. E. *Annu. Rep. Nucl. Magn. Reson. Spectrosc.* **1977**, *7*, 245.

350. Pulkkinen, A.; Hiltunen, Y.; Jokisaari, J. *Liq. Cryst.* **1988**, *3*, 737.

351. Grossmann, G.; Potrzebowski, M. J.; Fleischer, U.; Krüger, K.; Malkina, O. L.; Ciesielski, W. *Solid State Nucl. Magn. Reson.* **1998**, *13*, 71.

352. Kroeker, S.; Hanna, J. V.; Wasylishen, R. E.; Ainscough, E. W.; Brodie, A. M. *J. Magn. Reson.* **1998**, *135*, 208.

353. Sears, R. E. J.; Guo, Q. Zh.; Mackey, H. J. *J. Chem. Phys.* **1984**, *80*, 5448.

354. (a) Lantto, P.; Kaski, J.; Vaara, J.; Jokisaari, J. *Chem. Eur. J.* **1999**, *6*, 1395. (b) Kaski, J. *Dissertation*, University of Oulu, 1999.

355. Jokisaari, J.; Hiltunen, Y.; Lounila, J. *J. Chem. Phys.* **1986**, *85*, 3198.

356. Pople, J. A.; Santry, D. P. *Mol. Phys.* **1964**, *8*, 1.

357. Buckingham, A. D.; Love, I. *J. Magn. Reson.* **1970**, *2*, 338.

358. Pople, J. A.; McIver, J. W., Jr.; Ostlund, N. S. *Chem. Phys. Lett.* **1967**, *1*, 465.

359. (a) Blizzard, A. C; Santry, D. P. *J. Chem. Soc., Chem. Comm.* **1970**, 1085. (b) Schulman, J. M.; Venanzi, T. *J. Am. Chem. Soc.* **1976**, *98*, 4701.

360. Ostlund, N. S.; Newton, M. D.; McIver, J. W., Jr.; Pople, J. A. *J. Magn. Reson.* **1969**, *1*, 298.

361. (a) Fukui, H. in *Nuclear Magnetic Resonance: A Specialist Periodical Report*, Vol. 29; Webb, G. A., Ed.; Royal Society of Chemistry: Cambridge, 2000; Chapter 4. See also previous volumes in this series. (b) Contreras, R. H.; Facelli, J. C. *Annu. Rep. Nucl. Magn. Reson. Spectrosc.* **1993**, *27*, 255. (c) Enevoldsen, T.; Oddershede, J.; Sauer, S. P. A. *Theor. Chem. Acc.* **1998**, *100*, 275. (d) Fukui, H.; Miura, K.; Matsuda, H.; Baba, T. *J. Chem. Phys.* **1992**, *97*, 2299. (e) Pecul, M.; Sadlej, J. *Chem. Phys. Lett.* **1999**, *308*, 486. (f) Dickson, R. M.; Ziegler, T. *J. Phys. Chem.* **1996**, *100*, 5286. (g) Nooijen, M.; Perera, S. A.; Bartlett, R. J. *Chem. Phys. Lett.* **1997**, *266*, 456.

362. Contreras, R. H.; Peralta, J. E.; Giribet, C. G.; Ruiz de Azúa, M. C.; Facelli, J. C. *Annu. Rep. Nucl. Magn. Reson. Spectrosc.* **2000**, *41*, 55.

363. Fukui, H. *Prog. Nucl. Magn. Reson. Spectrosc.* **1999**, *35*, 267.

364. Enevoldsen, T.; Oddershede, J.; Sauer, S. P. A. *Theor. Chem. Acc.* **1998**, *100*, 275.

365. Aucar, G. A.; Saue, T.; Visscher, L.; Jensen, H. J. Aa. *J. Chem. Phys.* **1999**, *110*, 6208.

366. Vaara, J.; Ruud, K.; Vahtras, O. *J. Comput. Chem.* **1999**, *20*, 1314.

367. Visscher, L.; Enevoldsen, T.; Saue, T.; Jensen, H. J. A.; Oddershede, J. *J. Comput. Chem.* **1999**, *20*, 1262.

368. See for example: Åstrand, P.-O.; Mikkelsen, K. V.; Jørgensen, P.; Ruud, K.; Helgaker, T. *J. Chem. Phys.* **1998**, *108*, 2528.

369. Koch, W.; Holthausen, M. C. *A Chemist's Guide to Density Functional Theory*; Wiley-VCH: Weinheim, 2000; Chapter 11.

370. (a) Malkin, V. G.; Malkina, O. L.; Salahub, D. R. *Chem. Phys. Lett.* **1994**, *221*, 91. (b) Malkina, O. L.; Salahub, D. R.; Malkin, V. G. *J. Chem. Phys.* **1996**, *105*, 8793.

371. Dickson, R. M.; Ziegler, T. *J. Phys. Chem.* **1996**, *100*, 5286.

372. Khandogin, J.; Ziegler, T. *Spectrochim. Acta* **1999**, *A55*, 607.

373. Khandogin, J.; Ziegler, T. *J. Phys. Chem. A* **2000**, *104*, 113.

374. Sychrovský, V.; Gräfenstein, J.; Cremer, D. *J. Chem. Phys.* **2000**, *113*, 3530.

375. Helgaker, T.; Watson, M.; Handy, N. C. *J. Chem. Phys.* **2000**, *113*, 9402.

376. Robert, J. B.; Wiesenfeld, L. *Phys. Rep.* **1982**, *86*, 363.

377. (a) Jensen, H. J. Aa.; Jørgensen, P.; Ågren, H.; Olsen, J. *J. Chem. Phys.* **1988**, *88*, 3834. (b) Guilleme, J.; Fabián, J. S. *J. Chem. Phys.* **1998**, *109*, 8168.

378. Dunning, T. H. *J. Chem. Phys.* **1989**, *90*, 1007.

379. "Near Hartree-Fock Quality GTO Basis Sets for the Second-Row Atoms"; NASA Technical Memorandum 89449, May 1987. H. R. Partridge, NASA Ames Research Centre, Moffett Field, CA 94035.

380. Yamada, C.; Hirota, E. *J. Mol. Spectrosc.* **1992**, *153*, 91.

381. Lovas, F. J.; Tiemann, E. *J. Phys. Chem. Ref. Data.* **1974**, *3*, 765.

382. Buckingham, A. D. *J. Chem. Phys.* **1962**, *36*, 3096.

383. Bass, S. M.; DeLeon, R. L.; Muenter, J. S. *J. Chem. Phys.* **1987**, *86*, 4305.

384. Tipping, R. H.; Ogilvie, J. F. *J. Mol. Struct.* **1976**, *35*, 1.

385. Dunham, J. L. *Phys. Rev.* **1932**, *41*, 721.

386. Autschbach, J.; Ziegler, T. *J. Am. Chem. Soc.* **2001**, *123*, 3341.

387. Edwards, H. G. M.; Long, D. A.; Mansour, H. R. *J. Chem. Soc., Faraday Trans. 2* **1978**, *74*, 1200.

388. Špirko, V.; Blabla, J. *J. Mol. Spectrosc.* **1988**, *129*, 59.

389. Dolg, M. *Mol. Phys.* **1996**, *88*, 1645.

390. Pearson Jr., R.; Lovas, F. J. *J. Chem. Phys.* **1977**, *66*, 4149.

391. Johnson, D. R.; Lovas, F. J. *Chem. Phys. Lett.* **1972**, *15*, 65.

392. Swaminathan, S.; Craven, B. M.; McMullan, R. K. *Acta Cryst.* **1984**, *B40*, 300.

393. Krause, E. *Ber.* **1918**, *51*, 912.

394. Krause, E.; Becker, R. *Ber.* **1920**, *53B*, 173.

395. Kushlefsky, B.; Simmons, I.; Ross, A. *Inorg. Chem.* **1963**, *2*, 187.

396. Lippmaa, E. T.; Alla, M. A.; Pehk, T. J.; Engelhardt, G. *J. Am. Chem. Soc.* **1978**, *100*, 1929.

397. Harris, R. K.; Sebald, A. *Magn. Reson. Chem.* **1987**, *25*, 1058.

398. Wu, G.; Wasylishen, R. E. *Inorg. Chem.* **1992**, *31*, 145.

399. Wu, G.; Wasylishen, R. E. *Organometallics* **1992**, *11*, 3242.

400. (a) Fabricant, B.; Muenter, J. S. *J. Chem. Phys.* **1977**, *66*, 5274. (b) Davis, R. E.; Muenter, J. S. *J. Chem. Phys.* **1972**, *57*, 2836. (c) Janda, K. C.; Klemperer, W.; Novick, S. E. *J. Chem. Phys.* **1976**, *64*, 2698. (d) McGurk, J.; Norris, C. L.; Tigelaar, H. L.; Flygare, W. H. *J. Chem. Phys.* **1973**, *58*, 3118. (e) Ewing, J. J.; Tigelaar, H. L.; Flygare, W. H. *J. Chem. Phys.* **1972**, *56*, 1957.

401. (a) Flygare, W. H. *J. Chem. Phys.* **1964**, *41*, 793. (b) Gierke, T. D.; Flygare, W. H. *J. Am. Chem. Soc.* **1972**, *94*, 7277. (c) Jameson, C. J. In *Encyclopedia of Nuclear Magnetic Resonance*; Grant, D. M., Harris, R. K., Eds.; John Wiley & Sons: Chichester, UK, 1996; pp. 1273-1281.

402. Schlier, Ch. *Forschritte der Physik* **1961**, *9*, 455.

403. See reference *345*, caption of Table 7.

404. Boeckh, R. v.; Gräff, G.; Ley, R. *Z. Physik* **1964**, *179*, 285.

405. Note that in general there is no *a priori* reason to conclude that the direct portion of the spin-spin coupling tensor should be greater than the indirect portion. See reference *402*, section 3.3.9 and footnote 20.

406. Muenter, J. S.; Klemperer, W. *J. Chem. Phys.* **1970**, *52*, 6033.

407. Freeman, R. R.; Jacobson, A. R.; Johnson, D. W.; Ramsey, N. F. *J. Chem. Phys.* **1975**, *63*, 2597.

408. Cederberg, J.; Olson, D.; Soulen, P.; Urberg, K.; Ton, H.; Steinbach, T.; Mock, B.; Jarausch, K.; Haertel, P.; Bresnahan, M. *J. Mol. Spectrosc.* **1992**, *154*, 43.

409. Paquette, G.; Kotz, A.; Cederberg, J.; Nitz, D.; Kolan, A.; Olson, D.; Gunderson, K.; Lindaas, S.; Wick, S. *J. Mol. Struct.* **1988**, *190*, 143.

410. van Esbroeck, P. E.; McLean, R. A.; Gaily, T. D.; Holt, R. A.; Rosner, S. D. *Phys. Rev. A* **1985**, *32*, 2595.

411. Kowalewski, J. *Annu. Rep. Nucl. Magn. Reson. Spectrosc.* **1982**, *12*, 81.

412. See also the discussion of the basis-set dependence of the FC contribution in reference *119*.

413. (a) Hollowell, C. D.; Hebert, A. J.; Street, K., Jr. *J. Chem. Phys.* **1964**, *41*, 3540. (b) Gräff, G.; Werth, G. *Z. Physik* **1965**, *183*, 223.

414. König, F.; Weber, H. G. *Chem. Phys. Lett.* **1976**, *44*, 293.

415. Hammerle, R. H.; van Ausdal, R.; Zorn, J. C. *J. Chem. Phys.* **1972**, *57*, 4068.

416. Hammerle, R. H.; Dickinson, J. T.; van Ausdal, R. G.; Stephenson, D. A.; Zorn, J. C. *J. Chem. Phys.* **1969**, *50*, 2086.

417. Dickinson, J. T.; Stephenson, D. A.; Zorn, J. C. *J. Chem. Phys.* **1970**, *53*, 1525.

418. Stephenson, D. A.; Dickinson, J. T.; Zorn, J. C. *J. Chem. Phys.* **1970**, *53*, 1529.

419. O'Reilly, D. E.; Peterson, E. M. *J. Chem. Phys.* **1968**, *49*, 2872.

420. See for example: Hore, P. J. *Nuclear Magnetic Resonance*, Oxford Chemistry Primers, Volume 32; Oxford University Press: Oxford, 1995; p. 43.

421. Blicharski, J. S. *Z. Naturforsch.* **1972**, *27A*, 1355.

422. Brouwer, E. B.; Gougeon, R. D. M.; Hirschinger, J.; Udachin, K. A.; Harris, R. K.; Ripmeester, J. A. *Phys. Chem. Chem. Phys.* **1999**, *1*, 4043.

423. Herzog, K.; Peters, J.; Thomas, B.; Jäger, C. *Ber. Bunsenges. Phys. Chem.* **1996**, *100*, 1655.

424. (a) Ba, Y.; He, J.; Ratcliffe, C. I.; Ripmeester, J. A. *J. Am. Chem. Soc.* **1999**, *121*, 8387. (b) Fyfe, C. A.; Mueller, K. T.; Grondey, H.; Wong-Moon, K. C. *Chem. Phys. Lett.* **1992**, *199*, 198. (c) Blumenfeld, A. L.; Coster, D. J.; Fripiat, J. J. *Chem. Phys. Lett.* **1994**, *231*, 491.

425. Hilborn, R. C.; Gallagher, T. F. Jr.; Ramsey, N. F. *J. Chem. Phys.* **1972**, *56*, 855.

426. Cederberg, J.; Nitz, D.; Kolan, A.; Rasmusson, T.; Hoffman, K.; Tufte, S. *J. Mol. Spectrosc.* **1987**, *122*, 171.

427. Cederberg, J.; Olson, D.; Nelson, A.; Laine, D.; Zimmer, P.; Welge, M.; Feig, M.; Höft, T.; London, N. *J. Chem. Phys.* **1999**, *110*, 2431.

428. Cederberg, J.; Ward, J.; McAlister, G.; Hilk, G.; Beall, E.; Olson, D. *J. Chem. Phys.* **1999**, *111*, 8396.

429. Cederberg, J. *J. Chem. Phys.* **1977**, *66*, 5247.

430. Müller, H. S. P.; Gerry, M. C. L. *J. Chem. Phys.* **1995**, *103*, 577.

431. Wallerand, J.-P.; du Burck, F.; Mercier, B.; Goncharov, A. N.; Himbert, M.; Bordé, Ch. J. *Eur. Phys. J. D* **1999**, *6*, 63.

432. (a) Broyer, M.; Vigué, J.; Lehmann, J. C. *J. Phys.* **1978**, *39*, 591. (b) Landsberg, B. M. *Chem. Phys. Lett.* **1976**, *43*, 102.

433. Razet, A.; Picard, S. *Metrologia*, **1996**, *33*, 19.

434. Yokozeki, A.; Muenter, J. S. *J. Chem. Phys.* **1980**, *72*, 3796.

435. Pyykkö, P; Wiesenfeld, L. *Mol. Phys.* **1981**, *43*, 557.

436. Patchkovskii, S.; Autschbach, J.; Ziegler, T. *J. Chem. Phys.* **2001**, *115*, 26.

437. Spin-orbit (so) correction above and beyond the scalar correction is calculated as $|(J_{iso}(so) - J_{iso}(scalar) / J_{iso}(scalar)|$ x 100 %.

438. Barnes, R. G.; Smith, W. V. *Phys. Rev.* **1954**, *93*, 95, and references therein.

439. Reeves, L. W. *J. Chem. Phys.* **1964**, *40*, 2423 and 2425 and references therein.

440. Whiffen, D. H. *J. Chim. Phys.* **1964**, *61*, 1589.

441. Jameson, C. J.; Osten, H.-J. *J. Am. Chem. Soc.* **1986**, *108*, 2497.

442. Jameson, C. J. In *Isotopes in the Physical and Biomedical Sciences*, Vol. 2; Buncel, E. and Jones, J. R., Eds.; Elsevier: Amsterdam, 1991; Chapter 1.

443. Pervushin, K.; Ono, A.; Fernández, C.; Szyperski, T.; Kainosho, M.; Wüthrich, K. *Proc. Natl. Acad. Sci. USA* **1998**, *95*, 14147.

444. Hennig, M.; Geierstanger, B. H. *J. Am. Chem. Soc.* **1999**, *121*, 5123.

445. Majumdar, A.; Kettani, A.; Skripkin, E. *J. Biomol. NMR* **1999**, *14*, 67.

446. Hennig, M.; Williamson, J. R. *Nucleic Acids Res.* **2000**, *28*, 1585.

447. Dingley, A. J.; Masse, J. E.; Feigon, J.; Grzesiek, S. *J. Biomol. NMR* **2000**, *16*, 279.

448. Pervushin, K.; Fernández, C.; Riek, R.; Ono, A.; Kainosho, M.; Wüthrich, K. *J. Biomol. NMR* **2000**, *16*, 39.

449. Wang, Y.-X.; Jacob, J.; Cordier, F.; Wingfield, P.; Stahl, S. J.; Lee-Huang, S.; Torchia, D.; Grzesiek, S.; Bax, A. *J. Biomol. NMR* **1999**, *14*, 181.

450. Cordier, F.; Grzesiek, S. *J. Am. Chem. Soc.* **1999**, *121*, 1601.

451. Cornilescu, G.; Ramirez, B. E.; Frank, M. K.; Clore, G. M.; Gronenborn, A. M.; Bax, A. *J. Am. Chem. Soc.* **1999**, *121*, 6275.

452. Cordier, F.; Rogowski, M.; Grzesiek, S.; Bax, A. *J. Magn. Reson.* **1999**, *140*, 510.

453. Fierman, M.; Nelson, A.; Khan, S. I.; Barfield, M.; O'Leary, D. J. *Org. Lett.* **2000**, *2*, 2077.

454. Mishima, M.; Hatanaka, M.; Yokoyama, S.; Ikegami, T.; Wälchli, M.; Ito, Y.; Shirakawa, M. *J. Am. Chem. Soc.* **2000**, *122*, 5883.

455. Löhr, F.; Mayhew, S. G.; Rüterjans, H. *J. Am. Chem. Soc.* **2000**, *122*, 9289.

456. Benedict, H.; Shenderovich, I. G.; Malkina, O. L.; Malkin, V. G.; Denisov, G. S.; Golubev, N. S.; Limbach, H.-H. *J. Am. Chem. Soc.* **2000**, *122*, 1979.

457. Del Bene, J. E.; Ajith Perera, S; Bartlett, R. J. *J. Am. Chem. Soc.* **2000**, *122*, 3560.

458. Del Bene, J. E.; Bartlett, R. J. *J. Am. Chem. Soc.* **2000**, *122*, 10480.

459. Pecul, M.; Leszczynski, J.; Sadlej, J. *J. Phys. Chem. A* **2000**, *104*, 8105.

460. Jursa, J.; Kypr, J. *Gen. Physiol. Biophys.* **1993**, *12*, 410.

461. Stilbs, P.; Forsén, S. *Org. Magn. Reson.* **1976**, *8*, 384.

462. Shapiro, B. L.; Kopchik, R. M.; Ebersole, S. J. *J. Chem. Phys.* **1963**, *39*, 3154.

463. Pople, J. A.; Bothner-By, A. A. *J. Chem. Phys.* **1965**, *42*, 1339.

464. Bryce, D. L.; Wasylishen, R. E. *J. Am. Chem. Soc.* **2000**, *122*, 11236.

465. Cowley, A. H.; Kilduff, J. E.; Pakulski, M.; Stewart, C. A. *J. Am. Chem. Soc.* **1983**, *105*, 1655.

466. Harris, K. J.; Wasylishen, R. E. *unpublished results*, **2002**.

467. Schneider, C.; Dräger, M. *J. Organomet. Chem.* **1991**, *415*, 349.

468. Tjandra, N.; Bax, A. *Science* **1997**, *278*, 1111.

469. Wu, Z.; Tjandra, N.; Bax, A. *J. Am. Chem. Soc.* **2001**, *123*, 3617.

470. Gan, Z.; Gor'kov, P.; Cross, T. A.; Samoson, A.; Massiot, D. *J. Am. Chem. Soc.* **2002**, *124*, 5634.

471. McDermott, R.; Trabesinger, A. H.; Mück, M.; Hahn, E. L.; Pines, A.; Clarke, J. *Science* **2002**, *295*, 2247.

472. Service, R. F. *Science* **2002**, *295*, 2195.

473. Gaemers, S.; van Slageren, J.; O'Connor, C. M.; Vos, J. G.; Hage, R.; Elsevier, C. J. *Organometallics* **1999**, *18*, 5238.

474. Reger, D. L.; Mason, S. S.; Rheingold, A. L. *J. Am. Chem. Soc.* **1993**, *115*, 10406.